UNIVERSIDADE DE LISBOA
FACULDADE DE CIÊNCIAS
DEPARTAMENTO DE GEOLOGIA

Hydroclimate of Western Iberia over the last 2000 years: Insights from leaf wax *n*-alkanes of Lake Peixão sediments (Serra da Estrela, Portugal)

Ricardo Alexandre Neves dos Santos

Mestrado em Geologia
Especialização em Estratigrafia, Sedimentologia e Paleontologia

Dissertação orientada por:
Doutor Alexandre Ramos e Doutora Teresa Rodrigues

2021

"*Geology is like a book whose pages recount tales of the Earth's history.*
Each copy of this book has some pages missing.
Fortunately, the American, African, Asian, Australasian, and European editions all miss different pages.
Combining them lets us assemble a good picture of how Earth's climate has changed through time."
–Colin P. Summerhayes, 2015 (Earth's Climate Evolution)

ACKNOWLEDGMENTS

This section was the very last written part of this thesis and was especially difficult to finish… I might have forgotten to mention some key aspects or people, nevertheless, I know you know how grateful I am.

I would like to express my deepest gratitude to the people directly involved in this work whose insights and discussion make this experience truly enjoyable. But first of all, I would like to thank my family, for all the moral and financial support given, and to dedicate this thesis to two special persons: Aos manos Cremelinda e Pedro, duas almas gémeas e muito puras que partiram quase ao mesmo tempo no meio deste meu percurso, guardarei para sempre o vosso sorriso no fundo do meu coração. Obrigado Avó 'Calinda' e 'TiPedro'.

A big Thank You to my supervisors Teresa Rodrigues and Alexandre Ramos, for being so friendly and supportive throughout this time, not only related to the present work but also other aspects. To my 'non-official supervisors' Filipa Naughton and Armand Hernández, which deeply contribute to the brainstorming behind (the many versions of) this thesis. To Mária Padilha for all the practical work and teaching in the BioGeoLab. To Enno Schefuß for the willingness to contribute with the compound-specific isotopic analysis and general discussion on the *n*-alkane signal.

To Pedro Costa and Vera Lopes, a special thanks, for 'showing me the light' in such a good moment, and for getting me involved in so many different projects and activities.

To 'HOLMODRIVE' project, which granted me a research fellowship and the free use of the project's data, besides getting me evolved in such multidisciplinary environment between two great institutions: Instituto Dom Luiz (IDL) and Instituto Português do Mar e da Atmosfera (IPMA). From the project people, a special thanks to Dulce Oliveira and Filipa Naughton for the pollen counting, Manel Leira for the diatom data and hosting me in the University of A Coruña during my Erasmus+, Sandra Gomes for the assist in the age modeling and paper sharing, Alexandre Ramos for the blog post at EGU, Ricardo M. Trigo for getting me involved in the College on Polar and Extreme Environments (POLAR2E) and the desk office at IDL (which I unfortunately only used a couple of times due to the pandemic).

To the people directly involved in the sediment core field campaign in Lake Peixão, Serra da Estrela: Alexandre M. Ramos, Ricardo M. Trigo, Armand Hernández, Pedro Raposeiro, Pedro Costa, Santiago Giralt, Alberto Ruiz, and Gonçalo Vieira and Filipe Patrocínio for the support as members of the Estrela Geopark.

From IPMA, needless to say, a special thanks to my dear supervisor Teresa Rodrigues and Filipa Naughton for such a commitment and for inciting my profound passion for paleoclimatology! Thanks to the whole Paleoceanography and Paleoclimate group, in special to Dulce Oliveira, Lívia Geraba, Antje Voelker, Vitor Magalhães, Fátima Abrantes for seeding me so many papers, courses, opportunities, etc. Emília Salgueiro and and Isabelle Gil for the sympathy. Last but not the least, a big 'obrigadinho' to my dear and funny colleagues of 'sala dos bolseiros' (Mafalda Freitas, Warley Soares, Andreia Rebotim, Ana Lopes, Lélia Matos, Marta Salvado, André Santana, Sónia Silva, Aline Mega).

From the department of Geology - FCUL, in both my undergrad and my post-graduations, a special thanks to the enthusiastic professors which I found particular empathy and have learned a lot, such as Rui Taborda, Isabel R. Costa, Rui Baptista, Nuno Pimentel, João Mata, Francisco Fatela, Mário Cachão, César Andrade.

And of course… I am grateful to all the friends and people that I met while living in the beautiful city of Lisbon. Some of them I was lucky enough to build an authentic and great connection which I know will never be lost, thank you for all Marta Almeida, Fábio Neves, and José Xieto. Back in my hometown (Abrantes, a.k.a, Abrantexas), aquele abraço to my brothers-in-arms.

This thesis had the direct or indirect financial support of the following projects:

HOLMODRIVE (PTDC/CTA-GEO/29029/2018)
WarmWorlds (PTDC/CTA-GEO/29897/2017)
Ultimatum (F/01489/2015)
ENSOPT (POCI-01-0145-FEDER-022157)

ABSTRACT

Located between the temperate and arid climate of Europe and North Africa, Iberia is a key location to study the past climatic dynamics, such as the variations in the North Atlantic Oscillation (NAO) which predominantly control the Iberian hydroclimate.

This study focuses on the leaf wax *n*-alkanes signal (distribution and compound-specific isotopic signal) of Lake Peixão sedimentary record, which allowed for the first time a high resolution (decadal-scale) climate reconstruction of the last 2000 years in Serra da Estrela (Portugal). Our data shows that the *n*-alkane signal is dominated by odd long-chain compounds derived from higher plants of the watershed, with the C_{31} being the preferentially produced compound in the whole record. This pristine record shows that the variance of *n*-alkane concentration in the sediments has a remarkable teleconnection between solar variability and NAO.

The inferred climate reconstruction based on the *n*-alkane signal shows a relatively stable lake ecosystem under dry conditions during the Roman Period (0 – 500 AD), where is assumed a predominant positive NAO phase and Grand solar maxima. From Dark Ages until Medieval Climatic Anomaly (500 – 1300 AD) the climate was generally milder and wetter, with the second period being particularly unstable under an inferred nonstationary behavior of the NAO. The Little Ice Age (1350 – 1850 AD) registered a first phase of cold and wet conditions and a second particularly cold (centered at 1700 AD) under a predominant negative NAO phase, Grand solar minima, and a strong influence of the polar front. These conditions abruptly changed at ca. 1880 AD, with the climate turning to the current warm and dry conditions, under stronger seasonality, and indications of anthropogenic footprint and possible lake eutrophication.

This work reinforced the sensitive nature of the alpine ecosystems and contributed to the spatial coverage of the Iberian paleoclimate studies.

Keywords: Leaf wax *n*-alkanes; Hydroclimate reconstruction; Last 2000 years; Western Iberia; High-mountain lake

RESUMO

A Península Ibérica é uma das regiões da Europa mais vulneráveis às alterações climáticas, com eventos climáticos extremos cada vez mais severos e prolongados. Localizada entre o clima temperado da Europa e a aridez do Norte da África, a Península Ibérica é um local chave para estudar a dinâmica climática do passado e seus impactos no meio ambiente e ecologia. Devido à sua latitude média e por estar situada entre o Oceano Atlântico e o Mar Mediterrâneo, a Península e Margem Ibérica é considerada uma região estratégica para o estudo das interações oceano-atmosfera- continente, fundamentais para modelar os efeitos das mudanças climáticas e ajudar a mitigar o seu impacto no ambiente e na sociedade.

O hidroclima do oeste da Península Ibérica é particularmente controlado pelas flutuações do padrão atmosférico conhecido como Oscilação do Atlântico Norte (NAO, na sigla em inglês). A NAO tem uma grande influência na distribuição das massas atmosférica sobre o Atlântico Norte, exercendo um forte controle sazonal da precipitação no norte e sul da Europa. O índice da NAO tem por base o gradiente de pressão atmosférica ao nível do mar entre a zona de baixa pressão localizada perto da Islândia (depressão da Islândia) e a zona de alta pressão localizada entre o arquipélago dos Açores e a Península Ibérica (anticiclone dos Açores). Fases persistentemente negativas (positivas) da NAO geralmente levam a um aumento (diminuição) significativo na precipitação de inverno na Península Ibérica. Uma fase persistente da NAO pode promover alterações significativas nos ecossistemas ibéricos, deixando marcas nos registos geológicos, como diversos estudos têm demonstrado nas últimas décadas. No entanto, no que diz respeito à cobertura espacial destes estudos paleoclimáticos, existe um claro défice na zona oeste da Península Ibérica, sobretudo a nível de estudos em lagos de alta montanha onde a escassez destes registos promove uma maior dificuldade em compreender os efeitos das mudanças hidrológicas no espaço e no tempo.

Com o objetivo de avaliar as mudanças no hidroclima do passado e encontrar, ou confirmar, os principais fatores controladores do clima na região, foi estudado um registo sedimentar de um lago de alta montanha no oeste da Península Ibérica, concretamente na Lagoa do Peixão localizada no topo da Serra da Estrela (Portugal). Este estudo foca-se principalmente no sinal dos *n*-alcanos, compostos maioritariamente derivados das ceras foliares das plantas, cuja distribuição e sinal isotópico permitiu inferir pela primeira vez uma reconstrução climática de alta resolução (escala decadal) dos últimos 2000 anos na região.

Este registo mostra que o sinal dos *n*-alcanos é dominado por compostos ímpares de cadeia longa derivados da vegetação oro-mediterrânica presente na área de captação do lago. O tipo de vegetação não mudou significativamente ao longo do registo e do que é atualmente observado, ou seja, charnecas dominadas por formações arbustivas de urzais, zimbrais e giestais, intercaladas por mosaicos de gramíneas, onde se formam os escassos solos do planalto da Serra da Estrela. O C_{31} é o *n*-alcano preferencialmente produzido pela vegetação moderna e dominante em todo o registo sedimentar, controlando fortemente a concentração de *n*-alcanos nos sedimentos, e consequentemente os diferentes estágios biogeoquímicos aqui inferidos. Os homólogos C_{29} e C_{27} são os segundos compostos dominantes, cuja proporção relativa é mais variante, e o C_{33} apresenta também concentração significativas. A análise de componentes principais do total de *n*-alcanos de cadeias ímpares, em conjunto com o sinal isotópico específico destes compostos, revelou-se especialmente útil para constranger e avaliar a respostas da vegetação às mudanças climáticas. Onde se destaca as correlações significativas entre o primeiro componente principal e a mais recente reconstrução da NAO feita na Península Ibérica Central, bem como as reconstruções de radiação solar total.

É observada uma tendência geral de aridificação na região através do sinal δD dos *n*-alcanos analisados, no entanto são observadas oscilações significativas na disponibilidade de água, que aparenta ser fortemente controlada pela temperatura no topo da Serra da Estrela. O início do registo sedimentar mostra um ecossistema de lago relativamente estável, a vir de um período relativamente húmido para um período sob condições mais secas, provável sob um progressivo rebaixamento do nível médio das águas do lago, que compreendem o Período Romano (de ca. 0 – 500 AD). Todo Período Romano está em linha com uma fase predominantemente positiva da NAO, e grande irradiação solar que começou a diminuir gradualmente depois de ca. 500 AD. No entanto, também existe estágios biogeoquímicos cuja principal diferença se cifra na variação de temperatura,

como no estágio A (ca. 0 – 210 AD) sendo mais quente que o B (ca. 210 – 450 AD). Na idade média, durante os períodos climáticos conhecidos como "Idade das Trevas" (*Dark Ages* ou *Early Middle Ages*) e a "Anomalia Climática Medieval" (500 – 1300 AD), envolvendo os estágios C (ca. 450 – 830 AD) e D (ca. 830 – 1110 AD), o clima foi geralmente mais ameno e húmido, convergindo para o que é geralmente inferido em outros registos do Noroeste/Norte da Península Ibérica. O ecossistema do lago registou um evento abrupto a meio da Anomalia Climática Medieval, ca. 1145 AD, aparentemente, marcando o início da fase de transição entre a Anomalia Climática Medieval a Pequena Idade do Gelo, que compreende o estágio E (ca. 1110 – 1490 AD). Esta transição aparenta ser concomitante com uma NAO mais instável, descida da temperatura das águas superficiais do Oceano Atlântico e aparentemente coesa com um ponto inflexão a nível do número de manchas solar, i.e., atividade solar. A Pequena Idade do Gelo (ca. 1350 – 1850 AD) regista aqui duas fases, sendo o segundo intervalo centrado a ca. 1700 AD (estágio F [ca. 1490 – 1880 AD]) o mais frio do registo em estudo, onde a fase da NAO foi predominantemente negativa, é inferido uma forte influência da frente polar e é coincidente com o Mínimo de Maunder (ou *The Maunder Minimum*). A maior precipitação espectável durante esta fase foi possivelmente "mascarada" devido à localização e pequena dimensão do lago, onde os efeitos da cobertura de neve persistente e do lago congelado imprimiram as condições aparentemente secas em diferentes indicadores. Essas condições mudaram abruptamente a partir de ca. 1880 AD, com o início da Era Industrial, materializado pelo estágio G (ca. 1880 AD – presente), com o ecossistema do lago e o clima a adquirirem as condições modernas, i.e., condições mais quentes e secas, sob forte sazonalidade, crescente fase positiva da NAO e aumento da atividade solar. Concomitantemente, existem evidências para um aumento significativo nas atividades antrópicas no topo da Serra da Estrela durante este estágio, afetando significativamente a bacia hidrográfica da Lagoa do Peixão. Estas atividades são possivelmente relacionadas com um aumento da atividade pastorícia, que promoveu o aumento de degradação da matéria orgânica, aumento da taxa de sedimentação e onde existe indicação para um aumento dos processos de eutrofização da lagoa do Peixão ou dos pequenos charcos na sua envolvente.

Este trabalho sugere uma ligação entre da atividade solar, a a variabilidade NAO e a resposta da vegetação do topo da Serra da Estrela à variabilidade climáticas, aqui inferidas através do sinal dos *n*-alcanos produzidos nas suas ceras foliares. Estas compostos estão muito bem preservados nos sedimentos do Lago Peixão e são aqui sugeridos como uma importante ferramenta para estudos do clima do passado, principalmente no que diz respeito ao hidroclima. Este estudo reforça a natureza sensível dos ecossistemas alpinos e o aumento da cobertura espacial de estudos paleoclimáticos na Península Ibérica.

Palavras-chaves: *n*-alcanos de cera foliares; Hidroclima; Últimos 2000 anos; Ibéria Ocidental; Lago de alta montanha

CONTENTS

LIST OF FIGURES

LIST OF TABLES

ABBREVIATIONS AND ACRONYMS

a.k.a – Also known as
a.m.s.l – above mean sea level
ACL – average chain length
ACA – Abrupt changes analysis
AD – Anno Domini
AHP – African Humid Period
AMOC – Atlantic Meridional Overturning Circulation
APO – nonpolar fraction
BP – Before Present, where present is established by geologists and paleoclimatologists as 1950.
brGDGTs – branched glycerol dialkyl glycerol tetraethers
ca. – circa
cal – Calibrated
cc – cubic centimeters
CPI – Carbon Preference Index
CSSI – Compound-Specific Stable Isotope
DCM – Dichloromethane
D-O – Dansgaard–Oeschger
DOC – Dissolved Organic Carbon
EA – East Atlantic pattern
EMA – Early Middle Ages
ENSO – El Niño–Southern Oscillation
GHG – Greenhouse gases
Hex – Hexane
IP – Iberian Peninsula
IPCC – Intergovernmental Panel on Climate Change
IPMA – Portuguese Institute of the Sea and the Atmosphere
IR – Industrial Revolution
ITCZ – Inter-Tropical Convergence Zone
ka – kilo annum (thousands of years BP)
LIA – Little Ice Age
MAP – Mean Annual Precipitation
MCA – Medieval Climate Anomaly
MHT – Mid-Holocene Transition
MWP – Medieval Warm Period
NADW – North Atlantic Deep Water
n-Alk – *n*-Alkanes
NAO – North Atlantic Oscillation
NH – North Hemisphere
OM – Organic Matter
PAHs – Polycyclic Aromatic Hydrocarbons
P_{aq} – Proportion of Aquatic plants index
PC – Principal Component
PCA – Principal Component Analysis
Pol – Polar fraction
RP – Roman Period
RPLs – Relative Percentage of Long-chain *n*-alkanes
RPM – Revolutions Per Minute
SCAND – Scandinavia pattern
SR – Sedimentation Rate
SST – Sea Surface Temperature
TLE – Total Lipid Extraction
TOC – Total Organic Carbon
TSI – Total Solar Irradiance
VPDB – Vienna Pee Dee Belemnite
vs. – versus
VSMOW – Vienna Standard Mean Ocean Water
YD – Younger Dryas
δD_{aq} – δD signal of leaf wax *n*-alkanes derived from aquatic plants
δD_{terr} – δD signal of leaf wax *n*-alkanes derived from terrestrial plants
δD_{wax} – δD signal of leaf wax *n*-alkanes
ε_{bio} – biosynthetic fractionation
XRF – X-Ray Fluorescence

1. INTRODUCTION

1.1. Motivation and main objectives

Paleoclimatology is a broad and multidisciplinary field of science studying the past climate by reading and understanding natural phenomena capable of registering meaningful information about the climate. Following the Ruddiman, W. (2013) definition, "*climate is a broad composite of the average condition of a region, measured by its temperature, amount of rainfall or snowfall, snow and ice cover, wind direction and strength, and other factors. Climate change specifically applies to longer-term variations (years and longer), in contrast to the shorter fluctuations in weather that last hours, days, weeks, or a few months*".

Understanding how the climate system has changed in the past requires a wide range of well-dated paleoclimate data. Paleoclimate data provide ground-truth evidence of how the climate dynamics worked in both magnitude and frequency across the different spatiotemporal scales. Studying the past climate is a crucial component in evaluating the robustness of climate models and increasing confidence in future climate projections.

This thesis focuses on critical hydroclimate processes and climatic anomalies of Western Iberia. Here a sedimentary lake record from Serra da Estrela (Portugal) was used to infer how the vegetation has changed through leaf wax *n*-alkanes signal. Those changes were used to reconstruct the climate evolution of the region over the last 2000 years. The study of past climate conditions is especially critical since, despite the increasing number of studies on Iberian high-lakes records, there is still a paucity of suitable archives in this region, which hampers the understanding of how major climate drivers impacted the region and the spatial coherence of regional climate periods.

With this thesis it is intended to answer the following focal points and scientific questions:

(1) To thoroughly characterize leaf wax *n*-alkanes and their compound-specific isotopic signal in the Lake Peixão sediments.

(2) Reconstruct the past climate, focusing on the hydrology based on the *n*-alkane signal, modern baselines, and cross-validation with other independent proxies.

(3) How sensitive is the Lake Peixão ecosystem, the *n*-alkanes, to register climate and/or environmental changes over the last 2000 years?

(4) What are the main climate drivers promoting the observed changes in the sedimentary record?

Therefore, this thesis is briefly summarized as follows:

Chapter 1: The theoretical framework of Earth's climate system, from a global to a regional scale, addressing different timescales and main events for the Holocene. It will be emphasized how atmospheric circulations impacts the western Iberia hydroclimate, characterized the most well-known late Holocene climate anomalies (or regional periods) in Iberia, and summarized the different paleoclimate archives and proxy-based indicators, with a focus on lake sediments, leaf-wax biomarkers and their isotopic signal.

Chapter 2: Characterization of the study area and its importance for climate and environmental research. Reviewing the current state-of-art knowledge in terms of climate and bioclimate conditions over the last 2000 years.

Chapter 3: This chapter will primarily describe the methodology behind the sedimentary *n*-alkane extraction and analytical conditions and the different methods behind the data analysis, such as correlation, principal component analysis, and abrupt changes.

Chapter 4: Characterization of results of the prior mentioned methods of **Chapter 3**. A detailed *n*-alkane characterization of modern vegetation and the sedimentary signal, in terms of concentration, compound range distributions, and proportion of the main *n*-alkanes.

Chapter 5: This chapter provides a novel discussion about the leaf wax *n*-alkanes in Serra da Estrela both in modern vegetation and the upper 120 cm of lake Peixão sediments. Integration and cross-validation of different proxy-based indicators. How the vegetation in the lake catchment area has changed through time and how that information was used to infer a conceptual climate model.

Chapters 6 and 7: The main findings and hypothesis. How hydroclimate changed in general terms in the last 2000 years and the possible factors behind those changes. A series of follow-up studies or questions are suggested to enlighten possible future works.

1.2. The Earth's climate system

The Earth's climate system is driven by the continuous interactions between Earth's 'spheres' or subsystems (atmosphere, hydrosphere, cryosphere, biosphere, and lithosphere) and external forcing such as solar energy and astronomical positioning (Ruddiman, 2013).

Primarily controlling Earth's climate system is the energy-driven from the Sun. This energy comes in two categories: solar radiation (insolation) and solar wind (Tsuda et al., 2016). Being the first one is the most important to the following issues.

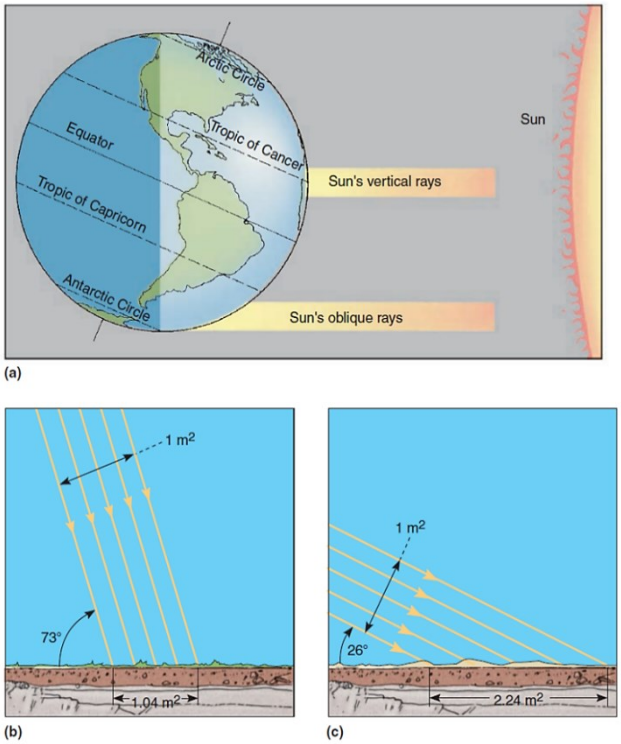

Figure 1.1 – Solar radiation variation depending on Earth's latitude and astronomical positioning determines the amount of solar energy received per area. (a) The June condition (summer in the northern hemisphere), when the Tropic of Cancer receives 90° angle of insolation; (b) and (c) Insolation angle of 73° and 26° respectively, leading to different energy intensity on Earth's surface. From: Gabler, et al. (2008).

Solar energy is not equally distributed on Earth's surface, which is mainly evident by latitudes discrepancies in insolation. Low latitudes receive more energy than high latitudes (Fig. 1.1a) due to the more direct (or higher) angle of insolation that leads to a higher energy per area unit (Fig. 1.1b and 1.1c) and less reflection. This angle is determined by astronomical positioning.

The unevenly distributed energy conducts the perpetual thermodynamics and mass rearrangement that is mainly controlled by winds and ocean currents. Moreover, the different subsystem interactions eventually generate different weather and seasonal conditions in other regions of the planet. The long-term average weather conditions of a region define the climate.

The role of the different subsystems depends considerably on their response time to changes and capability to store and transport mass and energy (Houghton et al., 2001[IPCC]). This subject is of great complexity as all the sub-systems are intimately inter-linked (or coupled). Changes in one subsystem may result in significant changes throughout the entire climate system (Bradley, 2015).

The interaction between climatic subsystems and feedback mechanisms on the climate system have positive or negative effects, depending on the tendency to reinforce or dampen the changes. Understanding the feedback mechanisms is crucial to comprehend the climatic system, which is often nonlinear. One good example evolves the effect of the different ranges of Earth's surface albedo (percentage of reflected insolation) (Fig. 1.2), e.g., fresh snow or ice (60-90), clouds (40-90), desert sand (30-50), grasslands (18-25), forests (5-20), water (5-10), etc. (Ruddiman, 2013 and references therein). With more solar radiation reflected from this surface, the reduction in absorbed heat leads to further cooling. Other important feedbacks include greenhouse gases (e.g., water vapor, CO_2, CH_4, O_3, etc.)

and bio/geochemical cycles that have the capacity to exchange carbon among subsystems (e.g., plant growing through photosynthesis) that will subsequently analyze (Houghton et al., 2001[IPCC]).

Earth's atmosphere and hydrosphere are the promptest to react to changes in the climate system since they have a relatively low heat capacity and are strongly connected being the climate's 'gears' (Rahmstorf, 2003). For instance, when heat warms the air, it expands, becomes less dense, and tends to rise. In its turn, the cooler air tends to sink. The same happens with water, even though at a much sluggish rate. Because it often also involves differences in salinity with salty water getting denser than freshwater, the term *thermohaline* (Fig. 1.3) is applied to that transport, where 'thermo-' is referred to temperature and '-haline' to salinity (Bryan, 1986).

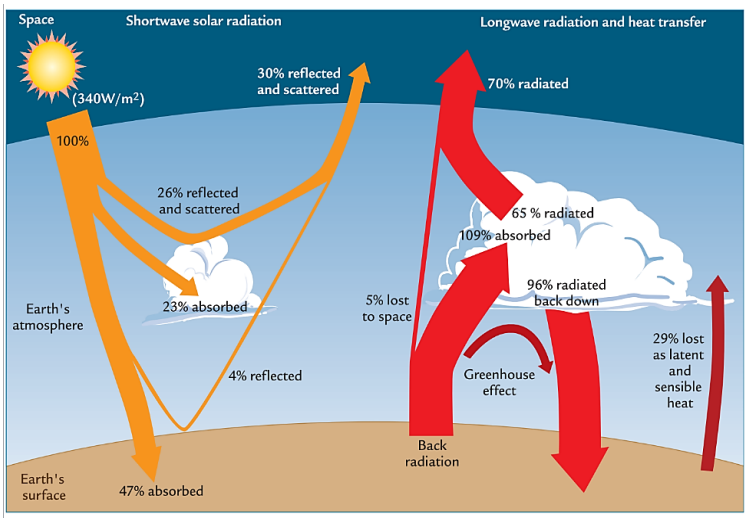

Figure 1.2 – Solar radiation striking Earth, indicated in 100% in orange, and the different reflections and absorptions in the climate system. From: Ruddiman., 2013.

The oceans —covering about 70% of the planet— play a critical role in the chemical balance of the atmospheric system, for instance, regarding the atmospheric CO_2 levels. Since oceans contain large quantities of this gas in solution, just as a slight change in the oceanic CO_2 content may have profound consequences Eath's climate (Bradley, 2015).

The land surface, which makes up about 30 percent of Earth's total surface area mostly present in the Northern Hemisphere 50º – 70ºN and poleward of 70ºS (Bradley, 2015). Its surface characteristics affect the way it absorbs solar energy or releases it into the atmosphere.

Earth's orography also plays a role in the climate system because the atmosphere becomes steadily cooler up at high altitudes. This effect, coupled with the above-mentioned low angles incidence at high latitudes, causes the snow line (the elevation above which snow does not completely melt in summer) to decrease toward the poles, impacting the albedo generally. Besides, moist air masses facing mountain ranges block its flow, are forced to rise to higher elevations, cool and causing water vapor to condense and produce heavy precipitation (orographic precipitation) on the sides of mountains that face upwind (Grotzinger and Jordan, 2014). Therefore, land geographic location and morphology of landmasses—a direct consequence of plate movements— affect air masses movement and is responsible for hemispheric asymmetries in the global climate system, capable of creating located settings like Monsoon variations.

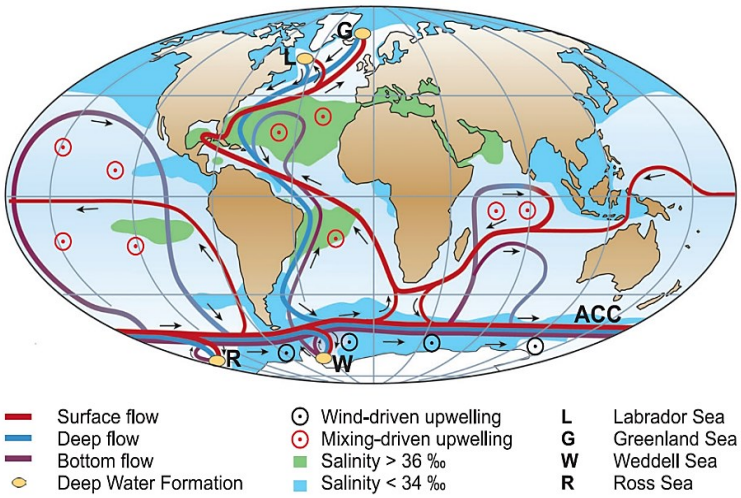

Figure 1.3 – Schematic representation of the global thermohaline circulation. Surface currents are shown in red, deep waters in light blue and bottom waters in dark blue. Where ACC corresponds to the Antarctic Circumpolar Current. The main deep-water formation sites are shown in yellow. From: Rahmstorf, 2006.

Thermohaline and wind-driven currents have non-linear and interlinked interactions driven by two distinctive physical forcing mechanisms. For instance, wind pressure changes can alter the thermohaline circulation and vice-versa (Rahmstorf, 2006).

The circulation patterns of prevailing winds and ocean currents encompass vertical and horizontal movements, an important means of energy transport on the globe. Ideally, without the influence of landmasses and other seasonal variations, the global atmospheric model is defined as shown in figure 1.4.

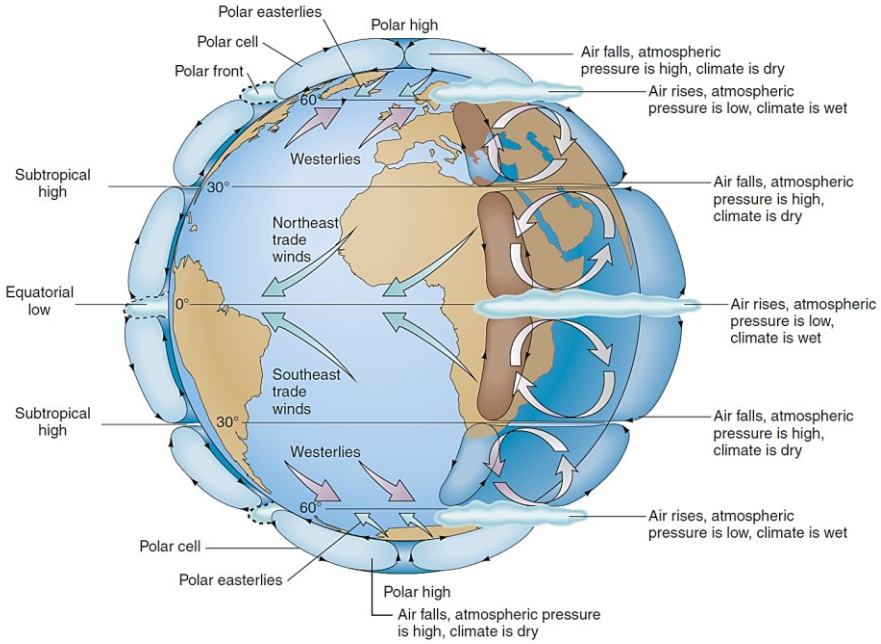

Figure 1.4 – The general circulation model for Earth's atmosphere. Noting worth noting the different pressure zones and prevailing winds systems depending on the latitude. From: Gabler et al., 2008.

The prevailing winds blowing across the oceans generate large-scale surface currents, many of those with assigned names (Fig. 1.5), together with the thermohaline circulation, control significant the temperature and salinity, precipitation, salt expulsion from the sea-ice, runoff, etc., in the globe (Boyle and Keigwin, 1987). Combined with Earth's rotation, these gradients produce an asymmetric transporting of both energy and mass around the planet, resulting in the different climate regions (Bradley, 2015, and references therein).

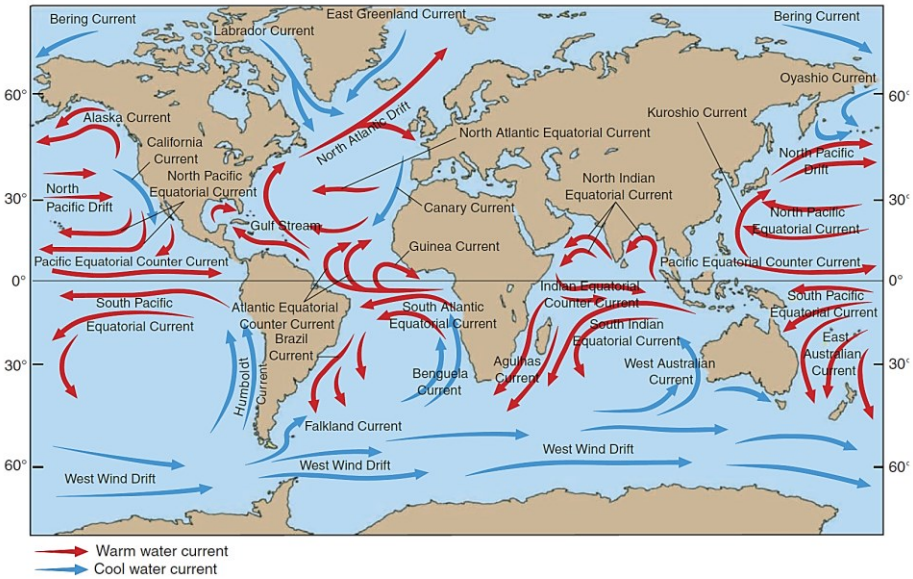

Figure 1.5 – Main currents wind-driven currents at the surface of the oceans. Currents moving out of the tropics carry heat poleward (red arrows), while cool currents (blue arrows) carry away from the poles cold water equatorward. From: Gabler et al., 2008.

1.2.1. Major climate forcing

According to Ruddiman (2013), three external forcings affect the Earth's climate system significantly, both in the long and short-term (see Fig. 1.6):

- Tectonic processes
- Changes in Earth's orbit around the Sun
- Changes in the strength of the Sun

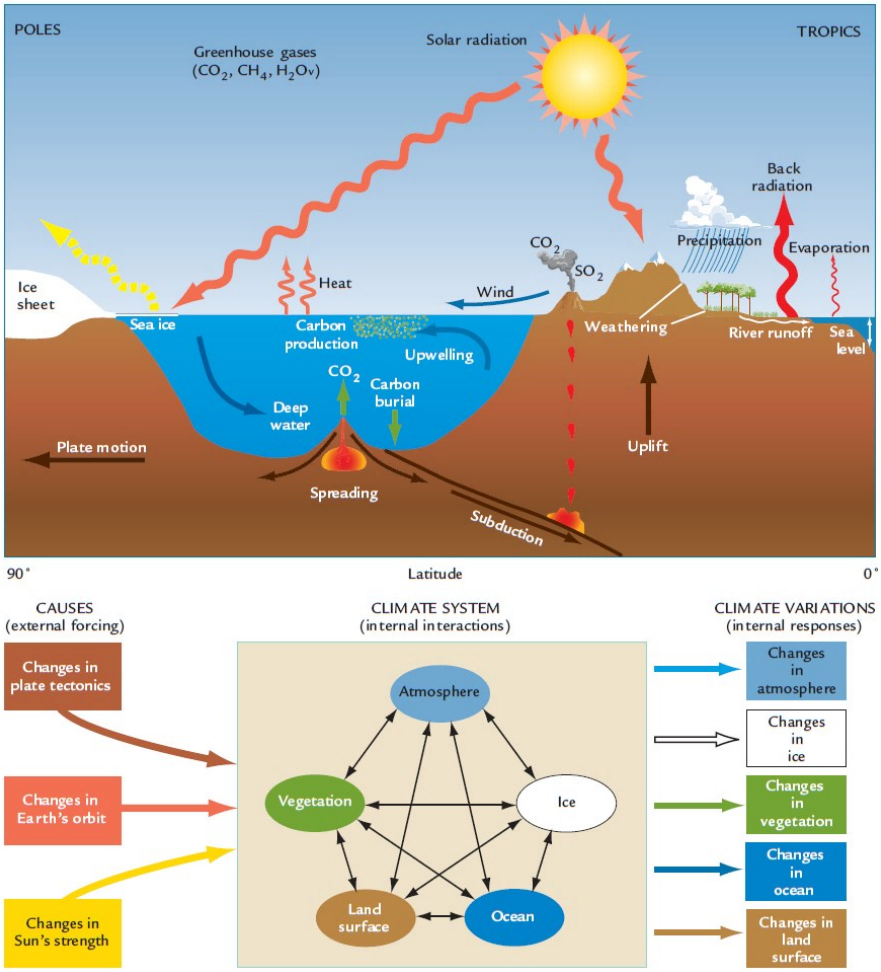

Figure 1.6 – Earth's climate system and interactions of its components Studies of Earth's climate cover a wide range of processes, indicated at the top. Climate scientists organize and simplify this complexity, as shown at the bottom. These factors cause interactions among the internal components of the climate system (air, water, ice, land surfaces, and vegetation). The results are measurable variations known as climate responses. From: Ruddiman., 2013.

The changes in the above-mentioned external forcings will induce different feedback responses and climate variations in space and time, based on a complex net of internal interactions of the other parts of the climate system.

Sun strength

The solar variability, which affects the insolation arriving at the Earth's surface, will be further detailed due to this work's scope and temporal scale.

The Sun is the most significant external source of energy to the Earth's surface. Therefore, any slight change in its radiative output affects the energy balance of the Earth's surface and atmosphere and, consequently, the Earth's climate (Solanki, 2002).

The sun is a sphere of gases that emits radiant energy from the long-term fusion rate of hydrogen to helium happening in its core (Fig. 1.7). The combination of two hydrogen atoms fuses to form one helium atom (Gough, 1977). Sun has slowly increased the amount of solar radiation throughout its lifetime, with its primordial stages radiating ~ 25-30% less energy than what is observed today, explained by the evolution of thermonuclear reaction in the Sun's core, and is the basis of the 'faint young Sun paradox' (Gough, 1981; Gribbin, 1991; Feulner et al., 2012). However, despite this very long-term feature, other variations occur in the Sun, capable of producing random (noncyclic) and cyclic energy variations (Solanki, 2004).

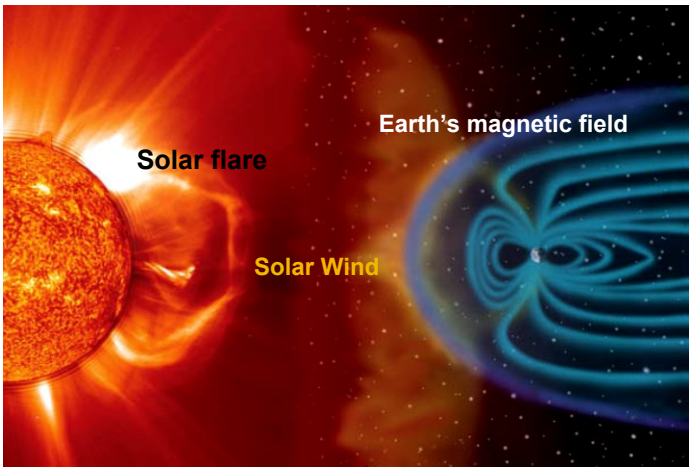

Figure 1.7 – Earth's magnetic field shielding Earth's surface from harmful radiation. Solar wind containing highly energetic charged particles, which distorts Earth's magnetic field lines, shown here in light blue. The distances in this picture are not to scale. [SOHO (ESA and NASA).] Adapted from: Grotzinger and Jordan, 2014

The outer-most layer of the atmosphere of the Sun, the corona (or crown), is constantly changing its shape by charged particles (plasma or ionized gas) trapped by the solar magnetic field. These particles can flow beyond the magnetic field into space as solar wind (see Fig. 1.7) (Galvin et al., 1996). Sunspots influence the intensity of these solar winds, dark regions in the Sun (Fig. 1.8) that are cooler than their surrounding areas thought to be linked with the magnetoconvection within the solar core (e.g., Solanki, 2004).

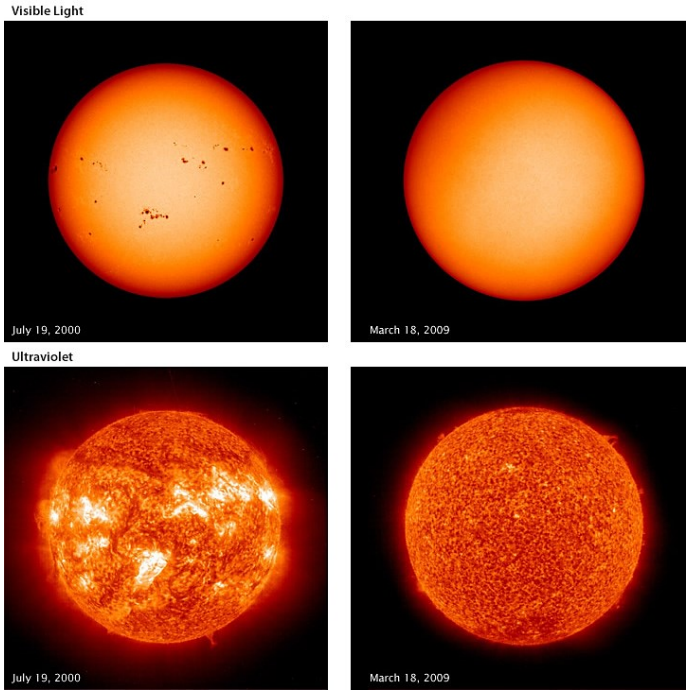

Figure 1.8 – A view of the Sun in visible light (upper images) and ultraviolet (lower images) comparing July 19, 2000 in both (left side image) high solar activity, with numerous sunspots, and March 18, 2009 (right side pictures) low solar activity with an almost sunspots free surface.[Image courtesy SOHO, EIT Consortium, and the MDI Team] From: https://www.climate.gov/news-features/understanding-climate/climate-change-incoming-sunlight

The presence of sunspots is inversely correlated with solar magnetic activity and, therefore, the shielding effect of the magnetosphere on the Earth (Fig. 1.8) (Lean, 2000). Thus, during years of abundant (reduced) sunspots, the sun is more (less) active.

The solar activity can have a distinct cyclicity, or sunspot cycles, one of the most well-known and studied is the 11-year cycle (a.k.a Schwabe sunspot cycle) (Lean, 1995). The modulation of 11-year cycle amplitude may control many other solar cycles, such as the 22-year Hale cycle (or double sunspot), the 88-year (Gleisberg cycle), the ~200-220 year (Suess cycle). There are also other longer time scales, the ~1,000-year and the ~2,200-year cycles (Hallstattzeit cycles) (Chambers and Blackford, 2001, Ogurtsov et al., 2002; Turner et al., 2016, Moreno, 2017 see references therein).

Recent satellite radiometer measurements estimated that oscillations on the 11-year cycle can have a significant impact on the total solar irradiance, as much as ca. 0.11% (Lean, 2010), which can significantly impact the mean global temperatures and global climatic system. Thus, reconstructing solar activity beyond instrumental measurements can provide important insights into the past and future climate. Moreover, the spectral irradiance and interactions between the solar wind and Earth's stratosphere can affect, for instance, the intensity of aurora borealis, the ozone layer chemistry, cloud formation, etc., which in turn can disturb the

earth climatic system in many ways, such the meridional pressure gradient in the North Atlantic (Haigh, 1994; Dean, 1997; Lockwood et al., 2001; Gray et al., 2010; Bender, 2013). Another remarkable example effect of solar variability is the ^{14}C and ^{10}Be isotopic production in the Earth's upper atmosphere, which have been widely used as a proxy to assess past solar activity/sunspots numbers (e.g., Usoskin et al., 2016).

For instance, Figure 1.9 shows the spikes of ~11 year-cycles, where is also evident two periods with a significantly reduced number of sunspots, one from ca. 1645–1715, a.k.a the Maunder Minimum period and the other from 1790–1830 (Dalton Minimum) (see Steinhilber et al., 2012). This period has been linked with a short-term cold period, 'Little Ice Age' (Porter, 1981; Solanki, 2002), which will be further analyzed in chapter 1.3.

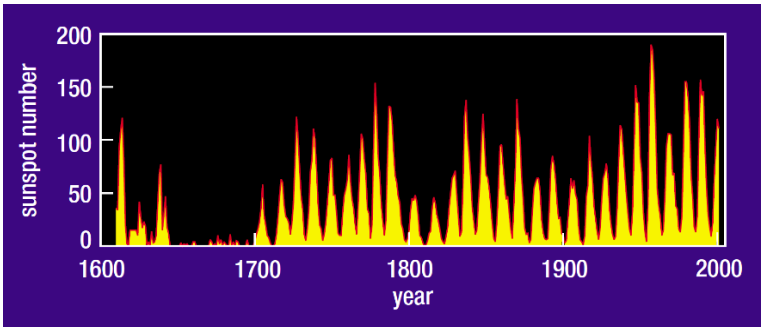

Figure 1.9 – Solar activity cycles measured by sunspots number. Distinctive period of roughly 11 years, with difference in amplitude. From 1600's years, since the beginning of telescopic observations to 2000's. From: Solanki, 2002

Climate variability timescale spectrum

The interaction and changes in internal and external climate factors fluctuate over a wide range of timescales (see Fig. 1.10) which can be at centurial scale or less. The most prominent example is the scaling behavior of the energy cascade in the very short-period (minutes or hours) atmospheric processes such as turbulence, which act as white noise to the more extended climate spectrum. Superimposed on the general climate background noise are specific peaks in the variance spectrum that correspond to forcing mechanisms operating over a restricted time domain (*i.e.,* periodic or quasiperiodic phenomena) (Bradley, 2015) (e.g. Fig. 1.10).

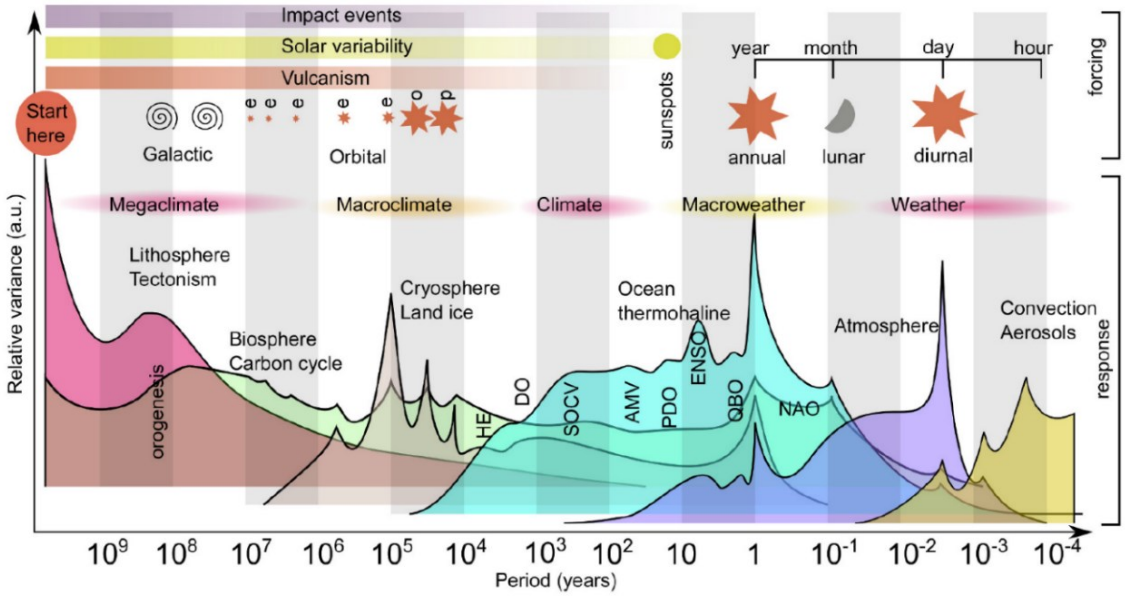

Figure 1.10 – A conceptual landscape of periodicities present in a typical climate signal from the atmosphere at the Earth's surface from von der Heydt., 2021, updated after Mitchell (1976). The external forcing is shown in the upper part of the diagram, where approximate periodic forcing from solar system orbital behavior. The landscape of responses and internal variability due to dynamics in various parts of the earth system is shown below, after background removal. The stepped experience indicates that short-term variability is only known from recent records. Orbital variability due to eccentricity (e), obliquity (o), and precession (p) are shown. Impact events, solar variability, and vulcanism events represent aperiodic forcing of highly variable amplitude.

Climatic forcing confined to sub-regional scales, such as the El Niño–Southern Oscillation (ENSO) and North Atlantic Oscillation (NAO), can be modified by changes in volcanic activity, atmospheric greenhouse gas concentrations, and solar irradiance (von der Heydt et al., 2021). These dynamic climate responses to natural forcing can have resulted in more or less persistent climatic spatial anomalies, such as the 'Medieval Warm Period' and a 'Little Ice Age' during the last millennium (see Masson-Delmotte et al., 2013[IPCC]).

From a climate perspective, these very shortchanges in forcing are less significant within the global climate system that requires much longer time-scales changes (e.g., the thermohaline circulation, build-up of ice sheets) (Beer and Geel, 2008).

1.3. Holocene general climatic context

The transition from the last glacial stage to the warmer current interglacial stage, the Holocene period (Rasmussen et al., 2014), is defined in stratigraphic records by the Pleistocene–Holocene boundary (Walker et al., 2009). The Holocene started circa 11.7 ka, after the end of the cold Younger Dryas event (YD, Rasmussen et al., 2006) (Fig. 1.11), marking the end of the last glacial (often referred to as Würm in alpine areas) with an abrupt rise of the mean temperatures (Alley et al., 1993). During that time interval, Earth's spin axis laid at the opposite point on the cycle from where it lies today, i.e., Earth was closest to the sun and Northern summertime insolation, reaching the peak at ca. 10 ka and declining until the present (Fig. 1.12). This resulted in the Northern Hemisphere receiving nearly 8% more solar radiation during summers than in modern days (Fig. 1.13). The orbital forcing is one of the most significant climate forces known during the Holocene climate evolution (e.g., Weber et al., 2001, 2004; Steinhilber et al., 2009), resulting in different feedback responses (see Wanner et al., 2008). For example, ca. 11 ka years ago, the eustatic level played about 40m below what is observed today, with the current level being reached at ca. 6 – 5 ka (Edwards et al., 1993) after the Holocene thermal optimum.

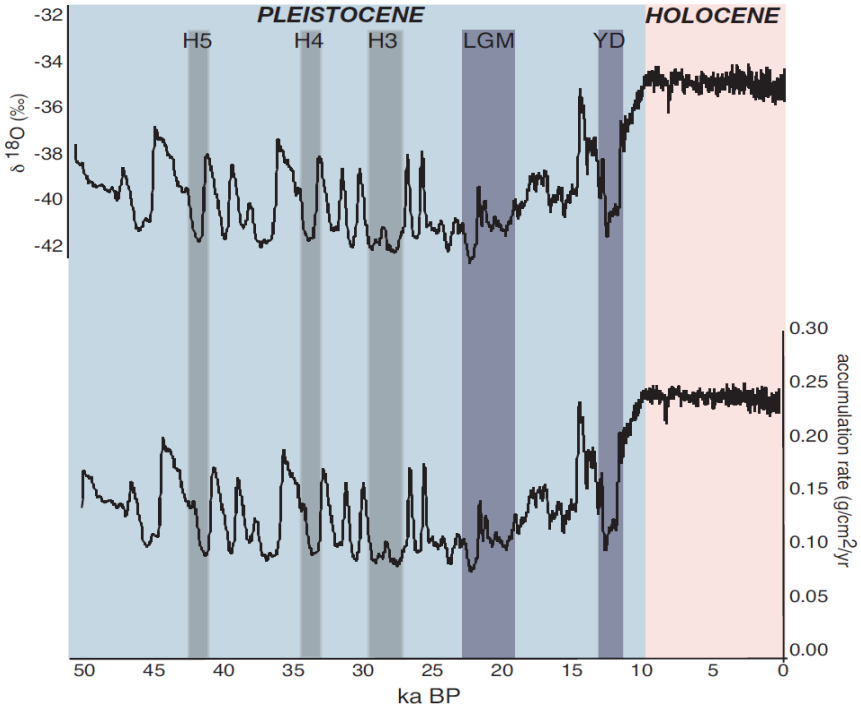

Figure 1.11 – Oxygen isotopes in ice (a complex proxy of temperature) and Ice accumulation rate over the past 50,000 years as measured in Greenland ice cores (Dansgaard et al., 1993). From: Oldfield and Alverson, (2003).

The general climate evolution of the Holocene can be evaluated using the oxygen isotope records of Greenland's Ice (Fig. 1.14). This broad view of the Holocene Climate starts with initial fast warming within two millennia, the 'Early Deglaciation Phase' (~ 11.7 – 9.5 ka), characterized by gradual sea-level rise with the North America and Eurasia ice sheets melt. Then, global temperature reconstructions suggest a general trend towards a warm and humid period often called 'Holocene Thermal Optimum' (9.5–5.5 ka), when global glaciers reach their minimum volume extent and the sea level changes cease. However, these relatively warm conditions of the early Holocene are still a matter of debate due to possible proxies related to bias to seasonality (Bova et al., 2021). A climate transition followed this period, often referred to as 'The Mid-Holocene Transition' (MHT) ~ 6 – 4.5 ka years BP to a long-term trend of cooling and drier climate, also known as 'Neoglacial', extending from 5.5 ka to ~100 years ago, with several cold relapses with great glacier advances highly asymmetrical and clustered around the world, that lasted until the beginning of industrialization that

interrupted this trend with global warming driven by anthropogenic forcing, mainly associated with greenhouse emissions (see Fig. 1.12) (Kaufman et al., 2004; Jansen et al., 2007[IPCC]; Wanner et al., 2008, 2011; Carlson et al., 2008; Miller et al., 2010; Roberts et al., 2011; Lowe and Walker, 2014; Solomina et al., 2015).

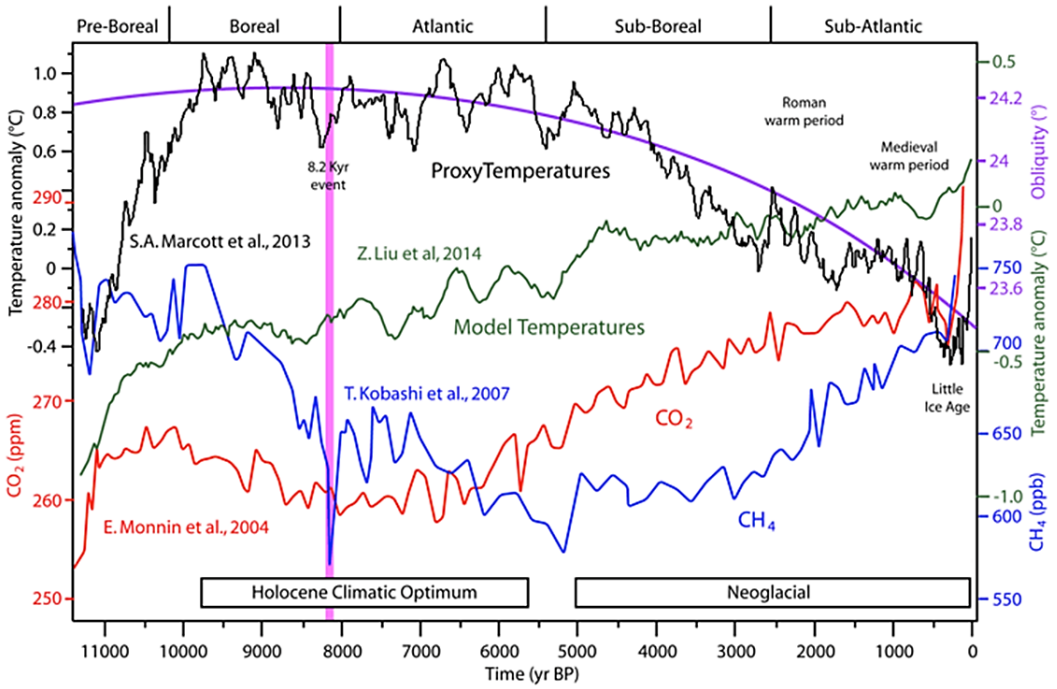

Figure 1.12 – Temperature, greenhouse gases, and Obliquity variations over the Holocene. The black curve corresponds to the global temperature reconstruction; the purple curve to Earth's axis obliquity cycle; the green curve, simulated global temperatures from an ensemble of three models (CCSM3, FAMOUS, and LOVECLIM); the red curve, to CO_2 levels as measured in Epica Dome C (Antarctica) ice core; the blue curve, to CH_4 methane levels as measured in GISP2 (Greenland) ice core. Their authors are indicated within the figure; the 8.2k climatic event marked as a pink column. It can seem some visual correlation with the black and blue curves, and the major Holocene climatic periods are indicated https://judithcurry.com/2017/04/30/nature-unbound-iii-holocene-climate-variability-part-a/.

The Holocene climate trends are, however, globally variable in magnitude, in space, and time. For instance, the relative extents of glacier advances in the two hemispheres were different. Glaciers in the Northern Hemisphere were most extensive in the late Holocene, whereas glaciers in the Southern Hemisphere were most extensive in the early Holocene (see Koch and Clague, 2006). These differences are most likely due to the asymmetry of solar insolation in the two hemispheres that increment with the onset of the Holocene (Koch and Clague, 2006). During the early Holocene, summer insolation was high in the Northern Hemisphere, with a peak around 11 – 10 ka, while low in the Southern Hemisphere and vice-versa during late Holocene (Fig. 1.13).

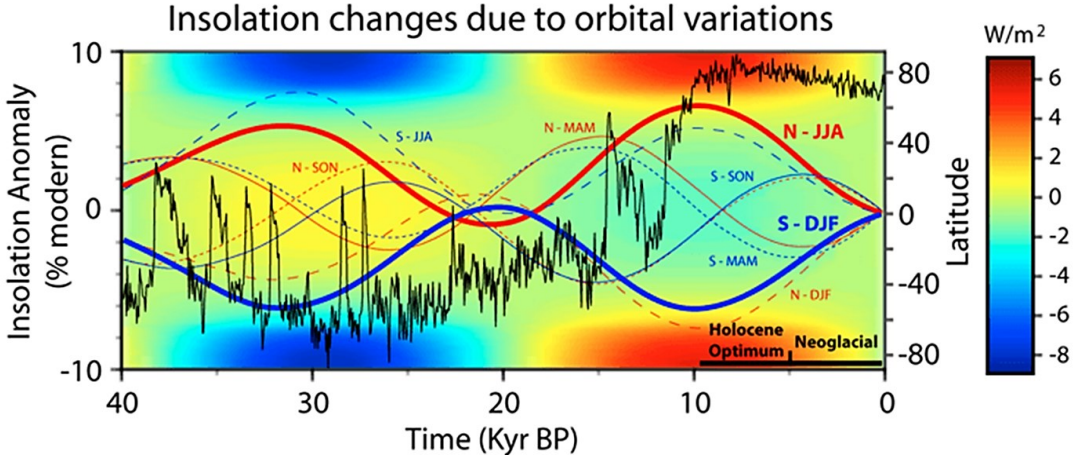

Figure 1.13 – The insolation changes over the last 40,000 years due to orbital variations of the Earth by latitude (background) and time due to changes in the Earth's axial tilt (obliquity). The black temperature proxy curve represents $\delta^{18}O$ isotope changes from the NGRIP Greenland ice core (Andersen et al., 2004) (without scale). The insolation curves (Polissar et al., 2013) are presented as the insolation anomaly for summer, winter, spring, and fall. N (red) or S (blue) is the Northern or Southern Hemisphere, and the three

letters are the month initials. Northern and southern summer insolation is represented with thick curves. The Holocene Climatic Optimum corresponds to a high insolation surplus in polar latitudes (red area), while Neoglacial conditions represent the first 5,000 years of a 10,000-year drop into a high glacial insolation deficit in polar latitudes (blue area). Figure from: https://judithcurry.com/2017/04/30/nature-unbound-iii-holocene-climate-variability-part-a/ sees other references therein

Towards the late Holocene's climate has experienced some significant climate shifts, agreeing with the decrease in the W/m^2 (see Fig. 1.13). The progressive solar energy redistribution due to orbital forcing causes substantial changes in a gradual southward shift of the Northern Hemisphere summer position of the Inter-Tropical Convergence Zone (ITCZ) (see Wanner and Brönnimann, 2012). The decreasing trend, both in summer insolation and changes in temperature in the world oceans, could have resulted in a reorganization of atmospheric and oceanic circulations, behind the pronounced weakening of the monsoon systems in Africa and Asia and increasing dryness and desertification on both continents (Mayewski et al., 2004; Wanner et al., 2008). This shift from enhanced northern monsoon circulation in the sub-tropics started to deteriorate with the decrease in northern summer insolation, turning to dryness in the modern Saharan, Arabian, and Thar deserts. This transition displaced the climatic equator, ended the African Humid Period (AHP), and increased El Niño activity (e.g., deMenocal et al., 2000; Wanner et al., 2008; Tierney et al., 2013).

The last two millennium

Ahmed et al. (2013) used a global temperature reconstruction for seven continental-scale regions. Over the last two millennia, the most coherent feature in nearly all the regional temperature reconstructions is the long-term cooling trend, which ended late in the nineteenth century (Fig. 1.14). These authors indicate no significant globally synchronous multi-decadal warm or cold intervals, although all reconstructions showed general cold conditions between AD 1580 and 1880. The transition to these colder conditions occurred earlier in the Arctic, Europe, and Asia than North America or the Southern Hemisphere. However, this generalized cooling was reversed by a rapid and recent global warming since AD 1971–2000, higher than any other time in nearly 1400 years (Ahmed et al., 2013).

It is worth mentioning that the most discussed multi-decadal climatic periods are often related to the NH, namely Europe, such as the Roman Period (RP) (~0 – 500 AD), the Dark Ages (DA: ~500 – 900 AD), the Medieval Climate Anomaly (MCA) a.k.a Medieval Warm Period (MWP) (~900 – 1300 AD), and Little Ice Age (LIA) (1350 – 1850 AD). However, the timing of these episodes is not well defined and varies regionally (Masson-Delmotte et al., 2021 [IPCC]).

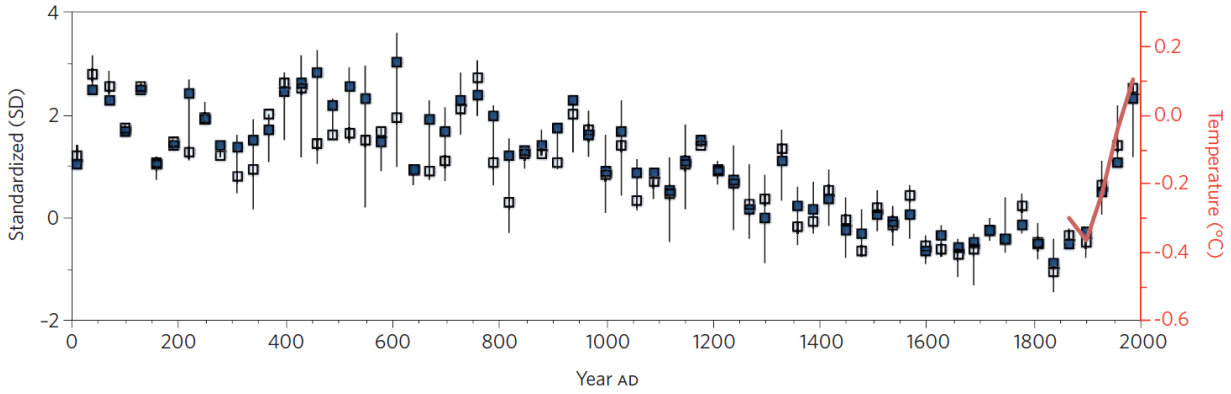

Figure 1.14 – Standardized 30-year-mean temperatures averaged across all seven continental-scale regions. Blue symbols are area-weighted averages using domain areas, and bars show twenty-fifth and seventy-fifth unweighted percentiles to illustrate the variability among regions; open black boxes are unweighted medians. The red line is the 30-year-average annual global temperature from the HadCRUT4 (Morice et al., 2012) instrumental time series relative to 1961–1990 and scaled visually to match the standardized values over the instrumental period. From Ahmed et al., 2013 see references therein.

Regarding the LIA, it is believed to correspond to the coldest multi-decadal to the multi-century interval since the 8.2 ka event associated with Bond event 0 (1200 – 1800 AD) (Wanner et al., 2011). Although it was not a literal 'ice age', it has been one of the most studied climate events, overlapping the interest of diverse scientific areas, such as archeology and climatology. Moreover, because it was a recent period, a wide range of well-preserved historical documents and high-resolution archives such as tree-rings can be used to assess the past climate conditions (see Oliva et al., 2018). Examples of the impacts for this period include European glaciers

readvances, reaching their maximum volumes over the last 10,000 years, sea ice also re-advanced, crop failure and deviate food crisis, etc. (see Lowe and Walker, 2014).However, on a global scale, the LIA only had a slight cooling impact on the Northern Hemisphere, ca. <1°C of temperature decrease (Mann et al., 2009). The explanations appear to lie in climatic forcing from solar variability (e.g., Owens et al., 2017), as seen in Chapter 1.2.1, when two significant episodes of reduced sunspot activity occurred between 1645 – 1715, *i.e.,* LIA, and 1790 –1830, and/or volcanic activity (see Fig. 1.15) that may have led the expelled plumes and dust to block the sunlight, with consequent temperatures drop in the short-term (decadal). Nevertheless, these mechanisms were probably modulated by various processes impacting the internal climate feedbacks.

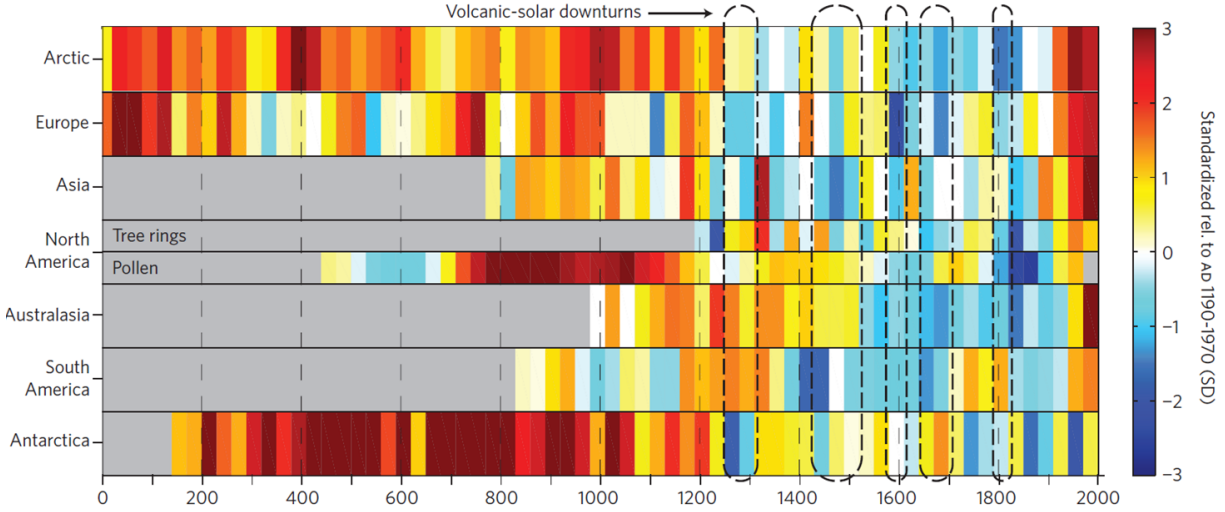

Figure 1.15 – Continental-scale temperature reconstructions. 30-year-mean temperatures for the seven PAGES 2k Network regions, standardized to have the same mean (0) and standard deviation (1) over the period of overlap among records (ad 1190–1970). North America includes shorter tree-ring-based and a longer pollen-based reconstruction. Dashed outlines enclose intervals of pronounced volcanic and solar negative forcing since ad 850 (from Ahmed et al., 2013 see references and methods used therein).

The climate transition MCA-LIA discussed by Graham et al., 2010 (see references therein) show a summary of possible triggers for such transitions: (i) changes in both solar and volcanic forcing, with MCA being characterized by relatively high irradiance and low volcanic forcing while the LIA by low solar and high volcanic forcing; ii) changes in oceanic heat transport and strength of the southwesterly flow across the high latitude North Atlantic, with prevalent positive NAO phases during the MCA, and negative NAO phases during the LIA; (iii) AMOC variability and (iv) the long term downward trend in summer SST. Nonetheless, it also highlights the changes in the Hadley circulation through differences in the warming of the tropical Indian and western Pacific Oceans relative to the other tropical ocean areas. This implies dynamical climate responses to natural radiative forcing changes involving El Niño/La Niña patterns and the NAO – Arctic Oscillation as proposed by Mann et al., 2009.

Over the last century, the decadal timescale variability of the natural climate variability has been dependent on events such as massive explosive volcanic eruptions, solar variability, and modulations of atmospheric patterns (Jones and Mann, 2004; Lean and Rind, 2008; Lean 2010; Tejedor et al., 2021). Nevertheless, the anthropogenic influence (mainly greenhouse gas and sulfate aerosol) is sufficiently large to upward this natural trend over the past 120 years. These previously mentioned climatic mechanisms contribute to global warming by around 10% or less (see Fig. 1.16a). Regarding the solar influence, for instance, the solar cycle 23 (circa 1996 – 2009) (Fig. 1.16d), Lean (2010) illustrated a broad consistency between past Sun–climate linkage and the contemporary response pattern of surface temperature, where regions with extreme hydrological cycles—monsoons, rainfall, drought—appear especially sensitive to these changes.

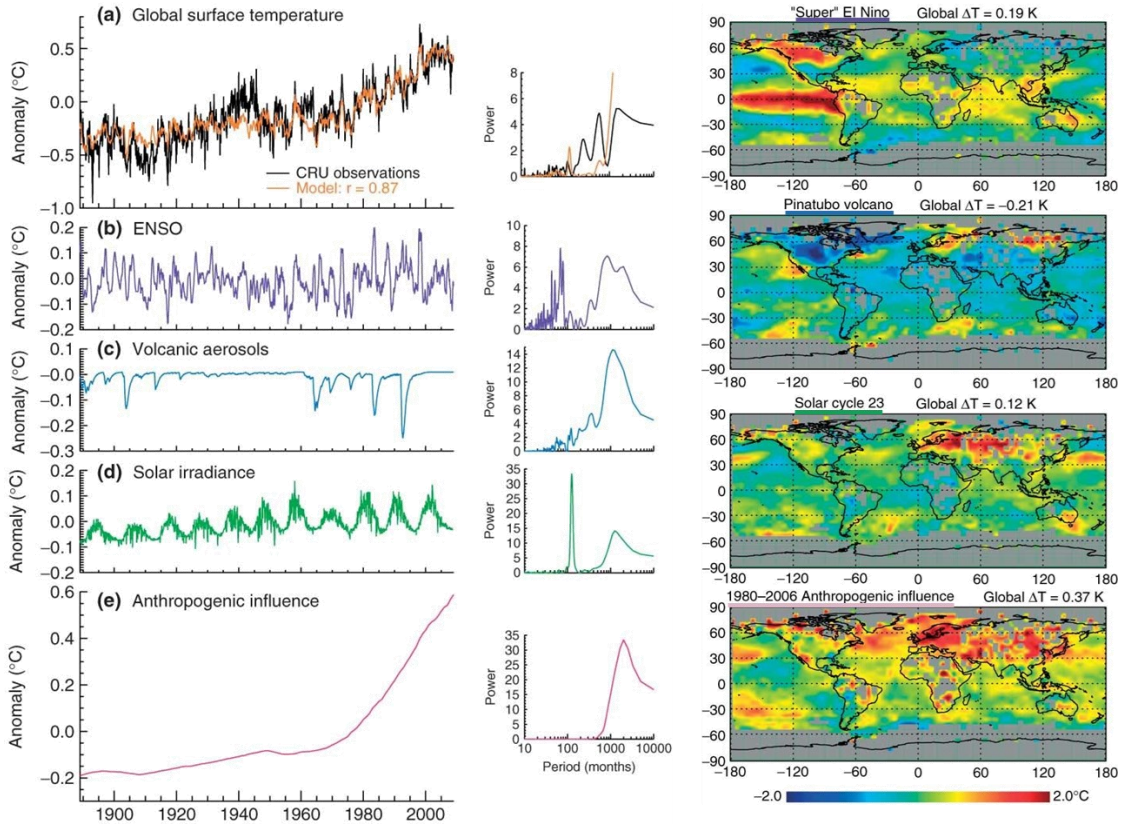

Figure 1.16 – Composite figure modified and adapted from Lean 2010, where it shows cycles and trends in the natural and anthropogenic influences from the last millennium (Left side graphs) and their responses to a particular timeframe (global maps to the right). The right side of the figure compares the monthly mean global temperature time series (hadcrut3vcgl) in (a) is an empirical mean global temperature time series (hadcrut3vcgl) is an empirical model obtained from multiple regression for the period from 1889 to 2008, inclusive (Lean and Rind, 2008); The value of r is the correlation coefficient for the global temperature observations and empirical model. Reconstructions of the contributions to the monthly mean global surface temperatures by an individual (b) ENSO, (c) volcanic, (d) solar, and (e) anthropogenic influences; The periodograms on the right illustrate cycles present in the monthly mean values of each of the four sources of global temperature variance. The Left side of the figure shows, the geographical response patterns in surface temperature are shown for the 1997–98 'super' ENSO, the Pinatubo volcano, solar cycle 23, and anthropogenic influences from 1980 to 2006, derived from the monthly surface temperatures on a 5"×5" grid. Gray regions indicate a lack of data, based on Lean and Rind, 2008.

1.4. Late Holocene Climate of Iberia

The overall climatic trends in the Iberia have been discussed in three main intervals: an early-Holocene humid period (~ 11.5 – 7.0 ka), a mid-Holocene characterized by an increase in climatic variability, linked to decreasing Northern Hemisphere insolation (~ 7.0 – 5.5 ka) with a relative humidity maximum been pointed to coastal Western Iberia (Roberts et al., 2011; Mauri et al., 2015; Walczak et al., 2015) with more Atlantic climate characteristics (Gomes et al., 2020), and a generalized late-Holocene period of aridification (since ~ 5.5 ka) (Jalut et al., 2009; Pérez-Obiol et al., 2011; Walczak et al., 2015). These terms refer to the Holocene's time intervals, such as 'Early Holocene', 'Middle or Mid Holocene', and 'Late Holocene' are often used (e.g., Walker et al., 2012; Magny et al., 2013; Thatcher et al., 2020a). However, they are currently being systematically replaced by the more recently defined Holocene subdivisions of the International Chronostratigraphic Chart/Geologic Time Scale of Greenlandian (11,700 – 8,200 years ago), Northgrippian (8,200 – 4,200 years ago), and Meghalayan (4,200 years ago – present), respectively.

The major climate drivers for the Iberia region have been changing throughout the Holocene, from a deglacial to a full interglacial stage. From the Early Holocene to the Late Holocene, the ITCZ migrated southward to its current position (Haug et al., 2001), the Azores High, and the descending limb of the Hadley circulation system (Fig. 1.17) changed the storm tracks stretching Iberia (Thatcher et al., 2020a). These changes in the Atlantic moisture transport would promote essential changes in the winter climate of Iberia (Trigo and DaCamara, 2000; Trigo et al., 2004). As a result, the climatic conditions have approached a more modern configuration,

especially after the 4.2 ka (Thatcher et al., 2020a), turning the Iberian climate to drier conditions and increasing seasonality (i.e., lower summer rainfall) (Walczak et al., 2015).

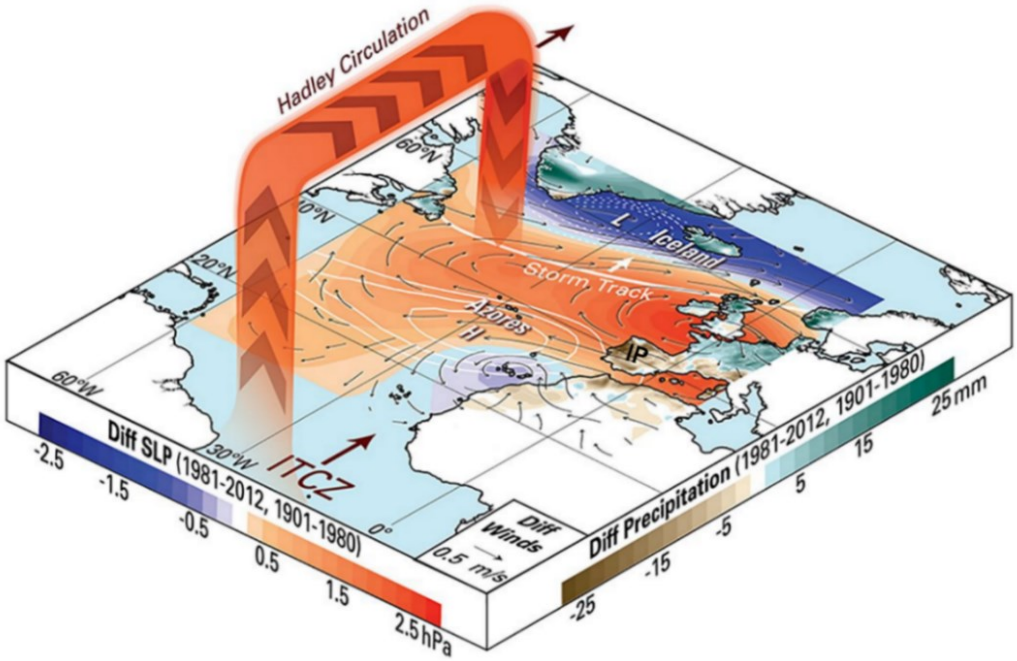

Figure 1.17 – Schematic depicting connections between Azores High, Hadley Circulation, and ITCZ in the Iberian framework. Red (blue) shading over the ocean indicates sea level pressure increase (decrease) during recent decades compared with the 20th-century long-term mean (white contours). Green (brown) shading over land indicates an increase (decrease) in precipitation and arrows indicate changes in surface winds during wintertime (December–March) climatic conditions during the period 1981–2013, relative to the long-term mean wintertime climate for the 20th century (i.e., 1901–1980). From: Thatcher et al., 2020a.

After 4.2 ka, although under a more modern climate configuration, some climate oscillations occurred in Iberia. For instance, most climate reconstructions in Europe distinguish five main climatic periods throughout the last two millennia. The following summary of these five climate periods is mainly based on the comparison made by Sánchez-López, et al., 2016 (see Fig. 1.18), which examines different climate reconstructions to identify and characterize the main climate changes and forcing mechanisms, such as the NAO.

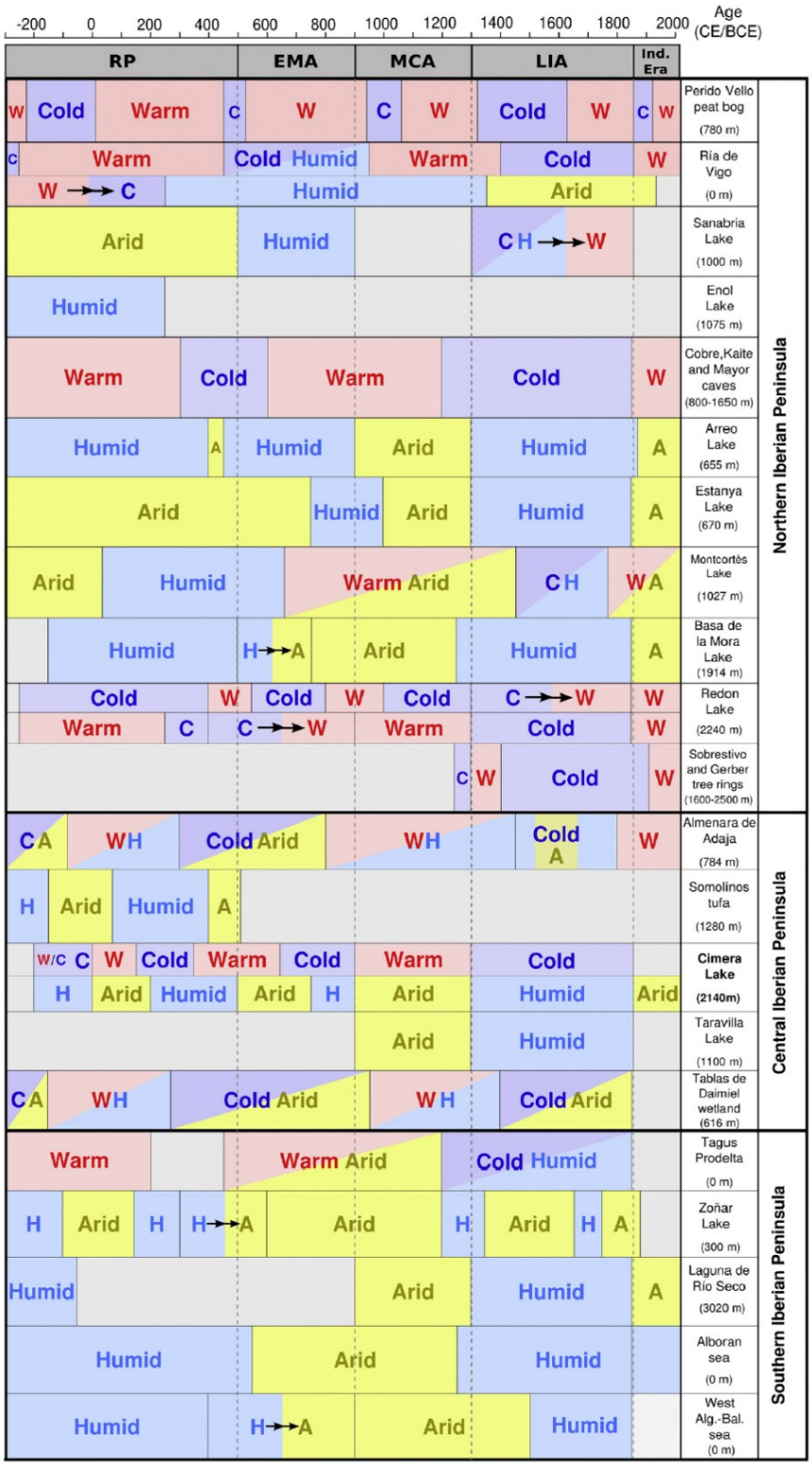

Figure 1.18 – Summary of the climatic conditions reconstructed from different records in Iberia for the last two millennia. A = arid, H = humid, C = cold, and W = warm, arrows indicate climate transitions. From: Sánchez-López, et al., 2016 see references therein.

The NAO index can be used to assess these atmospheric changes, with a positive NAO (NAO+) being characterized by higher-than-average pressure in the 'Azores High' and lower than average pressure in the 'Icelandic Low', while a negative NAO (NAO−) index phase, characterized by a weaken pressure gradient between the two regions. A persistent NAO+ often results in stronger westerlies and a northward displacement of Atlantic storm tracks, leading to dry and cold winters in southern Europe and mild and wet winters in Northern Europe. Contrariwise, during a persistent NAO− the northwesterly winds shift southwards, enhancing winter precipitation in the Iberian Peninsula (IP) and Mediterranean region (Rogers et al., 1997) (see Fig. 1.19).

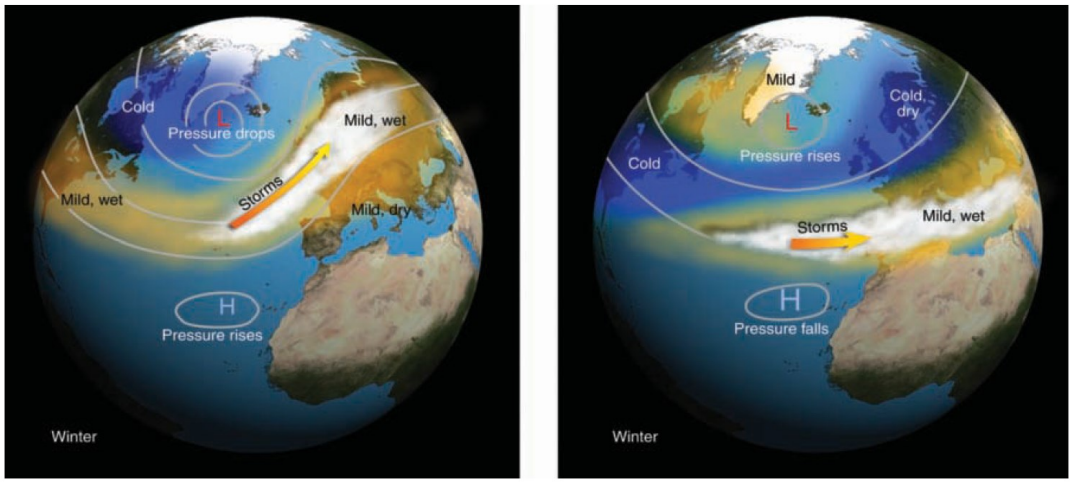

(a) Positive phase (b) Negative phase

Figure 1.19 – Relationship between the Azores (subtropical) High and the Icelandic (subpolar) Low. The positive vs. the negative phase of the North Atlantic Oscillation controlling the east-to-west seesaw motion of the Icelandic Low and the Azores High control the strength of the westerly winds and the direction of storm tracks across the North Atlantic. Figure from Petersen et al., 2008.

The Roman Period (RP: 0–500 years AD), is generally inferred as a warm period in Iberia, with is noted high SSTs in the Atlantic Margin (see Rodrigues et al., 2009), with early phases of relatively high humidity in southern Spain, where is seen a peak in forest growth (Martín-Puertas, et al., 2008). This period was followed by a more spatial heterogeny period called Dark Ages (DA: ~500–900 AD), often also referred to as the Early Middle Ages (EMA), which is characterized by a general North-South humidity gradient in the IP, with wetter conditions to the north and drier scenario to the southern area (see Sánchez-López, et al., 2016). The return to generalized arid conditions, especially in the Mediterranean margin (Moreno et al., 2012a), associated with an inferred persistent NAO+ (e.g., Fig. 1.20), initiated with the Medieval Climate Anomaly (MCA: ~900 – 1300 AD), which was characterized by an early phase of intense precipitation/flooding and warm winters and the second phase of cooler and relatively drier winters in the Atlantic region (Moreno et al., 2012a; Abrantes et al., 2017). After this, one of the main climate anomalies started coincident with the emplace of the Maunder Minimum, a cold period from 1645 to 1706 AD, and the Dalton Minimum (1796–1830) correlated with a cold stage spanning from 1810 to 1838 AD, both encompassing the cold period of the LIA (Fig. 1.21) which onset started ar ca. 1350 AD and lasted until 1850 AD (Oliva et al., 2018) with the beginning of the Industrial Era.

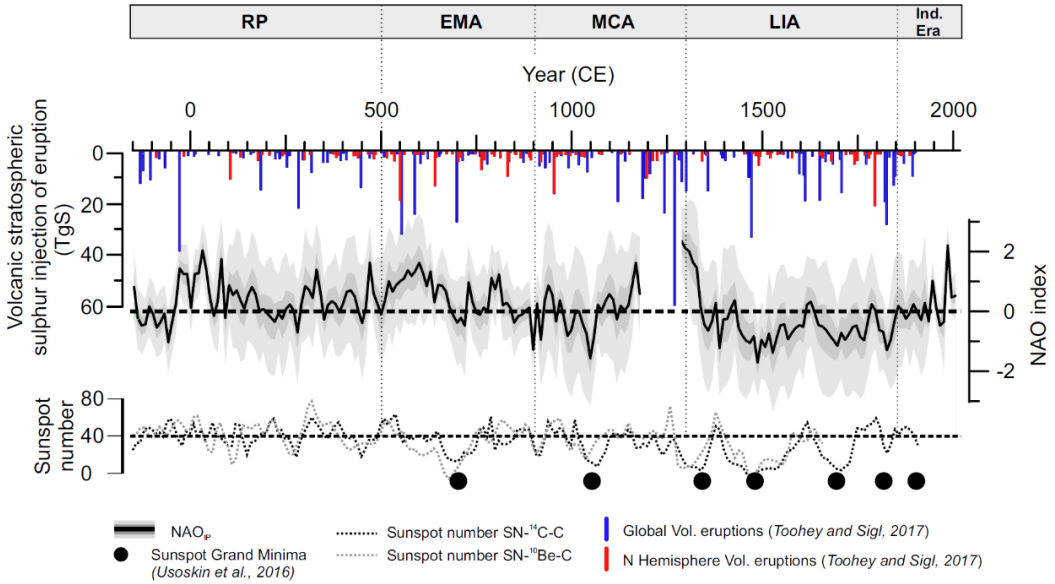

Figure 1.20 – Overlaying the Major global and North Hemisphere volcanic eruptions, Sunspot number, the major atmospheric circulation modes for the Iberian Peninsula, i.e., North Atlantic Oscillation (NAO) (with the median Central Iberian Peninsula, NAO$_{IP}$ (wide black line) with the greyscale 95% (light grey band) and 50% (dark grey band) uncertainty intervals are shown) for the last two millennia. The major climatic anomalies intervals are also evidenced, with the Roman Period (RP); Early Middle Ages (EMA); Medieval Climatic Anomaly (MCA), Little Ice Age (LIA), and Industrialized Era (Ind. Era). From: Hernández et al., 2020a, see references therein.

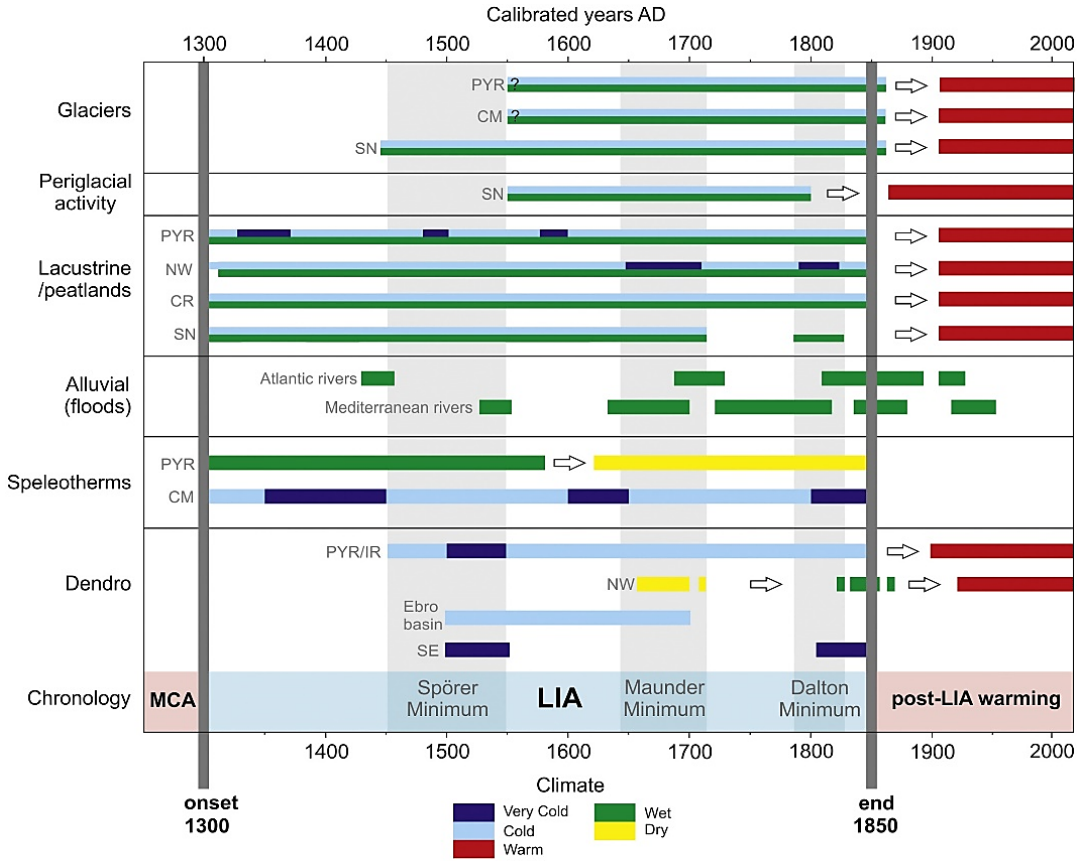

Figure 1.21 – Onset and end of the LIA, based on natural records from the main Iberian Mountain ranges (PYR: Pyrenees; CM: Cantabrian Mountains; CR: Central Range; IR: Iberian Range; SN: Sierra Nevada). From: Oliva et al., 2018.

1.4.1. Modern-day Iberian climate forcings

In a transition zone between subpolar and subtropical gyres (Siedler et al., 2001; Sprangers et al., 2004; Pérez-Brunius et al., 2004; Morley et al., 2011), the IP is a key region for the study of past climate changes and their effects on environment and socioeconomics (e.g. Lionello et al., 2012; Cortesi et al., 2014; Thatcher et al., 2020b; Schirrmacher et al., 2020). Moreover, with the recent post-industrial warming trend and its negative consequences, Iberia is one of the most fustigated regions in Europe, expecting more negative and profound impacts as a result of the ongoing climate changes, with more severe and longstanding heatwaves and droughts (Masson-Delmotte et al., 2021 [IPCC]).

The modern Iberian climate is roughly characterized by its Mediterranean climate, with dry summers and the wet season mostly constrained to winters. Iberia's overall atmospheric climate conditions are highly linked to the Hadley Circulation dynamics, whose descending branch results in the Azores High, the southern mode of the NAO dipole (e.g., Trigo and DaCamara 2000; Trigo et al., 2004). The NAO is one of the major climate drivers of Iberia, however other large-scale atmospheric circulation modes such the East Atlantic (EA) and Scandinavia patterns (SCAND) also play an important role in the climate variability (e.g., Sáenz et al., 2001; Moreno et al., 2012b; Casado and Pastor, 2012; Jerez and Trigo, 2013; Hernández et al., 2015; Sánchez-López et al., 2016; Mellado-Cano et al., 2019). The influence of these Atmospheric Circulation Modes (e.g., see Fig. 1.22), both in strength and latitude at annual and multidecadal scales ultimately control the Iberian hydroclimate via winter storminess (Comas-Bru and McDermott, 2014; Sánchez-López et al., 2016; Hernández et al., 2020a) and the extreme weather such as the atmospheric rivers intense precipitation (Ramos et al., 2015).

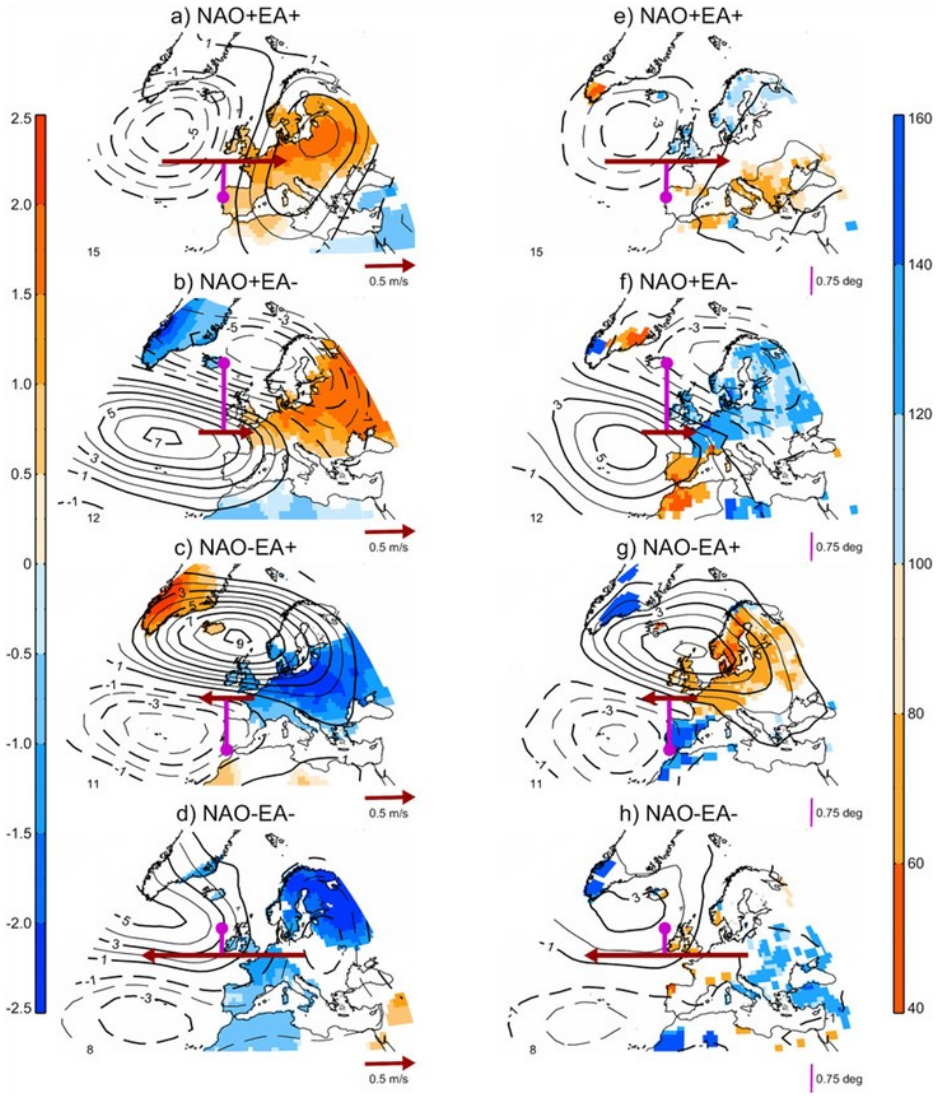

Figure 1.22 – Winter composites of: (a)–(d) near-surface temperature (shading, in °C) and geopotential height at 500 hPa (contours) anomalies; (e)–(h) precipitation (shading, in the percentage of normals) and SLP (contours, hPa) anomalies for different combinations of NAO and EA indices with absolute values larger than 0.5 SDs. Anomalies are computed with respect to 1901–2010. Numbers in the left bottom corner of each panel represent the number of cases employed in each composite. Horizontal red arrows and vertical purple lines summarize the composited winter anomalies of the jet speed and latitude, respectively, with the length being proportional to the anomaly. Eastward (westward) red arrows indicate a strengthening (weakening) of the jet. Purple lines pointing upward (downward) indicate a poleward (equatorward) shift of the jet. From: Mellado-Cano et al., 2019 (see references therein).

The orography is a rather important factor controlling much of the hydroclimate in Iberia, with mountain ranges having a strong influence on the response to low-pressure systems shielding the moisture brought by Atlantic Ocean winds (Vieira, 2004; Gimeno et al., 2010) and are closely related to snow abundance in the peninsula during the winter (López-Moreno et al., 2011).

The IP have experienced a wide spectrum of climatic and microclimate conditions, a result of the effects such as latitude (e.g., Moreno, et al., 2014a; Morellón et al., 2018; Naughton et al., 2019) and the orographic complexity and proximity to the ocean (continentality). These regional diversities and their interactions with the above-mentioned climate drivers could explain the spatiotemporal climate variability observed in the Iberia throughout the Holocene (e.g., Carrión et al., 2010; Tarroso et al., 2014; Sánchez-López et al. 2016; Abrantes, et al., 2017; Morellón et al., 2018; Baldini et al., 2019; Thatcher et al., 2020a; Naughton et al., 2019; Gomes et al., 2020). Consequently, although challenging due to the diversity of competing for climatic factors, the paleoclimate studies of this region can provide key insights into how the North Atlantic zone, particularly the Eastern North Atlantic, Southwestern European, and Western Mediterranean areas, respond to global climate change.

1.4.2. Modern Iberian hydroclimate

As prior mentioned, the hydroclimate in Iberia is highly affected by largescale patterns of atmospheric circulation modes which affect air temperatures, precipitation, and wind patterns (Hurrell 1995; Trigo et al., 2002, 2004). In this regard, the precipitation is rather affected when certain atmospheric patterns are modulated, such as negative (positive) NAO phase with positive (negative) phase of the EA pattern which promotes intense precipitation during winter (García-Herrera et al., 2007, Jerez et al., 2013, Trigo et al., 2004), especially when the presence of narrow moisture-rich corridors, also known as, atmospheric rivers are associated with latitudinal low jet stream (Ramos et al., 2015).

The modern hydroclimate has a steep gradient between the Northwest region, characterized by a temperate/Atlantic climate type, and the Southeast region of the IP, where the climate tends to be drier in a Mediterranean climate domain and more influenced by the Western Mediterranean Oscillation (Martin-Vide and Lopez-Bustins, 2006) (Fig. 1.23). This can be explained by the synchronized but often opposed response to NAO and other atmospheric dynamics operating between these two regions (Martin-Vide et al., 2006; Lopez-Bustins et al., 2008; López-Moreno et al., 2011; Moreno et al., 2012a; Sánchez-López et al., 2016; Schirrmacher et al., 2019).

The annual precipitation generally follows a strong NW-SE, decreasing from north to south and from west to east. In contrast, mean air temperatures follow an opposite pattern, increasing towards the south and the east (Fig. 1.23B). The same pattern applies to the snow line equilibrium in the Iberian Peninsula with the altitudinal limit increasing from the north to the south and from the west to the east (see Campos et al., 2019). These factors contributed to the present-day Temperate climate in the northwest while the predominant Mediterranean in the southeast. The first is characterized by wet and cool climate without marked summer drought warm, while the second is by dry and hot summers and relatively cool, wet winters (Carrión et al., 2010) (see Fig. 1.23).

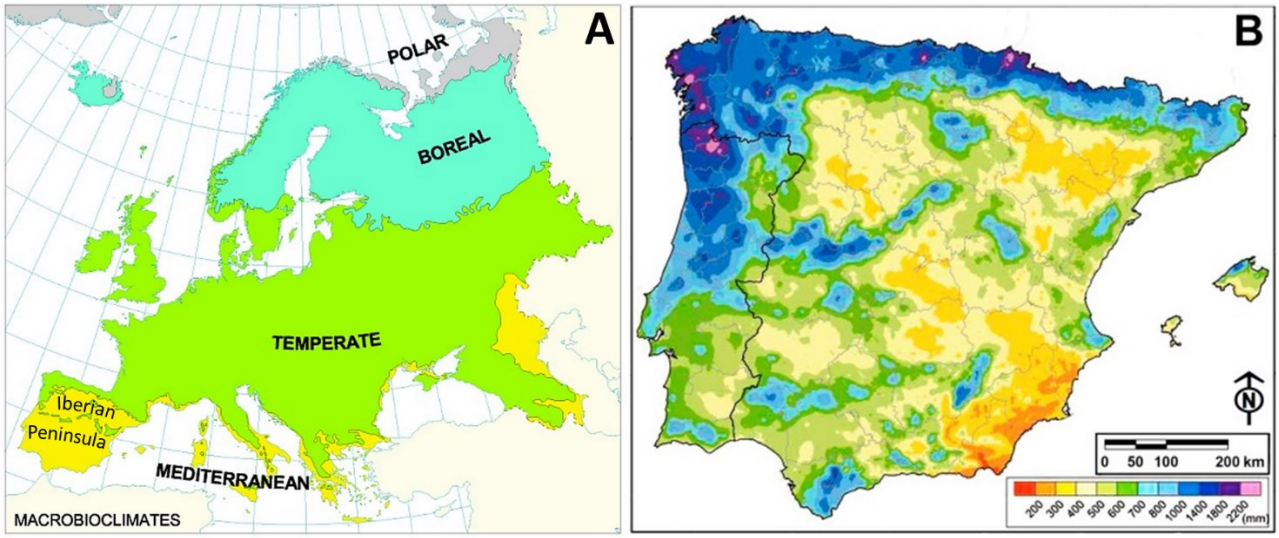

Figure 1.23 – A. Macrobioclimate map of Europe Adapted from Bioclimatic Map of Europe of Rivas-Martínez, 2011, available online: http://www.globalbioclimatics.org/form/bi_med.htm; B. Average total precipitation in the Iberia Peninsula (1971–2000) (Iberian Climate Atlas, 2010).

The polar front can significantly affect the Iberian climate, for instance, when coupled with the cyclonic trajectories (Boessenkool et al., 2001). This affects the vegetation of the Iberian Atlantic margin to anticipate large responses to changes in mean temperatures and moisture availability, *i.e.,* a key area for the study of interrelationships between the marine and terrestrial paleoclimate and paleoenvironments (Boessenkool et al., 2001). This is especially evident in the high mountain lake ecosystems, known for being highly sensitive to the changes in atmospheric circulation modes in North Atlantic (e.g., Hernández et al., 2017; García-Alix et al., 2017).

1.5. Paleoclimate archives and climate-proxies

Following Raymond Bradley (2015), the concept of climatic reconstruction, beyond instrumental records, is a staged process. The first stage is data collection, usually involving fieldwork, initial laboratory analyses, and measurements that result in the primary data. The second often requires data calibration and estimates to provide evidence of climatic variation through time at a particular location reflecting. This phase can be entirely qualitative and subjective (e.g., 'warmer', 'wetter', and "cooler" conditions), a result of statistical and model analysis, which implicitly assumes long-term stationarity in the natural response to climate (Jones and Mann, 2009).

The most used archives are sediments (marine and lacustrine), ice cores, and speleothems (e.g., Fig. 1.24). But there are also geomorphological features (e.g., glacial deposits, erosional features) and subfossil material such as tree rings and corals, which can provide very high-resolution data for recent periods. In this sense, the term 'sensor' has been suggested (Evans et al., 201; Shuman et al., 2021), which defines the entity reacting to the prevailing climatic conditions and can produce different physical, chemical, or biological indicators, or climate-based proxies, that can be preserved in the above-mentioned paleo archives.

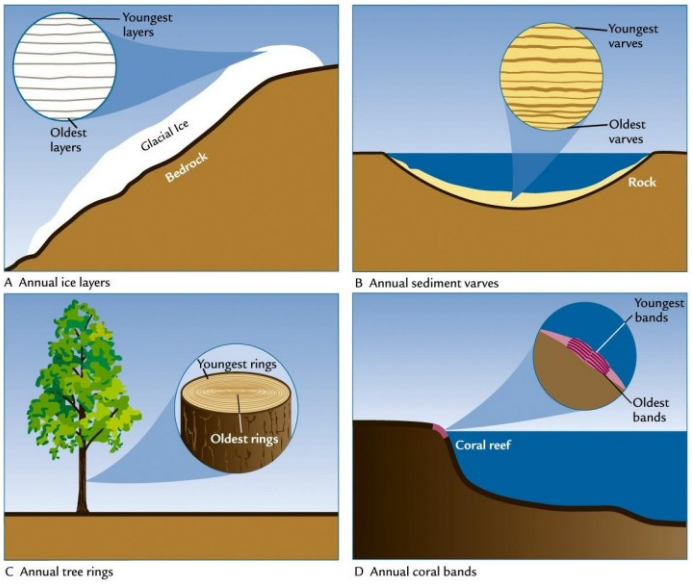

Figure 1.24 – Four kinds of natural "archives" used to retrieve paleoclimatic proxy data. A: Ice cores, B: varved lake sediments, C:tree rings (dendrochronology) and D: coral reef layers. From Ruddiman, 2013.

Paleoclimate reconstructions often require integrating and comprehending different factors in the signal, such as seasonality, thresholds, lagging responses, etc. (Bradley, 2015). For example, different sensors (e.g., vegetation cover) may respond differently to the prevailing climate, resulting in a complex outcome in the archive. Thus, interpreting paleoclimate records requires a great understanding of the archives and the different aspects of controlling a given sensor (Shuman et al., 2021).

The resolution on each archive may vary significantly for several reasons, such as minimum sampling interval and dating resolution, analytical method, etc., but usually, the high-resolution capability for climate proxies includes tree rings, corals, ice cores, and varved sediments, which can be used to provide detailed information on annual or near-annual climate variations. Other lower-resolution archives may include boreholes, glacial moraines, and non-laminated ocean sediment records that can usefully supplement high-resolution data (e.g., Fig. 1.25) (Houghton et al., 2001[IPCC]). For instance, the recent study of Kaufman et al., (2020) presented a global compilation of multi-proxy-based reconstruction of the temperature over the last 12 ka where it can be seen the global distribution of the archives. From the 679 sites gathered, 51% consisted of lake sediments, 31% marine sediment, 11% peat, and 3% glacier ice. Mainly from Northern Hemisphere (51%), within the zone of 60–30°N, and only a fraction (16%) is from the Southern Hemisphere (see Fig. 1.26).

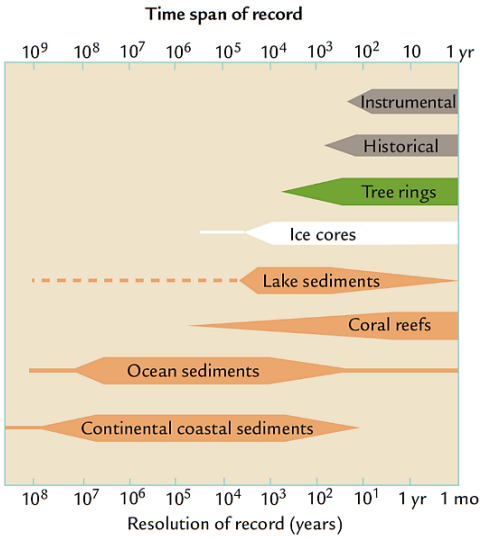

Figure 1.25 – Resolution of climate records Climate archives vary widely in the length of the records they contain and in the degree of resolution they yield. From Ruddiman., 2013 see references therein.

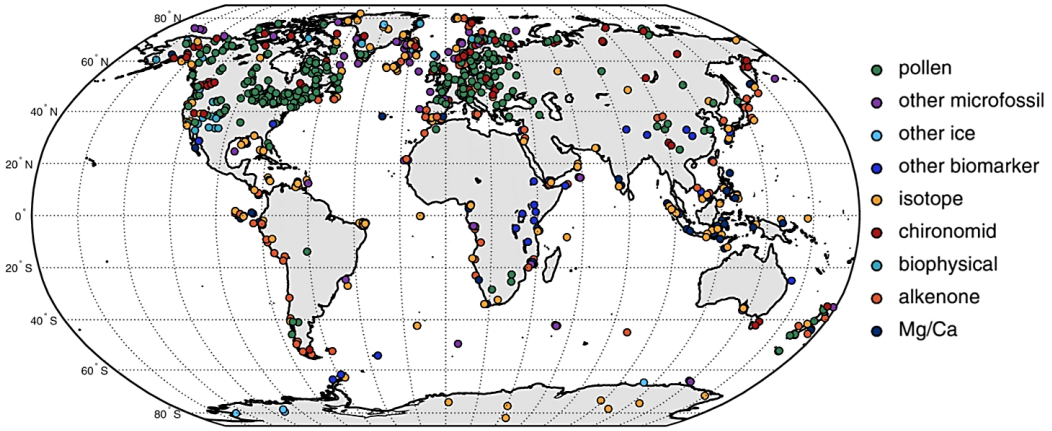

Figure 1.26 – Spatiotemporal data availability of records in the Temperature 12k database (v. 1.0). Geographical distribution of sites (n = 679) by proxy type, coded by color. Adapted from Kaufman et al., (2020) see references therein.

Different indicators may record different signals, including 'noise' often associated with local environmental and/or different time-responses to the climatic changes (Bradley, 2015; Hernández et al., 2020b). This is closely related to the sensitivity of a proxy to register a climatic signal, depending on the capability to achieve a state of equilibrium with a prevailing climate system. This turns a proxy to act as a natural filter while responding to the different competing climatic factors (e.g., Fig. 1.27) (see Gornitz, 2009; Bradley, 2015). Thus, the robustness of a proxy might be highly variable and subjective.

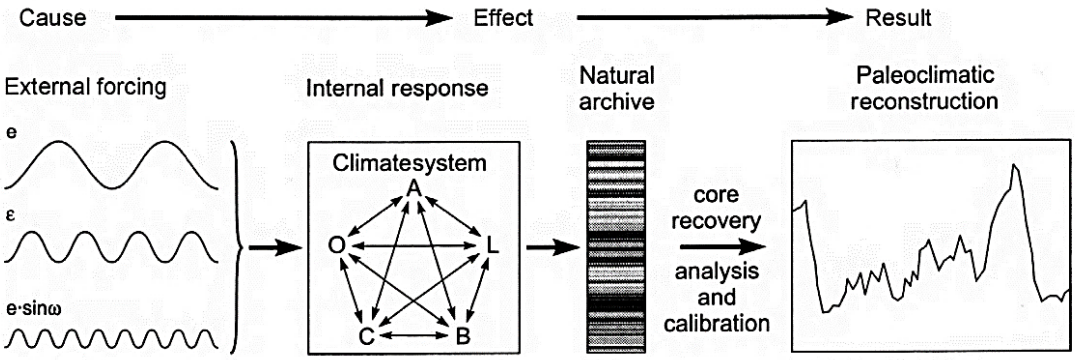

Figure 1.27 – Schematic diagram illustrating the relationship between orbital forcing and the signal that is eventually preserved in the sedimentary record. From: Bradley, 2015 (Paleoclimatology: Reconstructing Climates of the Quaternary: Third Edition, pg. 215).

A multi-proxy approach would therefore increase the reliability of a paleo study. Nonetheless, other limitations are inherent to paleo-studies due to dating uncertainties, archive preservation, and even the use of different statistical and calibration methods (see Hernández et al., 2020b).

Because billions of tons of sediment accumulate in ocean and lake basins each year (Holeman, 1968), these geological records can archive a vast amount of information about past climate changes. Several climate proxies can be retrieved from the sediments to allow the reconstruction of past environmental conditions, such as pollens (proxy of climate on land), tiny fossils/subfossil (typically proxy of climate in the ocean) (e.g., Fig. 1.28), and organic compounds (e.g., biomarkers, sedimentary DNA).

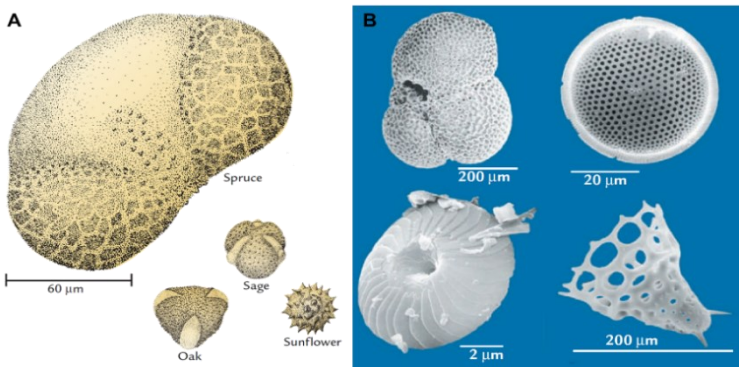

Figure 1.28 – Typical proxies on land and ocean. A. examples of types of pollen; B. different shelled remains of plankton, common in ocean sediments: $CaCO_3$ shells are represented by sand sized planktic foraminifera (upper left) and small clay-sized coccoliths (lower left); SiO2 shells include silt-sized diatoms (upper right) and sand-sized radiolaria (lower right). For comparison, small grains of sand are 60 µm or larger in diameter. Adapted from Ruddiman, W., 2013 (Earth's Climate: Past and Future, 3rd Edition, pg. 66) see references therein.

Lake records

Usually, under the low anthropogenic influence and with relatively small areas, lake ecosystems are known for their sensitive response to climate changes. Therefore, Lake sediments can record regional and global climate and environmental changes in a wide range of chemical and biological proxies (Castañeda and Schouten, 2011). This way, lake sediments are important archives for past environmental and climate changes, containing both organic and inorganic inputs within the lake, its catchment (runoff), and surrounding areas (by wind-driven sediments) (Meyers, 2003; Pearson et al., 2007; Wu et al., 2020). However, the linkage between climate, limnological processes, and environment is complex and leads to an inherent source of uncertainty in the record preservation in the sediments (Briffa and Cook, 2008). Several studies in Western Europe depicted that using a lake record for paleoclimate reconstructions can be highly variable, depending on factors such as sediment continuity, sedimentation rate, sampling resolution, and chronological accuracy (Moreno et al., 2014a). Table 1.1 summarizes the significant advantages and limitations of these archives for paleo-climate studies.

Table 1.1 – Advantages and limitations of lake sediments for paleoclimate reconstruction based on Moreno et al., 2014a and Hernández et al., 2020b.

Advantages	Limitations
➢ High-interpretable temporal resolution (from annual to decadal). ➢ Widespread distribution. ➢ A wide range of proxies can be obtained (biotic and abiotic). ➢ Some lake sediments contain tephra layer (for absolute dating). ➢ Independent varve chronologies (varved sediments). ➢ Usually, continuous record >1000 years in length.	➢ Lack of continuity in dry or cold climates. ➢ Dating is difficult beyond ^{14}C range (ca. 15 ka) or when sediments have low organic content. ➢ Age uncertainty up to > ±50 years. ➢ Lacustrine sedimentation is tightly linked to local factors – not always a good representation of past regional climate. ➢ Human impact.

Furthermore, lakes have a wide variety of size and shapes, vertical structure, and chemical composition, often receiving large amounts of allochthonous input from their surrounding watersheds, it is not a simple matter to interpret biomarkers from lake sediments in paleoclimatic terms, and site-specific calibrations may be required (von Gunten et al., 2012; Bradley, 2015). However, lakes can give huge and significant amounts of data, and considerable progress has been made in lacustrine biomarker paleoclimatology (Bradley, 2015). For example, in closed and small lakes, changes in effective moisture may be reconstructed from fluctuations in lake level and/or salinity inferred from physical and biological proxies, changes in ice cover, or temperature-driven changes in pH or Dissolved Organic Carbon (DOC) can give important information and can also be reconstructed from biological proxies (Briffa and Cook, 2008).

1.5.1. Biogeochemical indicators in lake sediments

The organic matter (OM) is a complex mixture of various organic compounds (Kolattukudy, 1980; Schimmelmann et al., 2006) such as lipids, carbohydrates, proteins, and other biochemical components, which can be present concomitantly in a sample but present different degrees of preservation (Meyers et al., 2003).

The OM of lake sediment can have contributions of several organisms that have lived in the lake, catchment area (watershed), and surrounding areas (e.g., Fig. 1.29) (Meyers et al., 2003), from all domains of life: archaea, eukarya, and bacteria. The OM can be classified according to its sources into two fractions: autochthonous (e.g., algae, macrophytes, and bacteria) and allochthonous (e.g., terrestrial plants and redeposition of other sedimentary rock OM) (Zhang et al., 2018).

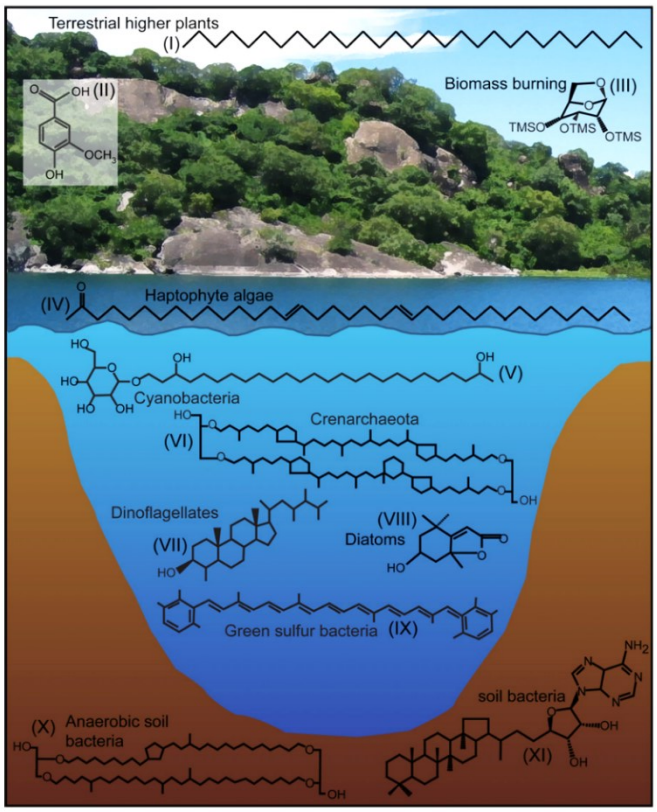

Figure 1.29 – Lacustrine sediments contain inputs from terrestrial and aquatic sources including higher land plants, microbes that live in the soils and sediments, various types of algae and microorganisms that live in the water column that eventually produce biomarker. See the I to XI biomarkers compounds and structural notations as examples. From Castañeda and Schouten, 2011, see references therein.

The organic matter content of lake sediments has been a central focal point of paleolimnological studies (Meyers et al., 2003). Bulk geochemical properties of organic matter commonly analyzed are the total organic carbon (TOC), total nitrogen (TN), carbon to nitrogen (C/N) ratios, and respective isotopic composition ($\delta^{13}C$ and $\delta^{15}N$), which are used to assess organic matter origins (Meyers et al., 2003). These parameters often reveal how lake ecosystems respond to environmental parameters such as atmospheric CO_2, water availability (e.g., Hodell, and Schelske, 1998; Jiang et al., 2020), light level, nutrient supply, temperature, etc., which affect, for instance, bioproductivity, degree of the OM preservation, sediment delivery routes and depositional processes (Summons et al., 2008).

The study of OM in the sediments is often used to assess the abundance and increases/decrease of primary productivity mass accumulation rates, typically mg cm^{-2} y^{-1}. For instance, high TOC and TN values, indicating high input of OM and good preservation, whereas bulk C/N and bulk OM $\delta^{13}C$ ratios are usually applied to give insight into sources of organic matter and vegetation type. In general, high values of C/N suggest terrestrial input, and low values indicate or low organic input or poor preservation from microbial/ chemical degradation. With high C/N values (e.g., ≥20) usually associated with land-plant, lower values (4 – 10) to algae sources and C3 plants which usually has associated high depletion in $\delta^{13}C$ (-30 to -25) when compared with C4 plants (-15 to -10) (Meyers et al., 2003). Along with these bulk OM proxies, more specific biogeochemistry proxies are also increasingly used, such as lipid biomarkers which narrows the research to more specific OM sources.

Biomarkers

Organic compounds that can trace a specific group organism or are indicative of a particular environmental process (e.g., photosynthesis, biomass burning) in the geological record are often called ‘biomarkers’ (Peters et al., 2005; Eglinton and Eglinton, 2008; Castañeda and Schouten, 2011). Biomarkers can be retrieved from diverse archives, such as ocean and lake sediments, rocks, and crude oil (e.g., Eglinton et al., 1964, Peters et al., 2005), and thus are also known as ‘molecular fossils’ (Peters et al., 2005; Diefendorf, et al., 2011; Schouten et al., 2013). Their structures and isotope ratios can be analyzed through refined analytical and highly sensitive chemistry instrumentation, such as mass spectrometers and gas and liquid chromatographs (Sachs et al., 2013).

Following Peters et al., 2005, three main characteristics distinguish biomarkers from many other organic compounds:

- Biomarkers have structures composed of repeating subunits, indicating that their precursors were components in living organisms.
- Each parent biomarker is common in certain organisms. These organisms can be abundant and widespread.
- The principal identifying structural characteristics of the biomarkers are chemically stable during sedimentation and early burial.

The optimal conditions to preserve the OM during and after sedimentation occurs in oxygen-depleted (anoxic) depositional environments (Peters et al., 2005), conditions usually found in ocean and lake sediments. However, other factors which directly determine this preservation vary with the depositional regime, such as the interaction between organic and inorganic materials over locally variable time scales (Hedges and Heil, 1995).

Sedimentary biomarkers provide an important tool to study OM sources (Volkman et al., 1980). In that regard, the lipid content is an important feature that may include compounds like fatty (alkanoic) acids, wax esters, ketones, hopanols, and sterols, compounds found in bacteria and algae membranes and higher plants (Sachse et al., 2012).

Lipids are the essential class of compound with many biological functions and a wide variety of diagnostic structural attributes of living organisms, some are known for their excellent capability to resist harsh environmental conditions and, therefore, they are considered remarkable biomarkers (Summons et al., 2008 and references therein). These compounds can provide vast amounts of information and have become an increasingly common tool in many disciplines. Structures, abundances, ratios, and stable isotopes of biomarkers can trait the ecology, climate, and environmental conditions of their source organisms and reflect processes that affect them, such as transportation and diagenesis (Pancost and Boot, 2004).

In the past decades, the development of molecular lipid biomarker proxies has received much research attention with several proxies have been suggested and developed, providing quantitative and qualitative approaches to reconstruct climate and environment changes, such as precipitation and atmospheric patterns, temperatures, salinity, upwelling, anoxia, soil erosion, etc. (e.g., Rieley et al., 1991; Meyers, 1997, Ficken et al., 2000; Schefuß et al., 2003; Jansen and Wiesenberg, 2017; Baqloul et al., 2021).

Typical terrestrial biomarkers are associated with lipids derived from photosynthesizing organisms such the epicuticular leaf wax, cutin, and suberin of plants (Eglinton et al., 1962, Eglinton and Hamilton, 1967; Kolattukudy, 1980). These compounds are mainly formed by condensation of acetic acid in the epidermal cells, which derived the *n*-Alkyl structures such *n*-alkanes, *n*-alkanols, *n*-alkanoic acids (*n*- meaning 'normal') and wax esters Pancost and Boot, 2004) by decarboxylation or acyl reduction of the long-chain fatty acids (Cheesbrough and Kolattukudy, 1984, Park et al., 2005, Wiesenberg et al., 2010). For instance, the acetogenic pathway from acetyl coenzyme-A (acetyl CoA) produces and elongates *n*-alkanoic acids that are then converted to *n*-alkanes by enzymatic decarboxylation or to *n*-alkanols by reduction (see references in Diefendorf and Freimuth, 2017).

Leaf waxes are essential for external protection (Eglinton and Hamilton, 1967), such as dehydration, pathogens, insects, and ultraviolet light exposure. Usually, each major taxonomic group has a predominant *n*-alkyl concentration and carbon chain length distribution pattern (see Suh and Diefendorf, 2020). Following Diefendorf and Freimuth's 2017 recommendations, the 'plant wax' term should be used in a general sense, referring to the different wax components sourced from plants, especially in soils and sediments, whereas the term 'leaf wax' should be referring to lipids sampled directly from leaves.

n-Alkanes

n-Alkanes are saturated straight-chain hydrocarbons with the general formula of $H_3C[CH_2]_nCH_3$. Because of their chemical structure and lack of functional group, these compounds are capable of persisting in sedimentary archives for millions of years (Eglinton and Logan, 1967; Logan et al., 1995; Peters et al., 2005; Feakins, et al., 2007, Summons et al., 2008).

Easily dispersed by wind and water, the *n*-alkanes end up in lakes and ocean sediments, providing important insights into how vegetation has changed in a particular catchment area (Schefuß et al., 2003; Rommerskirchen et al., 2006a). Their high preservation potential makes *n*-alkanes one of the most studied and important groups of biomarkers in paleo studies (e.g., Eglinton and Hamilton, 1967; Cranwell, 1981; Volkman et al., 1998; Sachse et al., 2006; Diefendorf et al., 2011; Castañeda and Schouten, 2011; Bush and McInerney, 2013; Jambrina-Enríquez et al., 2016; Li et al., 2020b). The two principal sources of *n*-alkanes in lake sediments are: (1) vascular plants that live in the lake surrounds, producing distinctively different suites and amounts of these compounds, and (2) algae, bacteria, and vascular plants that live within the lake (Meyers et al., 2003).

Plants produce a range of *n*-alkanes, mainly in their epicuticular leaf waxes, commonly with a strong odd-over-even predominance (OEP; Eglinton and Hamilton, 1967) and one or two dominant homologues (commonly referred C_n, where n is the carbon number in the chain,). Leaf waxes lipids are part of the external barrier protecting the plant from the outside environment and contributing to the hydrophobic properties of leaves (Eglinton and Hamilton, 1967; Post-Beittenmiller, 1996; Jetter et al., 2008). Therefore their synthesis is ultimately controlled by the prevailing climatic and environmental conditions (Shepherd and Griffiths, 2006).

Although widely variable, terrestrial plants are characterized by producing chains ranging from C_{25} to C_{35} (Eglinton et al., 1962, Eglinton and Hamilton, 1963, 1967), being the long-chain C_{27}, C_{29}, $C_{31,}$ and C_{33} the most commons (see Pancost and Boot, 2004). Indeed, these long-chain *n*-alkanes are among the most recognizable and utilized biomarkers in the paleo studies field (Bush and McInerney, 2013).

The amount of *n*-alkanes produced by plants are not always constant, it can depend on how a species response to environmental pressures, like temperature, aridity, or ablation of the wind and hence the seasonality (e.g., Schefuß et al., 2003; Rommerskirchen et al., 2006b; Cui et al., 2008; Jetter et al., 2008, Luo et al., 2012; Bush and McInerney, 2013; Jansen and Wiesenberg, 2017; Diefendorf and Freimuth, 2017; Stout, 2020; Jiang et al., 2020). For instance, the *n*-alkane productions can change with the seasonality, usually with Summer and Fall exhibiting the lower values, but also on broader timespans depending on the prevailing conditions (e.g., Shepherd and Griffiths, 2006; Freimuth et al., 2017; Diefendorf et al., 2021). Thus, the sedimentary *n*-alkane content results from net wax production and removal processes, where higher concentration in the sediments would result from either increased leaf wax production or higher leaf waxes removals, such as ablation by wind or rain (Shepherd and Griffiths, 2006). For instance, during the prevalence of windy conditions, plants might respond with a thickening of the *n*-alkane layer, as plants will demand further external protective mechanisms to overcome the water stress (Shepherd and Griffiths, 2006, Rommerskirchen et al., 2006b; Cui et al., 2008).

The use of *n*-alkanes as climate proxies depends on profound understandings gained from studying the relationship between climatic factors and *n*-alkanes in living plants (see Shi et al., 2021). For instance, the high amounts of *n*-alkanes seem to favor some plants to thrive during cold periods (Cui et al., 2008), grasses usually have higher production rates than trees (Rommerskirchen, et al., 2006b; Vogts et al., 2009). Several studies focusing on the relationship between the total concentration of *n*-alkanes in modern plants and precipitation and/or temperature (Shi et al., 2021, see references therein).

The predominance of a particular *n*-alkane pattern in the sediments may reflect the prevalence of particular vegetation (e.g., Jansen et al., 2013; Schäfer et al., 2016; van Manen et al., 2020). For instance, long-chain *n*-alkanes are typically higher in angiosperm trees and shrubs than in many gymnosperms (such conifers) (Diefendorf and Freimuth, 2017). In fact, the use of n-alkane can be used to reconstruct paleo vegetation in the geological record, with good agreement with pollen records (Schäfer et al., 2016, see references therein). In that regard, long-chain *n*-alkanes (C_{35}–C_{27}) are mainly derived from terrestrial higher plants (e.g. Schefuß et al., 2003: Peters et al., 2005) being the C_{33} and C_{31} usually derived from grasses or herbaceous plants (Maffei, 1996; Rommerskirchen et al., 2006b; Zech et al., 2010; Lie et al., 2010; Schäfer et al., 2016) and C_{31}, C_{29}, C_{27} typical from trees and shrubs (Cranwell, 1973; Baas et al., 2000; Pancost, et al., 2002; Schwark et al., 2002; Zech et al., 2010; Schäfer et al., 2016; Stout et al., 2020). C_{29} is the main *n*-alkane procuced by coniferous while C_{27} is usually associated with deciduous trees (e.g., Schwark et al., 2002; Ortiz et al., 2010; Leider et al., 2013; Schäfer et al., 2016).

Mid-chain lengths—C_{25}, C_{23}, and C_{21}—have been utilized to model peat moss and aquatic plants in freshwater and marine environments (Cranwell, 1984; Baas, et al., 2000, Ficken et al., 2000; Pancost, et al., 2002).

Shorter-chain molecular ($C_{<21}$) are mainly produced by phytoplankton and bacteria (Gelpi et al., 1970; Cranwell et al., 1987; Meyers and Ishiwatari, 1993; Sachse et al., 2012).

The process of *n*-alkane transferring to the soil or sediments and its preservation is of great importance to an accurate inferring of past ecological conditions. For instance, the *n*-alkane carbon chain pattern reduction during the transfer via plant litter to the soil or sediment (sedimentary waxes) (e.g., Schäfer et al., 2016; Howard et al., 2018; van Manen et al., 2020; Thomas et al., 2021). Although this may not affect the environmental information, as long as the relative abudance remains the same (e.g., Jansen et al., 2006; Schäfer et al., 2016; van Manen et al., 2020).

Different indices or indexes of *n*-alkane distribution have been developed to examine the distribution of *n*-alkanes in sediments, soil, and vegetation/litter samples. However, there is no general sense of calculating the first two. Indeed, Thomas et al., 2021 highlighted "*a lack of data transparency and standardization across studies of lipid biomarkers, making analysis and synthesis of published data time-consuming and difficult*."

Within the most used indices, the average chain length (ACL), the carbon preference index (CPI), and the proportion of aquatic plants (Paq) are the most commonly applied. ACL is used to identify the preferentially produced *n*-alkane. This indice uses the weighted average of the various carbon chain lengths (Poynter, 1989) and is defined as (1.1).

$$ACL = \sum (Cn \times n) / \sum (Cn) \qquad (1.1)$$

Where C_n is the concentration of a given *n*-alkane and *n* the respective carbon number length. The ACL in the sedimentary record is controlled by the dominant vegetation type of the source area, hereafter considering the C_{27}-C_{33} range, i.e., $ACL_{C27\text{-}C33}$. There is a general negative correlation between ACL and latitudes (Bush and McInerney, 2015; Feakins et al., 2016), whereas in terms of temperature that relation is positive in some regions of the globe, such in Europe (Sachse et al., 2012; Leider et al., 2013), North America (Bush and McInerney, 2015), Tibetan Plateau (Li et al., 2020a), China (Duan and He, 2011), Australia (Hoffmann et al., 2013) and Peru (Feakins et al., 2016). However, the use of ACL as a climate indicator should be taken cautiously since many factors can influence its variability, such as the biological regulation to evapotranspiration (Schefuß et al., 2003) of the different vegetation types (Zhou et al., 2005; Howard et al., 2018; Shi et al., 2021).

The CPI measures the relative abundance of odd over even carbon chain lengths (e.g., Freeman and Colarusso, 2001) and captures the degree to which odd carbon number *n*-alkanes dominate over even carbon numbers. It can be utilized to assess the general source of long-chain *n*-alkanes, level of degradation of the OM, and diagenesis processes of a sedimentary record, which ultimately ascertain the reliability of the use of a sample as a paleoclimatic indicator. First defined by Bray and Evans, 1961, CPI can be calculated as shown in the equation (1.2).

$$CPI = \tfrac{1}{2} [\sum_{odd} (C_i + C_{i+2} + \ldots + C_n) / \sum_{even} (C_{i-1} + C_{i+1} + \ldots + C_{n-1}) + \sum_{odd} (C_i + C_{i+2} + \ldots + C_n)) / \sum_{even} (C_{i+1} + C_{i+3} \ldots + C_{n+1})] \qquad (1.2)$$

C_i and C_n are the concentration of the initial and last considered *n*-alkane range, respectively, the typical ranges are centered at C_{27}-C_{31}. A value greater than 1 shows a predominance of odd over even chain lengths. In immature sediments and rocks, the *n*-alkane content is rather immobile, but as the maturity (or degradation) increases, the odd over even compounds preference is lost, decreasing the CPI values. Different CPI ranges are used and there are even equivalent equations (e.g., see Schefuß et al., 2003; Zech, et al., 2010; Diefendorf et al., 2011; Li et al., 2020b; Thomas et al., 2021). Nevertheless, high CPI values, such as 5 – 10, usually indicate a terrestrial plant source and thermal immaturity source rock implying that the sedimentary *n*-alkanes are reliable as a paleoclimatic indicator, lower values(~ 4), can indicate microbial and algal sources (Clark and Blumer, 1967), whereas CPI values of 1 – 2, indicate a considerable degree of degradation, diagenesis or

petroleum contaminations (Bray and Evans, 1961; Eglinton and Hamilton, 1967; Cranwell et al., 1987; Pancost and Boot, 2004).

OM degradative (or preservative) conditions are often linked with the different climatic conditions, that either enable or inhibit microbial proliferation (Zhou et al., 2005). For instance, normally, during cold and dry conditions, the OM degradation is slower (Kuder and Kruge, 1998), resulting in high CPI values (e.g., Xie et al., 2004; Ortiz et al., 2013). This explains why CPI values are often negatively correlated with precipitation/relative humidity in some areas of the globe, with higher CPI values associated with higher aridity (Luo et al., 2012; Li et al., 2020a). However, like ACL, CPI often has a regional significance and can be associated with other conditions such as temperature, and often have different interpretations (Zhou et al., 2005; Shi et al., 2021).

The Paq index is used to evaluate the relative contributions of aquatic plants and terrestrial higher plant *n*-alkanes in the sediments. It can be calculated following Ficken et al., 2000 as described in (1.3).

$$Paq = (C_{23}+C_{25}) / (C_{23}+C_{25} + C_{29}+C_{31}) \quad (1.3)$$

Following Ficken et al., 2000, Paq values <0.1 in the sediments indicate a dominant contribution from land plants, values of 0.1 to 0.4 significant input of emergent macrophytes, whereas > 0.4 are typical of sediments with major input from submerged/floating macrophytes.

Despite the exposed relevance of the *n*-alkanes, their interpretation for assessing and reconstructing past environments and climate can be relatively complex since there are different natural sources (natural, anthropogenic), processes (e.g., burial, diageneses), and transportation (e.g., runoff, by air) affecting the *n*-alkanes (see Schefuß et al., 2003; Pancost and Boot, 2004; Maioli et al., 2010; Li et al., 2020b). Moreover, the regional responses to environmental change can have regional meaning. Thus it is imperative to determine the specific *n*-alkane sources for the studied area to archive a proper reconstruction using recent sedimentary records (Leider et al., 2013; Hockun et al., 2016).

Compound-specific isotopic signal of long-chain n-alkanes

Over the past decade, substantial efforts have been made to constrain the factors that influence plant biomarkers and their isotope composition to improve their utility for paleo applications (Diefendorf and Freimuth, 2017). The compound-specific stable isotope (CSSI) of long-chain *n*-alkanes biomarkers can give accurate and precise insights about the carbon and hydrogen changes, enhancing the understanding of past OM sources, carbon and water cycles, and have been widely applied to the study of paleo- environmental, ecology and climate (e.g., Chikaraishi and Naraoka, 2003, Schimmelmann et al., 2006, Castañeda and Schouten, 2011; Sachse et al., 2012; Cooper et al., 2015; Mabit et al., 2018, Weiss et al., 2021).

Carbon isotopes ratios ($^{13}C/^{12}C$) in specific compounds of wax *n*-alkanes are a powerful tool in paleo climate and environmental studies, expressed by the $\delta^{13}C_{wax}$ in ‰ relative to the Vienna Pee Dee Belemnite (VPDB) standard, which often complements the $\delta^{13}C$ values of bulk organic matter (OM_{bulk}) (Meyers, 2003). $\delta^{13}C_{wax}$ can reflect the isotopic composition of the CO_2 source during carbon assimilation and plant biosynthesis fractionation that occurs during the photosynthetic process, such as the C_3 and C_4 pathways (e.g., Rommerskirchen et al., 2006a; Freeman and Colarusso, 2001; Schefuß et al., 2003, Leider et al., 2013; Moreno et al., 2014a; Diefendorf and Freimuth, 2017; Curtin et al., 2019). This provides information on how vegetation responds to climate change, where factors like temperature and aridity can also affect $\delta^{13}C_{wax}$ signature. For instance, the prevalence in aridity and low pCO_2 in tropical areas can lead to the predominance of C_4 over C_3 type of vegetation (Schefuß et al., 2003, Niedermeyer et al., 2010), with lower $\delta^{13}C_{wax}$ values typically associated with C_3 trees and shrubs and higher $\delta^{13}C_{wax}$ values are typical of C_4 plants, such as grasses and sedges (e.g., see Hahn et al., 2021). An essential feature of the $\delta^{13}C$ signature in paleo studies is the minimal influence in burial and diagenesis processes, which otherwise would complicate its evaluation (Diefendorf et al., 2011, see references therein).

The hydrogen isotopic ratios (D/H) of plant wax-derived biomarkers, usually expressed by δD_{wax} in ‰ relative to the Vienna Standard Mean Ocean Water (VSMOW) standard. The δD_{wax} results from a complex

net fractionation process involving water source isotopic signatures (e.g., meteoric water, groundwaters, lake water), soil evaporation and evapotranspiration, and biosynthetic fractionation (ε_{bio}) (see Fig. 1.30a).

The δD_{wax} signal is ultimately controlled by climatic conditions such as temperature, evaporation, and precipitation (Fig. 1.30b) is therefore used as a reliable proxy for assessing paleo hydrological conditions, including factors such as atmospheric sources (air masses), temperature, and hydrologic balance (Dawson et al., 2002; Sachse et al., 2006, 2012; Smith and Freeman, 2006; Hou et al., 2008; Sachse et al., 2012; Kahmen et al., 2013; Freimuth et al., 2017; Diefendorf and Freimuth, 2017; McFarlin et al., 2019). Another critical factor accounting for this net process is the ε_{bio} occurring in the leaf waxes synthesis, which is somewhat variable between organisms and ecosystems and comprises the most extensive negative isotope fractionation, D-depletion (Sessions et al., 1999, Sachse et al., 2004, 2012). The net offset between δD_{wax} and the δD of precipitation (δD_{prc}) is known as apparent fractionation (ε_{app} or $\varepsilon_{l/p}$), an important factor to examine the paleohydrology conditions, which despite being the prime source of uncertainty paleohydrology using leaf waxes, has show generally constant values, and therefore the leaf wax *n*-alkanes primarily reflect the isotopic composition of precipitation (Sachse et al., 2012; Freimuth et al., 2017). $\varepsilon_{l/p}$ typically follows the equation (1.4) (after Sessions et al., 1999), in units per mil, ‰.

$$\varepsilon_{l/p} = 1000[(\delta D_l + 1000)/(\delta Dp + 1000) - 1] \quad (1.4)$$

Where, *l* is the lipid biomarker and *p* precipitation.

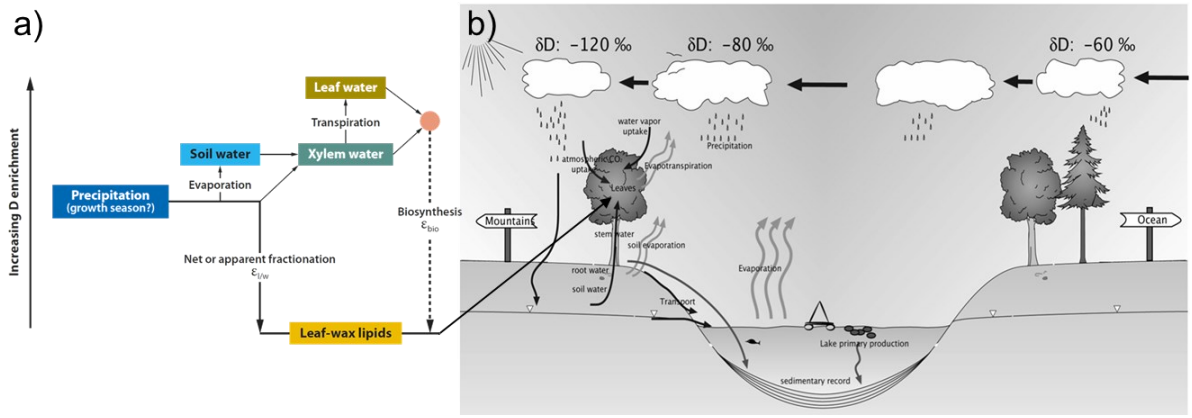

Figure 1.30 – Major factor controlling hydrogen-isotopic signal in leaf-wax n-alkanes. a) Conceptual diagram after Sachse et al., 2012, describing the hydrogen-isotopic relationships between precipitation and leaf-wax n-alkanes from terrestrial plants (not to scale). The red dot illustrates a hypothetical biosynthetic water pool, i.e., a potential mixture of different water pools within the leaf and the ultimate hydrogen source for lipid biosynthesis. b) Fractionation processes for hydrogen isotopes on the ecosystem scale and contribution of organic matter from various sources to sedimentary organic matter from Mügle, 2008.

The use of δD_{wax} as a paleo indicator, such as the isotopic signal of paleo precipitation, can be regionally constrained, usually requiring robust calibration studies of sedimentary waxes against modern-day precipitation isotopic signal (Sachse et al., 2012; McFarlin et al., 2019). In the tropics, δD_{wax} generally reflects changes in the precipitation amount, in the midlatitudes, it can have multiple responses, such as atmospheric sources and precipitation amount changes (Leider et al., 2013; Wirth and Sessions, 2016; Schäfer et al., 2018), whereas in high latitudes it is usually temperature dependent (Niedermeyer et al., 2010, Thomas et al., 2012).

The isotopic off-set between δD signal of terrestrial (δD_{terr}) and aquatics (δD_{aq}), often referred to as $\varepsilon_{terr\text{-}aq}$, can be used as a proxy for evapotranspiration conditions, which signal should be constrained with confidence in terms of the orign of both terrestrial and aquatic *n*-alkanes (Rach et al., 2014). For instances, in humid and temperate climate, such as the modern temperate regions of Europe $\varepsilon_{terr\text{-}aq}$ often display a positive signal (Sachse et al., 2004, 2006; Mügler et al., 2008a; Rach et al.,2014), while in opposite climate scenarios, like the cold and arid climate of the Tibetan plateau, $\varepsilon_{terr\text{-}aq}$ get more negative (Mügler et al., 2008b).

One possible issue involving δD_{wax}, is the information lost during diagenesis and thermal maturation. Even though the earliest stages of diagenesis do not affect most lipid biomarkers (Schimmelmann et al., 2006), with high levels of maturity, biomarkers become thermally unstable. They can experience degradation, with consequent large hydrogen isotope exchange (Sessions et al., 2004) which can limit paleoclimate information (Hoefs, 2018).

2. STUDY AREA

Serra da Estrela

Serra da Estrela (Estrela Mountain, or simply Estrela, 40°19′18.72″N, 7°36′46.68″W) is an intraplate mountain range with SW-NE direction located in the westernmost sector of the Iberian Central System (ICS) in central Portugal (Fig. 2.31). Estrela encompasses the highest point of continental Portugal, with its plateau reaching 1993 meters above mean sea level (a.m.s.l).

The ICS is a prominent feature of the Meseta Central, the inner Iberian plateau, that separates the Northern and Southern Meseta (see Ribeiro, 1990). This range was formed during the Alpine orogeny (mainly during the Miocene–Pliocene) by the uplift of the Hercynian (or Variscan) basement, around 25 million years ago (Casas-Sainz and De Vicente, 2009). Estrela is one of the two basement uplifts blocks in the region, compresing the Estrela-Gardunha and the Gata-Sierra de Francia ranges, both consequences of a compressive strike-slip corridor that comprises two main thrusts, the Seia-Lousã Fault and the Ponsul Fault (Vegas et al., 2019) were Estrela resulted as a pop-up structure (Ribeiro et al., 1990). A prominent the Bragança-Vilariça-Manteigas left-lateral fault cuts plateau summit of Estrela and is one of the major structures of the late-Variscan fault system network in Northwestern Iberia, that has major effects on the regional hydrology.

Estrela mountain is composed mainly composed by Variscan granitic rocks, some Precambrian-Cambrian metasedimentary rocks can be found in its surroundings beside the alluvium and Quaternary glacial deposits (see Marques et al., 2005).

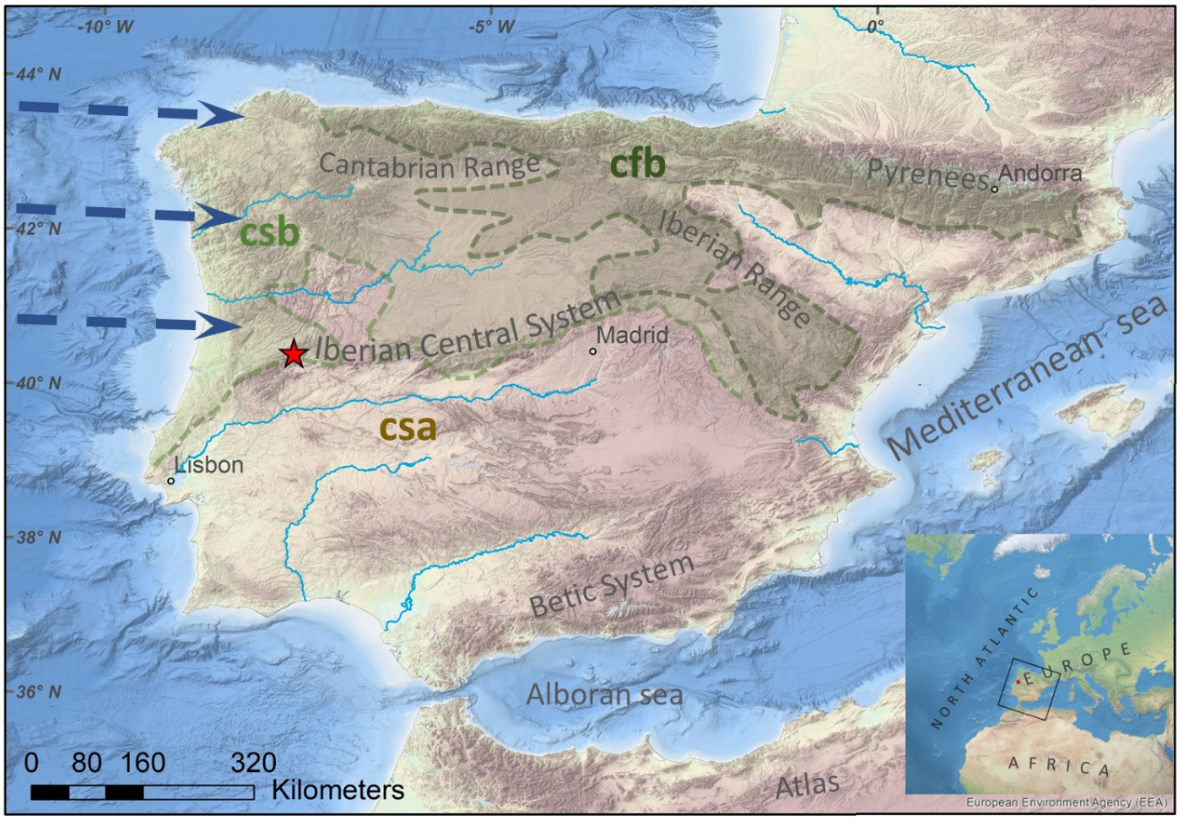

Figure 2.31 – Morphological map of the Iberian Peninsula, with the main rivers and bathymetry. Lake Peixão location identified a red star. Sources: Cultural data from Natural Earth (naturalearthdata.com); European map from (shadedrelief.com); River network from European Environment Agency (EEA); Topography and bathymetry from portal.emodnet-bathymetry.eu. Overlapped with the simplified Köppen-Geiger climate classification for the Iberian Peninsula (1971-2000) (adapted from the IM, Iberian Climate Atlas, 2011). Csa: Hot-summer Mediterranean; Csb: Mild-summer Mediterranean; Cfb: Oceanic. The dark-blue arrows represent the moist rich prevailing westerlies coming from the Atlantic Ocean entering in Iberia.

The upper part of Serra da Estrela relief is dominated by two major plateaus, the Torre-Penhas Douradas plateau (1450-1993m a.m.s.l), located in the western side, and the Alto da Pedrice–Curral do Vento plateau (1450-1760m), separated by the NNE-SSW Zêzere river headwaters (Vieira, 2004; Vieira et al., 2005). Late

Pleistocene glacial landforms and deposits are a distinctive feature on these plateaus (e.g., Fig. 2.32) which were glaciated during the Last Glacial Maximum, ca. 30 ka (e.g., Daveau et al.,1997, Vieira, 2004; Vieira et al., 2021).

At the glaciation peak, the ice cap would occupy most of the Torre – Fraga das Penas plateau (1993 – 1650 m a.m.s.l), responsible for developing several radiating valley glaciers Estrela that flowed downwards during the last glaciation (Vieira et al., 2005). The glaciated area corresponded to ca. 70 km^2 (Daveau, 1971; Vieira, 2008), with the snow equilibrium line reaching an altitude ca. 1650 m (a.m.s.l) (Vieira, 2008). The imposing Zêzere glacier occupied over 11 km in length, with ice reaching 340 m thick in some parts (Vieira et al., 2005; Vieira and Nieuwendam, 2020), being today a notable glacial feature of the Estrela UNESCO Geopark, known as Zêzere Glacial Valley (Fig. 2.32). On the central plateau, above 1400 m elevation, is where most traits of this glacial past can be seen, such as lakes and ponds (Daveau, 1971), but also other geomorphological features such as polished rock outcrops, Roches mouttonées, and glacial cirques (Vieira et al., 2005). This glacial history is directly related to the modern-day biotopes of Serra da Estrela, one of the most important European refugia for different flora and fauna during the Quaternary ice ages (Jansen, 2011).

The beginning of the Holocene in Serra da Estrela was marked by a period of *Betula alba*-dominated open woodland, at least up to the 1400 m altitude. The development of the oak forests is slower due to immature soils and low temperatures (van der Knaap and van Leeuwen, 1995). The earlier phases of the Holocene in Serra da Estrela were driven by climatic changes, with *Quercus* Forest gradually replacing the open woodland in higher altitudes. The *Quercus* incursion towards higher elevations was linked with forest dynamics reflecting warmer climate and possibly also wetter conditions (van der Knaap and van Leeuwen, 1997). Human influences are inferred to happen more consistently in later stages, stating at ca. 4550 BP, due to accelerated growth landscape degradation and soil erosion. Some large-scale deforestation is inferred from ca. 3220 to 955 BP, but the forests can still regenerate. After ca. 955 BP to the present-day, the anthropogenic pressure increases to such an extent that the *Quercus* and other forests virtually disappear, and organic soils are eroded and washed away for the more significant part. The principal agents of this anthropogenic pressure are grazing, burning, agriculture, and large-scale plantation of pines and, more recently, *Eucalyptus* (van der Knaap and van Leeuwen, 1995).

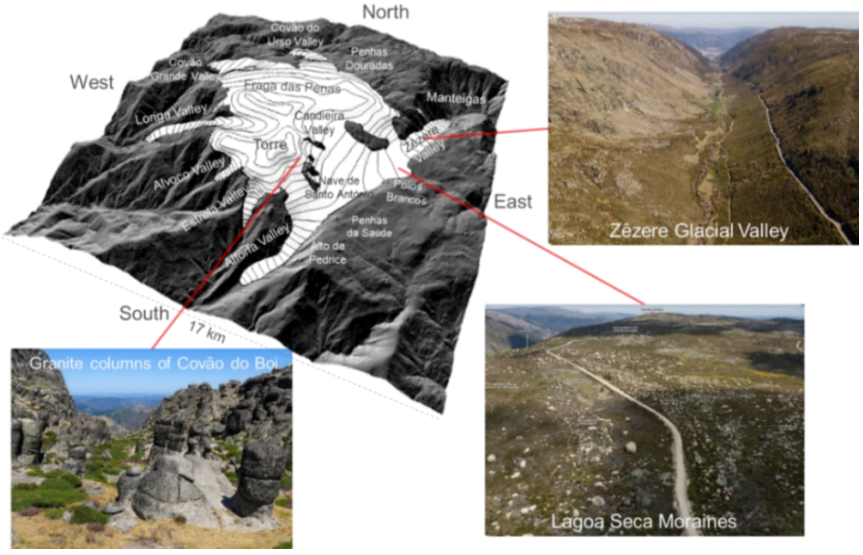

Figure 2.32 – Maximum glaciation reconstruction of Serra da Estrela plateau icefield and glacial valleys. Icecap in white tones, view from the South, with 50 m interval contours represented over the glacier surface (Adapted from Vieira et al., 2008) with present-day photos of the last glacial imprints in the Serra da Estrela landscape (from Gomes et al., 2019).

Today, Estrela is characterized by a typical Mediterranean climate with dry and warm summers, with the wet season extending from October to May. It is characterized by strong vertical gradients in both temperature and precipitation (Vieira et al., 2005). The simulated history climate of the region, using an ensemble model (see portaldoclima.pt) from 1971 to 2000, shows that the warmest and driest months are July and August with mean values of around 20ºC and 17 mm. In contrast, the coldest and wetter months are December and January, with mean values around ~5ºC and 150 mm. However, temperature and precipitation values can be

significantly lower in Estrela Mountain than in the surrounding region. The mean annual air temperature is usually lower, with a mean 7ºC and as low as 4ºC in the mountain summit (Torre). The precipitation is also more significant than the surrounding region, with annual precipitation around 2500 mm at Torre (Vieira and Mora, 1998).

The spatial variability of precipitation seems to be mainly controlled by the slope orientation and altitude, with the basal areas reaching circa half of the summit values (Vieira, 2004). During the colder months (starting in October), the precipitation is more or less constant and accumulates in the higher areas as snow (Carreira et al., 2009).

Estrela is a sensitive site for the study of past climate and ecology. About 100 kilometers away from the Atlantic Ocean is a key location for studying past atmospheric-oceanic-land dynamics, located in the transition between the temperate climate of the north, and a drier Mediterranean climate, to the south. The high altitude of the range constitutes one of the biggest physical barriers to air masses coming from the Atlantic Ocean (Vieira, 2004; Hernández et al., 2017). The vegetation reflexes this complex interaction in one of the most biodiverse regions in Europe (Janssen and Woldringh, 1981; Knaap and Van Leeuwen, 1997; Vieira, et al., 2005, Janssen, 2011, Connor et al., 2020). Estrela can be divided into three main bioclimatic altitudinal zones, following Connor et al., 2012 and references therein:

- The basal level, with meso-Mediterranean climate (<900 m), with cultural landscapes dominated by Pinus plantations and remnant oak forests.
- The Middle level, with supra-Mediterranean climate (ca. 900-1600 m), with abundant heathlands of Juniperus communis, *Calluna vulgaris*, *Erica spp.* and *Cytisus spp*, and a remnant of *Q. pyrenaica* and chestnut woods.
- The Upper level (>1600 m), in the mountain summit, has an oro-Mediterranean climate, characterized by grasslands, pastures, sparse herb fields, and juniper scrubs. Matgrass lawns, and aquatic communities are also found.

Several past climates and environmental reconstruction studies have been conducted in Estrela over the last decades, primarily focusing on ecology: (Romariz, 1950; Janssen and Woldringh, 1981; van den Brink and Janssen, 1985; van der Knaap and Van Leeuwen (1994, 1995, 1997); Connor et al., 2012; and glacial geomorphology related studies: Daveau, 1971; Vieira et al., 1998, 2001; Ferreira et al., 2001; Vieira, 2008; Daveau, et al., 2014; Vieira et al., 2021); with multiproxy studies in the lakes sediments only recently have been conducted in the region (Hernández et al., 2017).

Lake Peixão

The sediment core used in this study was retrieved from Lake Peixão (ca. 1670 a.m.s.l, 40°20'35"N; 7°36'19"W) on top of Serra da Estrela Mountain (Fig. 2.33). This glacial lake apparently did not become ice-free until the end of the late glacial period (Knaap and Van Leeuwen, 1997).

Lake Peixão has a relatively small area (16000 m^2), with ca. 70 m radii, and is enclosed by steep slopes of granitic rocks with poorly developed and scarce soils in the catchment area (~ 0.30 km^2).

The bioclimatic zone of the lake catchment lies in the transition between supra- and oro-Mediterranean climate, with a dominance of scrub vegetation, with a prevalence of *Genista sp*., *Cytisus sp*., and *Erica sp*., *Calluna vulgaris,* and *Juniperus communis* (Connor et al., 2020) and some grasslands dominated by *Agrostis delicatula* and *Nardus stricta*. Few and small ephemeral streams flow into the lake with a maximum water depth of ca. 5 meters, waters are slightly acidic, oligotrophic, and monomictic, the organic productivity in the lake is low, and there are abundant allochthonous sediments (Hernández et al., 2017). The lake has a spill point in the south that allows drainage into the Candieira valley.

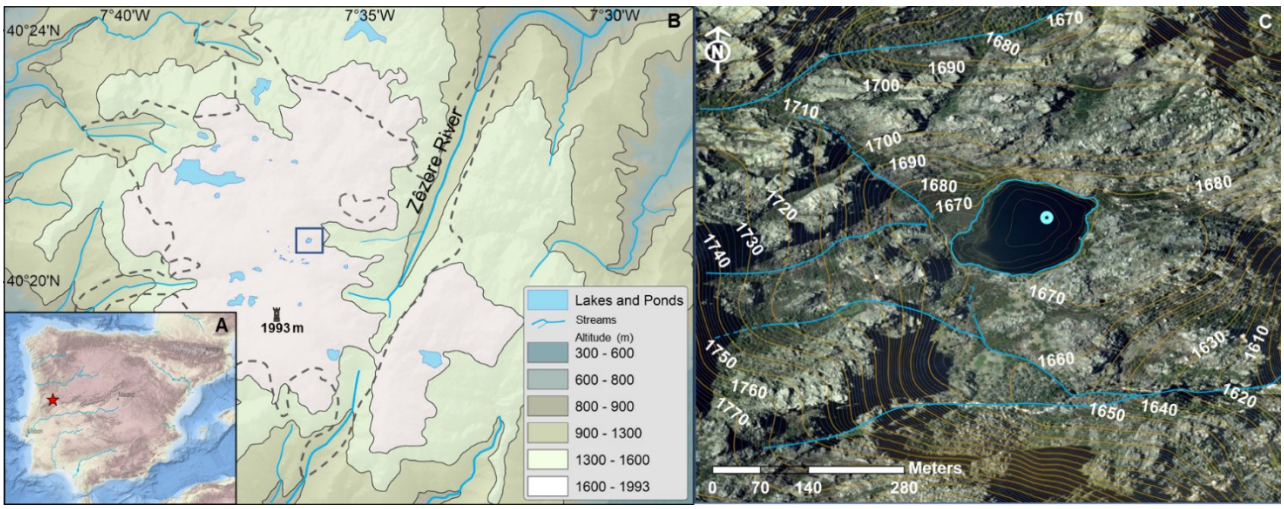

Figure 2.33 – A - Location of the Serra da Estrela, Portugal. B - Estrela plateau, with the icefield from the last glacial maximum is marked with a dashed line (after Vieira, 2008). The black circled zones are above the meso-Mediterranean bioclimates (>900m). The light brown level corresponds to the transition between meso-Mediterranean to full supra-Mediterranean climate. The yellowish green to corresponds to full supra-Mediterranean conditions and beige to oro-Mediterranean (adapted after Connor et al., 2012). C - Lake Peixão (constrained with a light blue line), the location of the sediment core used in this study are marked with a blue dot. Sources: The bathymetric metadata courtesy from EMODnet Bathymetry portal; Digital Elevation model courtesy of ©JAXA/METI ALOS PALSAR. Satellite Imagery from Esri

3. Material and Methods

3.1. Sedimentary coring and vegetation sampling

In Jun 2019, a coring campaign took place in Lake Peixão as part of the FCT-funded project (PTDC/CTA-GEO/29029/2018) 'HOLMODRIVE'. Multiple sediment cores were retrieved using a UWITEC Piston Corer from a floatable platform, using PVC tubes with 60 mm width. The sediment record used in this study was collected in the deeper part of the lake ca. the center (40°N20'35"; 7°W36'48") at 3.32 m water depth.

Each core section (hereafter referred as 'drives') were carefully sealed and tagged before being transported into the Centre Eau Terre Environnement - National de la Recherche Scientifique–Eau Terre Environnement in Québec City (Quebec, Canada) where the core was split longitudinally into two halves and performed a series of non-destructive methods.

Samples of dominant vegetation (leaves from shrubs and grasses), plant litter, and a soil sample were collected from Lake Peixão catchment area during September 2020 (see Fig. 3.34).

Figure 3.34 – Lake Peixão surroundings. Representative vegetation type (heathlands with grass mosaics), the left figure show shrubs (green squares) and grasses (orange squares) were analyzed in this study. The right figure shows two main aquatic-related plants (blue squares) on a small pond in the lake Peixão surroundings.

3.2. Core sub-sampling

Each core section (hereafter nominated 'drives') was carefully sealed and tagged before being transported and stored into a dark cool room at ± 4 °C at IPMA (Algés) until the sub-sampling and analytical approaches.

The sediment core was sub-sampled at the sedimentology laboratory of the Marine Geology division (IPMA) using adapted syringes. 3 cubic centimeter (cc) was collected every 2 cm in one half of the core for the n-alkane analysis (60 samples). The other proxies were made every 4 cm, in the case of bulk organic matter and diatoms analysis (31 samples each) and 16 cm resolution for pollen analysis (8 samples). Some of these proxies were pre-treated and sent to different institutions and collaborators whose results were part of the working group project outcomes.

3.3. Working-group project outcomes

Other analysis on the lake sediments were performed by other researchers under the framework of the HOLMODRIVE project, the present study uses:

- The non-destructive performed in the sediments consisted of analyzing the X-Ray Fluorescence (XRF), Magnetic susceptibility, Hyperspectral, and Computed tomography (CT) scanning. High-resolution photographs of each core section were also obtained using the Charge-Coupled Device (CCD) camera from the core scanner (see chapter 9.1, annexes). The XRF data were acquired using an ITRAX core scanner. High-resolution geochemical variations were measured using a molybdenum tube. The data acquisition was performed at 5 mm resolution with an exposure time of 15 s. Voltage and current were 30 kV and 30 mA. All elements were normalized by the total of counts for each spectrum.
- Pollen analysis. Sample preparation was performed in Ecole Pratique des Hautes Etudes (EPHE) from the Bordeaux University following the technique described by Desprat (2005). An exotic spike (Lycopodium) of known concentration has been added to each sample to permit the calculation of total pollen concentrations. A minimum of 100 pollen grains was counted (excluding Pinus, aquatic plants, spores, indeterminate and unknown pollen grains) using a transmitted light microscope at ×400 and ×1000 (oil immersion) magnifications.
- Bulk organic matter. After dried at 60 ºC for 48 h and manually ground, using an agate mortar until obtaining a fine powder, transferred to Eppendorf tubes and sent to Servizos de Apoio á Investigación, (University of A Coruna) for the determination of total carbon (TC), total nitrogen (TN), Carbon ($\delta^{13}C$) and nitrogen ($\delta^{15}N$). These analyses were carried out by combustion in a Flash IRMS analyzer coupled by means of a ConfloIV interface to a DeltaV Advantage isotope ratio mass spectrometer (ThermoScientific). The samples were weighed into tin capsules using a UMX-2 balance (Mettler Toledo). The results of $\delta^{15}N$ and $\delta^{13}C$ are expressed in ‰ relative to atmospheric air and VPDB (Vienna Pee Dee Belemmite), respectively. In each analytical sequence, the following are used as secondary standards for $\delta^{15}N$: USGS 40 (-4.52 ‰), USGS41a (+ 47.55 ‰) (IAEA-N-1 (+ 0.4 ‰), IAEA-N-2 (+ 20.3 ‰) and USGS -25 (-30.4 ‰). For $\delta^{13}C$ the following are used: USGS 40 (-26.39 ‰), USGS41a (+ 36.55 ‰) NBS 22 -30.031 ‰) and USGS 24 (-16.049 ‰). To evaluate the precision (standard deviation), acetanilide is used as a standard, resulting in ± 0.15 ‰ (n = 10).
- Diatom analysis. The sample preparation and analysis were performed in the Faculty of Sciences, University of A Coruña. ca. 0.3g of dry sediment were cleaned with 30% hydrogen peroxide (H_2O_2) and rinsed with distilled water. At least 300 diatoms frustules were counted under 40 × magnification diatom. The abundance of planktonic *vs.* benthic diatoms was determined on the basis of diatom percentages. Diatom assemblages are constituted by the planktonic genus *Aulacoseira* as the main component and the benthic genera with different life forms, *Eunotia*, *Pinnularia*, and *Gomphonema*, as secondary components (Hernández et al., 2017).
- The age-depth model of Pex19 was constructed using Bayesian statistics of the R package 'rbacon' version 2.5.7 (Blaauw et al., 2018) and the IntCal20 calibration curve for ^{14}C dates (Reimer et al.,

2020). The age model constraining the Pex19-01 used three ^{14}C AMS dates of pollen concentrates performed at Laboratoire de Radiochronologie (Université de Laval, Quebec, Canada) and ^{137}Cs and ^{210}Pb profiles from a prior sedimentary core retrieved in 2015 (Pex15) (Table 3.2) (Hernández et al., 2017) analyzed at the St. Croix Watershed Research Station, Science Museum of Minnesota (USA). The use of the ^{210}Pb dates was assumed to have only slight differences in depth between the two cores since both cores were retrieved at ca. the lake center and have significant data correlation in-depth on diatoms data (see chapter 9.2, annexes). Based on the age model (Fig. 3.35), the sedimentation has some significant changes (Fig. 3.36), with a mean age per cm of ~17± 5 years within the upper 120 cm, *n*-alkane data resolution of 34 years (±10, n=59), and 67 years (± 20, n=30) for bulk organic matter data. According with previous profile PEX15 it was dicided to reject the 30cm depth date in the modeling due to the abnormally derived sedimentation rates.

*Table 3.2 – Dating ages used in the age-depth model of Pex19-01 drive. The ^{210}Pb was derived from a core of 2015 collected near the Pex19 coring site. The ^{14}C dates were calibrated using the IntCal20 curve (Reimer et al., 2020). *The UCIAMS-249101/ ULA-9899 date was discarded in the modeling due to the abnormally derived sedimentation rates.*

Laboratory reference	Depth (cm)	Dating method	Age (^{14}C yr BP ± 1σ)	Calibrated age (BP yr 2σ range)
	0	Present		-69
	1	^{210}Pb		-58
	2	^{210}Pb		-48
	3	^{210}Pb		-39
	4	^{210}Pb		-27
	5	^{210}Pb		-15
	6	^{210}Pb		-4
	7	^{210}Pb		8
	8	^{210}Pb		19
	9	^{210}Pb		35
	10	^{210}Pb		61
	11	^{210}Pb		87
UCIAMS-249101/ ULA-9899	30*	^{14}C	1425 ± 15	1300 - 1346
UCIAMS-249102/ ULA-9900	80	^{14}C	1650 ± 15	1424 - 1570
UCIAMS-249103/ ULA-9901	118	^{14}C	2015 ± 15	1892 - 1998
UCIAMS-242267/ ULA-9486	150	^{14}C	2545 ± 15	2541 - 2742

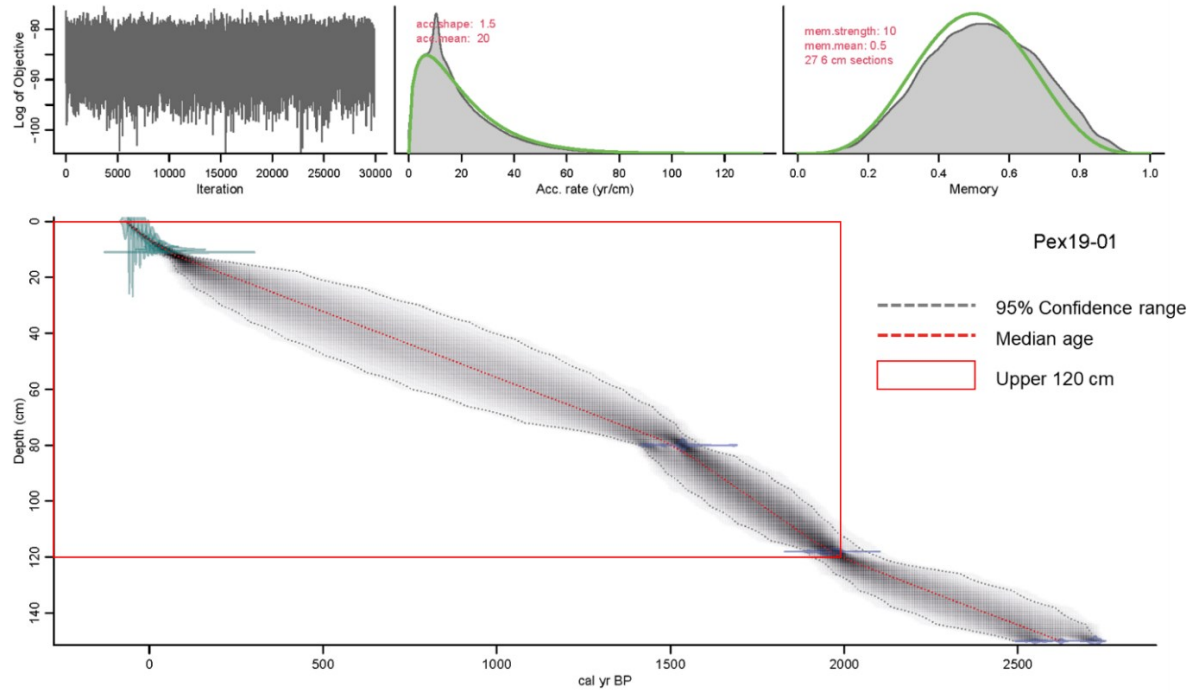

Figure 3.35 – Bayesian age-depth modeling of the Pex19-01 drive using the R package Bacon v. 2.5.7 (see Blaauw et al., 2018) based on ^{14}C dates (purple-blue, calibrated with IntCal20 (Reimer et al., 2020), and ^{137}Cs and ^{210}Pb (green) of Table 3.2.

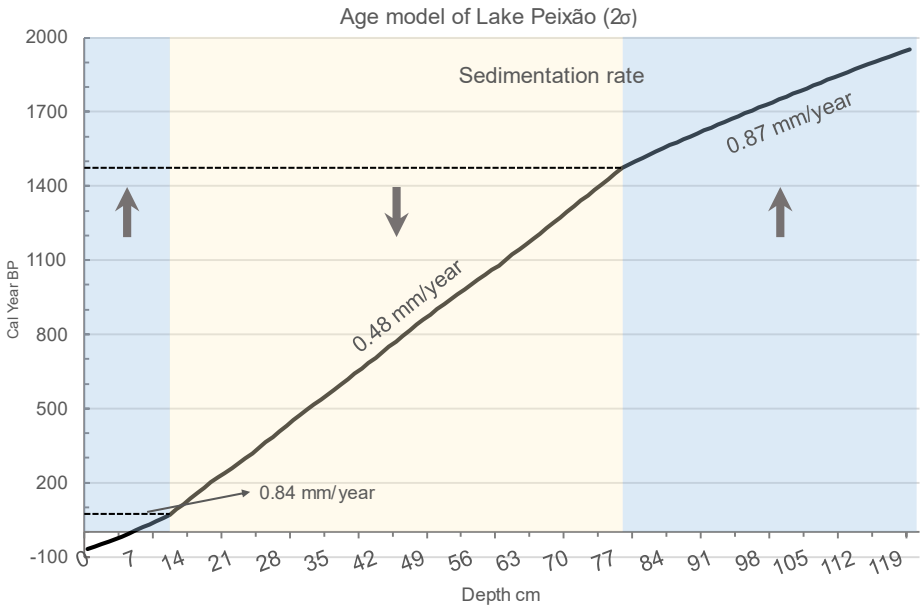

Figure 3.36 – Sedimentation rate for the last 2000 cal yrs BP of Lake Peixão sediments based on the age model of Pex19-1 core. The black arrows pointing down indicates a relatively low sedimentation rate, and vice-versa.

3.4. Laboratory Methodology

3.4.1. Sample preparation for biomarkers analysis

The samples for biomarker analysis were carefully wrapped in aluminum foil, put in a tagged zip-lock plastic bag, and stored at -20 ºC in a freezer to avoid OM degradation.

After completely frozen, samples were freeze-drying for 24h in a Freeze Dryer (Heto Power Dry PL3000) connected to a heat controller (Heto HSC 500) and vacuum pump. This way, the interstitial water in the sediments is efficiently removed without heating and therefore avoiding any eventual compound modification. The analytical procedures for biomarkers determination were performed at the biogeochemistry laboratory of the Marine Geology division (at IPMA).

3.4.2. Sedimentary leaf wax *n*-alkanes extraction

After sample homogenization (Fig. 3.37A) the Total Lipid Extraction (TLE) was performed manually, starting by adding of 10µl of internal standard solution (hexatriacontane, tetracontane respectively and nonadecanol-1-ol) (Fig. 3.37B) and 8 ml of Dichloromethane (DCM) in each and a blank tube. The internal standard was used as a reference to the lipid extraction and quantification process.

The tubes with samples are then placed in the vortex at 2800 RPM (15 sec) (Fig. 3.37C) and ultrasonic bath (15 min) (Fig. 3.37D), and went to a centrifugation process (Eppendorf 5702 R) for 5 min at 10 º C and a speed of 3200 rotation per minute (Fig. 3.37E). This step helps to segregate the solvent from the sediment, i.e., phase separation (solid /liquid) (Fig. 3.37F). After that upper liquid phase (solvent) was carefully pumped to a new centrifuge tube using a Pasteur pipette glass, and then the tubes were placed in an N_2 evaporator (Stuart SBHCONC/1 Sample Concentrator) at 37.6 º C in order to reduce the solvent content, ensuing enough roam for the next 2 extractions of solvent (DCM) with the prior mention methodology (without adding the standard). After the last one, the solvent was evaporated until dryness

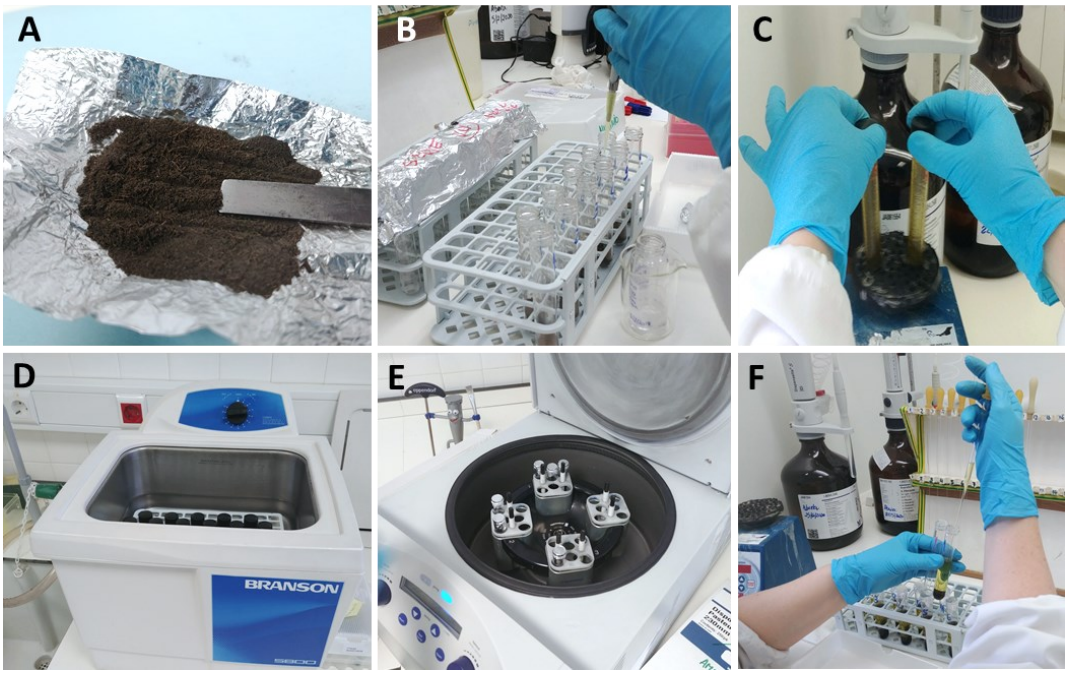

Figure 3.37 – Some of the major laboratory workflow performed in the Biogeochemical laboratory at IPMA. A – Sample homogenization; B – Addition of internal standard solution and organic solvents; C – sediment homogenization at Vortex; D – Ultrasonic bath; E – Samples at the centrifuge; F – Manual phase separation of the TLE.

The obtained TLE were saponified through hydrolysis, by adding 100µl of Toluene and 3 mL of potassium hydroxide (6%) dissolved in methanol solution (KOH / MeOH, 1:1), this process purifies the extracts by removing the esters and long-chain acidic compounds, that otherwise would make the quantification process of the compounds more difficult and prematurely damage the chromatographic column. After being carefully sealed with aluminum foil, the sediments in the tube are homogenized in the vortex (15 sec) and placed in an ultrasonic bath for 15 min. The obtained mixture is left to react overnight (at least 12 hours) at room temperature.

After the prior mention reaction, it is added 2 mL of *n*-hexane (Hex) in each tube and placed in the vortex (15 sec) and ultrasonic bath for 2 min, after it is important to ensure the emulsions formed between phases are reduced, for that the samples are gently spined by hand (Fig. 3.38A). The upper phase (the TLE in Hex) is recovered into a new centrifuge tube, using the respective Pasteur pipette of each sample. This step is repeated 2 times more, without an ultrasonic bath.

1.5 mL of ultrapure H_2O milli-Q into each sample to absorb traces of KOH that have eventually gone into the purified extract (Hex phase). The tubes are covered with aluminum foil placed in the vortex (15 sec.) and the upper phase is extracted into a new centrifuge tube, using a new Pasteur pipette for each sample (Fig. 3.38B). In this step, emulsions between phases can be formed. The H_2O phase left was then extracted with an additional 2 ml of Hex and transferred into the previously extracted Hex phase.

The nonpolar here referred to as 'APO' (*n*-alkanes), and polar 'POL' fractions from the TLE were obtained via liquid chromatography. The APO fractions were carried by eluting the 1 ml of the TLE over 5 cm of activated (120 ºC) silica gel (0.040 – 0.063 mesh) in a 2 ml Pasteur pipette, plugged with small cotton at the bottom (Fig. 3.38C). This procedure is repeated 2 times more with 1 ml of Hex to recover the APO fraction of each sample into the respective new 'APO tube'. The POL fraction was obtained with the same analogy, uninterrupted, using DCM:MeOH (1:1), which drained into a 'POL' tube. These procedures are in a continuous workflow and are extremely important to ensure that microcolumn never run dry.

The target APO fraction was then eluted with hexane in a microcolumn of chromatography filled with 5 cm of $AgNO_3$-Silica gel. This process removes unsaturated components from the hydrocarbon fraction. Next, the column was flushed 3 times with Hex before adding the prior obtained APO fraction, two additional 1 ml of Hex are then added to ensure that all the *n*-alkanes will pass through the high-purity grade silica, obtaining this way the 'APO clean'. Both the APO 'clean' and POL fraction are then dried under a N_2 to dryness (Fig. 3.38D)

and transferred from the tubes into vials 3 times with 300 µL of the respective solvents used in the microcolumn, i.e., Hex for APO 'clean' and DCM-MeOH (1: 1) for POL.

Figure 3.38 – Major steps in the APO fraction 'Clean-up' process. A – TLE saponification process; B – Upper phase separation after with H_2O milli-Q; C – Silica microcolumn separation eluted with HEX; D – Apo clean drying under a N_2 flow.

The vails (APO and POL) (Fig. 3.39A) then evaporate in a rotary evaporator (Speed Vac carousel Savant SPD111V) (Fig. 3.39B). The APO fraction takes about 45 min. At 35 ºC to evaporate while the POL fraction usually takes more than 3 hours. After dried, 60 µL of toluene were added into the APO vials and 60 µL of N,O-Bis(trimethylsilyl)trifluoroacetamide (BSTFA) is added into the POL. The BSTFA is used to derivatize labile groups such as hydroxyl on other chemicals with the more stable trimethylsilyl group allowing the compounds to be analytical processed. The vials are then tightly cased with a septum cap and stirred in the vortex. After that APO and POL vials are stored in a refrigerator for at least 24 hours until gas chromatography (GC) analysis (Fig. 3.39C) or 5 hours at room temperature (18ºC). Only the *n*-alkane fraction (APO) was analyzed in this study, the POL vials were stored for future work. The general view of these analytical procedures is summarized in figure 3.40.

Figure 3.39 – Steps before the gas chromatography. A – Addition of toluene using a micropipette; B – Placement of the different vails in the rotary evaporator; C – Placement of the vials in the gas chromatographer carrousel.

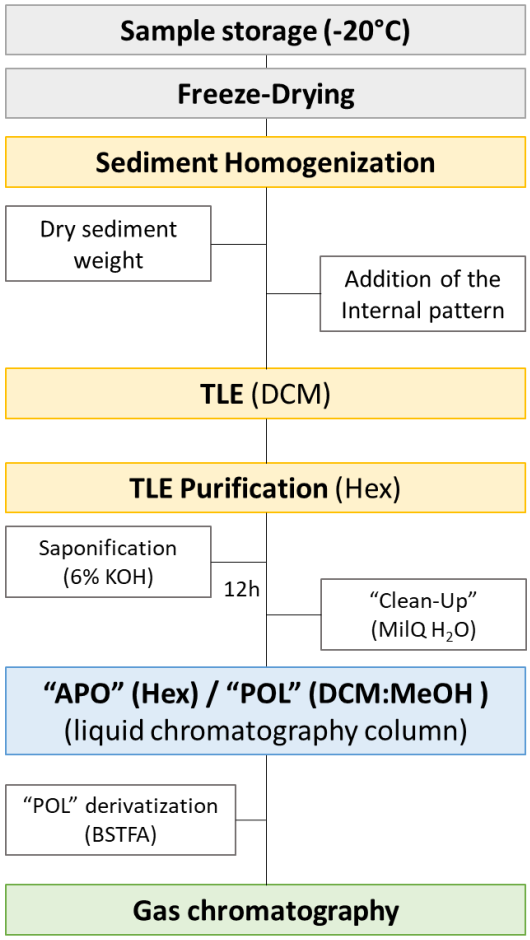

Figure 3.40 – Flowchart summarizes the methodology applied to obtain non-polar (APO) and polar compounds (POL). Hex: Hexane; DCM: Dichloromethane; KOH: Potassium hydroxide BSTFA: Bis(trimethylsilyl)trifluoroacetamide. Box coloring suggests the different step phases involved.

3.4.1. Gas chromatography conditions

All the obtained extracts were analyzed using gas chromatography-flame ionization detection (GC-FID; Varian chromatograph model 3400) equipped with septum programmable injector - SPI) and with CPSIL-5 CB 100% dimethylsiloxá capillary column of 50 m length × 0.3 mm internal diameter × 0.12 µm 100% methyl polysiloxane film coating), connected with a fused silica pre-column with an internal diameter of 0.32 mm and an approximate length of 5 m. Extracts were injected (1 µL) in splitless mode using H_2 (~3 mL/min) as carrier gas using the GC oven heating ramp as shown in Fig. 3.41. The injector was maintained at 310 ºC and detector at 320 ºC receiving 35 mL/min H_2 flow, 300 mL/min of Airflow, and 30 mL/min of N_2 flow. The total compound separation time for each sample is 63.83 minutes.

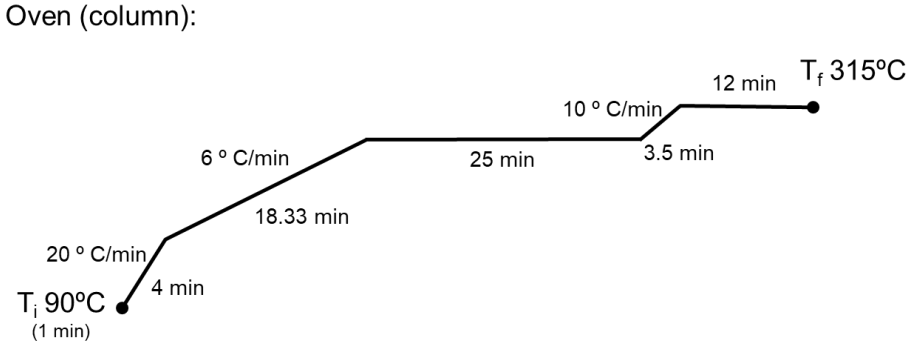

Figure 3.41 – Oven temperature ramp for the chromatography column. Where Ti meaning Initial Time and T_f final time.

The electrical signal from the detector was processed with the CompassCDS® software. The *n*-alkanes were identified by comparing the retention times with a standard external mixture (*n*-alkanes from C_{17}-C_{36}), assuming the same response factor. Then, the quantification of each compound concentration (*ng/g*), were determined by peak areas integration using the internal standard *n*-hexatriacontane (C_{36}) of known concentration as a reference, using the following formula (3.4):

$$C_i\ (ng/g) = (C_{i\ area} / C_{36^*\ area}) \times (ng\ C_{36} / g\ Ds) \qquad (3.4)$$

Where $C_{i\ area}$ corresponds to the area of the biomarker peak in the chromatogram to determine, i.e., the C_i, the C_{36^*} is the concentration of the *n*-hexatriacontane internal standard, and Ds corresponds to the dry weight of the analyzed sample.

3.4.2. Isotope analysis

After GC analysis, selected lipid extracts were dried and sent to Hinrichs Lab - Isotope Ratio Mass Spectrometry (IRMS) at MARUM-Center for Marine Environmental Science, University of Bremen (Germany) for the specific compound's isotope analysis. The isotopic signal of Carbon ($\delta^{13}C$) and Hydrogen (δD) were determined both in the modern vegetation and sediments samples, where concentration allowed, using a Gas Chromatography - Isotope Ratio Mass Spectrometer (GC-IRMS).

The $\delta^{13}C$ analysis was measured using a Thermo Trace GC Ultra, coupled to a Finnigan MAT 252 mass spectrometer. The *n*-alkanes were injected using a splitless mode, a HP-5ms capillary column separates the compounds (30 m length × 0.25 mm internal diameter × 0.25 µm film coating), with helium as carrier gas (purity 99.999%), at a constant flow of 1.5 mL/min where they oxidized to CO_2 by a combustion reactor at 1000°C. The CO_2 produced was then injected into the mass spectrometer to be analyzed. The injector temperature was programmed to be constant at 250 °C and the injections (2µL) were done in splitless mode. The GC temperature was programmed from 120 °C (hold time of 3 min), followed by heating at 5 °C/min to 320 °C (hold time of 15 min). The $\delta^{13}C$ values for individual compounds were calibrated by injecting pulses of CO_2 of an external reference gas that was automatically introduced into IRMS at the beginning and end of each analysis. Samples were run in duplicate when *n*-alkane concentrations were adequate for multiple runs, and a standard mixture of *n*-alkanes was analyzed every 6 runs. The reported $\delta^{13}C$ values are reported in per mil (‰) relative to the VPDB standard and represent an average of duplicates with a standard deviation less than 0.5‰.

The δD analysis of *n*-alkanes was performed on a Thermo Trace GC, equipped with a HP-5ms column (30 m length 0.25 mm internal diameter x 1.0 µm film coating), coupled to a Thermo Fisher MAT 253 (IRMS) via a pyrolysis reactor (operated at 1420 °C). The GC oven program was similar to the conditions used for the analysis of the carbon isotopic composition. The measurement accuracy was controlled by the injection of standards of known isotopic composition after every six measurements and by the daily determination of the H^{3+} factor using H_2 reference gas. The δD values were calibrated against the external H_2 reference gas and reported in ‰ VSMOW. When *n*-alkane concentrations permitted multiple runs, samples were run in duplicate, the reported values represent the mean with a standard deviation less than 3‰.

3.5. Statistics and data analysis

The statistical and data analysis was performed applying different approaches and methods.

A stratigraphically constrained clustering was conducted on the odd *n*-alkane concentrations using the weighted pair-group average algorithm and cross-validate with a different iteration of *k*-means non-hierarchical clustering cluster analysis of PAST 4.04 software (Hammer et al., 2001). To examine the optimal number of clusters to be used in the *k*-means, the NbClust package (Charrad et al., 2014) was used in R 3.6 (R Core Team, 2019). This function computes about 30 methods for determining the appropriate number of clusters, proposing a clustering number scheme from the different results obtained by varying all combinations of several clusters, distance measures, and clustering methods (Fig. 3.42) (see Charrad et al., 2014).

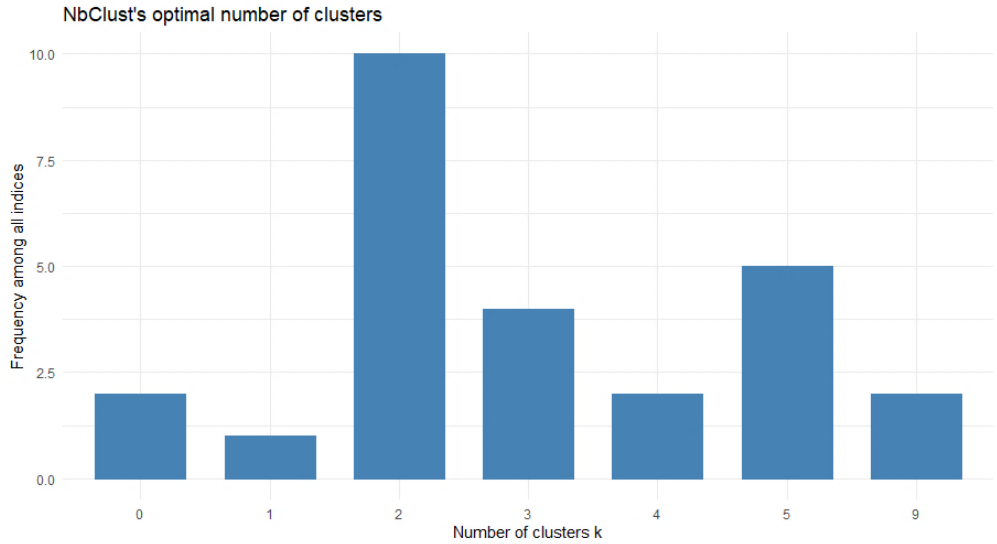

Figure 3.42 – NbClust's optimal number for clustering the sedimentary n-alkane concentration for the last 2000 cal yrs BP.

Data correlation analysis was performed using either the 'corrplot' R package (Wei et al., 2017) or the correlation function of PAST4.05. The correlation analysis for sedimentary odd *n*-alkane was reworked with 'heatmap.2' function from the 'gplots' R package (Warnes et al., 2016) with the Euclidean method to obtain distance matrix and complete agglomeration method for clustering encoded as a grid of colored cells, the rows and columns of the matrix were ordered to highlight patterns and are often accompanied by 'dendrograms'. To assess the displacement of one independent variable in respect to another in the time-series it was used the cross-correlation function of PAST4.05 (see Hammer et al., 2001), where the positive or negative lags (data points) were found considering the smallest *p*-value and highest correlation in the matrix.

The principal component analysis (PCA) was carried out in the odd *n*-alkanes concentration of the sediments using the variance-covariance matrix, using the PAST4.05 software (Hammer et al., 2001). This method mainly reduces the data dimensionality into different principal components (PCs) based on data variance, easing the data interpretation (see Hammer et al., 2001).

To examine changes in the abruptness regime, a novel 'asdetect' R package (Boulton and Lenton, 2019) was used to analyze the different indicators' gradients (See 9.7, annexes).

4. RESULTS

4.1. Sediment characterization

The upper 120 cm of the studied record consists of a homogenous soft brown-black gyttja with common remains of plant rhizoids and virtually no sand-size sediments (see chapter 9.1, annexes).

4.2. *n*-Alkane characterization

4.2.1. Modern soil and vegetation analyses

The *n*-alkanes extracted from the soil sample taken from the lake watershed show a great contribution of the long-chain *n*-alkanes (Fig. 4.43), resulting in high ACL_{27-33} and CPI_{27-33} values of 30.5 and 11.15, respectively, and a relative deficiency in mid-and short-chain *n*-alkanes ($<C_{27}$).

The sum of odd $C_{27} – C_{33}$ counts for ~85% of the *n*-Alk_{Total}, corresponding to 3.78 µg/g of dry soil. For the sake of simplicity, it was determined the relative abundance of the main *n*-alkanes (e.g., $\%C_{29} = C_{29}/C_{27}+C_{29}+C_{31}+C_{33}$), or relative percentage of long-chain *n*-alkanes (RPLs). The RPLs for the modern soil sample is: $\%C_{31} = 35$, $\%C_{29} = 25$, $\%C_{33} = 18$ and $\%C_{27} = 7$.

The modern vegetation samples were used to evaluate the contribution of primary *n*-alkane sources to the soil and lake sediments. A diverse *n*-alkane distribution can be observed, usually with a dominant homologue, which in most cases is C_{31} (Table 4.3). The total *n*-alkane concentration on different vegetation ranges between 21 ng/g and 1365 ng/g of dry weight. However, these concentrations are here presented as only a qualitative indicator due to the possible constraints on lipid extraction subjective to each vegetation type.

Erica sp. is one of the most dominant plant types in modern settings and is highlighted as a possible major *n*-alkane source in the area, but also in other Regions of Iberia (see Ortiz et al., 2011), maximized at C_{31} and displaying nearly as twice as *Juniperus communis* and Grasses (*Nardus stricta* and *Agrostis delicatula)* (see Fig. A67, annexes). The soft rush *Juncus sp.*, mainly produces C_{27} and has produce the lower *n*-alkane concentration , as observed in other areas of Iberia (Ortiz et al., 2011). *Juniperus communis*, on the other hand display a remarkable reversed *n*-alkane pattern distribution of *Juncos sp*, i.e., producing the longest *n*-alkane chains, maximizing at C_{33} but also producing significant amounts of C_{35}. The broom-scrub *Cytisus oromediterraneus* stands out by producing particularly high amounts of mid-chain *n*-alkanes, C_{21} and C_{25}.

The grasses analyzed *Antinoria agrostidea* (Aquatic grass) has a wide window of *n*-alkanes, that although maximizing at C_{25} it also has relatively high production of C_{31}, C_{33}, and C_{27} homologues. Similar with *Agrostis delicatula*, whose main homologues are C_{29} and C_{31}, but also produces similar amounts of C_{27}. This contrasts with *Nardus stricta* which has a narrow distribution centralized at C_{31}.

Table 4.3 – n-alkane predominant homologues in the different predominant vegetation of Lake Peixão surrounding area. The vegetation tab has the identified species or genus and the common vegetation type designation in parathesis.

Vegetation	Predominant *n*-alkane(s)
Nardus stricta (grass leaves)	**C_{31}**
Agrostis delicatula (grass leaves)	**$C_{29} + C_{31} + C_{27}$**
Antinoria agrostidea (?) (aquatic plant leaves)	**C_{25}**
Juncos sp. (soft rush stems)	**C_{27}**
Cytisus oromediterraneus (shrub stems)	**$C_{23} + C_{25} + C_{31}$**
Erica australis (shrub leaves)	**$C_{31} + C_{29}$**
Juniperus communis (shrub leaves)	**C_{33}**

The major difference between leaves and respective plant litter is the lower *n*-alkane concentration on the litter, for instance with *Juniperus communis* displaying a 52% decrease on the predominate *n*-alkane, 89% on *Nardus stricta* and 97% on *Erica australis*.

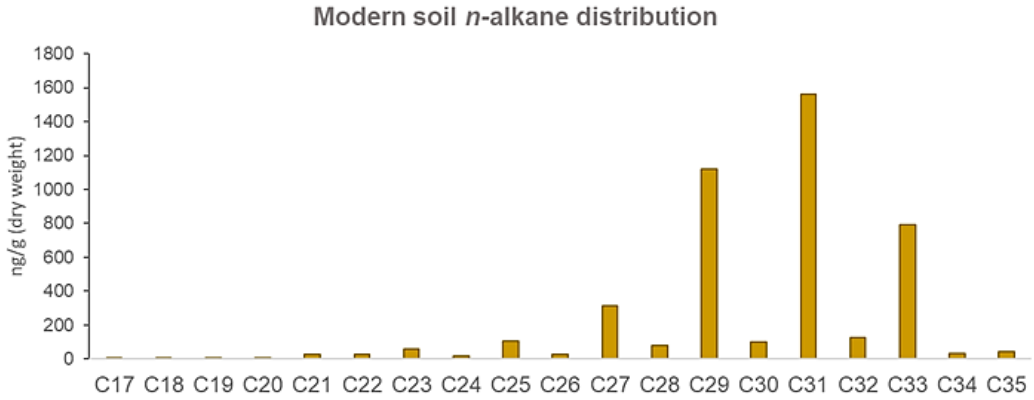

Figure 4.43 – n-alkane distribution of the modern soil sample collected near Lake Peixão.

4.2.2. Compound specific δD and ^{13}C signal of modern vegetation

The δD and ^{13}C analysis on *n*-alkane of modern vegetation of Lake Peixão catchment area, show a wide range of fractionation with no clear general trend on the most depleted/enriched *n*-alkane (Table 4.4). Therefore, a mean value was computed using the values of the analyzed *n*-alkanes to have a general idea of what are the fractionation ranges of each species. Grasses have the most depleted signals in both δD and ^{13}C in the homologues analyzed, either using the mean value of the dominant homologue.

Considering the δD, the most depleted species are *Agrostis delicatula* and *Nardus stricta with* -205 ± 9‰ (n=5) and -223 ±13 ‰ (n=5), respectively. The aquatic-related plants, *Antinoria agrostidea (?)* and *Juncus sp*. have mean values of -183 ±8 ‰ (n=5) and -176 ±7 ‰ (n=4, with no δD of C_{33}), respectively. Bushes have the most enriched signals, *Erica australis* with -156 ±4 ‰ (n=4, with no δD of C_{25}), *Juniperus communis* with -141 ±6 ‰ (n=2, C_{31} and C_{33}) and *Cytisus oromediterraneus,* the more enriched, with -124 ±5 ‰ (n=5).

The mean values for *n*-alkane ^{13}C analysis for *Agrostis delicatula*, *Nardus stricta* and *Antinoria agrostidea* (?) are very similar -35 ± 1 ‰ (n=5), -36 ± 1 ‰ (n=5), -36 ± 1 ‰ (n=5), respectively. *Juncos sp*. and *Cytisus oromediterraneus* also display similar values, -33± 2 ‰ (n=5) and -33± 1 ‰ (n=5), respectively. The bushes *Erica australis* and *Juniperus communis* display the depleted $\delta^{13}C$ values -31± 1 ‰ (n=5) and -30± 1 ‰ (n=4), respectively.

Table 4.4 – Compound specific δD and $\delta^{13}C$ signal of the n-alkanes of the dominant modern vegetation in Lake Peixão catchment area. The upper three samples area vegetation litter collected underneath the respective plant; the other samples correspond to leaves.

VEGETATION	δD C_{25}	δD C_{27}	δD C_{29}	δD C_{31}	δD C_{33}	$\delta^{13}C$ C_{25}	$\delta^{13}C$ C_{27}	$\delta^{13}C$ C_{29}	$\delta^{13}C$ C_{31}	$\delta^{13}C$ C_{33}
***Erica australis* litter**	-	-	-165	-183	-169	-30.6	-32.4	-33.7	-32.9	-32.3
***Nardus stricta* litter**	-	-	-193	-216	-200	-33.1	-33.4	-35.2	-36.0	-35.1
***Juniperus communis* litter**	-	-	-156	-157	-151	-29.0	-28.9	-31.7	-31.4	-29.0
Agrostis delicatula	-215	-207	-203	-209	-191	-34.8	-34.8	-35.5	-35.7	-36.2
Nardus stricta	-236	-212	-236	-218	-211	-34.5	-35.3	-36.3	-36.3	-36.6
Antinoria agrostidea (?)	-200	-185	-177	-184	-186	-34.8	-35.2	-35.9	-37.1	-36.3
Juncos sp.	-170	-187	-175	-173	-	-33.4	-33.9	-34.6	-33.1	-29.6
Erica australis	-	-156	-161	-155	-151	-31.2	-32.1	-32.4	-31.2	-30.3
Juniperus communis	-	-	-	-137	-146	-	-	-31.3	-30.6	-29.4
Cytisus oromediterraneus	-121	-122	-131	-129	-119	-31.1	-32.0	-33.3	-34.2	-32.2

4.2.3. Apparent fractionation of modern sediments

The mean annual precipitation isotopic composition (δD_{MAP}), ultimately controlling the δD_{wax} signal of the lipid biosynthesis (Sachse et al., 2012), was estimated for the site using the Online Isotopes in Precipitation Calculator (OIPC3.1; Bowen and Revenaugh, 2003). Constraining the latitude, longitude, and elevation of Lake Peixão area in the OIPC3.1, it was estimated a δD_{MAP} value of -56‰, similarly to the -53‰ estimated for the main growing season (From March to April). This resulted in an apparent fractionation of the relationship between δD signal of C_{29} of the core-top sediments and δD_{MAP} of -128.9‰ ($\varepsilon C_{29/MAP}$).

4.2.4. Lake sediments *n*-alkane signal and distribution

The *n*-alkanes from the Lake Peixão sediments show a strong odd-over-even carbon predominance of long-chain *n*-alkanes. Concentrations per gram of dry sediment can have significant variations throughout the record where the sum of total *n*-alkane (*n*-Alk_{Total}, C_{17} – C_{35}) ranges from 79.9 to 192.8 µg/g. The sum of the long-chain *n*-alkanes (*n*-$Alk_{C27-C35}$, odd C_{27} – C_{35}) represents 77.5% of the *n*-Alk_{Total}, ranging from 61.0 to 145.2 µg/g. Middle chains (odd C_{23}-C_{25}) vary between 8.0 to 19.2 µg/g while short chains (odd C_{17}-C_{21}) from 2.1 to 5.9 µg/g. Changes in the *n*-alkane concentrations controlled the 7 main biogeochemical stages (from A to G) in the record, where the C_{31} is the predominant compound, generally followed by C_{29} > C_{33} > C_{27} homologues (Fig. 4.44).

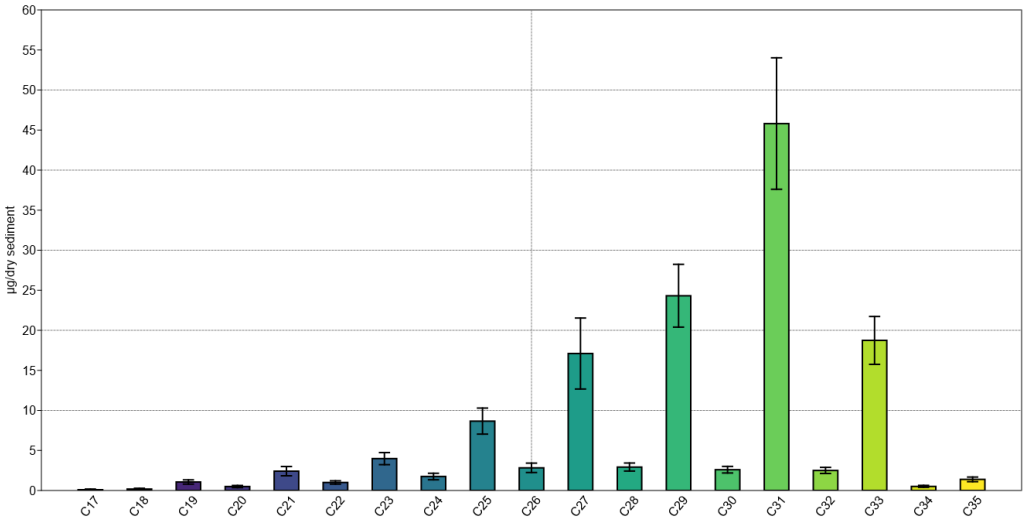

Figure 4.44 – Avenged n-alkane concentration for each compound analysed, in ng/g of the dried sediments with one sigma standard error whisker, for the first 120 cm of PEX19-01 in a 2 cm resolution (60 samples).

A correlation analysis on *n*-alkane concentrations (n = 60) (see Fig. 4.45) show that, for $p < 0.05$, C_{29} is positively correlated with most of other homologues, especially with C_{31} (r =0.89). C_{31} and C_{33} are highly correlated (r = 0.83) with the latter being particularly highly correlated with the C_{35} (r = 0.84). Whereas C_{27}, when compared with the other three main homologues, correlation is lower, showing, however, high correlation with the C_{25} (r = 0.87).

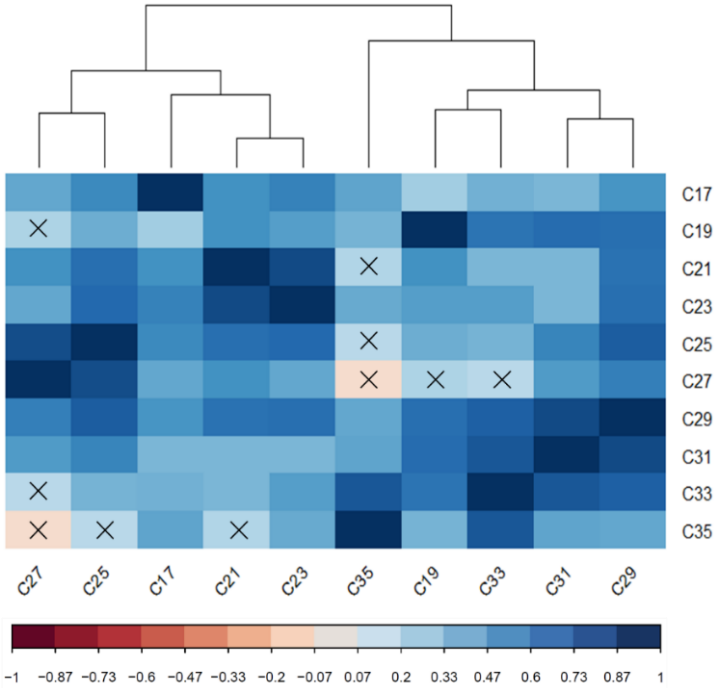

Figure 4.45 – Correlation clustered heat map of Pex19-01 for the first 121 cm, encompassing ca. 2000 cal yrs BP. The correlation analysis was performed with the heatmap.2 function from the gplots package of R with the Euclidean method to obtain distance matrix and complete agglomeration method for clustering. The 'X' marked squares represent values above p = 0.05.

For the studied time interval, the averaged values for RPLs are: $\%C_{31}$ = 43.2 (± 2.13), $\%C_{29}$ = 23.0 (± 0.94), $\%C_{33}$ = 17.8 (± 1.87), $\%C_{27}$ = 16.1 (± 2.98). In a general, both $\%C_{29}$ and $\%C_{33}$ display a less variable long trend when compared with $\%C_{31}$ and $\%C_{27}$ (see Fig. 5.53f). $\%C_{31}$ and $\%C_{27}$ show an inverse pattern, with $\%C_{31}$ presenting two major peaks, the largest centered ca. 1028 AD (ca. 52 cm depth), and the other centered at ca. 139 AD (ca. 106 cm depth) whereas $\%C_{27}$ has one major peak centered at ca. 1235 AD (ca. 42 cm depth) (Fig. 5.53).

To assess the preferentially produced *n*-alkane chain length in the catchment area, it was used two ACL ranges, the $ACL_{27\text{-}33}$, constraining the main *n*-alkanes producers, i.e.., the higher plants, varying between 30 and 30.5, as well as the $ACL_{17\text{-}33}$ which provides the general signal of Peixão area, ranging from 29 to 29.8. The $ACL_{17\text{-}33}$ shows a relatively high variability when compared with $ACL_{27\text{-}33}$, nonetheless, both follow a similar general trend ($r = 0.43$, $p < 0.001$). Hereafter the term ACL is referred to the $ACL_{27\text{-}33}$

ACL signal is relatively constant, mostly centered between 30.2 – 30.4 in the last 2000 cal yrs BP (Fig. 5.53b). However, it is observed a significant relative decrease of ca. 0.2 encompassing the whole Dark Ages and Medieval Climate Anomaly (ca. 76-40 cm depths). The change in ACL seems to be mostly controlled by the relation of C_{31} and C_{27} sources, resulting in an often-antiphase relation. For instance, ACL is positively correlated with $\%C_{31}$ ($r = 0.62$, $p < 0.001$) while negatively with $\%C_{27}$ ($r = -0.98$, $p < 0.05$).

A $CPI_{27\text{-}33}$ was calculated to assess the degree of degradations between the long chains. The $CPI_{27\text{-}33}$, ranges from 7.5 to 14.5 (Fig. 5.53d). The general trend shows a steady and constant CPI signal increase from the oldest sediments until mid-F stage, i.e., middle of LIA (650 AD, ca. 46-48 cm depth) where it was reached a maximum at ca. 1671 AD (ca.22 cm depth), LIA, from there a steep and steady decrease occur until reaching the modern lowest values in the record of the G stage.

The Paq calculated show that the relative contribution of the *n*-alkanes form of aquatic plants, in comparison with terrestrial plants in the lake sediments, is relatively low, ranging from 0.11 to 0.19 (Fig. 5.53e), something corroborated by the rare aquatic plants observed in the modern lake settings. Nevertheless, the record shows some variability, with different peaks coincidently constrained by the defined biogeochemical stages (Fig. 5.53e) in an expectable inverse relationship with ACL signal, especially with $ACL_{17\text{-}33}$ (Table 4.5). A local maximum is observed between C/D stages, at ca. 871 AD (ca. 60 cm depth) that decreasing steeply until reaching the record minimum during F stage, ca. 1710 AD (ca. 20 cm depth), and then rapid increase to the modern-day values.

Table 4.5 –Pearson correlation matrix of the correlation analysis for the different n-alkanes indices analyzed in this study. Lower triangle: r value (correlation coefficient); upper triangle: p-value.

	$ACL_{17\text{-}33}$	$ACL_{27\text{-}33}$	ACL_{DIF}	$CPI_{27\text{-}33}$	P_{AQ}	$\%C_{27}$	$\%C_{29}$	$\%C_{31}$	$\%C_{33}$	PC1	PC2
$ACL_{17\text{-}33}$		<0.001	<0.001	<0.001	<0.001	<0.001	<0.001	<0.001	0.123	0.207	<0.001
$ACL_{27\text{-}33}$	0.43		0.334	0.058	<0.001	<0.001	0.894	<0.001	<0.001	0.767	<0.001
ACL_{DIF}	-0.84	0.13		<0.001	0.002	0.091	<0.001	0.002	0.021	0.114	0.586
$CPI_{27\text{-}33}$	0.60	-0.25	-0.81		<0.001	0.050	<0.001	<0.001	<0.001	0.000	0.399
P_{AQ}	-0.66	-0.57	0.39	-0.53		<0.001	<0.001	<0.001	0.113	0.004	<0.001
$\%C_{27}$	-0.34	-0.98	-0.22	0.25	0.58		0.386	<0.001	<0.001	0.962	<0.001
$\%C_{29}$	-0.89	0.02	0.99	-0.79	0.46	-0.11		<0.001	0.117	0.103	0.795
$\%C_{31}$	0.69	0.62	-0.39	0.48	-0.83	-0.66	-0.46		0.282	0.007	<0.001
$\%C_{33}$	0.20	0.86	0.30	-0.56	-0.21	-0.79	0.20	0.14		0.031	<0.001
PC1	0.17	-0.04	-0.21	0.48	-0.37	-0.01	-0.21	0.35	-0.28		1.000
PC2	-0.47	-0.97	-0.07	0.11	0.68	0.97	0.03	-0.73	-0.75	0.00	

4.2.5. Sedimentary *n*-alkane δD and $\delta^{13}C$ signal

The δD values from odd C_{25} to C_{33} show a similar pattern throughout the whole record. However, there is a clear discrepancy in magnitude between lighter and heavier compounds (Fig. 5.53h). The δD values C_{25} and C_{27}, appear to be less sensitive in recording hydrologic changes when compared with the signal of C_{29} – C_{33}

homologues. In fact, there is a high correlation between δD signal of C_{25} and C_{27} (r = 0.83, p<0.001), and among C_{29} – C_{33} (r = 0.94, p<0.001) (Fig. 5.53h).

The δD values show a general negative correlation with ACL while having a strong and positive correlation $\%C_{27}$. Focusing on the δD signal of most abundant homologue, C_{31}, these correlations are r = -0.86 (p<0.001) for $ACL_{27\text{-}33}$ and r = 0.82 (p<0.001).

The overall trend points to an increase δD values from the early record until a maximum from RP to DA (62 - 42 cm depth), from there a rapid decrease in the δD signal occurred, the lowest values in the record occurred during the LIA (16-22 cm depth), then returning to less depleted values towards the modern-day.

On the contrary, the $\delta^{13}C$ signal of odd C_{25} – C_{33} homologues shows higher variability, especially C_{25} and C_{27}. These homologues display a common deflection towards enriched $\delta^{13}C$ values when compared with the other homologues.

The gradual increase in $\delta^{13}C$ of C_{25} and C_{27} from the early sediments until a maximum by the early phase of the LIA (36 cm depth), similarly to the δD signal, there is a rapid decrease in the $\delta^{13}C$ signal during the second phase of the LIA, i.e., reaching the local minimum and tipping point towards less depleted values at ca. 16 cm depth. Both the magnitude and pattern of $\delta^{13}C$ signal in odd C_{29} – C_{33} are rather similar throughout the record (Fig. 5.53i). A highlighted correlation is observed between $\delta^{13}C_{29}$ and $\delta D\ C_{29}$ (r = 0.89, p<0.001) (Table 4.6) and between $\delta^{13}C_{27}$ and $\%C_{27}$ (r = 0.72, p<0.001).

Table 4.6 – Pearson correlation matrix of the correlation analysis for compound-specific δD and $\delta^{13}C$ signal of the dominant modern vegetation of Lake Peixão catchment area. Lower triangle: r value (correlation coefficient); upper triangle: p-value.

	δD C_{25}	**δD C_{27}**	**δD C_{29}**	**δD C_{31}**	**δD C_{33}**	**$\delta^{13}C\ C_{25}$**	**$\delta^{13}C\ C_{27}$**	**$\delta^{13}C\ C_{29}$**	**$\delta^{13}C\ C_{31}$**	**$\delta^{13}C\ C_{33}$**
δD C_{25}		<0.001	<0.001	<0.001	<0.001	0.04	<0.001	0.03	0.86	0.37
δD C_{27}	0.83		<0.001	<0.001	<0.001	0.02	<0.001	<0.001	0.01	0.82
δD C_{29}	0.57	0.73		<0.001	<0.001	<0.001	<0.001	<0.001	<0.001	0.41
δD C_{31}	0.57	0.62	0.94		<0.001	<0.001	<0.001	<0.001	<0.001	0.55
δD C_{33}	0.67	0.76	0.94	0.93		<0.001	<0.001	<0.001	0.01	0.55
$\delta^{13}C\ C_{25}$	0.36	0.39	0.55	0.64	0.64		<0.001	<0.001	<0.001	0.51
$\delta^{13}C\ C_{27}$	0.54	0.62	0.64	0.68	0.68	0.88		<0.001	<0.001	0.02
$\delta^{13}C\ C_{29}$	0.37	0.64	0.89	0.64	0.82	0.60	0.64		<0.001	<0.001
$\delta^{13}C\ C_{31}$	0.03	0.44	0.49	0.52	0.44	0.50	0.49	0.84		<0.001
$\delta^{13}C\ C_{33}$	-0.16	-0.04	-0.14	0.10	-0.11	-0.11	-0.38	0.48	0.50	

4.2.6. Principal component analysis (PCA)

The PCA routine performed on the concentrations of the odd *n*-alkanes (C_{17} – C_{35}) concentrations (see Fig. 5.48 or chapter 9.5, annexes), reduced data dimensionality into two PCs, which together account for 98.8% of the observed data variance. PC1 represents most of the PC loads (82%) (Fig. 4.46), which appears to materialize the variance in the total *n*-alkane concentrations, with a strong positive correlation with the sum of long-chains *n*-alkane concentrations (r = 0.99).

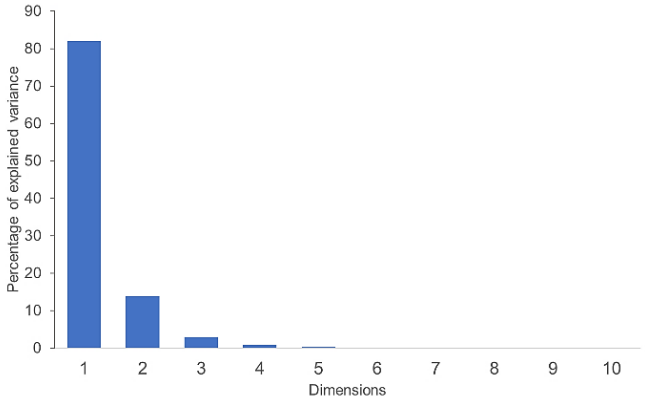

Figure 4.46 – Variance accounted for each eigenvector (components).

PC2 counts for 13.8% of (Fig. 4.46) and has a strong negative correlation with ACL (r = -0.90 and r = -0.97, for $ACL_{17\text{-}33}$ and $ACL_{27\text{-}33}$, respectively), $\%C_{31}$ (r = -0.73), $\%C_{35}$ (r = -0.75) and positive strong correlation with

the C_{27} concentration (r = 0.78) and $\%C_{27}$ (r = 0.97). These correlations are also evident by analyzing the eigendecomposition, where distinct variance is seen between C_{27} and the other long-chain homologues (e.g., 4.47). C_{29} seems to have a transition behavior between C_{27} and the other homologues (>C_{31}),leading and there is evident a clear differentiation between two main *n*-alkane groups: C_{25} and C_{27}, and C_{31}, C_{33}, and C_{35}. (Fig. 4.46).

To examine data clustering that would possibly constrain the distribution and associations of main vegetation associations from the *n*-alkane concentration data variance, the PCA was clustered using the *k*-means function and the prior mentioned 2 and 5 optimal number of clusters (see Fig. A68 and A69, annexes).

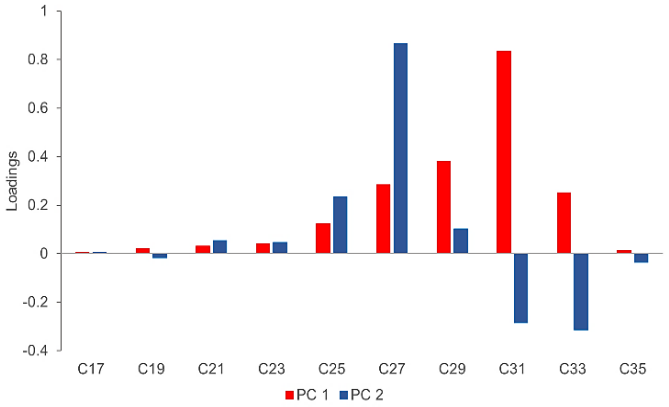

Figure 4.47 – Variance accounted for each eigenvector (components).

4.2.7. Abrupt changes analysis (ACA)

The ACA analyses was performed in the different indices (ACL, CPI, Paq, etc.) and δD and $\delta^{13}C$ of the *n*-alkanes. CPI shown the greatest abrupt changes in the gradient, while the more abrupt changes in the isotopic signal can be seen in the δD signal of ≥ C_{29}, especially the C_{29}. The opposite situation occurs in the $\delta^{13}C$ signal, with C_{25} and C_{27} having the most abrupt changes (see chapter A.75, annexes). Other indicators such as RPLs and individual ratios show relatively small changes.

A general and synchronous abruptness increase is present in most of the gradients at ca. 1145 AD (46 cm depth) in the middle of the MCA period. From there, the gradients became more abrupt, reaching a peak at ca. the LIA (e.g., Fig. 5.55). Then a significant shift in the abruptness regime occurs at ca. 1880 AD (12 cm depth), leading to less abrupt changes.

On the other hand, the $\delta^{13}C$ signal of C_{31} shows a distinct pattern, with main changes only during the RP (see A75, annexes).

5. DISCUSSION

5.1. Lake Peixão biogeochemistry data as response to climate variability

5.1.1. Interpretation of the sedimentary *n*-alkane signal based on modern vegetation

The *n*-alkanes from modern vegetation show that the strong odd-over-even carbon chain predominance, along with high ACL and low Paq values (Fig. 5.48b, e), suggest that the sedimentary *n*-alkanes are mainly derived from higher plants in the Lake surrounding area. This was expectable due to the small catchment area enclosed by steep and wind-sheltered rock walls. According to the small variance in ACL and $\delta^{13}C$ signal of the long-chain *n*-alkanes (excluding C_{27}) (Fig. 5.48i), modern-day vegetation (Table 4.4), and pollen counts (Fig. 5.49b-e) is assumed in the last 2000 cal yrs BP the vegetation type in the study area has not to change significantly from what is observed today.

The *n*-alkane signal in the catchment area is mainly controlled by heathland species, essentially *Erica spp*., which dominate the land cover and produce high amounts of long-chain *n*-alkanes (Fig. A67, annexes). Significantly below − 26‰ carbon signal of both bulk OM and the analysis *n*-alkanes show no evidence of C4 plants source in the Lake Peixão (Fig. 5.49l,i) area (e.g., Garcin et al., 2014; Ortiz et al., 2021).

The high CPI values (>5) indicate that Lake Peixão sedimentary record (Fig. 5.48d) has a pristine condition for organic matter preservation, with the most likely neglectful presence of petroleum-based pollutants in the sediments and, therefore, a reliable paleoclimatic archive (Pancost and Boot, 2004). The εC_{29}/MAP value of −129 ‰, relatively close to global mean values of −121 ‰, also reveals trustworthiness of compound-specific hydrogen isotopic data of *n*-alkanes as a paleo hydrological indicator (Sachse et al., 2012; McFarlin et al., 2019).The PC eigenvector loadings (Fig. 5.48) and correlation analysis of *n*-alkane concentrations (Fig. 5.48) in the lake sediments evidence two major distinct *n*-alkane sources in Lake Peixão area, $>C_{29}$ (PC1) and C_{25} and C_{27} (PC2). Based on modern vegetation analysis PC1 appears to be mainly associated with bushes like *Juniperus spp.* and *Erica spp* but also grasses, as *Nardus stricta* while PC2 is associated with aquatic-related vegetation like *Juncos spp.* and *Antinoria agrostidea* (?).

The low values of Paq (0.11 – 0.19) may imply that the use of Paq as an indicator for lake water level should be used cautiously (Xie et al., 2020) and that the aquatic inputs may come from emergent plants. In this sense, $\%C_{27}$ (Fig. 5.48f) is significantly correlated with Paq (r = 0.58), suggesting that part of the aquatic signal may in fact derive from plants like *Juncus spp.*, an emerged macrophyte mainly constrained to small pounds and the lake margins and which are associated with wetness or water availability (Mann and Wetzel, 1999).

The antiphase observed between ACL and Paq was expected and is more evident with the $ACL_{17\text{-}33,}$ (r = -0.66) than $ACL_{27\text{-}33}$ (r = -0.57) since $ACL_{17\text{-}33}$ encompasses the smaller chain lengths. However, this difference between ACLs, i.e., ACL_{dif}, highlights one possible indicator of autochthonous *n*-alkane (produced within the lake) vs. allochthonous *n*-alkanes (produced by higher plants catchment area) (Fig. 5.48c). With low (higher) ACL_{dif} meaning low (higher) contributions of autochthonous *n*-alkanes of the lake. The correlation between Paq and ACL_{dif} ($r = 0.43$, $p<0.05$) suggests that aquatic plants only contribute partially to the autochthonous inputs, with shorter chain sources mainly coming from algae as suggested by the percentage of planktonic diatoms ($r = 0.67$, $p<0.001$, see Fig.5.48 c) and/or the fact that non-aquatics can also contribute compounds like C_{25} which are considered in the Paq.

The least depleted $\delta^{13}C$ signal of C_{25} and C_{27} further suggests an aquatic origin (Fig. 5.48i) (e.g., Jiménez-Moreno et al., 2013; Ortiz et al., 2021), as expected based on the modern-day aquatics signal (Table 4 and 5). Nonetheless, grasses like *Agrostis delicatula* can also contribute as a C_{27} source (see chapter 9.4, annexes) since are widely presented in the catchment area. The $\delta^{13}C$ signal of the modern vegetation *Juncus spp.* has the least depleted signals when compared with *Antinoria agrostidea* and *Agrostis delicatula*, however, the latter two show a clearer pattern towards more enriched C_{25} and C_{27} when compared with other homologues. Despite both aquatics and *Agrostis delicatula* could contribute the PC2, and indicators such as $\%C_{27}$, the C_{27} source is relatively well constrained due to the significant correlation between the C_{27} concentrations and $\delta^{13}C$ signal ($r = 0.72$, $p<0.001$). Therefore, an improved interpretation and dissociation between the two groups (aquatics vs. grass) can be made when assessing the $\delta^{13}C$ signal concomitantly with $\%C_{27}$ and Paq (Fig. 5.48f,e). For example, when $\delta^{13}C$ signal of C_{25} and C_{27}, detach from other long chains (e.g., see Fig. 5.48), and there is a peak in Paq there is more solid evidence from the increase in aquatic plants.

The correlation between δD signal and *n*-alkane concentrations shows that C_{25} and C_{27} are also well constrained in vegetation source when compared with C_{29} and C_{31} homologues, which have no significant correlation with the respective δD signal (Table 5). This evidenced the vast production of C_{29} and C_{31} by different plants, such as grass and bushes, with distinct hydrogen net fractionation and further corroborating the aquatic origin of C_{25} and C_{27} due to the relative enrichment (Mügler et al. 2008a). Moreover, C_{25} and C_{27} display a relatively enriched and constant δD signal when compared with the other homologues analyzed (Fig. 5.48h), suggesting a less variable source of hydrogen, i.e., lake water (Mügler et al., 2008b).

The isotopic fractionation between source water and leaf-waxes is seemed to be consistent over the last 2000 years, cal yrs BP based on a strong correlation between δD and δ13C values (see Table 4.6), reinforcing that there were no major changes in vegetation type and therefore ensuring the use of sedimentary leaf waxes δD signal is viable paleo hydrological indicator (Hou et al., 2007). Nonetheless, the δD signal of C_{29} points to be the *n*-alkane with the more robust in the area since is widely produced by several higher plants (see chapter 9.4, annexes) and has the highest correlation with δC_{13} (Table 4.6), suggesting a less inhibited potential to study the fractionation processes (see Norström et al., 2017). This supports the studies of Sachse et al., 2012

and McFarlin et al., 2019, which highlighted C_{29} as a remarkably global consistent homologue for reconstructing δD precipitation values, emphasized by the above-discussed $\varepsilon C_{29}/_{MAP}$ value in the core-top sediments. Therefore, the δD signal of C_{29} will be hereafter referred to as δD_{terr} since is representative of the higher terrestrial plants.

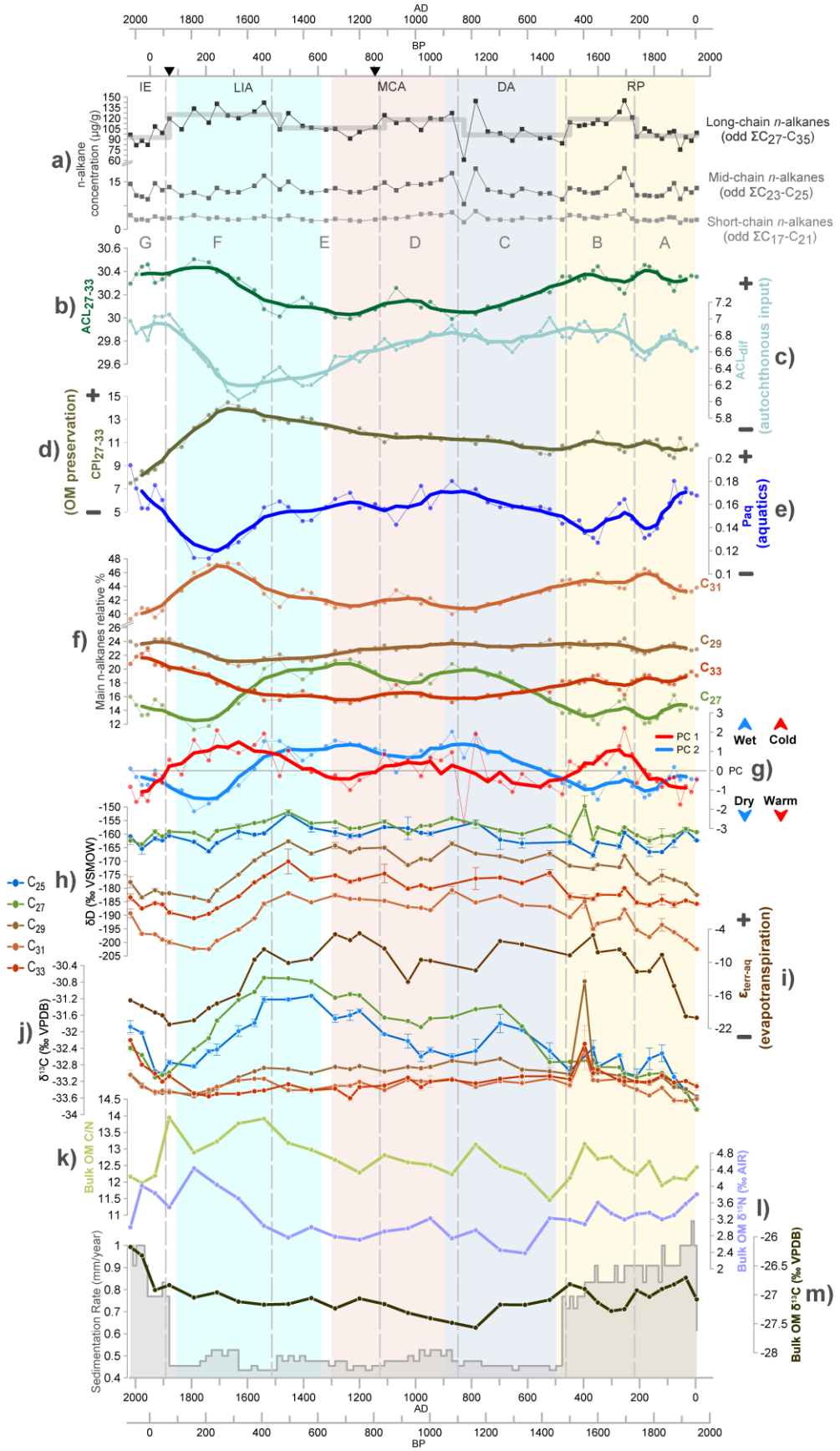

Figure 5.48 – Biogeochemical proxies from Lake Peixão sediments over the last 2000 cal yrs BP, with colored vertical bands corresponding to the main climatic period, RP – Roman Period (0 – 500 AD); DA – Dark Ages (500 – 900 AD); MCA – Medieval Climatic Anomalies (900 – 1300 AD); LIA – Little Ice Age (1350 – 1850 AD); IE – Industrial Era (1850 – present). Gray-dashed lines delineate the A-G biogeochemical stages and bold curves above the scatter plots correspond to the running average mean of 5 data-point. The thick step gray line in the odd C_{27}-C_{35} represents the mean values for each biogeochemical stage. The inverted black triangles to the abrupt event changes detected in the sedimentary n-alkane signal.

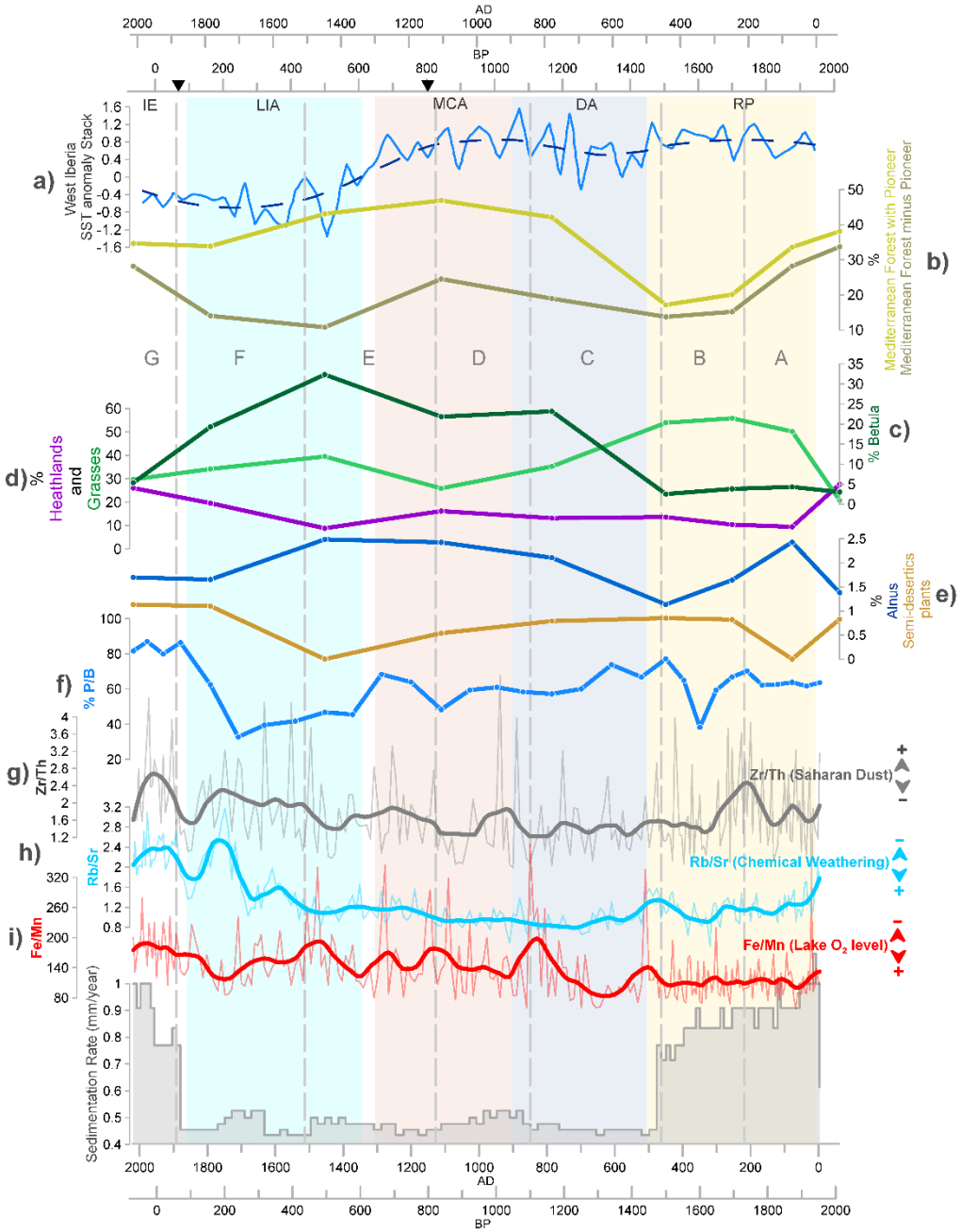

Figure 5.49 – Comparison between pollen counts from, XRF ratios from Lake Peixão for the last 2000 cal yrs and West Iberia Sea Surface Temperature (SST) anomaly stack from Abrantes et al., 2017, with a LOESS (locally estimated scatterplot smoothing span) blue dashed line curve defined with 0.5 span. %P/B meaning the percentage of planktonic vs. benthonic diatoms. The bold curves of Rb/Sr, Zr/Th and Fe/Mn correspond to the LOESS curve with a span of 0.1. Gray-dashed lines delineate the A-G biogeochemical stages. Colored vertical bands corresponding to the last 2000 years' main climatic period (see figure 5.48).

5.1.2. Factors controlling the δD signal of leaf waxes *n*-alkanes

Numerous factors influence the $\delta D_{prc,}$ which ultimately controls the hydrogen-isotopic composition of leaf waxes. As prior mentioned, these major factors include temperature, precipitation amount, and moisture source isotopic composition, besides the isotopic fractionation that occurred on the lipid biosynthesis of different vegetation types (see Sache et al., 2012).

Moisture source in the region is almost exclusively originated from the prevailing westerly Atlantic air masses (Carreira et al., 2009; Cortesi et al., 2013; Thatcher et al., 2020b). These moisture-rich westerlies are predominantly during winter NAO− phases and have a gradual D-depletion from the coast through inland (Carreira et al., 2009). This well-constrain source contrasts with other parts of the peninsula, namely the southeast region, which can also be significantly influenced by Mediterranean sources (Cortesi et al., 2013; Taylor et al., 2018; Schirrmacher et al., 2020; Toney et al., 2020).

The δD_{prc} signal of the study area is thought to be substantially driven by temperature, owing to the high elevation effect, which usually leads to enhanced condensation and progressive depletion of heavy isotopes of the rainwater (Carreira et al., 2009; Oliveira and Lima, 2010), a prevailing factor also found in other Iberian mountains (Giménez et al., 2021). This is supported by a strong relationship between mean values of $\delta^{18}O$ and δD *vs.* temperature of monthly rainfall for the Portugal mainland (Carreira et al., 2009). In fact, the simulated history climate data from 1971 to 2000 (portaldoclima.pt) for the Serra da Estrela region reveal that during the wetter months of the growing season, i.e., April and May, it can be seen a strong negative correlation between temperature and precipitation ($r = -0.6$ and -0.7, respectively, for $p < 0.001$). This is important since the seasonal timing and duration of leaf waxes are produced during discrete time intervals and are biased toward those specific to the growing season (Freimuth et al., 2017). Therefore, the δD_{terr} signal over the last 2000 cal yrs BP in the Lake Peixão sediments may be ultimately controlled by changes in temperature, biased towards growing season temperatures.

Since lower temperatures in the areas often imply an increase in condensation (Carreira et al., 2009) low (high) δD_{terr} values in the sedimentary record are interpreted as a decrease (increase) in temperatures and/or increase (decreased) in snow/rainfall.

The positive correlation between δD_{terr} and PC2 ($r = 0.78$, $p<0.001$) point PC2 as a hydrological indicator, most likely water availability, a hypothesis supported by other indicators like Paq, $\%C_{27}$, pollen counts of *Betula*, *Alnus*, and Mediterranean forest with *Pionner* domain (Fig. 52e,f, 53b,c,e.) and by runoff variations (sedimentation rate). On the other hand, the PC1 association with cold and arid-adapted taxa (Janssen, 2011) suggests that PC1 is a temperature indicator, with higher PC1 z-cores indicating lower temperatures (Fig. 5.50).

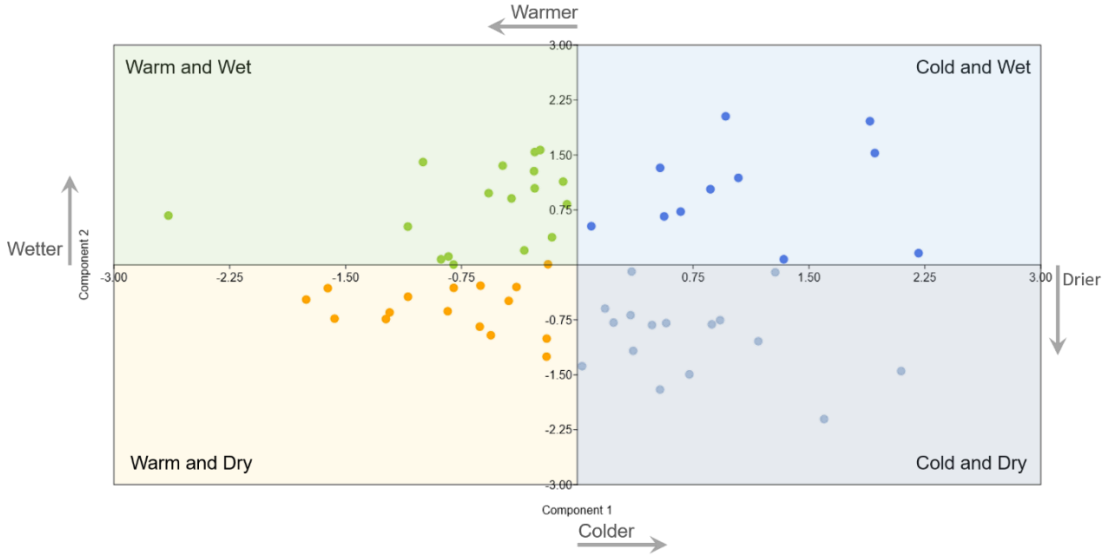

Figure 5.50 – PCA diagram with PC1 and PC2 axis variation for odd n-alkanes concentrations of Lake Peixão sediments for the last 2000 cal yr BP. Colors and arrows indicate general tendencies of the interpreted climate based on PC1 and PC2 scores considering a z-score of 0 as a qualitative threshold.

5.1.3. Climate reconstruction over the last 2000 cal years

A stage, from ca. -3 – 211 AD (120 – 100 cm depth) is characterized by an ongoing centennial-scale decrease in water availability and increase to a warm climate and $\varepsilon_{terr\text{-}aq}$, δD signal indicating an increase in evapotranspiration and an important decrease in precipitation (Fig. 5.48i,h). The warm and arid conditions are commonly reported in other parts of the Iberian Central System during this interval of the RP (Sánchez-López et al., 2016). The aridity of the RP is also evident in speleothems of Western Iberia (Thatcher et al., 2020a), but also in Southern Iberia and Northwest Africa, based on a increase in xerophytic taxa (Fletcher et al., 2007) after and important humid period (2460–2140 cal yr BP) (Martín-Puertas et al., 2009; López-Avilés et al., 2021). The $\delta^{13}C$ signal suggests the local maximum of the aquatic signal was mostly controlled by emergent macrophytes like *Juncus spp.* possibly due to the lake level lowering (Fig. 5.48f,j). The relatively high sedimentation rates of this stage could be the result of contrasting seasonal temperatures, promoting intense snowmelt and higher runoff energy (Sánchez-López et al., 2016), but also due to diminished vegetation

capacity to buffer the runoff energy, i.e., lower vegetation cover or density. The human influence in this high sedimentation rate is discarded since the Roman activity was concentrated at the lowlands (see Connor et al., 2012).

B stage [211 – 450 AD (100 – 80 cm depth)] has no significant changes in the sedimentation rate, but is noticed an increase in sedimentary *n*-alkane concentrations, possibly related to the inferred decrease in temperature (Fig. 5.48a) which have been reported in Northern Iberia (Martín-Chivelet et al., 2011) and Central Iberia (Sánchez-López et al., 2016), but also in other parts of the Northern Hemisphere (see Martín-Chivelet et al., 2011). The high Zr/Th ratio values (Fig. 5.48g), an indicator of Saharan dust (see Jiménez-Espejo et al., 2014; Toney et al., 2020), along with other pollen influx and speleothem data, suggests that these arid conditions were widespread over Western Mediterranean and North Africa during this interval (see Fletcher et al., 2007; Thatcher et al., 2020a). Although both A and B stages comprise a dry phases within the RP, the B stage is generally drier and colder than the prior stage, as suggested by the increase in δD_{terr}, decrease in planktonic diatoms (Fig. 5.53f) and minima in aquatic plants (Fig. 5.48e), conditions also reported in Southeastern Iberia and other Mediterranean areas (e.g., López-Avilés et al., 2021). Pollen analysis shows an important decrease in the Mediterranean and temperate forests but an increase in grasses (Fig. 5.48b,c,e), possibly linked with an increase in local fires in the region (Connor et al., 2012). The cold and dry climate of this stage ended with the onset of the DA, (Stage C; Fig. 5.48g).

The stage C [450 – 828 AD (80 – 62 cm depth)] constrain the DA period, characterized by warm and wet conditions (Fig. 5.48g), where is seen a decrease in the sedimentary *n*-alkane concentrations this time in line with a decrease in the sedimentation rate (Fig. 5.48). The less depleted values δD_{terr} (Fig. 5.48h) may indicate low precipitation, similarity to what is inferred in Central and Southern Iberia (Sánchez-López et al., 2016; López-Avilés et al., 2021). However, different indicators suggest an increase in water availability, such as the aquatic plants' inputs (Fig. 5.48e) and an increase in temperate forests with *Betula*, *Alnus*, and Mediterranean forest with Pioneer suggest contrariwise (Fig. 49c,e,b). This suggests a convergence with the wet conditions inferred in Northwestern/Northern Iberia (Julià et al. 2007; Martín-Chivelet et al., 2011; Jambrina-Enríquez et al., 2014; Smith et al. 2016) instead of the drier phases reported in Central and Southern Iberia (Martín-Puertas et al., 2008; Currás et al., 2012; Ramos-Román et al., 2018). The significant increase in aquatics is supported by the *n*-alkane δC_{13} signal offset of C_{25} and C_{27} and by the $\%C_{27}$ overtaking $\%C_{33}$ for the first time in the record shows a clear increase of aquatic plants (Fig. 5.48j,f). The relatively warm and wet conditions could explain the increase in chemical weathering or pedogenesis in the catchment area indicated by the Rb/Sr values (Fig. 5.49h) in the XRF data (Jin et al., 2006), but also the bottom anoxia due to lake increased water stratification (e.g., Fig. 5.51) inferred low Fe/Mn values (see Naeher et al., 2013). The bulk OM analysis further support bottom anoxia and increase in algal inputs due to the low C/N and $\delta^{15}N$ values (Fig. 5.48k,j), with the latter, interpreted since denitrification is primarily performed under aerobic conditions (see Matheson et al., 2002; Torres et al., 2012). These conditions were then disturbed by a cold and dry D stage (Fig. 5.48).

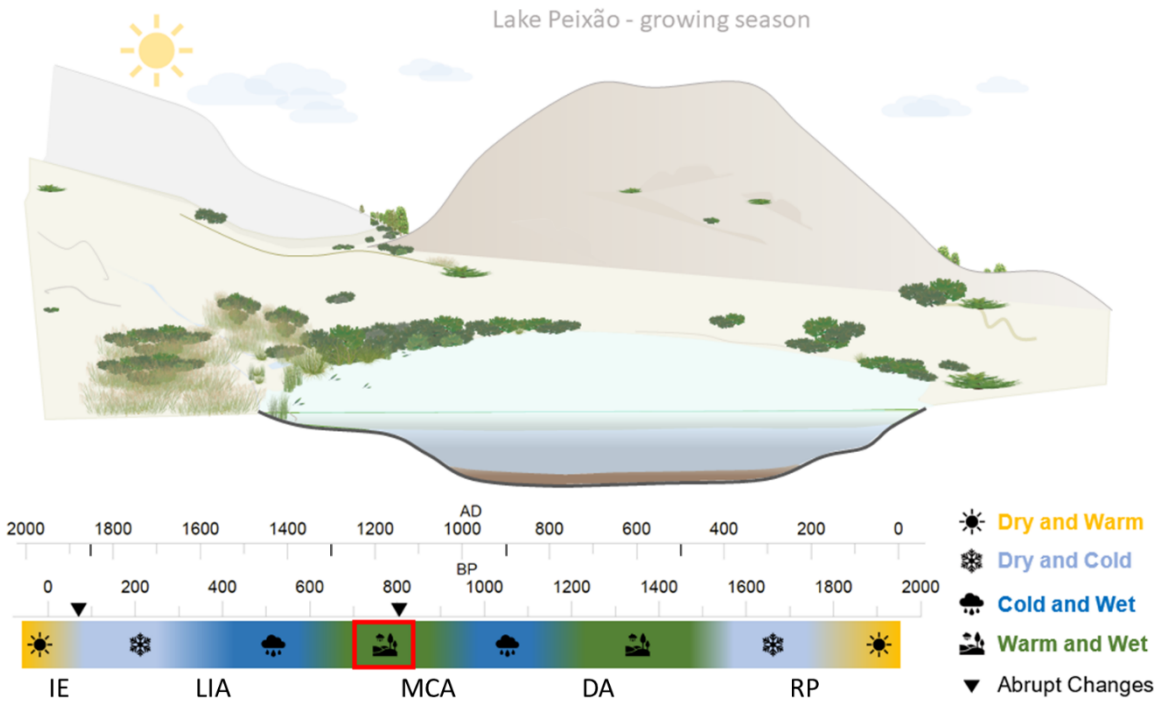

Figure 5.51 – Conceptual model with the inferred climate reconstruction during the growing season at the Lake Peixão for the time interval marked by the red square, corresponding to the MCA period. The climate for this time interval is warm and wet. The enhanced water column stratification, bottom lake anoxia, and abundance of emergent aquatic plants, like Juncus spp. The inverted black triangles point to the abrupt change events (1880 and 1145 AD).

Stage D [828 – 1112 AD (62 – 48 cm depth)] encompasses a short interval of cold and wet conditions, although under a relative decrease in water availability (Fig. 5.48g,h). There is no evidence of pronouncing dry conditions in the studied record, but it is often reported dry conditions in other parts of Iberia during the same period (Sánchez-López et al., 2016), including speleothems in Western Iberia (Thatcher et al., 2020a). The increase in *n*-alkane concentration is yet again associated with the decrease in temperatures. In fact, from ca. 1000 to 1200 AD there was a decline in mean annual or summer temperatures and regional hydrological anomalies in the Northern Hemisphere, reflecting the 'anomalous' character of the MCA (see Bradley et al., 2003). In the study record, the hydrological changes are reflected by the decrease in δD_{terr} (Fig. 5.48a,h) while a significant decrease in aquatic plants and algae (Fig. 5.48e and 5.49f). Although highly localized at the onset of this stage, the highest Zr/Th ratios are observed in this stage are temporally congruent inferred enhanced Saharan eolian input record in the Algerian–Balearic basin records (Moreno et al., 2012b). This might be due to prevailing in northwest African winds (Moreno et al., 2012b) which explains above mentioned short-term dry events in some parts of Iberia and relative decrease in the study record (Fig. 5.48e,g,i). The onset of the E stages (ca 1112 AD) is marked by an increase in temperature and water availability climate (Fig. 5.48g) coeval with important changes in geochemical data and a surface boundary at ca. 0.9 ka BP in a sedimentary record in the Iberian Central System, possibly due to a shift from arid to wet conditions (Turu et al., 2021).

The E stage [1112 – 1486 AD (48 – 30 cm depth)] seems to be linked with the abrupt event at 1145 AD (ca. 46 cm depth) (Fig. 5.55) and constrain the climatic transition from MCA to the LIA. The stages D/E boundary also points to significant changes in the C_{27} sources (i.e., vegetation changes), with the $\delta^{13}C$ signal (Fig. 5.48j) possibly reflecting a relative decrease in grasses as observed in the pollen counts (Fig. 5.49d). However, these changes in *n*-alkane sources could also be explained by other factors, such as the invasion of macrophytes due to a drop in water level or lake productivity (Leng et al., 2006; Ortiz et al., 2021). Moreover, at the beginning of this stage, the $\varepsilon_{terr\text{-}aq}$ values reach their maximum (Fig. 5.48i), suggesting enhanced evapotranspiration conditions. Nevertheless, this hypothesis is difficult to confirm since different indicators suggest water availability (Fig. 5.48e,f; 49c,e,f). In fact, this interval encompasses a maximum in $\%C_{27}$, temperate forests, and disappearance of semi-deserts (Fig. 5.49c,e) coeval with the wetter conditions of Northern Iberia (see

Morellón et al., 2012; Moreno et al., 2014a; Desprat et al., 2013), while general dry conditions reported in the Southern Iberia (e.g., Moreno et al., 2012b; López-Avilés et al., 2021). The relatively warm temperatures would explain lower levels of dissolved oxygen in the lake water column suggested by the different peaks of in Fe/Mn during this interval (Fig. 5.49i) (see Naeher et al., 2013). Nonetheless, by the end of this interval, in the onset of the LIA, the climate became colder (Fig. 5.48g), in line with the significant decline observed in the Western Iberian SST record (Abrantes et al., 2017) (Fig. 5.49a).

The stage F [1486 – 1880 AD (30 – 12 cm depth)] corresponds to the coldest interval of the studied record encompassing the second phase of the LIA, a widespread cold interval reported in the whole Iberia (see Oliva et al., 2018). The highest *n*-alkane concentrations, OM preservation, (Fig. 5.48a,b,d) seems to be associated with these cold conditions, which are also inferred in the Northwestern region of Iberia (e.g., Diz et al. 2002; Julià et al., 2007; De la Rosa et al., 2012; Moreno et al., 2014b). Despite the expected higher precipitation deduced from the lower δD_{terr} signal, several indicators, such as a substantial decrease in aquatics, planktonic diatoms (Fig. 5.48e; 49f), Betula and Alnus (Fig. 5.49c,e), lowest $\varepsilon_{terr\text{-}aq}$ (Fig. 5.48i), ACL_{dif} values and high dissolved oxygen in the lake (Fig. 5.49i, k) point to less water availability (Fig. 5.49g). The dry conditions inferred in the study area may be the result of a possible 'mask effect', since under particularly cold conditions snow would persist accumulated in the catchment area, imprinting the dry effect in the inferred indicators. Extended conditions of frozen lake are suggested during this interval (e.g., Fig. 5.52), where is seen a sharp decline of aquatic-related plants and algae (Fig. 5.48f, e,j; 49f). These cold and dry conditions are also reported at ca. 400 cal BP in Iberian Central System (Turu et al., 2021).

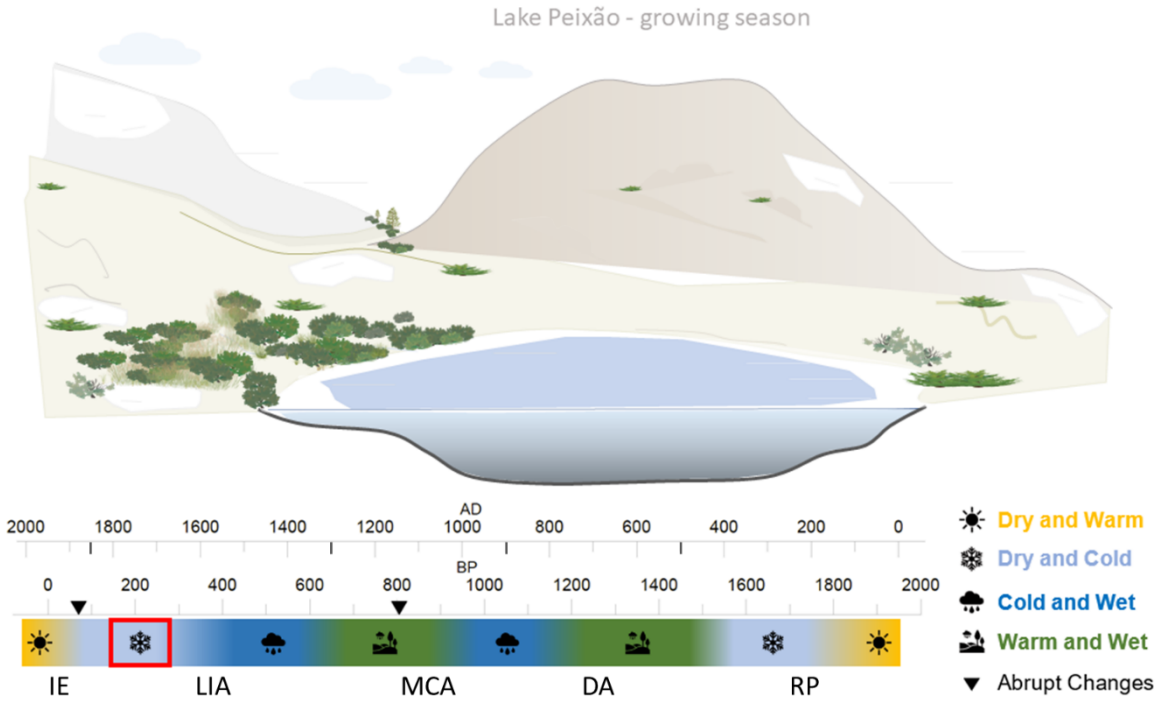

Figure 5.52 – Conceptual model with the inferred climate reconstruction during the growing season at the Lake Peixão for the time interval marked by the red square, corresponding to early stages of LIA. The climate for this time interval is dry and cold, with enhanced monomictic conditions, the prevalence of frozen lake margins, and a relatively high abundance of bushes, like Juniperus and Erica spp. The inverted black triangles point to the abrupt change events (1880 and 1145 AD).

The stage G [1880 AD – present (12 – 0 cm depth)] started with an important shift towards more abrupt regime in the *n*-alkane signal, with climate conditions becoming warmer, drier (Fig.48g,h) and with an possible increase in seasonality suggested by increase in Mediterranean forest (Fig. 5.49b), heathlands (Fig. 5.49d), and high sedimentation rate (Fig. 5.48). High Saharan dust (Fig. 5.49g) is inferred in this stage, which is coherent with SE records of Iberia (see López-Avilés, et al., 2021). The *n*-alkane δC_{13} signal (Fig. 5.48j) suggests that the apparent maximum in aquatics (Fig. 5.48e) may result from plants like emergent macrophytes, possibly due to lower lake level, and both ACL_{dif} and diatom data (Fig. 5.48c; 49f) suggest an increase of algae. These

changes appear to be linked with environmental conditions, possibly related to the beginning of the Industrial Revolution, with signs of a substantial increase in bacterial degradation, low C/N (Fig. 5.48d,k), and dissolved oxygen (Fig. 5.49i). This suggests an increase in the productivity or eutrophication of the lake, which can explain the high bulk $\delta^{13}C$ values (Fig. 5.48m) (Mügler et al., 2010, López-Avilés et al., 2021; Ortiz et al., 2021). Concomitantly, anthropogenic footprint in both *n*-alkane signal of bulk organic matter is also reported in other Iberian lakes (e.g., Jambrina-Enríquez et al., 2016; García-Alix et al., 2017, 2020; Toney et al., 2020; López-Avilés et al., 2021) and lacustrine records (De la Rosa et al., 2012).

5.2. Centennial-scale climate drivers

5.2.1. Solar and atmospheric pattern influence

The long-term decrease in precipitation in the region suggested by the δD_{terr} data (Fig. 5.52h), reinforced the aridification trend of Iberia for the last 2000 years (Ramos-Román et al., 2016; Thatcher et al. 2020a; Toney et al., 2020), possibly related to more persistent NAO+ phase, due to changes in Hadley Circulation and southward migration of the Intertropical Convergence Zone since 4.2 ka event BP (see Thatcher et al., 2020a). However, different and independent indicators evidence a decadal-to-centennial timescales changes in water availability in the Lake Peixão ecosystem. The inferred water variability indicator (PC2) is not always consistent with what is expected, i.e., increase in water availability under prevailing NAO–, and vice-versa (see Fig. 5.53). This might reinforce the weight of temperature factor on the hydroclimate in this high-lake setting, but it also can be due to the modulated effect of patterns such as EA (see Mellado-Cano et al., 2019) that can control the type of precipitation (snow vs. rain).

The quasi-antiphase relation between the inferred temperature indicator (PC1) (Fig. 5.53e) and water availability (PC2) (Fig. 5.53d), suggested the first as a significant long-term driver for the hydrology in the area. The NAO reconstruction raw values of Hernández et al., 2020a show a significant inverse correlation (-0.5, $p < 0.05$) with the smoothing line of the inferred temperature (see Fig. 5.53). Furthermore, there is a significant inverse correlation between the solar variability (Fig. 5.53f-h), for instance, with the smooth lines of temperature total solar irradiance of Steinhilber et al., 2012 and Vieira et al., 2011, having a correlation of $r = -0.4$ and $r = 0.5$, respectively for $p < 0.01$. Moreover, the cross-correlation analysis reveals that the PC2 lags behind the solar irradiance signal under significant values (see Table A8, annexes).

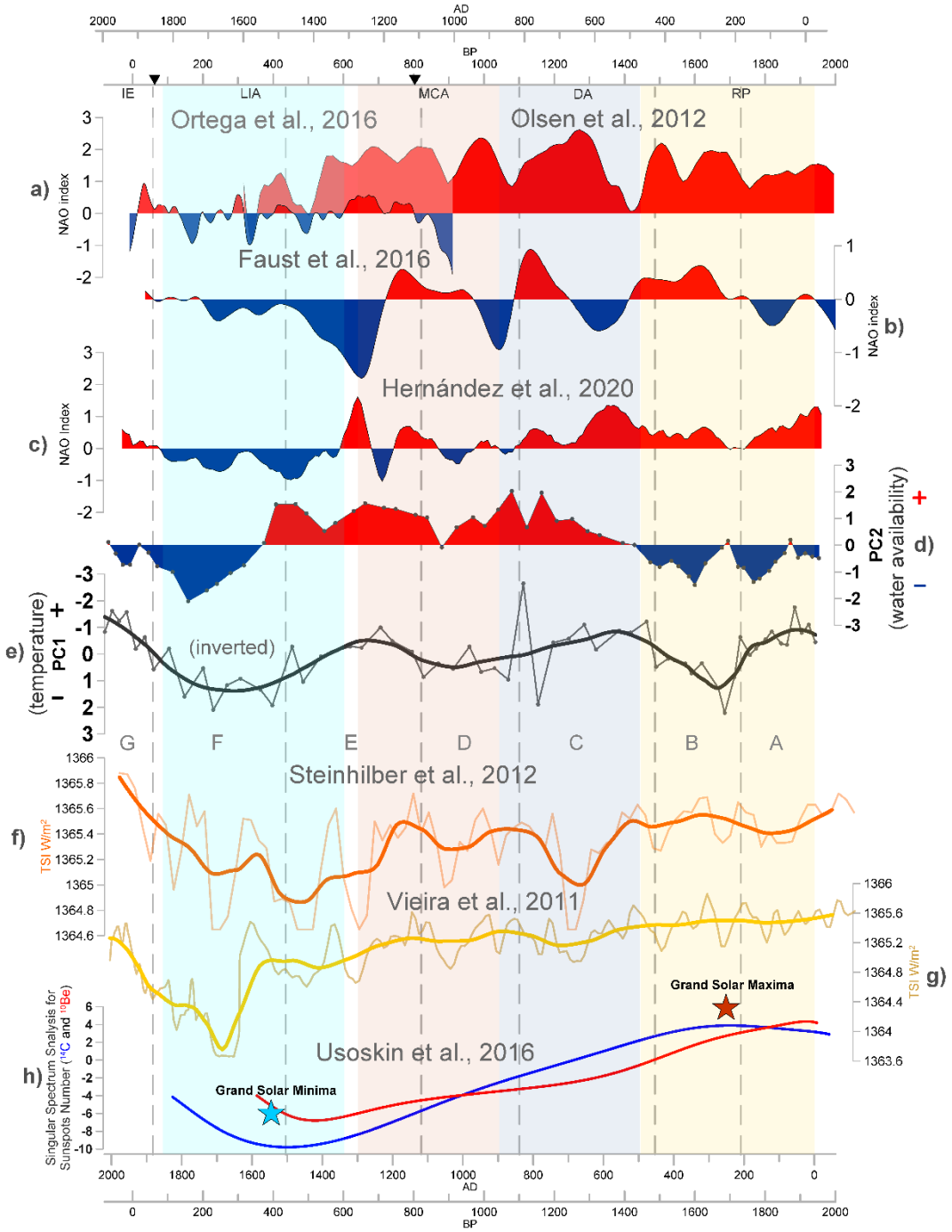

Figure 5.53 – Comparison between different NAO reconstructions for the late Holocene, PCs of the Lake Peixão sediments for the last 2000 cal yrs, reconstructions of Total Solar Irradiance (TSI), and anomalies of sunspots, see references in the graph. For visual ease, the NAO values here presented to have the respective smoothing: spline 2 for Olsen et al., 2012; spline 4 for Faust et al., 2016; running mean of 30 years and spline of 1 for Ortega et al., 2016; running mean of 40 years for Hernández et al., 2020a. The bold lines in PC1 and TSI curves represent a LOESS smoothing line with a 0.2 span. Notice that PC1 and PC2 are visually different to ease visual comparison with the upper and above graphs, respectively. Gray-dashed lines delineate the A-G biogeochemical stages. Colored vertical bands corresponding to the last 2000 years' main climatic periods.

In fact, evidence of solar forcing on vegetation and water availability changes has been proven in other alpine areas of Iberia (García-Alix et al., 2017). The solar-induced climate changes have been widely studied since changes in irradiance can lead to the disturbance of the polar vortex, the tropospheric jet streams, and have important effects on atmospheric patterns such as the NAO (e.g., Shindell et al., 2001; Jiang et al., 2005; Gray et al., 2010; Martín-Puertas et al., 2011; Wirth et al., 2013; Thiéblemont et al., 2015).

Over the last 2000 cal yrs, the general trend of low (high) solar activity is coupled with persistent NAO– (NAO+) conditions (see Fig. 5.53). For instances with the long succession of strong Grand Solar Minima (Wölf, Spörer, Maunder and Dalton Minima) is aligned with a prevailing NAO– (Shindell, et al., 2001; Mann et al..2009) (Fig. 5.53h, a-c), and the coldest interval centered at ca. 1700 AD (Owens et al., 2017) associated

with Bond event 0 (Wanner et al., 2011), coeval with the F stage of the Lake Peixão record and other Iberian records (Desprat et al., 2003; Oliva et al., 2018), including a particularly extreme cold interval in Southern Portugal (Alcoforado et al., 2000). The Grand Solar Maxima, centered at ca. 300 AD and relatively stable insolation (Fig. 5.53h,f,e), is in line with the persistent NAO+ and warmer sea surface temperature and dry climate of the RP (see Fig. 5.53a,c). Different studies point to aridity events in Iberia to be associated with high TSI periods (Pyrina et al. 2019; Thatcher et al., 2020a).

However, the similar inferred conditions in both late RP (B stage) and the second phase of the LIA (F stage) could be either the result of the variability of the coupled climate system (Hall and Stouffer, 2001) or the prior mentioned snow/ice 'mask effect' of the F stage, that may in fact imprinted in the inferred dry conditions, enlightening the already mentioned complex factors behind the LIA conditions. The second hypothesis could explain the often-reported higher precipitation or wet climate in lower altitudes studies with less temperature-dependent records. An example of this is the relatively close speleothem of Buraca Gloriosa (Thatcher et al., 2020a) or the western river discharges (see Abrantes et al., 2017).

The processes controlling the *n*-alkanes concentration in the sediments, under the inferred cold and arid (warmer and wetter) intervals, indicates that something in the Peixão ecosystem leads towards an increase (decrease) in the *n*-alkanes concentration, as seen in the mean values of odd C_{27}-C_{35} (Fig. 5.54 and 5.48a).

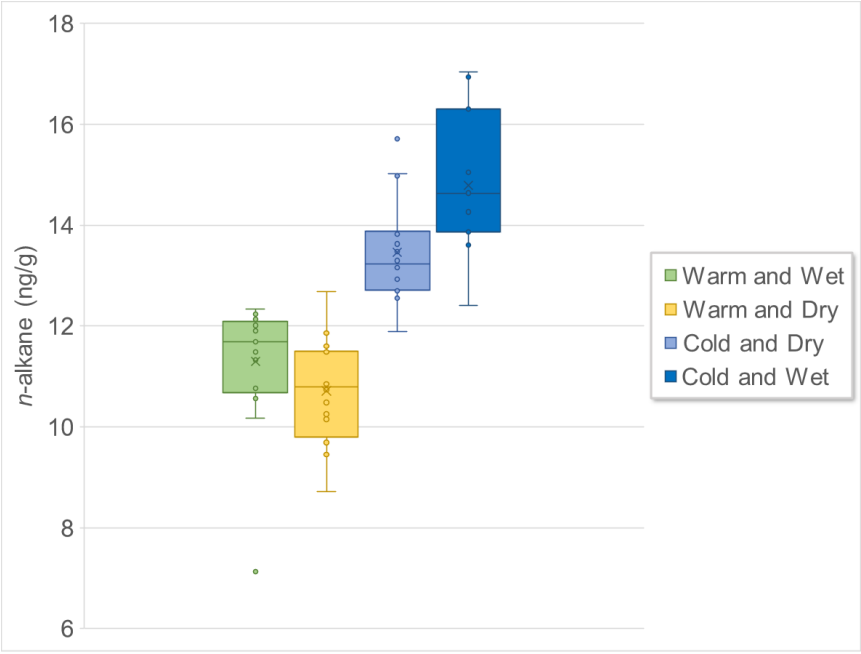

Figure 5.54 – Box plot of the climatic constrained odd n-alkane concentration of dry sediment based on the Lake Peixão paleo reconstruction for the last 2000 cal yrs BP.

This increase in the *n*-alkane concentration can be explained by at least two independent hypotheses: 1) result of increase/decrease of leaf waxes productions, for instance, with harsh extended conditions, such as cold and arid conditions, the vegetation type would benefit by enhancing the external barrier that better protected from evaporative water loss, i.e., thickening of the *n*-alkane layer (Shepherd and Griffiths, 2006, Rommerskirchen et al., 2006b; Cui et al., 2008), whereas in an opposite scenario, i.e., during milder conditions (warmer and wetter) the vegetation would not develop to produce additional leaf waxes (Sachse et al., 2006). 2) the differences seen arise due to the contrasting mean of *n*-alkane transport into the lake. For instance, with an increment of the runoff conditions, one might expect rather *n*-alkane concentrations dilutions, primarily due to the increment in the sediment load capacity. However, the opposite would be confirmed with the increase in gustiness and decrease in the runoff, where the leaves ablation by a strong wind, would eventually lead to the relative increase in the concentration of *n*-alkanes in the lake sediments (Fig. 5.48a).

The second hypothesis seems to be better constrained since intervals with contrasting climates can have substantially different *n*-alkanes concentrations under similar sedimentation rates, such as in the case of the A and B stages (Fig. 5.48). Moreover, this hypothesis is further supported since the second phase of the LIA in the studied record, which conditions of prevailing NAO− (e.g., Mann et al., 2009, Trouet et al., 2009) and SST

minima in the North Atlantic (Jiang et al., 2005), support the inferred higher wind speeds in Western Iberia, especially when combined with the EA− (Zubiate et al., 2017; Mellado-Cano et al., 2019). This would also explain the highest abruptness in all the indicators of Lake Peixão record (e.g., Fig. 5.55) and possibly linked with the particularly cold conditions in Iberia evidenced by several authors (see Fletcher and Zielhofer, 2013; Moreno et al., 2014b; Oliva et al., 2018). Moreover, other studies also point to the linkage between higher wind speed and other especially cold intervals in Western Iberia (e.g., Clarke and Rendell, 2009; Costas et al., 2012; Taylor et al., 2018). Conditions consistent with the southward position of the jet stream under a weakened polar vortex (Costas et al., 2016) and depleted δD values due to the suppressed tropical moisture source (Taylor et al., 2018).

5.2.2. Unstable phases

As seen, processes such as the significant explosive volcanic eruptions and slowdown of the thermohaline circulation in the North Atlantic (Weber et al., 2004; Renssen et al., 2007) could have been behind the especially cold intervals (Wanner et al., 2011). However, no major global or Northern Hemisphere volcanic events before or in line with the B stage (Toohey and Sigl, 2017) could explain the inferred conditions. In fact, even the mid-6th to 7th-century volcanic eruptions (Stothers, 1984; Rampino et al., 1988), thought to be the strongest decadal volcanic forcing in the last 2000 years (Larsen et al., 2008; Sigl et al., 2015), and responsible for the cooling period a.k.a Late Antiquity Little Ice Age (LALIA) (Büntgen et al. 2016, Toohey et al., 2016) show no evidence in the Lake Peixão record, although with a cold phase recorded in the Lake Sanabria (Northwest Iberia) between 650 and 725 AD (Julià et al., 2007). This suggests that LALIA might not have reached the necessary threshold in the Western Iberia region to imprint the cold conditions in the here used indicators.

In fact, recent studies showed that volcanism events, such as LALIA, could not have a centennial-scale impact in precipitation and temperature decrease at a regional climate (van Dijk et al., 2021). Although might have sustained changes in ocean/atmospheric interactions decades after the volcanic eruptions (Zhong et al. 2011; Miller et al. 2012). This could be the case of the apparent cold reversal centered at ca. 650 AD in the western Iberia margin SST (Abrantes et al., 2017) (see Fig. 5.49a), and inferred changes in NAO phases occurring with the onset of the DA (C stages) (Fig. 5.49a-c). These changes may have been linked with important perturbations in the atmospheric organization (e.g., Zubiate et al., 2017) despite not being evident in the Lake Peixão record.

Nonetheless, the post-RP and pre-LIA (ca. C – E stages) seem to constrain a general transition period from high to low solar activity (Usoskin et al., 2016) (Fig. 5.53h), with a tipping point in the number of sunspots coeval with the first abrupt event (1145 AD) in the study record during the middle MCA (see Fig. 5.55) and particularly unstable phase in the Central Iberia (Turu et al., 2021). The increased disturbance of the Lake Peixão ecosystem seems to materialize the whole E stage (Fig. 5.53), coeval with the increasing changes in the climatic system, such the Atlantic Ocean circulation and sea surface temperatures (Jiang et al., 2005) that the relatively stable from 0 to 900 AD (Eiríksson et al., 2006) and non-stationary NAO phase of the MCA (Hernández et al., 2020a) (Fig. 5.57), possibly linked with change in solar irradiance (Mann et al., 2009). This could explain the highly variable and asymmetric conditions between Atlantic/Mediterranean zones in Iberia during this interval (see Moreno et al., 2014b; Smith et al. 2016; Sánchez-López et al., 2016). Something evidenced in model simulations, possibly also affected by the important role of internal natural variability (Mann et al., 2009).

The possible anthropogenic origin of the 1145 AD event in the record cannot be discarded since during Medieval times, there was evidence of human activities relatively near of the Lake Peixão area (see Connor et al., 2012). However, the constant changes and extent of those changes do not support that long-term human influence. Therefore, it is hypothesized that since 1145 AD the observed changes occurred as a response to the increasing unstable NAO phase under a non-stationarity solar forcing (see Hernández et al., 2020a).

On the other hand, the modern Great Solar Maximum, 1940 – 2000 AD (Usoskin et al., 2016) (Fig. 5.53h), along with the unprecedented increase in anthropogenic effects such as greenhouse gases (Masson-Delmotte

et al., 2021 [IPCC]) and dominant NAO+ (Fig. 5.53a-c) and EA+ can explain concurring phase of warming and drought in IP.

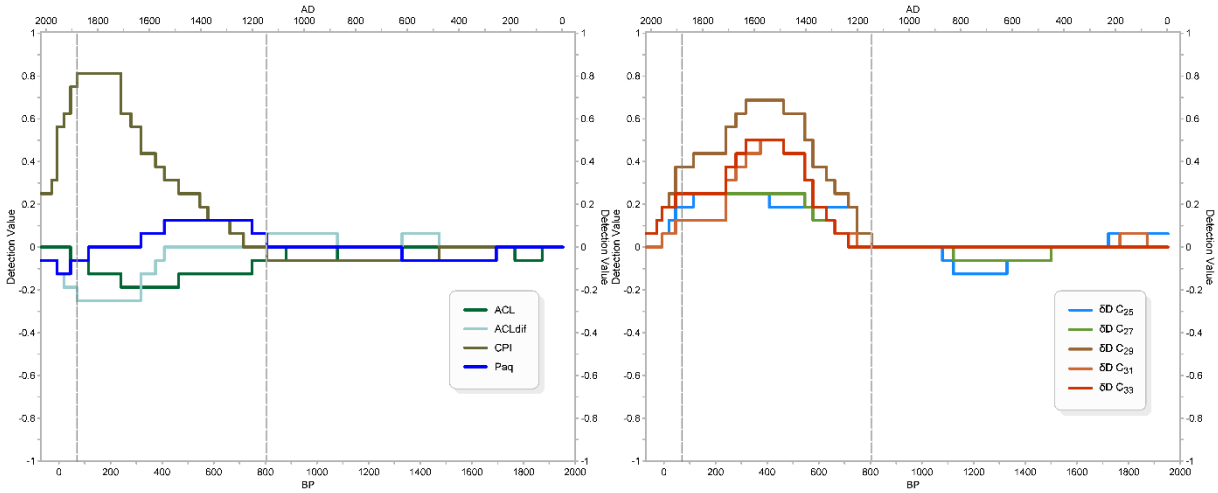

Figure 5.55 – Example of two abrupt changes analysis performed on n-alkane climate indicator used in this study. The dashed lines represent general abrupt change events detected on the gradient of the indicators, with the darker line of 1880 indicating higher abruptness.

The 1880 AD event

The event centered at ca. 1880 AD (12 cm depth, min/max 25-105 BP age) marks the passage to the modern-day climatic settings of the Industrial Era with a second significant change in the abruptness regime (Fig. 5.55). Due to the magnitude, timing, and inferred changes on indicators such as Paq, CPI, and C/N (Fig. 5.48e,d,j), this event could be the result of an anthropogenic effect in the lake ecosystem that brought a significant and constant rate of changes into the ecosystem. These effects are most likely related to the upsurge of the grazing activity and/or other activities on top of the mountain. This increase coincides with the changes in the law of private property in the 19th century, which might have forced shepherds to find places on top of the mountain (Morgado, 2013) and/or the diminishing of the severe climatic conditions of the LIA (e.g., Fig. 5.52).

Sheep and goat grazing in Serra da Estrela Mountain has been a notorious and well-establish cultural activity in the region for millennia (Batista, 1988; van der Knaap and van Leeuwen, 1995), whose last decades of the local economy was largely dependent, primarily through wool and cheese production. The agro-pastoral practices and associated fire usage (*queimadas*) to open grazing patches (Conor et al., 2012; Batista, 1988) would significantly affect soil, and vegetation cover on top of the mountain (van der Knaap and van Leeuwen, 1995; Connor et al., 2012). Despite the complexities of N-transformation pathways (e.g., Zhu-Barke and Steenwerth, 2018) the observed drop on ^{15}N values (Fig. 5.48k) during this period may further indicate important changes in the nitrification/denitrification process in the lake catchment area or possibly reflecting a decrease in dissolved oxygen in the lake, since nitrification is performed preferentially under anaerobic conditions (Matheson et al., 2002; Torres et al., 2012). Diminishing the vegetation capability to buffer the runoff energy will promote the observed high sedimentation rates during this period. Bacterial proliferation associated with grazing and other human activities would explain the sudden and steep drop observed in the CPI (Fig. 5.48d) and the prior-mentioned inferred signals of lake eutrophication.

6. CONCLUSIONS

The *n*-alkane signal (distribution and isotopic signal) of Lake Peixão record allowed to infer for the first time a high resolution (decadal-scale) climate reconstruction for the last 2000 cal yrs in Serra da Estrela (Portugal). This pristine record shows that the *n*-alkane signal is dominated by long-chain compounds derived from the higher plants in the Lake Peixão catchment area.

The vegetation type has not changed significantly throughout the record, with the heathlands and grass mosaics controlling the poorly developed soils of the mountain summit. C_{31} is the preferentially produced and dominant *n*-alkane in the whole sedimentary record, mainly contributing to the PC1 of the odd *n*-alkanes. The variance of the *n*-alkanes has high and significant correlations with total solar irradiance reconstructions of and the NAO reconstruction of Iberia. On the other hand, C_{29} show evidence of being the most robust palaeohydrological indicator, with the δD signal showing a general aridification trend in the region. Nevertheless, there were significant oscillations in water availability suggested by different and independent indicators, such as inputs of aquatic plants which signals were further constrained using the compound-specific δC signal of C_{25}-C_{33}.

The early record shows a stable lake ecosystem, under an increase in dry conditions (RP [ca. 0 – 500 AD], A – B stages), a predominant NAO+ phase, and Grand solar maxima, which gradually decreased after ca. 500 AD. From DA until MCA ([ca. 500 – 1300 AD] C – E stages), the climate was relatively milder or more Atlantic influenced. The lake ecosystem is starting to record an increase in abruptness in all the *n*-alkane indicators by mid-MCA, ca. 1145 AD. This event marks the beginning of the MCA/LIA transition phase to a colder and wet climate, materialized by the E stage (1112 – 1486 AD), under a nonstationary behavior of the NAO, cooling sea surface temperature in the Western margin and possible tipping point towards lower solar irradiance. The LIA (ca. 1350 – 1850 AD) appears to have two distinct phases, the first phase under cold and wet conditions which turned cooler with the second phase (F stage, centered at ca. 1700 AD) where is recorded the coldest conditions in the studied record, coeval with other records of the North Atlantic realm. During this second phase, the NAO phase was predominantly negative, and there was a strong influence of the polar front, coincident with The Maunder Minimum. The effects of the expected higher precipitation during this phase were possibly masked due to the small lake size and effect of persistent snow cover and frozen lake, which imprinted dry conditions in the considered indicators. These conditions abruptly changed at ca. 1880 AD with the onset of the G stage (ca. 1880 AD). The climate turned warmer and drier, with strong seasonality and significant indications of increased anthropogenic footprints and lake eutrophication.

This work suggests a remarkable teleconnection between solar variability, NAO, and leaf waxes *n*-alkanes to registry those changes in the Lake Peixão sediments, reenforcing the sensitive nature of the alpine ecosystems and extending the spatial coverage of the Iberian paleoclimate studies.

7. FUTURE WORKS

Logical follow-up studies would include:

- A more detailed study of the modern vegetation leaf-wax compounds signal, covering the three main bioclimatic zones of Serra da Estrela. This will enhance the understanding of altitudinal changes of the dominant vegetation in time, and the robustness of C_{29} as a palaeohydrological indicator for the area, especially in terms of hydrogen isotope fractionation.
- Study other biogeochemical compounds such as the Polycyclic Aromatic Hydrocarbons (PAHs), a proxy for biomass burning, and branched glycerol dialkyl glycerol tetraethers (brGDGTs) lipids to further understand the paleoenvironmental changes or anthropogenic footprints occurring at soil level but also to assess the mean annual air temperature.
- Proceed to the whole core analysis, which will allow understanding how long-term climatic shifts since the lake formation, i.e., since the last deglaciation, and important events such as the Younger-Dryas, 8.2 and 4.2 ka, impacted the hydroclimate of the region.

8. REFERENCES

Abrantes, F., Rodrigues, T., Rufino, M., Salgueiro, E., Oliveira, D., Gomes, S., ... and Naughton, F. (2017). The climate of the Common Era off the Iberian Peninsula. *Climate of the Past*, 13(12), 1901-1918. https://doi.org/10.5194/cp-13-1901-2017

Alcoforado, M. J., Nunes, M. D. F., Garcia, J. C., and Taborda, J. P. (2000). Temperature and precipitation reconstruction in southern Portugal during the late Maunder Minimum (AD 1675–1715). *The Holocene*, 10(3), 333-340. https://doi.org/10.1191/095968300674442959

Alley, R. B., and Ágústsdóttir, A. M. (2005). The 8k event: cause and consequences of a major Holocene abrupt climate change. *Quaternary Science Reviews*, 24(10-11), 1123-1149. https://doi.org/10.1016/j.quascirev.2004.12.004

Alley, R. B., Meese, D. A., Shuman, C. A., Gow, A. J., Taylor, K. C., Grootes, P. M., ... and Zielinski, G. A. (1993). Abrupt increase in Greenland snow accumulation at the end of the Younger Dryas event. *Nature*, 362(6420), 527-529.

Andersen, K. K., Azuma, N., Barnola, J.-M., Bigler, M., Biscaye, P., Caillon, N., … members, N. G. I. C. P. (2004). High-resolution record of Northern Hemisphere climate extending into the last interglacial period. *Nature*, 431(7005), 147–151. https://doi.org/10.1038/nature02805

Assessment Report of the Intergovernmental Panel on Climate Change [Masson-Delmotte, V., P. Zhai, A. Pirani, S. L. Connors, C. Péan, S. Berger, N. Caud, Y. Chen, L. Goldfarb, M. I. Gomis, M. Huang, K. Leitzell, E. Lonnoy, J. B.R. Matthews, T. K. Maycock, T. Waterfield, O. Yelekçi, R. Yu and B. Zhou (eds.)]. Cambridge University Press. In Press

Azuara, J., Sabatier, P., Lebreton, V., Jalali, B., Sicre, M. A., Dezileau, L., ... and Combourieu-Nebout, N. (2020). Mid-to Late-Holocene Mediterranean climate variability: Contribution of multi-proxy and multi-sequence comparison using wavelet spectral analysis in the northwestern Mediterranean basin. *Earth-Science Reviews*, 208, 103232. https://doi.org/10.1016/j.earscirev.2020.103232

Baas, M., Pancost, R., van Geel, B., and Damsté, J. S. S. (2000). A comparative study of lipids in Sphagnum species. *Organic Geochemistry*, 31(6), 535-541. https://doi.org/10.1016/S0146-6380(00)00037-1

Baldini, L. M., Baldini, J. U., McDermott, F., Arias, P., Cueto, M., Fairchild, I. J., ... and Ontañón, R. (2019). North Iberian temperature and rainfall seasonality over the Younger Dryas and Holocene. *Quaternary Science Reviews*, 226, 105998. https://doi.org/10.1016/j.quascirev.2019.105998

Baqloul, A., Schefuß, E., Kölling, M., Dupont, L., Groeneveld, J., Zhao, X., ... and Bouimetarhan, I. (2021). Climate and land-use effects on hydrological and vegetation signals during the last three millennia: Evidence from sedimentary leaf waxes in southwestern Morocco. *The Holocene*, 31(5), 699-708. https://doi.org/10.1177/0959683620988053

Barber, D. C., Dyke, A., Hillaire-Marcel, C., Jennings, A. E., Andrews, J. T., Kerwin, M. W., ... and Gagnon, J. M. (1999). Forcing of the cold event of 8,200 years ago by catastrophic drainage of Laurentide lakes. *Nature*, 400(6742), 344-348. https://doi.org/10.1038/22504

Batista, J. D. L. (1988). *O povoamento da Serra da Estrela de 1055 a 1233: e outros estudos*. Instituto de cultura e língua portuguesa.

Beer J. and van Geel B., (2008). Holocene climate change and the evidence for solar and other forcings. In: R.W. Battarbee and H.A. Binney (eds.) *Natural Climate Variability and Global Warming: a Holocene Perspective*. Wiley-Blackwell, Chichester, 254-268.

Beer J., Vonmoos M. and Muscheler R. (2006) Solar variability over the past several millennia. *Space Science Reviews*, doi:10.1007/s11214-006-9047-4.

Bender, M. L. (2013). *Paleoclimate - Princeton Primers in Climate (Vol. 9)*. Princeton University Press. Princeton, NJ

Bhushan, R., Sati, S. P., Rana, N., Shukla, A. D., Mazumdar, A. S., and Juyal, N. (2018). High-resolution millennial and centennial scale Holocene monsoon variability in the Higher Central Himalayas.

Palaeogeography, Palaeoclimatology, Palaeoecology, 489, 95-104. https://doi.org/10.1016/j.palaeo.2017.09.032

Blaauw, M., Christen, J. A., and Aquino, L. M. A. (2018). rbacon: Age-depth modelling using Bayesian statistics. R package version, 2(4).

Boessenkool, K. P., Brinkhuis, H., Schönfeld, J., and Targarona, J. (2001). North Atlantic sea-surface temperature changes and the climate of western Iberia during the last deglaciation; a marine palynological approach. *Global and Planetary Change*, 30(1-2), 33-39. https://doi.org/10.1016/S0921-8181(01)00075-3

Bond, G., Kromer, B., Beer, J., Muscheler, R., Evans, M. N., Showers, W., ... and Bonani, G. (2001). Persistent solar influence on North Atlantic climate during the Holocene. *Science*, 294(5549), 2130-2136.

Bond, G., Showers, W., Cheseby, M., Lotti, R., Almasi, P., deMenocal, P., ... and Bonani, G. (1997). A pervasive millennial-scale cycle in North Atlantic Holocene and glacial climates. *Science*, 278(5341), 1257-1266. https://doi.org/10.1126/science.278.5341.1257

Boulton, C. A., and Lenton, T. M. (2019). A new method for detecting abrupt shifts in time series. [In press]

Bova, S., Rosenthal, Y., Liu, Z., Godad, S. P., and Yan, M. (2021). Seasonal origin of the thermal maxima at the Holocene and the last interglacial. *Nature*, 589(7843), 548-553. https://doi.org/10.1038/s41586-020-03155-x

Bowen, G. J., and Revenaugh, J. (2003). Interpolating the isotopic composition of modern meteoric precipitation. *Water Resources Research*, 39(10). https://doi.org/10.1029/2003WR002086

Boyle, E. A., and Keigwin, L. (1987). North Atlantic thermohaline circulation during the past 20,000 years linked to high-latitude surface temperature. *Nature*, 330(6143), 35-40. https://doi.org/10.1038/330035a0

Bradley, R. S. (2015). *Paleoclimatology: Reconstructing Climates of the Quaternary*: Third Edition. ISBN: 978-0-12-386913-5

Bradley, R. S., Alverson, K., and Pedersen, T. F. (2003). *Challenges of a changing earth: past perspectives, future concerns. In Paleoclimate, global change and the future* (pp. 163-167). Springer, Berlin, Heidelberg.

Bradley, R. S., Hughes, M. K., and Diaz, H. F. (2003). Climate in medieval time. *Science*, 302(5644), 404-405. https://doi.org/10.1126/science.1090372

Bradley, R., and Bakke, J. (2019). Is there evidence for a 4.2 ka BP event in the northern North Atlantic region?. Climate of the Past, 15(5), 1665-1676. http://doi.org/10.5194/cp-15-1665-2019

Bray, E. E., and Evans, E. D. (1961). Distribution of n-paraffins as a clue to recognition of source beds. *Geochimica et Cosmochimica Acta*, 22(1), 2-15. https://doi.org/10.1016/0016-7037(61)90069-2

Briffa, K. R., and Cook, E. R. (2008). Reducing and representing uncertainties in high-resolution proxy climate data. In Workshop on Reducing and Representing Uncertainties in High Resolution Proxy Climate Data. *PAGES/CLIVAR*, Trieste, Italy.

Broecker, W. S. (1998). Paleocean circulation during the last deglaciation: a bipolar seesaw?. *Paleoceanography*, 13(2), 119-121. https://doi.org/10.1029/97PA03707

Bryan, F., 1986. “High-latitude salinity effects and interhemispheric thermohaline circulations.” Science, 323, 301–304.

Büntgen, U., Myglan, V. S., Ljungqvist, F. C., McCormick, M., Di Cosmo, N., Sigl, M., ... and Kirdyanov, A. V. (2016). Cooling and societal change during the Late Antique Little Ice Age from 536 to around 660 AD. *Nature geoscience*, 9(3), 231-236. https://doi.org/10.1038/ngeo2652

Bush, R. T., and McInerney, F. A. (2013). Leaf wax *n*-alkane distributions in and across modern plants: implications for paleoecology and chemotaxonomy. *Geochimica et Cosmochimica Acta*, 117, 161-179. https://doi.org/10.1016/j.gca.2013.04.016

Bush, R. T., and McInerney, F. A. (2015). Influence of temperature and C4 abundance on n-alkane chain length distributions across the central USA. *Organic Geochemistry*, 79, 65-73. https://doi.org/10.1016/j.orggeochem.2014.12.003

Campos, N., Palacios, D., and Tanarro, L. M. (2019). Glacier reconstruction of La Covacha Massif in Sierra de Gredos (central Spain) during the Last Glacial Maximum. *Journal of Mountain Science*, 16(6), 1336-1352. https://doi.org/10.1007/s11629-019-5382-2

Carlson, A. E., Clark, P. U., Haley, B. A., and Klinkhammer, G. P. (2009). Routing of western Canadian Plains runoff during the 8.2 ka cold event. *Geophysical Research Letters*, 36(14)., https://doi.org/10.1029/2009GL038778.

Carlson, A. E., LeGrande, A. N., Oppo, D. W., Came, R. E., Schmidt, G. A., Anslow, F. S., ... and Obbink, E. A. (2008). Rapid early Holocene deglaciation of the Laurentide ice sheet. *Nature Geoscience*, 1(9), 620-624.https://doi.org/10.1038/ngeo285

Carreira, P. M., Nunes, D., Valério, P., and Araújo, M. F. (2009). A 15-year record of seasonal variation in the isotopic composition of precipitation water over continental Portugal. *Journal of radioanalytical and nuclear chemistry*, 281(1), 153-156. https://doi.org/10.1007/s10967-009-0064-0

Carrión, J. S., Fernández, S., González-Sampériz, P., Gil-Romera, G., Badal, E., Carrión-Marco, Y., ... and Burjachs, F. (2010). Expected trends and surprises in the Lateglacial and Holocene vegetation history of the Iberian Peninsula and Balearic Islands. *Review of Palaeobotany and Palynology*, 162(3), 458-475. https://doi.org/10.1016/j.revpalbo.2009.12.007

Casas-Sainz, A. M., and De Vicente, G. (2009). On the tectonic origin of Iberian topography. *Tectonophysics*, 474(1-2), 214-235. https://doi.org/10.1016/j.tecto.2009.01.030

Castañeda, I. S., and Schouten, S. (2011). A review of molecular organic proxies for examining modern and ancient lacustrine environments. *Quaternary Science Reviews*, 30(21-22), 2851-2891. https://doi.org/10.1016/j.quascirev.2011.07.009

Chambers, F. M., and Blackford, J. J. (2001). Mid-and late-Holocene climatic changes: a test of periodicity and solar forcing in proxy-climate data from blanket peat bogs. *Journal of Quaternary Science*: Published for the Quaternary Research Association, 16(4), 329-338. https://doi.org/10.1002/jqs.596

Charrad, M., Ghazzali, N., Boiteau, V., and Niknafs, A. (2014). Determining the best number of clusters in a data set. J Stat Softw.

Cheesbrough, T. M., and Kolattukudy, P. E. (1984). Alkane biosynthesis by decarbonylation of aldehydes catalyzed by a particulate preparation from Pisum sativum. *Proceedings of the National Academy of Sciences*, 81(21), 6613-6617. https://doi.org/10.1073/pnas.81.21.6613

Chikaraishi, Y., and Naraoka, H. (2003). Compound-specific δD–δ13C analyses of *n*-alkanes extracted from terrestrial and aquatic plants. *Phytochemistry*, 63(3), 361-371. https://doi.org/10.1016/S0031-9422(02)00749-5

Clark, Jr, R. C., and Blumer, M. (1967). Distribution Of N-Paraffins In Marine Organisms And Sediment. *Limnology and Oceanography*, 12(1), 79-87. https://doi.org/10.4319/lo.1967.12.1.0079

Clark, P. U., Alley, R. B., and Pollard, D. (1999). Northern Hemisphere ice-sheet influences on global climate change. *Science*, 286(5442), 1104-1111. https://doi.org/10.1126/science.286.5442.1104

Clark, P. U., Marshall, S. J., Clarke, G. K., Hostetler, S. W., Licciardi, J. M., and Teller, J. T. (2001). Freshwater forcing of abrupt climate change during the last glaciation. *Science*, 293(5528), 283-287. https://doi.org/10.1126/10.1126/science.1062517

Clarke, G. K., Leverington, D. W., Teller, J. T., and Dyke, A. S. (2004). Paleohydraulics of the last outburst flood from glacial Lake Agassiz and the 8200BP cold event. *Quaternary Science Reviews*, 23(3-4), 389-407. https://doi.org/10.1016/j.quascirev.2003.06.004

Clarke, M. L., and Rendell, H. M. (2009). The impact of North Atlantic storminess on western European coasts: a review. *Quaternary International*, 195(1-2), 31-41. https://doi.org/10.1016/j.quaint.2008.02.007

Comas-Bru, L., and McDermott, F. (2014). Impacts of the EA and SCA patterns on the European twentieth century NAO–winter climate relationship. *Quarterly Journal of the Royal Meteorological Society*, 140(679), 354-363. https://doi.org/10.1002/qj.2158

Connor, S. E., Araújo, J., van der Knaap, W. O., and Van Leeuwen, J. F. (2012). A long-term perspective on biomass burning in the Serra da Estrela, Portugal. Quaternary Science Reviews, 55, 114-124. https://doi.org/10.1016/j.quascirev.2012.08.007

Connor, S. E., van Leeuwen, J. F., Akindola, R. B., Adeleye, M. A., and Mariani, M. (2020). Pollen and plant diversity relationships in a Mediterranean montane area. *Vegetation History and Archaeobotany*, 1-12. https://doi.org/10.1007/s00334-020-00811-0

Cooper, R. J., Pedentchouk, N., Hiscock, K. M., Disdle, P., Krueger, T., and Rawlins, B. G. (2015). Apportioning sources of organic matter in streambed sediments: an integrated molecular and compound-specific stable isotope approach. *Science of the Total Environment*, 520, 187-197. https://doi.org/10.1016/j.scitotenv.2015.03.058

Cortesi, N., Gonzalez-Hidalgo, J. C., Trigo, R. M., and Ramos, A. M. (2014). Weather types and spatial variability of precipitation in the Iberian Peninsula. *International Journal of Climatology*, 34(8), 2661-2677. https://doi.org/10.1002/joc.3866

Cortesi, N., Trigo, R. M., Gonzalez-Hidalgo, J. C., and Ramos, A. M. (2013). Modelling monthly precipitation with circulation weather types for a dense network of stations over Iberia. *Hydrology and Earth System Sciences*, 17(2), 665-678. https://doi.org/10.5194/hess-17-665-2013

Costas, S., Jerez, S., Trigo, R. M., Goble, R., and Rebêlo, L. (2012). Sand invasion along the Portuguese coast forced by westerly shifts during cold climate events. *Quaternary Science Reviews*, 42, 15-28. https://doi.org/10.1016/j.quascirev.2012.03.008

Costas, S., Naughton, F., Goble, R., and Renssen, H. (2016). Windiness spells in SW Europe since the last glacial maximum. *Earth and Planetary Science Letters*, 436, 82-92. https://doi.org/10.1016/j.epsl.2015.12.023

Cranwell, P. A. (1973). Chain-length distribution of n-alkanes from lake sediments in relation to post-glacial environmental change. *Freshwater Biology*, 3(3), 259-265. https://doi.org/10.1111/j.1365-2427.1973.tb00921.x

Cranwell, P. A. (1981). Diagenesis of free and bound lipids in terrestrial detritus deposited in a lacustrine sediment. *Organic Geochemistry*, 3(3), 79-89. https://doi.org/10.1016/0146-6380(81)90002-4

Cranwell, P. A. (1984). Lipid geochemistry of sediments from Upton Broad, a small productive lake. *Organic Geochemistry*, 7(1), 25-37. https://doi.org/10.1016/0146-6380(84)90134-7

Cranwell, P. A., Eglinton, G., and Robinson, N. (1987). Lipids of aquatic organisms as potential contributors to lacustrine sediments—II. *Organic Geochemistry*, 11(6), 513-527. https://doi.org/10.1016/0146-6380(87)90007-6

Cui, J., Huang, J., and Xie, S. (2008). Characterstics of seasonal variations of leaf *n*-alkanes and *n*-alkenes in modern higher plants in Qingjiang, Hubei Province, China. *Chinese Science Bulletin*, 53(17), 2659-2664. https://doi.org/10.1007/s11434-008-0194-8

Curtin, L., D'Andrea, W. J., Balascio, N., Pugsley, G., de Wet, G., and Bradley, R. (2019). Holocene and Last Interglacial climate of the Faroe Islands from sedimentary plant wax hydrogen and carbon isotopes. *Quaternary Science Reviews*, 223, 105930. https://doi.org/10.1016/j.quascirev.2019.105930

Dansgaard, W., Johnsen, S. J., Clausen, H. B., Dahl-Jensen, D., Gundestrup, N. S., Hammer, C. U., ... and Bond, G. (1993). Evidence for general instability of past climate from a 250-kyr ice-core record. *Nature*, 364(6434), 218-220.

Daveau, S. (1971). La glaciation de la Serra da Estrela. *Finisterra*, 6(11). https://doi.org/10.18055/Finis2431

Daveau, S., de Brum Ferreira, A., Ferreira, N., and Vieira, G. T. (2014). *Novas observações acerca da glaciação da Serra da Estrela. Estudos do Quaternário*/Quaternary Studies, 1(1).

Daveau, S., Ferreira, A. B., Ferreira, N. and Vieira, Gt (1997). Novas observações acerca da glaciação da Serra da Estrela. Estudos do Quaternário. *Estudos do Quaternário*. Lisboa, 1: 41-51.

Davis, J. C., and Sampson, R. J. (1986). *Statistics and data analysis in geology* (Vol. 646). New York: Wiley.

Dawson, T. E., Mambelli, S., Plamboeck, A. H., Templer, P. H., and Tu, K. P. (2002). Stable isotopes in plant ecology. *Annual review of ecology and systematics*, 33(1), 507-559. https://doi.org/10.1146/annurev.ecolsys.33.020602.095451

Dean, W. E. (1997). Rates, timing, and cyclicity of Holocene eolian activity in north-central United States: Evidence from varved lake sediments. *Geology*, 25(4), 331-334. https://doi.org/10.1130/0091-7613(1997)025<0331:RTACOH>2.3.CO;2

De la Rosa, J. M., Araújo, M. F., González-Pérez, J. A., González-Vila, F. J., Soares, A. M., Martins, J. M., ... and Fatela, F. (2012). Organic matter sources for tidal marsh sediment over the past two millennia in the Minho River estuary (NW Iberian Peninsula). *Organic geochemistry*, 53, 16-24. https://doi.org/10.1016/j.orggeochem.2012.06.014

deMenocal, P., Ortiz, J., Guilderson, T., Adkins, J., Sarnthein, M., Baker, L., and Yarusinsky, M. (2000). Abrupt onset and termination of the African Humid Period:: rapid climate responses to gradual insolation forcing. *Quaternary science reviews*, 19(1-5), 347-361. https://doi.org/10.1016/S0277-3791(99)00081-5

Desprat, S., Goñi, M. F. S., and Loutre, M. F. (2003). Revealing climatic variability of the last three millennia in northwestern Iberia using pollen influx data. *Earth and Planetary Science Letters*, 213(1-2), 63-78. https://doi.org/10.1016/S0012-821X(03)00292-9

Desprat, S., Goñi, M. S., Turon, J. L., McManus, J. F., Loutre, M. F., Duprat, J., ... and Peypouquet, J. P. (2005). Is vegetation responsible for glacial inception during periods of muted insolation changes?. *Quaternary Science Reviews*, 24(12-13), 1361-1374. https://doi.org/10.1016/j.quascirev.2005.01.005

Diefendorf, A. F., and Freimuth, E. J. (2017). Extracting the most from terrestrial plant-derived *n*-alkyl lipids and their carbon isotopes from the sedimentary record: A review. *Organic Geochemistry*, 103, 1-21. https://doi.org/10.1016/j.orggeochem.2016.10.016

Diefendorf, A. F., Freeman, K. H., Wing, S. L., and Graham, H. V. (2011). Production of *n*-alkyl lipids in living plants and implications for the geologic past. *Geochimica et Cosmochimica Acta*, 75(23), 7472-7485. https://doi.org/10.1016/j.gca.2011.09.028

Diz, P., Francés, G., Pelejero, C., Grimalt, J. O., and Vilas, F. (2002). The last 3000 years in the Ría de Vigo (NW Iberian Margin): climatic and hydrographic signals. *The Holocene*, 12(4), 459-468. https://doi.org/10.1191/0959683602hl550rp

Dorado-Liñán, I., Sanchez-Lorenzo, A., Merino, E. G., Planells, O., Heinrich, I., Helle, G., and Zorita, E. (2016). Changes in surface solar radiation in Northeastern Spain over the past six centuries recorded by tree-ring δ 13 C. *Climate Dynamics*, 47(3-4), 937-950. https://doi.org/10.1007/s00382-015-2881-x

Duan, Y., and He, J. (2011). Distribution and isotopic composition of *n*-alkanes from grass, reed and tree leaves along a latitudinal gradient in China. *Geochemical Journal*, 45(3), 199-207. https://doi.org/10.2343/geochemj.1.0115

Edwards, R. L., Beck, J. W., Burr, G. S., Donahue, D. J., Chappell, J. M. A., Bloom, A. L., ... and Taylor, F. W. (1993). A large drop in atmospheric 14C/12C and reduced melting in the Younger Dryas, documented with 230Th ages of corals. *Science*, 260(5110), 962-968. https://10.1126/science.260.5110.962

Eglinton, G., and Hamilton, R. J. (1963). The distribution of alkanes. *Chemical plant taxonomy*, 187, 217. ISBN 0323146244

Eglinton, G., and Hamilton, R. J. (1967). Leaf epicuticular waxes. *Science*, 156(3780), 1322-1335. https://doi.org/10.1126/science.156.3780.1322

Eglinton, G., Gonzalez, A. G., Hamilton, R. J., and Raphael, R. A. (1962). Hydrocarbon constituents of the wax coatings of plant leaves: a taxonomic survey. *Phytochemistry*, 1(2), 89-102. https://doi.org/10.1016/S0031-9422(00)88006-1

Eglinton, T. I., and Eglinton, G. (2008). Molecular proxies for paleoclimatology. *Earth and Planetary Science Letters*, 275(1-2), 1-16. https://doi.org/10.1016/j.epsl.2008.07.012

Eiríksson, J., Bartels-Jonsdottir, H. B., Cage, A. G., Gudmundsdottir, E. R., Klitgaard-Kristensen, D., Marret, F., ... & Sejrup, H. P. (2006). Variability of the North Atlantic Current during the last 2000 years based on shelf bottom water and sea surface temperatures along an open ocean/shallow marine transect in western Europe. *The Holocene*, 16(7), 1017-1029. https://doi.org/10.1177/0959683606hl991rp

Evans, M. N., Tolwinski-Ward, S. E., Thompson, D. M., & Anchukaitis, K. J. (2013). Applications of proxy system modeling in high resolution paleoclimatology. *Quaternary science reviews*, 76, 16-28. https://doi.org/10.1016/j.quascirev.2013.05.024

Feakins, S. J., Eglinton, T. I., and demenocal, P. B. (2007). A comparison of biomarker records of northeast African vegetation from lacustrine and marine sediments (ca. 3.40 Ma). *Organic Geochemistry*, 38(10), 1607-1624. https://doi.org/10.1016/j.orggeochem.2007.06.008

Feakins, S. J., Peters, T., Wu, M. S., Shenkin, A., Salinas, N., Girardin, C. A., ... and Asner, G. P. (2016). Production of leaf wax *n*-alkanes across a tropical forest elevation transect. *Organic Geochemistry*, 100, 89-100. https://doi.org/10.1016/j.orggeochem.2016.07.004

Ferreira, A. B., Alcoforado, M. J., Vieira, G. T., Mora, C., and Jansen, J. (2001). Metodologias de análise e de classificação das paisagens. O exemplo do projecto Estrela. *Finisterra*, 36(72). https://doi.org/10.18055/Finis1632

Ficken, K. J., Li, B., Swain, D. L., and Eglinton, G. (2000). An *n*-alkane proxy for the sedimentary input of submerged/floating freshwater aquatic macrophytes. *Organic geochemistry*, 31(7-8), 745-749. https://doi.org/10.1016/S0146-6380(00)00081-4

Fletcher, W. J., and Zielhofer, C. (2013). Fragility of Western Mediterranean landscapes during Holocene rapid climate changes. *Catena*, 103, 16-29. https://doi.org/10.1016/j.catena.2011.05.001

Fletcher, W. J., Boski, T., & Moura, D. (2007). Palynological evidence for environmental and climatic change in the lower Guadiana valley, Portugal, during the last 13 000 years. *The Holocene*, 17(4), 481-494. https://doi.org/10.1177/0959683607077027

Freeman, K. H., and Colarusso, L. A. (2001). Molecular and isotopic records of C4 grassland expansion in the late Miocene. Geochimica et Cosmochimica Acta, 65(9), 1439-1454. https://doi.org/10.1016/S0016-7037(00)00573-1

Freimuth, E. J., Diefendorf, A. F., and Lowell, T. V. (2017). Hydrogen isotopes of *n*-alkanes and *n*-alkanoic acids as tracers of precipitation in a temperate forest and implications for paleorecords. *Geochimica et Cosmochimica Acta*, 206, 166-183. http://dx.doi.org/10.1016/j.gca.2017.02.027

Gabler, R. E., Petersen, J. F., Trapasso, L. M., and Sack, D. (2008). *Physical geography*. Cengage Learning.

Galvin, A. B., Ipavich, F. M., Gloeckler, G., Coplan, M., Hovestadt, D., Hilchenbach, M., ... and Balsiger, H. (1996). Solar Wind Composition: First Results from SOHO and Future Expectations. *Bulletin of the American Astronomical Society*, 28, 897.

García-Alix, A., Jiménez-Espejo, F. J., Toney, J. L., Jiménez-Moreno, G., Ramos-Román, M. J., Anderson, R. S., ... and Kuroda, J. (2017). Alpine bogs of southern Spain show human-induced environmental change superimposed on long-term natural variations. *Scientific reports*, 7(1), 1-12. https://doi.org/10.1038/s41598-017-07854-w

García-Alix, A., Camuera, J., Ramos-Román, M. J., Toney, J. L., Sachse, D., Schefuß, E., ... and Yanes, Y. (2021). Paleohydrological dynamics in the Western Mediterranean during the last glacial cycle. *Global and Planetary Change*, 103527. https://doi.org/10.1016/j.gloplacha.2021.103527

Garcin, Y., Schefuß, E., Schwab, V. F., Garreta, V., Gleixner, G., Vincens, A., ... and Sachse, D. (2014). Reconstructing C3 and C4 vegetation cover using n-alkane carbon isotope ratios in recent lake sediments from Cameroon, Western Central Africa. *Geochimica et Cosmochimica Acta*, 142, 482-500. https://doi.org/10.1016/j.gca.2014.07.004

Gelpi, E., Schneider, H., Mann, J., and Oro, J. (1970). Hydrocarbons of geochemical significance in microscopic algae. *Phytochemistry*, 9(3), 603-612.

Giménez, R., Bartolomé, M., Gázquez, F., Iglesias, M., and Moreno, A. (2021). Underlying climate controls in triple oxygen (16O, 17O, 18O) and hydrogen (1H, 2H) isotopes composition of rainfall (Central Pyrenees). *Frontiers in Earth Science*, 9, 209.

Gimeno, L., Nieto, R., Trigo, R. M., Vicente-Serrano, S. M., and López-Moreno, J. I. (2010). Where does the Iberian Peninsula moisture come from? An answer based on a Lagrangian approach. *Journal of Hydrometeorology*, 11(2), 421-436. https://doi.org/10.1175/2009JHM1182.1

Gomes, H., Loureiro, F., Cezar, L., Castro, E., and Vieira, G. (2019). Interpreting Late Pleistocene Paleoenvironments through the geosites of the Estrela Geopark, Central Portugal. *In International Meeting on Paleoclimate: change and adaptation*.

Gomes, S., Fletcher, W. J., Rodrigues, T., Stone, A., Abrantes, F., and Naughton, F. (2020). Time-transgressive Holocene maximum of temperate and Mediterranean forest development across the Iberian Peninsula reflects orbital forcing. *Palaeogeography, Palaeoclimatology, Palaeoecology*, 550, 109739 https://doi.org/10.1016/j.palaeo.2020.109739

Goñi, M. S., Cacho, I., Turon, J. L., Guiot, J., Sierro, F. J., Peypouquet, J. P., ... and Shackleton, N. J. (2002). Synchroneity between marine and terrestrial responses to millennial scale climatic variability during the last glacial period in the Mediterranean region. *Climate dynamics*, 19(1), 95-105. https://doi.org/10.1007/s00382-001-0212-x

Gornitz, V (eds.). (2009). *Encyclopedia of paleoclimatology and ancient environments*. Springer Netherlands. 978-1-4020-5197-5

Gough, D. O. (1977). *Theoretical predictions of variations in the solar output. In The solar output and its variation* (p. 451).

Gough, D. O. (1981). Solar interior structure and luminosity variations. *Physics of Solar Variations* (pp. 21-34). Springer, Dordrecht. http://doi.org/10.1007/978-94-010-9633-1_4

Gray, L. J., Beer, J., Geller, M., Haigh, J. D., Lockwood, M., Matthes, K., ... and Luterbacher, J. (2010). Solar influences on climate. *Reviews of Geophysics*, 48(4). https://doi.org/10.1029/2009RG000282

Gribbin, J., (1991). *Blinded by light, the secret life of the sun*: New York, Harmony books

Grotzinger, J. P., and Jordan, T. H. (2014). *Understanding Earth* (Seventh Ed). New York, NY 10010: W. H. Freeman and Company.

Hahn, A., Neumann, F. H., Miller, C., Finch, J., Frankland, T., Cawthra, H. C., ... and Zabel, M. (2021). Mid- to Late Holocene climatic and anthropogenic influences in Mpondoland, South Africa. *Quaternary Science Reviews*, 261, 106938. https://doi.org/10.1016/j.quascirev.2021.106938

Haigh, J. D. (1994). The role of stratospheric ozone in modulating the solar radiative forcing of climate. *Nature*, 370(6490), 544-546p.

Hall, A., and Stouffer, R. J. (2001). An abrupt climate event in a coupled ocean–atmosphere simulation without external forcing. *Nature*, 409(6817), 171-175. https://doi.org/10.1038/35051544

Haug, G. H., Hughen, K. A., Sigman, D. M., Peterson, L. C., and Röhl, U. (2001). Southward migration of the intertropical convergence zone through the Holocene. *Science*, 293(5533), 1304-1308. https://doi.org/10.1126/science.1059725

Hays, J. D., Imbrie, J., and Shackleton, N. J. (1976). Variations in the Earth's orbit: pacemaker of the ice ages. *Science*, 194(4270), 1121-1132.

Hedges, J. I., and Keil, R. G. (1995). Sedimentary organic matter preservation: an assessment and speculative synthesis. *Marine chemistry*, 49(2-3), 81-115. https://doi.org/10.1016/0304-4203(95)00008-F

Hernández, A., Leira, M., Trigo, R., Vázquez-Loureiro, D., Carballeira, R., and Sáez, A. (2017). The influences of the AMO and NAO on an Iberian alpine lake during the Late Holocene. In *EGU General Assembly Conference Abstracts* (Vol. 19, p. 13079).

Hernández, A., Martin-Puertas, C., Moffa-Sánchez, P., Moreno-Chamarro, E., Ortega, P., Blockley, S., ... and Xu, G. (2020b). Modes of climate variability: Synthesis and review of proxy-based reconstructions through the Holocene. *Earth-Science Reviews*, 103286. https://doi.org/10.1016/j.earscirev.2020.103286

Hernández, A., Sánchez-López, G., Pla-Rabes, S., Comas-Bru, L., Parnell, A., Cahill, N., ... and Giralt, S. (2020a). A 2,000-year Bayesian NAO reconstruction from the Iberian Peninsula. *Scientific reports*, 10(1), 1-15. https://doi.org/10.1038/s41598-020-71372-5

Hernández, A., Trigo, R. M., Pla-Rabes, S., Valero-Garcés, B. L., Jerez, S., Rico-Herrero, M., ... and Giralt, S. (2015). Sensitivity of two Iberian lakes to North Atlantic atmospheric circulation modes. *Climate dynamics*, 45(11-12), 3403-3417. https://doi.org/10.1007/s00382-015-2547-8

Hijma, M. P., and Cohen, K. M. (2010). Timing and magnitude of the sea-level jump preluding the 8200 yr event. *Geology*, 38(3), 275-278. https://doi.org/10.1130/G30439.1

Hockun, K., Mollenhauer, G., Ho, S. L., Hefter, J., Ohlendorf, C., Zolitschka, B., ... and Schefuß, E. (2016). Using distributions and stable isotopes of *n*-alkanes to disentangle organic matter contributions to sediments of Laguna Potrok Aike, Argentina. *Organic Geochemistry*, 102, 110-119. https://doi.org/10.1016/j.orggeochem.2016.10.001

Hodell, D. A., and Schelske, C. L. (1998). Production, sedimentation, and isotopic composition of organic matter in Lake Ontario. *Limnology and Oceanography*, 43(2), 200-214. https://doi.org/10.4319/lo.1998.43.2.0200

Hoefs, J., (2018). *Stable isotope geochemistry* (Vol. 285). Earth Sciences, Geography and Environment, Springer (2018). 374 p Berlin: Springer. https://doi.org/10.1007/978-3-319-78527-1

Hoffman, J. S., Carlson, A. E., Winsor, K., Klinkhammer, G. P., LeGrande, A. N., Andrews, J. T., and Strasser, J. C. (2012). Linking the 8.2 ka event and its freshwater forcing in the Labrador Sea. *Geophysical Research Letters*, 39(18). https://doi.org/10.1029/2012GL053047

Hoffmann, B., Kahmen, A., Cernusak, L. A., Arndt, S. K., and Sachse, D. (2013). Abundance and distribution of leaf wax n-alkanes in leaves of Acacia and Eucalyptus trees along a strong humidity gradient in northern Australia. *Organic Geochemistry*, 62, 62-67. https://doi.org/10.1016/j.orggeochem.2013.07.003

Holeman, J. N. (1968). The sediment yield of major rivers of the world. *Water resources research*, 4(4), 737-747. https://doi.org/10.1029/WR004i004p00737

Hou, J., D'Andrea, W. J., and Huang, Y. (2008). Can sedimentary leaf waxes record D/H ratios of continental precipitation? Field, model, and experimental assessments. *Geochimica et Cosmochimica Acta*, 72(14), 3503-3517. https://doi.org/10.1016/j.gca.2008.04.030

Hou, J., D'Andrea, W. J., MacDonald, D., and Huang, Y. (2007). Hydrogen isotopic variability in leaf waxes among terrestrial and aquatic plants around Blood Pond, Massachusetts (USA). *Organic Geochemistry*, 38(6), 977-984. https://doi.org/10.1016/j.orggeochem.2006.12.009

Houghton, J. T., Ding, Y. D. J. G., Griggs, D. J., Noguer, M., van der Linden, P. J., Dai, X., ... and Johnson, C. A. (eds.) (2001). [IPCC], *Climate change 2001: The Scientific Basis*. Cambridge University Press, Cambridge, United Kingdom and New York, NY, USA, 881pp.

Howard, S., F. A. McInerney, S. Caddy-Retalic, P. A. Hall, and J. W. Andrae. (2018). Modelling leaf wax n-alkane inputs to soils along a latitudinal transect across Australia. *Organic Geochemistry*, 121, 126-137. https://doi.org/10.1016/j.orggeochem.2018.03.013

IM, A. (2010). Iberian Climate Atlas, AIR TEMPERATURE AND PRECIPITATION (1971-2000). *Instituto de Meteorologia Portugês and Agencia Estatal de Meteorologia Española*, 978847837079-5.

IPCC, 2013: Climate Change 2013: *The Physical Science Basis.* Contribution of Working Group I to the Fifth Assessment Report of the Intergovernmental Panel on Climate Change, Cambridge University Press, Cambridge, United Kingdom and New York, NY, USA, 2013.

IPCC, 2021: Climate Change 2021*: The Physical Science Basis*. Contribution of Working Group I to the Sixth Assessment Report of the Intergovernmental Panel on Climate Change [Masson-Delmotte, V., P. Zhai, A. Pirani, S. L. Connors, C. Péan, S. Berger, N. Caud, Y. Chen, L. Goldfarb, M. I. Gomis, M. Huang, K. Leitzell, E. Lonnoy, J. B. R. Matthews, T. K. Maycock, T. Waterfield, O. Yelekçi, R. Yu and B. Zhou (eds.)]. Cambridge University Press. In Press.

Jalut, G., Dedoubat, J. J., Fontugne, M., and Otto, T. (2009). Holocene circum-Mediterranean vegetation changes: climate forcing and human impact. Quaternary international, 200(1-2), 4-18. https://doi.org/10.1016/j.quaint.2008.03.012

Jambrina-Enríquez, M., Rico, M., Moreno, A., Leira, M., Bernárdez, P., Prego, R., ... & Valero-Garcés, B. L. (2014). Timing of deglaciation and postglacial environmental dynamics in NW Iberia: the Sanabria Lake record. *Quaternary Science Reviews*, 94, 136-158. https://doi.org/10.1016/j.quascirev.2014.04.018

Jambrina-Enríquez, M., Sachse, D., and Valero-Garcés, B. L. (2016). A deglaciation and Holocene biomarker-based reconstruction of climate and environmental variability in NW Iberian Peninsula: the Sanabria Lake sequence. *Journal of paleolimnology*, 56(1), 49-66. https://doi.org/10.1007/s10933-016-9890-6

Jansen, B., and Wiesenberg, G. L. (2017). Opportunities and limitations related to the application of plant-derived lipid molecular proxies in soil science. *Soil*, 3(4), 211-234. https://doi.org/10.5194/soil-3-211-2017

Jansen, B., de Boer, E. J., Cleef, A. M., Hooghiemstra, H., Moscol-Olivera, M., Tonneijck, F. H., and Verstraten, J. M. (2013). Reconstruction of late Holocene forest dynamics in northern Ecuador from biomarkers and pollen in soil cores. *Palaeogeography, Palaeoclimatology, Palaeoecology*, 386, 607-619. https://doi.org/10.1016/j.palaeo.2013.06.027

Jansen, B., Nierop, K. G., Hageman, J. A., Cleef, A. M., and Verstraten, J. M. (2006). The straight-chain lipid biomarker composition of plant species responsible for the dominant biomass production along two altitudinal transects in the Ecuadorian Andes. *Organic Geochemistry*, 37(11), 1514-1536. https://doi.org/10.1016/j.orggeochem.2006.06.018

Jansen, E., Overpeck, J., Briffa, K. R., Duplessy, J. C., Joos, F., Masson-Delmotte, V., ... and Ramesh, R. (2007). Paleoclimate. Climate change 2007: the physical science basis; contribution of Working Group I to the Fourth Assessment Report of the Intergovernmental Panel on Climate Change (IPCC).

Jansen, J. (2011). Managing Natura 2000 in a Changing World: the Case of the Serra da Estrela, Portugal. PhD thesis, Radboud University.

Janssen, C., and Woldringh, R. (1981). A preliminary radiocarbon dated pollen sequence from the Serra da Estrela, Portugal. *Finisterra*, 16(32). https://doi.org/10.18055/Finis2176

Jetter, R., Kunst, L., and Samuels, A. L. (2008). *Composition of plant cuticular waxes. Biology of the plant cuticle*. Blackwell Publishing, Oxford. 23, 145-181. ISBN 9781405171571

Jiang, H., Eiríksson, J., Schulz, M., Knudsen, K. L., & Seidenkrantz, M. S. (2005). Evidence for solar forcing of sea-surface temperature on the North Icelandic Shelf during the late Holocene. *Geology*, 33(1), 73-76. https://doi.org/10.1130/G21130.1

Jiang, H., Feakins, S. J., Sun, H., Feng, X., Zhang, X., and Liu, X. (2020). Dynamic changes in leaf wax n-alkanes and δ13C during leaf development in winter wheat under varied irrigation experiments. *Organic Geochemistry*, 146, 104054. https://doi.org/10.1016/j.orggeochem.2020.104054

Jiménez-Moreno, G., García-Alix, A., Hernández-Corbalán, M. D., Anderson, R. S., & Delgado-Huertas, A. (2013). Vegetation, fire, climate and human disturbance history in the southwestern Mediterranean area during the late Holocene. *Quaternary research*, 79(2), 110-122. 110-122. doi:10.1016/j.yqres.2012.11.008

Jones, P. D., and Mann, M. E. (2004). Climate over past millennia. *Reviews of Geophysics*, 42(2). https://doi.org/10.1029/2003RG000143

Jones, P. D., Briffa, K. R., Osborn, T. J., Lough, J. M., van Ommen, T. D., Vinther, B. M., ... and Xoplaki, E. (2009). High-resolution palaeoclimatology of the last millennium: a review of current status and future prospects. *The Holocene*, 19(1), 3-49. https://doi.org/10.1177/0959683608098952

Julià Brugués, R., Luque Marín, J. A., Riera i Mora, S., and Alejandro, J. A. (2007). Climatic and land use changes in the NW of Iberian Peninsula recorded in a 1,500-year record from Lake Sanabria. *Contributions to Science*, 2008, vol. 3, num. 3, p. 355-369. https://doi.org/10.2436/20.7010.01.13

Kahmen, A., Hoffmann, B., Schefuß, E., Arndt, S. K., Cernusak, L. A., West, J. B., and Sachse, D. (2013). Leaf water deuterium enrichment shapes leaf wax n-alkane δD values of angiosperm plants II: Observational evidence and global implications. *Geochimica et Cosmochimica Acta*, 111, 50-63.

Kaufman, D. S., Ager, T. A., Anderson, N. J., Anderson, P. M., Andrews, J. T., Bartlein, P. J., ... and Dyke, A. S. (2004). Holocene thermal maximum in the western Arctic (0–180 W). *Quaternary Science Reviews*, 23(5-6), 529-560.https://doi.org/10.1016/j.quascirev.2003.09.007

Kaufman, D., McKay, N., Routson, C., Erb, M., Davis, B., Heiri, O., ... and Brussel, T. (2020). A global database of Holocene paleotemperature records. *Scientific data*, 7(1), 1-34. https://doi.org/10.1038/s41597-020-0445-3

Keigwin, L. D., and Lehman, S. J. (1994). Deep circulation change linked to Heinrich event 1 and Younger Dryas in a middepth North Atlantic core. *Paleoceanography*, 9(2), 185-194. https://doi.org/10.1029/94PA00032

Koch, J., and Clague, J. J. (2006). Are insolation and sunspot activity the primary drivers of global Holocene glacier fluctuations. *Pages Newsletter*, 14(3), 20-21.

Kolattukudy, P. E. (1980). Cutin, suberin, and waxes. In Lipids: structure and function (pp. 571-645). *Academic Press*. https://doi.org/10.1016/B978-0-12-675404-9.50024-2

Labeyrie, L., Skinner, L., Cortijo, E. (2007) Paleoclimate reconstructions. Sub-Milankovitch (DO/Heinrich) events. *Encyclopedia of Quaternary Sciences*, Elsevier, 1964-1974

Lamy, F., Kaiser, J., Arz, H. W., Hebbeln, D., Ninnemann, U., Timm, O., ... and Toggweiler, J. R. (2007). Modulation of the bipolar seesaw in the Southeast Pacific during Termination 1. *Earth and Planetary Science Letters*, 259(3-4), 400-413. https://doi.org/10.1016/j.epsl.2007.04.040

Landais, A., Masson-Delmotte, V., Stenni, B., Selmo, E., Roche, D. M., Jouzel, J., ... and Vinther, B. (2015). A review of the bipolar see–saw from synchronized and high resolution ice core water stable isotope records from Greenland and East Antarctica. Quaternary Science Reviews, 114, 18-32. https://doi.org/10.1016/j.quascirev.2015.01.031

Larsen, L. B., Vinther, B. M., Briffa, K. R., Melvin, T. M., Clausen, H. B., Jones, P. D., ... and Nicolussi, K. (2008). New ice core evidence for a volcanic cause of the AD 536 dust veil. *Geophysical Research Letters*, 35(4). https://doi.org/10.1029/2007GL032450

Lean, J. L. (2000). Short term, direct indices of solar variability. *Space Science Reviews*, 94(1-2), 39-51.

Lean, J. L. (2010). *Cycles and trends in solar irradiance and climate*. Wiley interdisciplinary reviews: climate change, 1(1), 111-122.

Lean, J. L., and Rind, D. H. (2008). How natural and anthropogenic influences alter global and regional surface temperatures: 1889 to 2006. *Geophysical Research Letters*, 35(18). https://doi.org/10.1029/2008GL034864

Lean, J., Beer, J., and Bradley, R. (1995). Reconstruction of solar irradiance since 1610: Implications for climate change. *Geophysical Research Letters*, 22(23), 3195-3198.

Leider, A., Hinrichs, K. U., Schefuß, E., and Versteegh, G. J. (2013). Distribution and stable isotopes of plant wax derived n-alkanes in lacustrine, fluvial and marine surface sediments along an Eastern Italian transect and their potential to reconstruct the hydrological cycle. *Geochimica et Cosmochimica Acta*, 117, 16-32. https://doi.org/10.1016/j.gca.2013.04.018

Leng, M. J., Lamb, A. L., Heaton, T. H., Marshall, j. D., Wolfe, B. B., Jones, M. D., ... and Arrowsmith, C. (2006). Isotopes in lake sediments. *In Isotopes in palaeoenvironmental research* (pp. 147-184). Springer, Dordrecht. https://doi.org/10.1007/1-4020-2504-1_04

Li, C., Ma, S., Xia, Y., He, X., Gao, W., and Zhang, G. (2020a). Assessment of the relationship between ACL/CPI values of long chain *n*-alkanes and climate for the application of paleoclimate over the Tibetan Plateau. *Quaternary International*. https://doi.org/10.1016/j.quaint.2020.02.028

Li, H., Cheng, H., Sinha, A., Kathayat, G., Spötl, C., André, A. A., ... and Edwards, R. L. (2018). Hydro-climatic variability in the southwestern Indian Ocean between 6000 and 3000 years ago. *Climate of the Past*, 14(12). http://doi.org/10.5194/cp-14-1881-2018

Li, Z., Sun, Y., and Nie, X. (2020b). Biomarkers as a soil organic carbon tracer of sediment: Recent advances and challenges. *Earth-Science Reviews*, 103277. https://doi.org/10.1016/j.earscirev.2020.103277

Lionello, P., Abrantes, F., Congedi, L., Dulac, F., Gacic, M., Gomis, D., ... and Xoplaki, E. (2012). Introduction: mediterranean climate—background information. In The climate of the Mediterranean region: *From the past to the future* (pp. xxxv-xc). Elsevier Inc.. https://doi.org/10.1016/B978-0-12-416042-2.00012-4

Lisiecki, L. E., and Raymo, M. E. (2005). A Pliocene-Pleistocene stack of 57 globally distributed benthic δ18O records. *Paleoceanography*, 20(1).

Lockwood, M. (2001). Long-term variations in the magnetic fields of the Sun and the heliosphere: Their origin, effects, and implications. *Journal of Geophysical Research: Space Physics*, 106(A8), 16021-16038. https://doi.org/10.1029/2000JA000115

Logan, G. A., Smiley, C. J., and Eglinton, G. (1995). Preservation of fossil leaf waxes in association with their source tissues, Clarkia, northern Idaho, USA. *Geochimica et Cosmochimica Acta*, 59(4), 751-763. https://doi.org/10.1016/0016-7037(94)00362-P

López-Avilés, A., García-Alix, A., Jiménez-Moreno, G., Anderson, R. S., Toney, J. L., Mesa-Fernández, J. M., and Jiménez-Espejo, F. J. (2021). Latest Holocene paleoenvironmental and paleoclimate reconstruction from an alpine bog in the Western Mediterranean region: The Borreguil de los Lavaderos de la Reina record (Sierra Nevada). *Palaeogeography, Palaeoclimatology, Palaeoecology*, 573, 110434. https://doi.org/10.1016/j.palaeo.2021.110434

López-Moreno, J. I., Vicente-Serrano, S. M., Morán-Tejeda, E., Lorenzo-Lacruz, J., Kenawy, A., and Beniston, M. (2011). Effects of the North Atlantic Oscillation (NAO) on combined temperature and precipitation winter modes in the Mediterranean mountains: Observed relationships and projections for the 21st century. *Global and Planetary Change*, 77(1-2), 62-76. https://doi.org/10.1016/j.gloplacha.2011.03.003

Luo, P., Peng, P., Lü, H., Zheng, Z., and Wang, X. (2012). Latitudinal variations of CPI values of long-chain n-alkanes in surface soils: Evidence for CPI as a proxy of aridity. *Science China Earth Sciences*, 55(7), 1134-1146. https://doi.org/10.1007/s11430-012-4401-8

Luterbacher, J., Rickli, R., Xoplaki, E., Tinguely, C., Beck, C., Pfister, C., and Wanner, H. (2001). The late Maunder minimum (1675–1715)–a key period forstudying decadal scale climatic change in Europe. *Climatic Change*, 49(4), 441-462. https://doi.org/10.1023/A:1010667524422

Mabit, L., Gibbs, M., Mbaye, M., Meusburger, K., Toloza, A., Resch, C., ... and Alewell, C. (2018). Novel application of Compound Specific Stable Isotope (CSSI) techniques to investigate on-site sediment origins across arable fields. *Geoderma*, 316, 19-26. https://doi.org/10.1016/j.geoderma.2017.12.008

Maffei, M. (1996). Chemotaxonomic significance of leaf wax alkanes in the Gramineae. *Biochemical systematics and ecology*, 24(1), 53-64. https://doi.org/10.1016/0305-1978(95)00102-6

Magny, M., Combourieu-Nebout, N., De Beaulieu, J. L., Bout-Roumazeilles, V., Colombaroli, D., Desprat, S., ... and Peyron, O. (2013). *North-south palaeohydrological contrasts in the central Mediterranean during the Holocene*: tentative synthesis and working hypotheses. https://doi:10.5194/cp-9-2043-2013

Maioli, O. L., Rodrigues, K. C., Knoppers, B. A., and Azevedo, D. A. (2010). Pollution source evaluation using petroleum and aliphatic hydrocarbons in surface sediments from two Brazilian estuarine systems. *Organic Geochemistry*, 41(9), 966-970. https://doi.org/10.1016/j.orggeochem.2010.03.013

Mann, C. J., and Wetzel, R. G. (1999). Photosynthesis and stomatal conductance of Juncus effusus in a temperate wetland ecosystem. *Aquatic Botany*, 63(2), 127-144. https://doi.org/10.1016/S0304-3770(98)00111-9

Mann, M. E., Zhang, Z., Rutherford, S., Bradley, R. S., Hughes, M. K., Shindell, D., … Ni, F. (2009). Global Signatures and Dynamical Origins of the Little Ice Age and Medieval Climate Anomaly. *Science*, 326(5957), 1256–1260. https://doi.org/10.1126/science.1177303

Marques, J. E., Marques, J. M., Chaminé, H. I., Afonso, M. J., Carreira, P. M., Fonseca, P. E., ... and Gomes, A. (2005). *Hydrogeological study of a high mountain area (Serra da Estrela, Central Portugal): a multidisciplinary approach*. ISSN: 0213-4497

Martín-Chivelet, J., Muñoz-García, M. B., Edwards, R. L., Turrero, M. J., & Ortega, A. I. (2011). Land surface temperature changes in Northern Iberia since 4000 yr BP, based on δ13C of speleothems. *Global and Planetary Change*, 77(1-2), 1-12. https://doi.org/10.1016/j.gloplacha.2011.02.002

Martín-Chivelet, J., Muñoz-García, M. B., Edwards, R. L., Turrero, M. J., & Ortega, A. I. (2011). Land surface temperature changes in Northern Iberia since 4000 yr BP, based on δ13C of speleothems. *Global and Planetary Change*, 77(1-2), 1-12. https://doi.org/10.1016/j.gloplacha.2011.02.002

Martín-Puertas, C., Matthes, K., Brauer, A., Muscheler, R., Hansen, F., Petrick, C., ... and Van Geel, B. (2012). Regional atmospheric circulation shifts induced by a grand solar minimum. *Nature Geoscience*, 5(6), 397-401. https://doi.org/10.1038/ngeo1460

Martín-Puertas, C., Valero-Garcés, B. L., Brauer, A., Mata, M. P., Delgado-Huertas, A., & Dulski, P. (2009). The Iberian–Roman Humid Period (2600–1600 cal yr BP) in the Zoñar Lake varve record (Andalucía, southern Spain). *Quaternary Research*, 71(2), 108-120. https://doi.org/10.1016/j.yqres.2008.10.004

Martín-Puertas, C., Valero-Garcés, B. L., Pilar Mata, M., González-Sampériz, P., Bao, R., Moreno, A., & Stefanova, V. (2008). Arid and humid phases in southern Spain during the last 4000 years: the Zonar Lake record, Cordoba. The Holocene, 18(6), 907-921. https://doi.org/10.1177/0959683608093533

Martín-Puertas, C., Valero-Garcés, B. L., Pilar Mata, M., González-Sampériz, P., Bao, R., Moreno, A., and Stefanova, V. (2008). Arid and humid phases in southern Spain during the last 4000 years: the Zonar Lake record, Cordoba. *The Holocene*, 18(6), 907-921. https://doi.org/10.1177/0959683608093533

Masson-Delmotte, V. and Schulz, M. and Abe-Ouchi, A. and Beer, J. and Ganopolski, J. and González Rouco, J. F. and Jansen, E. and Lambeck, K. and Luterbacher, J. and Naish, T. and Osborn, T. and Otto-Bliesner, B. and Quinn, T. and Ramesh, R. and Rojas, M., A. (2013). Information from paleoclimate archives. In P. M. Stocker, T. F. and Qin, D. and Plattner, G.-K. and Tignor, M. and Allen, S. K. and Doschung, J. and Nauels, A. and Xia, Y. and Bex, V. and Midgley (Ed.), [IPCC] *Climate Change 2013 the Physical Science Basis*: Working Group I Contribution to the Fifth Assessment Report of the Intergovernmental Panel on Climate Change (Vol. 9781107057, 383–464). https://doi.org/10.1017/CBO9781107415324.013

Mauri, A., Davis, B. A. S., Collins, P. M., and Kaplan, J. O. (2015). The climate of Europe during the Holocene: a gridded pollen-based reconstruction and its multi-proxy evaluation. *Quaternary Science Reviews*, 112, 109-127. https://doi.org/10.1016/j.quascirev.2015.01.013

Mayewski, P.A., Rohling, E.E., Stager, J.C., et al. (2004). Holocene climate variability. *Quaternary Research* 62, 243–255. https://doi.org/10.1016/j.yqres.2004.07.001

McManus JF, Francois R, Gherardi J-M, Keigwin LD, Brown-Leger S (2004). Collapse and rapid resumption of Atlantic meridional circulation linked to deglacial climate changes. *Nature*, 428, 834–837. https://doi.org/10.1038/nature02494

Meyers, P. A. (1997). Organic geochemical proxies of paleoceanographic, paleolimnologic, and paleoclimatic processes. *Organic geochemistry*, 27(5-6), 213-250. https://doi.org/10.1016/S0146-6380(97)00049-1

Meyers, P. A. (2003). Applications of organic geochemistry to paleolimnological reconstructions: a summary of examples from the Laurentian Great Lakes. *Organic geochemistry*, 34(2), 261-289. https://doi.org/10.1016/S0146-6380(02)00168-7

Meyers, P. A., and Ishiwatari, R. (1993). Lacustrine organic geochemistry—an overview of indicators of organic matter sources and diagenesis in lake sediments. *Organic geochemistry*, 20(7), 867-900. https://doi.org/10.1016/0146-6380(93)90100-P

Milankovitch. M. (1941). Kanon der Erdbestrahlung une sei Eiszeitenproblem. Acad. R. Serbe (Belegrade), ed. Spec. 133 Sect. *Sci. Math. Naturaies*. 633. (translated by the Israel Program for Scientific Translations. Jerusalem, 1970).

Miller, G. H., Brigham-Grette, J., Alley, R. B., Anderson, L., Bauch, H. A., Douglas, M. S. V., ... and Funder, S. V. (2010). Temperature and precipitation history of the Arctic. *Quaternary Science Reviews*, 29(15-16), 1679-1715.https://doi.org/10.1016/j.quascirev.2010.03.001

Miller, G. H., Geirsdóttir, Á., Zhong, Y., Larsen, D. J., Otto-Bliesner, B. L., Holland, M. M., ... and Thordarson, T. (2012). Abrupt onset of the Little Ice Age triggered by volcanism and sustained by sea-ice/ocean feedbacks. *Geophysical Research Letters*, 39(2). https://doi.org/10.1029/2011GL050168

Morellón, M., Aranbarri, J., Moreno, A., González-Sampériz, P., and Valero-Garcés, B. L. (2018). Early Holocene humidity patterns in the Iberian Peninsula reconstructed from lake, pollen and speleothem records. *Quaternary Science Reviews*, 181, 1-18. https://doi.org/10.1016/j.quascirev.2017.11.016

Morellón, M., Pérez-Sanz, A., Corella, J. P., Büntgen, U., Catalán, J., González-Sampériz, P., ... and Valero-Garcés, B. (2012). A multi-proxy perspective on millennium-long climate variability in the Southern Pyrenees. *Climate of the Past*, 8(2), 683-700. https://doi.org/10.5194/cp-8-683-2012

Morellón, M., Valero-Garcés, B., González-Sampériz, P., Vegas-Vilarrúbia, T., Rubio, E., Rieradevall, M., ... and Soto, J. (2011). Climate changes and human activities recorded in the sediments of Lake Estanya (NE Spain) during the Medieval Warm Period and Little Ice Age. *Journal of Paleolimnology*, 46(3), 423-452. https://doi.org/10.1007/s10933-009-9346-3

Moreno, A., González-Sampériz, P., Morellón, M., Valero-Garcés, B. L., and Fletcher, W. J. (2012a). Northern Iberian abrupt climate change dynamics during the last glacial cycle: a view from lacustrine sediments. *Quaternary Science Reviews*, 36, 139-153. https://doi.org/10.1016/j.quascirev.2010.06.031

Moreno, A., Pérez, A., Frigola, J., Nieto-Moreno, V., Rodrigo-Gámiz, M., Martrat, B., ... and Belmonte, Á. (2012b). The Medieval Climate Anomaly in the Iberian Peninsula reconstructed from marine and lake records. *Quaternary Science Reviews*, 43, 16-32. https://doi.org/10.1016/j.quascirev.2012.04.007

Moreno, A., Svensson, A., Brooks, S. J., Connor, S., Engels, S., Fletcher, W., ... and Peyron, O. (2014a). A compilation of Western European terrestrial records 60–8 ka BP: towards an understanding of latitudinal climatic gradients. *Quaternary Science Reviews*, 106, 167-185. https://doi.org/10.1016/j.quascirev.2014.06.030

Moreno, J. (2017). *Reconstituição Paleoclimática e Paleoambiental em Estuários com Base no Registo Micropaleontológico de Foraminíferos: Relação com Indicadores de Escala Local, Regional e Global*. Ph.D. Thesis. University of Lisbon.

Moreno, J., Fatela, F., Leorri, E., José, M., Pereira, I., Araújo, M. F., ... and Medeiros, A. (2014b). Marsh benthic Foraminifera response to estuarine hydrological balance driven by climate variability over the last 2000 yr (Minho estuary, NW Portugal). *Quaternary Research*, 82(2), 318-330. http://doi.org/10.1016/j.yqres.2014.04.014

Morgado, D. M. G. (2013). Pastoreio em Manteigas: transumância no passado e no presente. Master dissertation. University of Coimbra.

Morice, C. P., Kennedy, J. J., Rayner, N. A., and Jones, P. D. (2012). Quantifying uncertainties in global and regional temperature change using an ensemble of observational estimates: The HadCRUT4 data set. *Journal of Geophysical Research: Atmospheres*, 117(D8). https://doi.org/10.1029/2011JD017187

Morley, A., Schulz, M., Rosenthal, Y., Mulitza, S., Paul, A., and Rühlemann, C. (2011). Solar modulation of North Atlantic central Water formation at multidecadal timescales during the late Holocene. *Earth and Planetary Science Letters*, 308(1-2), 161-171. https://doi.org/10.1016/j.epsl.2011.05.043

Mügler, I. (2008a). Palaeoclimate Reconstruction Using Compound-specific Hydrogene Isotope Ratios of n-Alkanes. Ph. D. thesis, Friedrich Schiller University Jena. https://www.db-thueringen.de/receive/dbt_mods_00011372.

Mügler, I., Gleixner, G., Günther, F., Mäusbacher, R., Daut, G., Schütt, B., ... and Yi, C. (2010). A multi-proxy approach to reconstruct hydrological changes and Holocene climate development of Nam Co, Central Tibet. *Journal of Paleolimnology*, 43(4), 625-648. https://doi.org/10.1007/s10933-009-9357-0

Mügler, I., Sachse, D., Werner, M., Xu, B., Wu, G., Yao, T., and Gleixner, G. (2008b). Effect of lake evaporation on δD values of lacustrine n-alkanes: A comparison of Nam Co (Tibetan Plateau) and Holzmaar (Germany). *Organic Geochemistry*, 39(6), 711-729. https://doi.org/10.1016/j.orggeochem.2008.02.008

Naughton, F., Costas, S., Gomes, S. D., Desprat, S., Rodrigues, T., Goñi, M. S., ... and Salgueiro, E. (2019). Coupled ocean and atmospheric changes during Greenland stadial 1 in southwestern Europe. *Quaternary Science Reviews*, 212, 108-120. https://doi.org/10.1016/j.quascirev.2019.03.033

Niedermeyer, E. M., Schefuß, E., Sessions, A. L., Mulitza, S., Mollenhauer, G., Schulz, M., and Wefer, G. (2010). Orbital-and millennial-scale changes in the hydrologic cycle and vegetation in the western African Sahel: insights from individual plant wax δD and δ13C. *Quaternary Science Reviews*, 29(23-24), 2996-3005. https://doi.org/10.1016/j.quascirev.2010.06.039

Nieuwendam A, Vieira G, Schaefer C, Woronko B, Johansson M (2020). Reconstructing cold climate paleoenvironments from micromorphological analysis of relict slope deposits (Serra da Estrela, Central Portugal). *Permafrost Periglac Process* (accepted)

Norström, E., Katrantsiotis, C., Smittenberg, R. H., & Kouli, K. (2017). Chemotaxonomy in some Mediterranean plants and implications for fossil biomarker records. *Geochimica et Cosmochimica* Acta, 219, 96-110. https://doi.org/10.1016/j.gca.2017.09.029

Ogurtsov, M. G., Nagovitsyn, Y. A., Kocharov, G. E., and Jungner, H. (2002). Long-period cycles of the Sun's activity recorded in direct solar data and proxies. *Solar Physics*, 211(1-2), 371-394. http://dx.doi.org/10.1023/A:1022411209257

Oldfield, F., and Alverson, K. (2003). The societal relevance of paleoenvironmental research. *Paleoclimate, global change and the future* (pp. 1-11). Springer, Berlin, Heidelberg. http://doi.org/10.1007/978-3-642-55828-3_1

Oliva, M., Ruiz-Fernández, J., Barriendos, M., Benito, G., Cuadrat, J. M., Domínguez-Castro, F., ... and López-Costas, O. (2018a). The little ice age in Iberian mountains. *Earth-Science Reviews*, 177, 175-208. https://doi.org/10.1016/j.earscirev.2017.11.010

Oliveira, A., C. and Lima, A. S. (2010). Spatial variability in the stable isotopes of modern precipitation in the northwest of Iberia. *Isotopes in environmental and health studies*, 46(1), 13-26. https://doi.org/10.1080/10256010903388154

Ortiz, J. E., Díaz-Bautista, A., Aldasoro, J. J., Torres, T., Gallego, J. L. R., Moreno, L., & Estébanez, B. (2011). n-Alkan-2-ones in peat-forming plants from the Roñanzas ombrotrophic bog (Asturias, northern Spain). *Organic Geochemistry*, 42(6), 586-592. https://doi.org/10.1016/j.orggeochem.2011.04.009

Ortiz, J. E., Moreno, L., Torres, T., Vegas, J., Ruiz-Zapata, B., García-Cortés, Á., ... and Pérez-González, A. (2013). A 220 ka palaeoenvironmental reconstruction of the Fuentillejo maar lake record (Central Spain) using biomarker analysis. *Organic Geochemistry*, 55, 85-97. https://doi.org/10.1016/j.orggeochem.2012.11.012

Ortiz, J. E., Torres, T., Delgado, A., Llamas, J. F., Soler, V., Valle, M., ... and Díaz-Bautista, A. (2010). Palaeoenvironmental changes in the Padul Basin (Granada, Spain) over the last 1 Ma based on the biomarker content. *Palaeogeography, Palaeoclimatology, Palaeoecology*, 298(3-4), 286-299. https://doi.org/10.1016/j.palaeo.2010.10.003

Ortiz, J. E., Torres, T., Delgado, A., Valle, M., Soler, V., Araujo, R., ... and Vega-Panizo, R. (2021). Bulk and compound-specific δ13C and n-alkane indices in a palustrine intermontane record for assessing environmental changes over the past 320 ka: the Padul Basin (Southwestern Mediterranean realm). *Journal of Iberian Geology*, 1-15. https://doi.org/10.1007/s41513-021-00175-y

Owens, M. J., Lockwood, M., Hawkins, E., Usoskin, I., Jones, G. S., Barnard, L., ... and Fasullo, J. (2017). The Maunder minimum and the Little Ice Age: an update from recent reconstructions and climate simulations. *Journal of Space Weather and Space Climate*, 7, A33. https://doi.org/10.1051/swsc/2017034

Pancost, R. D., and Boot, C. S. (2004). The palaeoclimatic utility of terrestrial biomarkers in marine sediments. *Marine Chemistry*, 92(1-4), 239-261. https://doi.org/10.1016/j.marchem.2004.06.029

Pancost, R. D., Baas, M., van Geel, B., and Damsté, J. S. S. (2002). Biomarkers as proxies for plant inputs to peats: an example from a sub-boreal ombrotrophic bog. *Organic geochemistry*, 33(7), 675-690. https://doi.org/10.1016/S0146-6380(02)00048-7

Park, J., Park, J., Yi, S., Kim, J. C., Lee, E., and Choi, J. (2019). Abrupt Holocene climate shifts in coastal East Asia, including the 8.2 ka, 4.2 ka, and 2.8 ka BP events, and societal responses on the Korean peninsula. *Scientific reports*, 9(1), 1-16. http://doi.org/10.1038/s41598-019-47264-8

Park, M. O. (2005). New pathway for long-chain n-alkane synthesis via 1-alcohol in Vibrio furnissii M1. *Journal of bacteriology*, 187(4), 1426-1429. https://doi.org/10.1128/JB.187.4.1426–1429.2005

Pedro, J. B., Jochum, M., Buizert, C., He, F., Barker, S., and Rasmussen, S. O. (2018). Beyond the bipolar seesaw: Toward a process understanding of interhemispheric coupling. *Quaternary Science Reviews*, 192, 27-46.

Pérez-Brunius, P., Rossby, T., and Watts, D. R. (2004). Absolute transports of mass and temperature for the North Atlantic Current–subpolar front system. *Journal of physical oceanography*, 34(8), 1870-1883. https://doi.org/10.1175/1520-0485(2004)034<1870:ATOMAT>2.0.CO;2

Pérez-Obiol, R., Jalut, G., Julià, R., Pèlachs, A., Iriarte, M. J., Otto, T., and Hernández-Beloqui, B. (2011). Mid-Holocene vegetation and climatic history of the Iberian Peninsula. *The Holocene*, 21(1), 75-93. https://doi.org/10.1177/0959683610384161

Peters, K. E., Peters, K. E., Walters, C. C., and Moldowan, J. M. (2005). *The biomarker guide* (Vol. 1). Cambridge University Press. ISBN: 0521781582, 9780521781589

Polissar, P. J., Abbott, M. B., Wolfe, A. P., Vuille, M., and Bezada, M. (2013). Synchronous interhemispheric Holocene climate trends in the tropical Andes. *Proceedings of the National Academy of Sciences,* 110(36), 14551-14556. https://doi.org/10.1073/pnas.1219681110

Porter, S. C. (1981). *Climate and History: Glaciological evidence of Holocene climatic change*, Cambridge, Cambridge University Press, 82–110.

Post-Beittenmiller, D. (1996). Biochemistry and molecular biology of wax production in plants. *Annual review of plant biology*, 47(1), 405-430.

Poynter, J. G. (1989). Molecular stratigraphy: The recognition of palaeoclimatic signals in organic geochemical data. Ph.D. thesis, School of Chemistry, University of Bristol, Bristol.

Pyrina, M., Moreno-Chamarro, E., Wagner, S., and Zorita, E. (2019). Spatial signature of solar forcing over the North Atlantic Summer Climate in the past millennium. *Earth System Dynamics Discussions*, 1-24. https://doi.org/10.5194/esd-2019-50

Rach, O., Brauer, A., Wilkes, H., and Sachse, D. (2014). Delayed hydrological response to Greenland cooling at the onset of the Younger Dryas in western Europe. *Nature Geoscience*, 7(2), 109-112. https://doi.org/10.1038/ngeo2053

Rahmstorf, S. (2003). Thermohaline circulation: The current climate. *Nature*, 421(6924), 699-699.

Rahmstorf, S. (2006). Thermohaline ocean circulation. *Encyclopedia of quaternary sciences*, 5.

Ramos, A. M., Trigo, R. M., Liberato, M. L., and Tomé, R. (2015). Daily precipitation extreme events in the Iberian Peninsula and its association with atmospheric rivers. *Journal of Hydrometeorology*, 16(2), 579-597. https://doi.org/10.1175/JHM-D-14-0103.1

Rampino, M. R., Self, S., and Stothers, R. B. (1988). Volcanic winters. *Annual Review of Earth and Planetary Science*s, 16, 73-99.

Rasmussen, S. O., Andersen, K. K., Svensson, A. M., Steffensen, J. P., Vinther, B. M., Clausen, H. B., ... and Bigler, M. (2006). A new Greenland ice core chronology for the last glacial termination. *Journal of Geophysical Research*: Atmospheres, 111(D6). https://doi.org/10.1029/2005JD006079

Rasmussen, S. O., Bigler, M., Blockley, S. P., Blunier, T., Buchardt, S. L., Clausen, H. B., ... and Gkinis, V. (2014). A stratigraphic framework for abrupt climatic changes during the Last Glacial period based on three synchronized Greenland ice-core records: refining and extending the INTIMATE event stratigraphy. *Quaternary Science Reviews*, 106, 14-28. https://doi.org/10.1016/j.quascirev.2014.09.007

Reimer, P. J., Austin, W. E., Bard, E., Bayliss, A., Blackwell, P. G., Ramsey, C. B., ... and Talamo, S. (2020). The IntCal20 Northern Hemisphere radiocarbon age calibration curve (0–55 cal kBP). *Radiocarbon*, 62(4), 725-757. https://doi.org/10.1017/RDC.2020.41

Renssen, H., Goosse, H., and Fichefet, T. (2007). Simulation of Holocene cooling events in a coupled climate model. *Quaternary Science Reviews*, 26(15-16), 2019-2029. https://doi.org/10.1016/j.quascirev.2007.07.011

Ribeiro, A., Kullberg, M. C., Kullberg, J. C., Manuppella, G., and Phipps, S. (1990). A review of Alpine tectonics in Portugal: foreland detachment in basement and cover rocks. *Tectonophysics*, 184(3-4), 357-366. https://doi.org/10.1016/0040-1951(90)90448-H

Rivas-Martínez, S. (2011). *Mapa de series, geoseries y geopermaseries de vegetación de España*. Asociacion Española de Fitosociologia (AEFA).

Roberts, N., Brayshaw, D., Kuzucuoğlu, C., Perez, R., and Sadori, L. (2011). The mid-Holocene climatic transition in the Mediterranean: causes and consequences. *The Holocene*, 21(1), 3-13. https://doi.org/10.1177/0959683610388058

Rodrigues, T., Grimalt, J. O., Abrantes, F. G., Flores, J. A., and Lebreiro, S. M. (2009). Holocene interdependences of changes in sea surface temperature, productivity, and fluvial inputs in the Iberian continental shelf (Tagus mud patch). *Geochemistry, Geophysics, Geosystems*, 10(7). https://doi.org/10.1029/2008GC002367

Rogers, J. C. (1997). North Atlantic storm track variability and its association to the North Atlantic Oscillation and climate variability of northern Europe. *Journal of Climate*, 10(7), 1635-1647. https://doi.org/10.1175/1520-0442(1997)010<1635:NASTVA>2.0.CO;2

Rohling, E. J., and Pälike, H. (2005). Centennial-scale climate cooling with a sudden cold event around 8,200 years ago. *Nature*, 434(7036), 975-979. https://doi.org/10.1038/nature03421

Romariz, C. (1950). Contribuição da análise polínica no estudo da vegetação primitiva da Serra da Estrela. Comptes Rendus do Congrès Internacional de Géographie. Lisbonne 1949. Tome II, *Travaux des Sections II et III*, 824-830.

Rommerskirchen, F., Eglinton, G., Dupont, L., and Rullkötter, J. (2006a). Glacial/interglacial changes in southern Africa: Compound-specific δ13C land plant biomarker and pollen records from southeast Atlantic continental margin sediments. *Geochemistry, Geophysics, Geosystems*, 7(8). https://doi.org/10.1029/2005GC001223

Rommerskirchen, F., Plader, A., Eglinton, G., Chikaraishi, Y., and Rullkötter, J. (2006b). Chemotaxonomic significance of distribution and stable carbon isotopic composition of long-chain alkanes and alkan-1-ols in C4 grass waxes. *Organic Geochemistry*, 37(10), 1303-1332. https://doi.org/10.1016/j.orggeochem.2005.12.013

Ruddiman, W. F. (2013). *Earth's climate: past and future* (3rd Editio). New York: W. H. Freeman and Company.

Ruddiman, W. F., and McIntyre, A. (1981). The mode and mechanism of the last deglaciation: oceanic evidence. *Quaternary Research*, 16(2), 125-134.

Sachs, J. P., Pahnke, K., Smittenberg, R. and Zhang, Z (2013). *Biomarker Indicators of Past Climate. Encyclopedia of Quaternary Science* 2nd edn (eds Elias, S., Mock C.) 775–779 (Elsevier Science, 2013). ISBN: 978-0-444-53642-6

Sachse, D., Billault, I., Bowen, G. J., Chikaraishi, Y., Dawson, T. E., Feakins, S. J., ... and Polissar, P. (2012). Molecular paleohydrology: interpreting the hydrogen-isotopic composition of lipid biomarkers from photosynthesizing organisms. *Annual Review of Earth and Planetary Sciences*, 40, 221-249. https://doi.org/10.1146/annurev-earth-042711-105535

Sachse, D., Radke, J., and Gleixner, G. (2004). Hydrogen isotope ratios of recent lacustrine sedimentary *n*-alkanes record modern climate variability. *Geochimica et Cosmochimica Act*a, 68(23), 4877-4889. https://doi.org/10.1016/j.gca.2004.06.004

Sachse, D., Radke, J., and Gleixner, G. (2006). δD values of individual n-alkanes from terrestrial plants along a climatic gradient–Implications for the sedimentary biomarker record. *Organic Geochemistry*, 37(4), 469-483. https://doi.org/10.1016/j.orggeochem.2005.12.003

Sánchez-López, G., Hernández, A., Pla-Rabès, S., Trigo, R. M., Toro, M., Granados, I., ... and Giralt, S. (2016). Climate reconstruction for the last two millennia in central Iberia: The role of East Atlantic (EA), North Atlantic Oscillation (NAO) and their interplay over the Iberian Peninsula. *Quaternary science reviews*, 149, 135-150. https://doi.org/10.1016/j.quascirev.2016.07.021

Schäfer, I. K., Bliedtner, M., Wolf, D., Kolb, T., Zech, J., Faust, D., and Zech, R. (2018). A δ13C and δ2H leaf wax record from the Late Quaternary loess-paleosoil sequence El Paraíso, Central Spain. *Palaeogeography, Palaeoclimatology, Palaeoecology*, 507, 52-59. https://doi.org/10.1016/j.palaeo.2018.06.039

Schäfer, I. K., Lanny, V., Franke, J., Eglinton, T. I., Zech, M., Vysloužilová, B., and Zech, R. (2016). Leaf waxes in litter and topsoils along a European transect. *Soil*, 2(4), 551-564. doi:10.5194/soil-2-551-2016

Schefuß, E., Ratmeyer, V., Stuut, J. B. W., Jansen, J. F., and Damsté, J. S. S. (2003). Carbon isotope analyses of n-alkanes in dust from the lower atmosphere over the central eastern Atlantic. *Geochimica et Cosmochimica Acta*, 67(10), 1757-1767. https://doi.org/10.1016/S0016-7037(02)01414-X

Schimmelmann, A., Sessions, A. L., and Mastalerz, M. (2006). Hydrogen isotopic (D/H) composition of organic matter during diagenesis and thermal maturation. *Annu. Rev. Earth Planet. Sci*., 34, 501-533. https://doi.org/10.1146/annurev.earth.34.031405.125011

Schirrmacher, J., Andersen, N., Schneider, R. R., and Weinelt, M. (2020). Fossil leaf wax hydrogen isotopes reveal variability of Atlantic and Mediterranean climate forcing on the southeast Iberian Peninsula between 6000 to 3000 cal. BP. *PLoS One*, 15(12), e0243662. https://doi.org/10.1371/journal.pone.0243662

Schirrmacher, J., Weinelt, M., Blanz, T., Andersen, N., Salgueiro, E., and Schneider, R. R. (2019). Multi-decadal atmospheric and marine climate variability in southern Iberia during the mid-to late-Holocene. *Climate of the Past*, 15(2), 617-634. https://doi.org/10.5194/cp-15-617-2019

Schouten, S., Hopmans, E. C., and Damsté, J. S. S. (2013). The organic geochemistry of glycerol dialkyl glycerol tetraether lipids: a review. *Organic geochemistry*, 54, 19-61. https://doi.org/10.1016/j.orggeochem.2012.09.006

Sessions, A. L., Burgoyne, T. W., Schimmelmann, A., and Hayes, J. M. (1999). Fractionation of hydrogen isotopes in lipid biosynthesis. *Organic Geochemistry*, 30(9), 1193-1200. https://doi.org/10.1016/S0146-6380(99)00094-7

Sessions, A. L., Sylva, S. P., Summons, R. E., and Hayes, J. M. (2004). Isotopic exchange of carbon-bound hydrogen over geologic timescales. *Geochimica et Cosmochimica Acta*, 68(7), 1545-1559. https://doi.org/10.1016/j.gca.2003.06.004

Severinghaus, J. P., et al. (2003), A method for precise measurement of argon 40/36 and krypton/argon ratios in trapped air in polar ice with applications to past firn thickness and abrupt climate change in Greenland and at Siple Dome, Antarctica, *Geochimica Et Cosmochimica Acta*, 67, 325-343.

Shepherd, T., and Wynne Griffiths, D. (2006). The effects of stress on plant cuticular waxes. *New Phytologist*, 171(3), 469-499. https://doi.org/10.1111/j.1469-8137.2006.01826.x

Shi, M., Han, J., Wang, G., Wang, J., Han, Y., and Cui, L. (2021). A long-term investigation of the variation in leaf wax *n*-alkanes responding to climate on Dongling Mountain, north China. *Quaternary International*. https://doi.org/10.1016/j.quaint.2021.04.020

Shindell, D. T., Schmidt, G. A., Mann, M. E., Rind, D., and Waple, A. (2001). Solar forcing of regional climate change during the Maunder Minimum. *Science*, 294(5549), 2149-2152. https://doi.org/10.1126/science.1064363

Shuman, B.N. (2021). Approaches to paleoclimate reconstruction, p. 299-308. In Elias, S.A. and Mock, C.J. (eds.) *Encyclopedia of Geology* (second edition). Elsevier, 978-0-08-102909-1

Siedler, G., Gould, J., and Church, J. A. (2001). *Ocean circulation and climate: observing and modelling the global ocean*. Elsevier. ISBN: 0-12-641351-7

Sigl, M., Winstrup, M., McConnell, J. R., Welten, K. C., Plunkett, G., Ludlow, F., ... and Woodruff, T. E. (2015). Timing and climate forcing of volcanic eruptions for the past 2,500 years. *Nature*, 523(7562), 543-549. https://doi.org/10.1038/nature14565

Smith, A. C., Wynn, P. M., Barker, P. A., Leng, M. J., Noble, S. R., & Tych, W. (2016). North Atlantic forcing of moisture delivery to Europe throughout the Holocene. *Scientific Reports*, 6(1), 1-7. https://doi.org/10.1038/srep24745

Smith, F. A., and Freeman, K. H. (2006). Influence of physiology and climate on δD of leaf wax n-alkanes from C3 and C4 grasses. *Geochimica et Cosmochimica Acta*, 70(5), 1172-1187. https://doi.org/10.1016/j.gca.2005.11.006

Solanki, S. K. (2002). Solar variability and climate change: is there a link? *Astronomy and Geophysics*, 43(5), 5.09-5.13. https://doi.org/10.1046/j.1468-4004.2002.43509.x

Solanki, S. K., Usoskin, I. G., Kromer, B., Schüssler, M., and Beer, J. (2004). Unusual activity of the Sun during recent decades compared to the previous 11,000 years. *Nature*, 431(7012), 1084-1087. https://doi.org/10.1038/nature02995

Solomina, O. N., Bradley, R. S., Hodgson, D. A., Ivy-Ochs, S., Jomelli, V., Mackintosh, A. N., ... and Young, N. E. (2015). Holocene glacier fluctuations. *Quaternary Science Reviews*, 111, 9-34. https://doi.org/10.1016/j.quascirev.2014.11.018

Sprangers, M., Dammers, N., Brinkhuis, H., van Weering, T. C., and Lotter, A. F. (2004). Modern organic-walled dinoflagellate cyst distribution offshore NW Iberia; tracing the upwelling system. *Review of Palaeobotany and Palynology*, 128(1-2), 97-106. https://doi.org/10.1016/S0034-6667(03)00114-3

Steinhilber, F., Abreu, J. A., Beer, J., Brunner, I., Christl, M., Fischer, H., ... and Miller, H. (2012). 9,400 years of cosmic radiation and solar activity from ice cores and tree rings. *Proceedings of the National Academy of Sciences*, 109(16), 5967-5971. https://doi.org/10.1073/pnas.1118965109

Steinhilber, F., Beer, J., and Fröhlich, C. (2009). Total solar irradiance during the Holocene. *Geophysical Research Letters*, 36(19). https://doi.org/10.1029/2009GL040142

Stocker, T. F. (1998). The seesaw effect. *Science*, 282(5386), 61-62. https://doi.org/10.1126/science.282.5386.61

Stocker, T. F., and Johnsen, S. J. (2003). A minimum thermodynamic model for the bipolar seesaw. *Paleoceanography*, 18(4). https://doi.org/10.1029/2003PA000920

Stothers, R. B. (1984). Mystery cloud of AD 536. *Nature*, 307(5949), 344-345. https://doi.org/10.1038/307344a0

Stout, S. A. (2020). Leaf wax n-alkanes in leaves, litter, and surface soil in a low diversity, temperate deciduous angiosperm forest, Central Missouri, USA. *Chemistry and Ecology*, 1-17.

Summons, R. E., Albrecht, P., McDonald, G., and Moldowan, J. M. (2008). Molecular biosignatures. *Space Science Reviews*, 135(1-4), 133-159.

Tarroso, P., Carrión, J., Dorado-Valiño, M., Queiroz, P., Santos, L., Valdeolmillos-Rodríguez, A., ... and Cheddadi, R. (2016). Spatial climate dynamics in the Iberian Peninsula since 15 000 yr BP. *Climate of the Past*, 12(5), 1137-1149. https://doi:10.5194/cpd-10-3901-2014

Tejedor, E., de Luis, M., Cuadrat, J. M., Esper, J., and Saz, M. Á. (2016). Tree-ring-based drought reconstruction in the Iberian Range (east of Spain) since 1694. *International journal of biometeorology*, 60(3), 361-372. https://doi.org/10.1007/s00484-015-1033-7

Tejedor, E., Steiger, N. J., Smerdon, J. E., Serrano-Notivoli, R., and Vuille, M. (2021). Global hydroclimatic response to tropical volcanic eruptions over the last millennium. *Proceedings of the National Academy of Sciences*, 118(12). https://doi.org/10.1073/pnas.2019145118

Teller, J. T., Leverington, D. W., and Mann, J. D. (2002). Freshwater outbursts to the oceans from glacial Lake Agassiz and their role in climate change during the last deglaciation. *Quaternary Science Reviews*, 21(8-9), 879-887. https://doi.org/10.1016/S0277-3791(01)00145-7

Thatcher, D. L., Wanamaker, A. D., Denniston, R. F., Asmerom, Y., Polyak, V. J., Fullick, D., ... and Haws, J. A. (2020a). Hydroclimate variability from western Iberia (Portugal) during the Holocene: Insights from a composite stalagmite isotope record. *The Holocene*. https://doi.org/10.1177/0959683620908648

Thatcher, D. L., Wanamaker, A. D., Denniston, R. F., Ummenhofer, C. C., Regala, F. T., Jorge, N., ... and Gillikin, D. P. (2020b). Linking the karst record to atmospheric, precipitation, and vegetation dynamics in Portugal. *Chemical Geology*, 558, 119949.

Thiéblemont, R., Matthes, K., Omrani, N. E., Kodera, K., and Hansen, F. (2015). Solar forcing synchronizes decadal North Atlantic climate variability. *Nature communications*, 6(1), 1-8. https://doi.org/10.1038/ncomms9268

Thomas, C. L., Jansen, B., van Loon, E. E., and Wiesenberg, G. L. (2021). Transformation of n-alkanes from plant to soil: a review. *SOIL Discussions*, 1-40. https://doi.org/10.5194/soil-2020-107

Thomas, E. K., McGrane, S., Briner, J. P., and Huang, Y. (2012). Leaf wax δ2H and varve-thickness climate proxies from proglacial lake sediments, Baffin Island, Arctic Canada. *Journal of paleolimnology*, 48(1), 193-207. https://doi.org/10.1007/s10933-012-9584-7

Tierney, J. E., Smerdon, J. E., Anchukaitis, K. J., and Seager, R. (2013). Multidecadal variability in East African hydroclimate controlled by the Indian Ocean. *Nature*, 493(7432), 389-392. https://doi.org/10.1038/nature11785

Toney, J. L., García-Alix, A., Jiménez-Moreno, G., Anderson, R. S., Moossen, H., and Seki, O. (2020). New insights into Holocene hydrology and temperature from lipid biomarkers in western Mediterranean alpine wetlands. *Quaternary Science Reviews*, 240, 106395. https://doi.org/10.1016/j.quascirev.2020.106395

Toohey, M., Krüger, K., Sigl, M., Stordal, F., and Svensen, H. (2016). Climatic and societal impacts of a volcanic double event at the dawn of the Middle Ages. *Climatic Change*, 136(3), 401-412. https://doi.org/10.1007/s10584-016-1648-7

Torres, I. C., Inglett, P. W., Brenner, M., Kenney, W. F., and Reddy, K. R. (2012). Stable isotope (δ 13 C and δ 15 N) values of sediment organic matter in subtropical lakes of different trophic status. *Journal of Paleolimnology*, 47(4), 693-706. https://doi.org/10.1007/s10933-012-9593-6

Trigo, R. M., and DaCamara, C. C. (2000). Circulation weather types and their influence on the precipitation regime in Portugal. *International Journal of Climatology*: *A Journal of the Royal Meteorological Society*, 20(13), 1559-1581. https://doi.org/10.1002/1097-0088(20001115)20:13<1559::AID-JOC555>3.0.CO;2-5

Trigo, R. M., Osborn, T. J., and Corte-Real, J. M. (2002). The North Atlantic Oscillation influence on Europe: climate impacts and associated physical mechanisms. *Climate research*, 20(1), 9-17. https://doi.org/10.3354/cr020009

Trigo, R. M., Pozo-Vázquez, D., Osborn, T. J., Castro-Díez, Y., Gámiz-Fortis, S., and Esteban-Parra, M. J. (2004). North Atlantic Oscillation influence on precipitation, river flow and water resources in the Iberian Peninsula. *International Journal of Climatology: A Journal of the Royal Meteorological Society*, 24(8), 925-944. https://doi.org/10.1002/joc.1048

Trigo, R. M., Valente, M. A., Trigo, I. F., Miranda, P. M., Ramos, A. M., Paredes, D., and García-Herrera, R. (2008). The impact of North Atlantic wind and cyclone trends on European precipitation and significant wave height in the Atlantic. *Annals of the New York Academy of Sciences*, 1146(1), 212-234. https://doi.org/10.1196/annals.1446.014

Tsuda, T., Yamamoto, M., Hashiguchi, H., Shiokawa, K., Ogawa, Y., Nozawa, S., … Yoshikawa, A. (2016). A proposal on the study of solar-terrestrial coupling processes with atmospheric radars and ground-based observation network. *Radio Science*, 51(9), 1587–1599. https://doi.org/10.1002/2016RS006035

Turner, T. E., Swindles, G. T., Charman, D. J., Langdon, P. G., Morris, P. J., Booth, R. K., … Nichols, J. E. (2016). Solar cycles or random processes? Evaluating solar variability in Holocene climate records. *Scientific Reports*, 6(April). https://doi.org/10.1038/srep23961

van den Brink, L. M., and Janssen, C. R. (1985). The effect of human activities during cultural phases on the development of montane vegetation in the Serra de Estrela, Portugal. *Review of Palaeobotany and Palynology*, 44(3-4), 193-215. https://doi.org/10.1016/0034-6667(85)90016-8

van der Knaap, W. O., and Van Leeuwen, J. (1994). *Holocene vegetation, human impact, and climatic change in the Serra da Estrela, Portugal*. https://doi.org/10.7892/boris.81078

van der Knaap, W. O., and Van Leeuwen, J. F. N. (1995). Holocene vegetation succession and degradation as responses to climatic change and human activity in the Serra de Estrela, Portugal. *Review of Palaeobotany and Palynology*, 89(3-4), 153-211. https://doi.org/10.1016/0034-6667(95)00048-0

van der Knaap, W. O., and Van Leeuwen, J. F. N. (1997). Late Glacial and early Holocene vegetation succession, altitudinal vegetation zonation, and climatic change in the Serra da Estrela, Portugal. *Review of Palaeobotany and Palynology*, 97(3-4), 239-285. https://doi.org/10.1016/S0034-6667(97)00008-0

van Dijk, E., Jungclaus, J., Lorenz, S., Timmreck, C., and Krüger, K. (2021). Was there a volcanic induced long lasting cooling over the Northern Hemisphere in the mid 6th–7th century?. *Climate of the Past Discussions*, 1-33. https://doi.org/10.5194/cp-2021-49

van Geel, B., Bokovenko, N. A., Burova, N. D., Chugunov, K. V., Dergachev, V. A., Dirksen, V. G., ... and Vasiliev, S. S. (2004). Climate change and the expansion of the Scythian culture after 850 BC: a hypothesis. *Journal of Archaeological Science*, 31(12), 1735-1742. https://doi.org/10.1016/j.jas.2004.05.004

van Manen, M. L. T., Jansen, B., Cuesta, F., León-Yánez, S., and Gosling, W. D. (2020). From leaf to soil: n-alkane signal preservation, despite degradation along an environmental gradient in the tropical Andes. *Biogeosciences*, 17(21), 5465-5487. https://doi.org/10.5194/bg-17-5465-2020

Vasskog, K., Langebroek, P. M., Andrews, J. T., Nilsen, J. E. Ø., and Nesje, A. (2015). The Greenland Ice Sheet during the last glacial cycle: Current ice loss and contribution to sea-level rise from a palaeoclimatic perspective. *Earth-Science Reviews*, 150, 45–67. https://doi.org/10.1016/j.earscirev.2015.07.006

Vegas, R., de Vicente, G., Casas-Sainz, A., and Cloetingh, S. A. (2019). Alpine Orogeny: Intraplate Deformation. In The Geology of Iberia: A Geodynamic Approach (pp. 507-518). Springer, Cham. Vegas, R., de Vicente, G., Casas-Sainz, A., and Cloetingh, S. A. P. L. (2019). Alpine Orogeny: Intraplate Deformation. *Regional Geology Reviews*, 507–518. https://doi.org/10.1007/978-3-030-11295-0_12

Vieira, G. (2004). Geomorfologia dos planaltos e altos vales da Serra da Estrela: ambientes frios do Plistocénico Superior e dinâmica actual. Ph.D. thesis Universidade de Lisboa, Lisboa.

Vieira, G. (2008) Combined numerical and geomorphological reconstruction of the Serra da Estrela plateau icefield, Portugal. *Geomorphology,* 97, 190-207. https://doi.org/10.1016/j.geomorph.2007.02.042

Vieira, G. T., and Ferreira, A. B. (1998). General characteristics of the glacial geomorphology of the Serra da Estrela. Glacial and periglacial geomorphology of the Serra da Estrela. *Guidebook for the fieldtrip*, IGU Commission on Climate Change and Periglacial Environments, 26-28.

Vieira, G., and Nieuwendam, A. (2020). *Glacial and periglacial landscapes of the Serra da Estrela. In Landscapes and Landforms of Portuga*l (pp. 185-198). Springer, Cham. https://doi.org/10.1007/978-3-319-03641-0_27

Vieira, G., Ferreira, A. B., Mycielska-Dowgiallo, E., Woronko, B., and Olszak, I. (2001). *Thermoluminescence dating of fluvioglacial sediments* (Serra da Estrela, Portugal). V REQUI–I CQPLI, 23-27.

Vieira, G., Jansen, J., and Ferreira, N. (2005). Environmental setting of the Serra da Estrela, Portugal: a short-note. Landscape ecology series, IALE UK.

Vieira, G., Palacios, D., Andrés, N., Mora, C., Selem, L. V., Woronko, B., ... and Goyanes, G. (2021). Penultimate Glacial Cycle glacier extent in the Iberian Peninsula: New evidence from the Serra da Estrela (Central System, Portugal). *Geomorphology*, 388, 107781. https://doi.org/10.1016/j.geomorph.2021.107781

Vieira, L. E. A., Solanki, S. K., Krivova, N. A., & Usoskin, I. (2011). Evolution of the solar irradiance during the Holocene. *Astronomy & Astrophysics*, 531, A6. https://doi.org/10.1051/0004-6361/201015843

Vogts, A., Moossen, H., Rommerskirchen, F., and Rullkötter, J. (2009). Distribution patterns and stable carbon isotopic composition of alkanes and alkan-1-ols from plant waxes of African rain forest and savanna C3 species. *Organic Geochemistry*, 40(10), 1037-1054.

Volkman, J. K., Barrett, S. M., Blackburn, S. I., Mansour, M. P., Sikes, E. L., and Gelin, F. (1998). Microalgal biomarkers: a review of recent research developments. *Organic Geochemistry*, 29(5-7), 1163-1179. https://doi.org/10.1016/S0146-6380(98)00062-X

Volkman, J. K., Johns, R. B., Gillan, F. T., Perry, G. J., and Bavor Jr, H. J. (1980). Microbial lipids of an intertidal sediment—I. Fatty acids and hydrocarbons. Geochimica et Cosmochimica Acta, 44(8), 1133-1143. https://doi.org/10.1016/0016-7037(80)90067-8

von der Heydt, A. S., Ashwin, P., Camp, C. D., Crucifix, M., Dijkstra, H. A., Ditlevsen, P., and Lenton, T. M. (2020). Quantification and interpretation of the climate variability record. Global and Planetary Change, 103399. https://doi.org/10.1016/j.gloplacha.2020.103399

von Gunten, L., Grosjean, M., Kamenik, C., Fujak, M., and Urrutia, R. (2012). Calibrating biogeochemical and physical climate proxies from non-varved lake sediments with meteorological data: methods and case studies. *Journal of paleolimnology*, 47(4), 583-600. https://doi.org/10.1007/s10933-012-9582-9

Walczak, I. W., Baldini, J. U., Baldini, L. M., McDermott, F., Marsden, S., Standish, C. D., ... and Slater, J. (2015). Reconstructing high-resolution climate using CT scanning of unsectioned stalagmites: A case study identifying the mid-Holocene onset of the Mediterranean climate in southern Iberia. *Quaternary Science Reviews*, 127, 117-128. https://doi.org/10.1016/j.quascirev.2015.06.013

Walker, M. J., Berkelhammer, M., Björck, S., Cwynar, L. C., Fisher, D. A., Long, A. J., ... and Weiss, H. (2012). Formal subdivision of the Holocene Series/Epoch: a Discussion Paper by a Working Group of INTIMATE (Integration of ice-core, marine and terrestrial records) and the Subcommission on Quaternary Stratigraphy (International Commission on Stratigraphy). *Journal of Quaternary Science*, 27(7), 649-659. https://doi.org/10.1002/jqs.2565

Walker, M., Head, M. J., Berkelhammer, M., Björck, S., Cheng, H., Cwynar, L., ... and Weiss, H. (2018). Formal ratification of the subdivision of the Holocene Series/Epoch (Quaternary System/Period): two new Global Boundary Stratotype Sections and Points (GSSPs) and three new stages/subseries. *Episodes*, 41(4), 213-223. https://doi.org/10.18814/epiiugs/2018/018016

Walker, M., Johnsen, S., Rasmussen, S. O., Popp, T., Steffensen, J. P., Gibbard, P., ... and Cwynar, L. C. (2009). Formal definition and dating of the GSSP (Global Stratotype Section and Point) for the base of the Holocene using the Greenland NGRIP ice core, and selected auxiliary records. *Journal of Quaternary Science*: Published for the Quaternary Research Association, 24(1), 3-17.

Wanner, H., and Brönnimann, S. (2012). Is there a global Holocene climate mode?. PAGES news, (1), 44-45.

Wanner, H., Beer, J., Bütikofer, J., Crowley, T. J., Cubasch, U., Flückiger, J., ... and Küttel, M. (2008). Mid- to Late Holocene climate change: an overview. *Quaternary Science Reviews*, 27(19-20), 1791-1828. https://doi.org/10.1016/j.quascirev.2008.06.013

Wanner, H., Solomina, O., Grosjean, M., Ritz, S. P., and Jetel, M. (2011). Structure and origin of Holocene cold events. *Quaternary Science Reviews*, 30(21-22), 3109-3123. https://doi.org/10.1016/j.quascirev.2011.07.010

Warnes, M. G. R., Bolker, B., Bonebakker, L., Gentleman, R., and Huber, W. (2016). Package 'gplots'. Various R programming tools for plotting data.

Weber, S. L. (2001). The impact of orbital forcing on the climate of an intermediate-complexity coupled model. *Global and Planetary Change*, 30(1-2), 7-12. https://doi.org/10.1016/S0921-8181(01)00077-7

Weber, S. L., Crowley, T. J., and Van der Schrier, G. (2004). Solar irradiance forcing of centennial climate variability during the Holocene. *Climate Dynamics*, 22(5), 539-553. https://doi.org/10.1007/s00382-004-0396-y

Wei, T., Simko, V., Levy, M., Xie, Y., Jin, Y., and Zemla, J. (2017). Package 'corrplot'. *Statistician*, 56(316), e24.

Weiss, G. M., Lattaud, J., van der Meer, M. T., and Eglinton, T. I. (2021). Co-evolution of terrestrial and aquatic ecosystem structure with hydrological change in the Holocene Baltic Sea. *Climate of the Past Discussions*, 1-27. https://doi.org/10.5194/cp-2020-163

Weiss, H. (2017). 4.*2 ka BP megadrought and the Akkadian collapse, in: Megadrought and Collapse: from early agriculture to Angkor*. Oxford University Press, Oxford, 93–160. ISBN: 0199329214

Wirth, S. B., and Sessions, A. L. (2016). Plant-wax D/H ratios in the southern European Alps record multiple aspects of climate variability. *Quaternary Science Reviews*, 148, 176-191. https://doi.org/10.1016/j.quascirev.2016.07.020

Wirth, S. B., Glur, L., Gilli, A., and Anselmetti, F. S. (2013). Holocene flood frequency across the Central Alps–solar forcing and evidence for variations in North Atlantic atmospheric circulation. *Quaternary Science Reviews*, 80, 112-128. https://doi.org/10.1016/j.quascirev.2013.09.002

Wu, C., Tuo, J., Chen, R., Zhang, M., and Liu, Y. (2020). Relationships between Source Inputs and Lipid Geochemistry of Lake Sediments on the Northern Tibetan Plateau, China. *Geomicrobiology Journal*, 1-14. https://doi.org/10.1080/01490451.2020.1764674

Xie, M., Sun, Q., Dong, H., Liu, S., Shang, W., Ling, Y., ... and Chu, G. (2020). n-Alkanes and compound carbon isotope records from Lake Yiheshariwusu in the Hulun Buir sandy land, northeastern China. *The Holocene*, 30(10), 1451-1461. https://doi.org/10.1177/0959683620932968

Xie, S., Guo, J., Huang, J., Chen, F., Wang, H., and Farrimond, P. (2004). Restricted utility of δ13C of bulk organic matter as a record of paleovegetation in some loess–paleosol sequences in the Chinese Loess Plateau. *Quaternary Research*, 62(1), 86-93. https://doi:10.1016/j.yqres.2004.03.004

Zech, M., Buggle, B., Leiber, K., Marković, S., Glaser, B., Hambach, U., ... and Zöller, L. (2010). Reconstructing Quaternary vegetation history in the Carpathian Basin, SE-Europe, using n-alkane biomarkers as molecular fossils: Problems and possible solutions, potential and limitations. EandG *Quaternary Science Journal*, 58(2), 148-155. http://dx.doi.org/10.3285/eg.58.2.03

Zhang, Y., Su, Y., Liu, Z., Kong, L., Yu, J., and Jin, M. (2018). Aliphatic hydrocarbon biomarkers as indicators of organic matter source and composition in surface sediments from shallow lakes along the lower Yangtze River, Eastern China. *Organic Geochemistry*, 122, 29-40. https://doi.org/10.1016/0146-6380(87)90007-6

Zhong, Y., Miller, G. H., Otto-Bliesner, B. L., Holland, M. M., Bailey, D. A., Schneider, D. P., and Geirsdottir, A. (2011). Centennial-scale climate change from decadally-paced explosive volcanism: a coupled sea ice-ocean mechanism. *Climate Dynamics*, 37(11-12), 2373-2387. https://doi.org/10.1007/s00382-010-0967-z

Zhou, W., Xie, S., Meyers, P. A., and Zheng, Y. (2005). Reconstruction of late glacial and Holocene climate evolution in southern China from geolipids and pollen in the Dingnan peat sequence. *Organic Geochemistry*, 36(9), 1272-1284. https://doi.org/10.1016/j.orggeochem.2005.04.005

Zubiate, L., McDermott, F., Sweeney, C., and O'Malley, M. (2017). Spatial variability in winter NAO–wind speed relationships in western Europe linked to concomitant states of the East Atlantic and Scandinavian patterns. *Quarterly Journal of the Royal Meteorological Society*, 143(702), 552-562. https://doi.org/10.1002/qj.2943

9. ANNEXES

9.1. Core scan images

Figure A.56 – Half of the 'PEX 19' sediment cores in a color scan image with +25% luminosity. Total length: 8.43 m in length; width: 90 mm. The numbers identify the section number (1 – 5, from left to the right).

9.2. Pex15 and Pex19-01 diatom and biogenic silica data

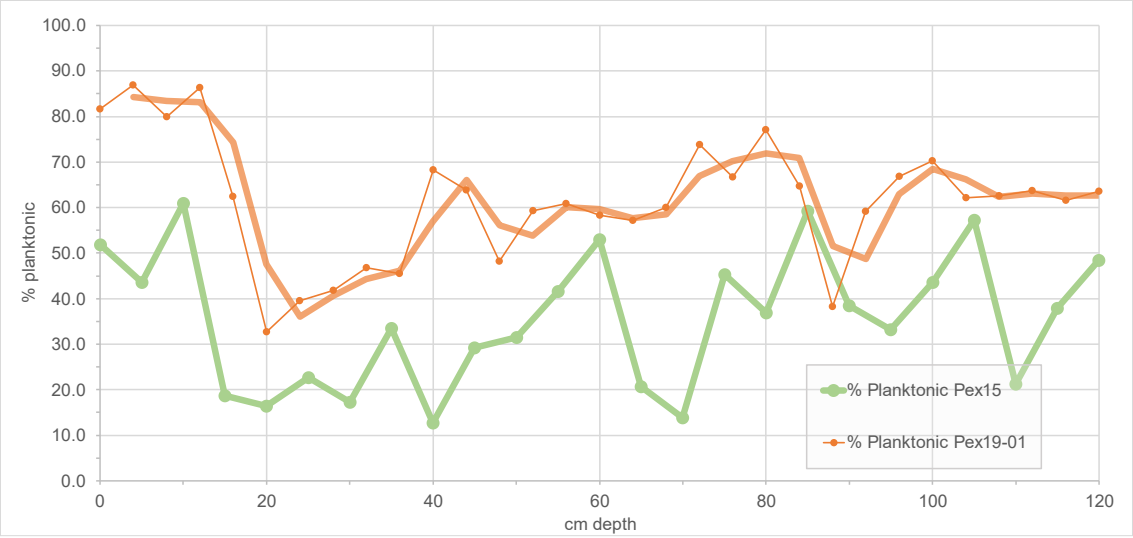

Figure A57 – Comparison in depth between planktonic diatoms of Pex19-01 and Pex15 cores. Orange bold line correspond to running averaged of 2 data points

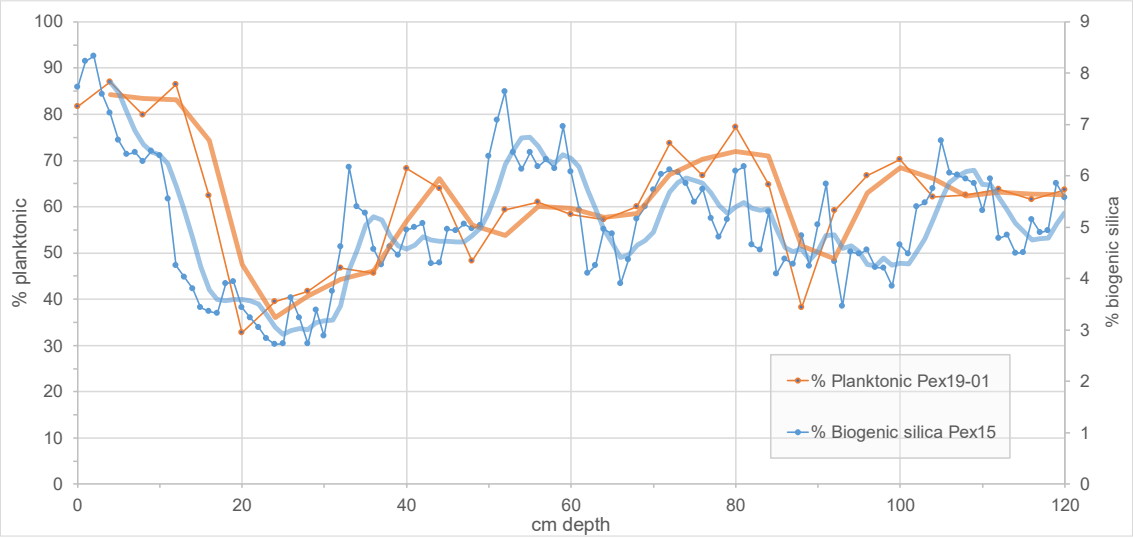

Figure A58 – Comparison in depth between planktonic diatoms of Pex19-01 and Biogenic silica of Pex15 core. Orange bold line correspond to running averaged of 2 data points, blue bold line corresponds to running averaged of 5 data points.

9.3. ACL_{dif} *vs.* Planktonic diatoms in Pex19-01

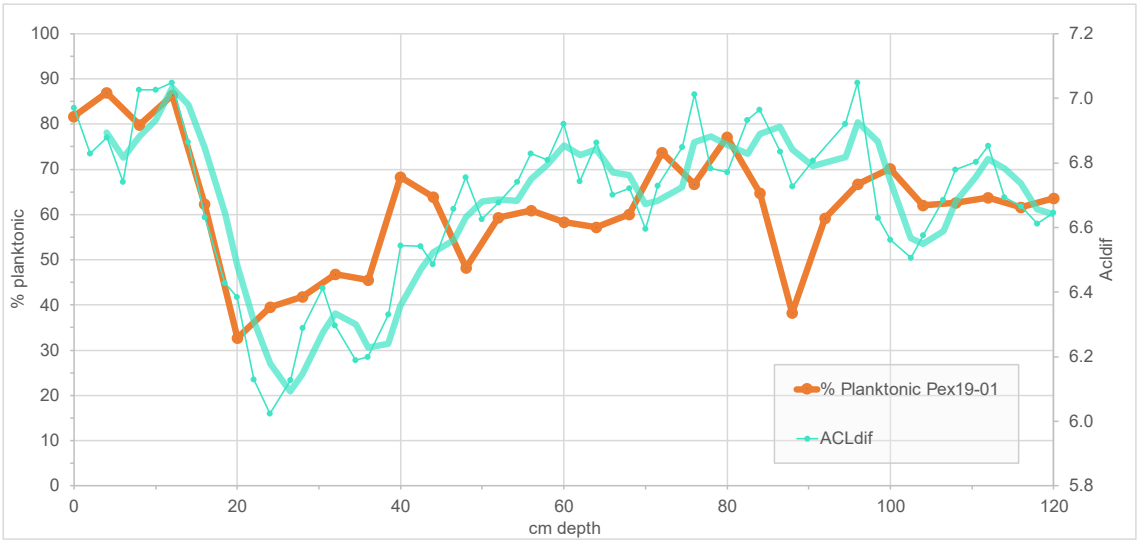

Figure A59 – Comparison in depth between planktonic diatoms of Pex19-01 and ACL_{dif}. Bue bold line corresponds to running averaged of 3 data points.

9.4. *n*-alkane distribution of dominant vegetation in Lake Peixão area

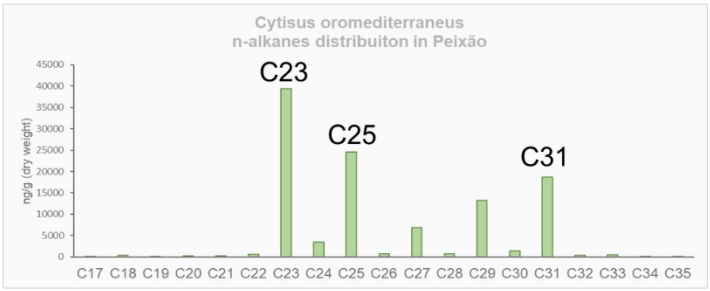

Figure A60 – n-alkane distribution of modern-day Cytisus oromediterraneus.

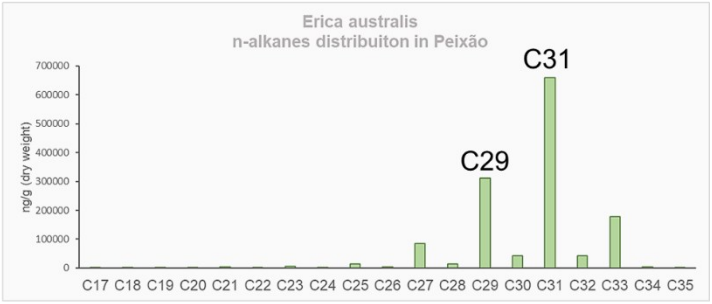

Figure A61 – n-alkane distribution of modern-day Erica australis.

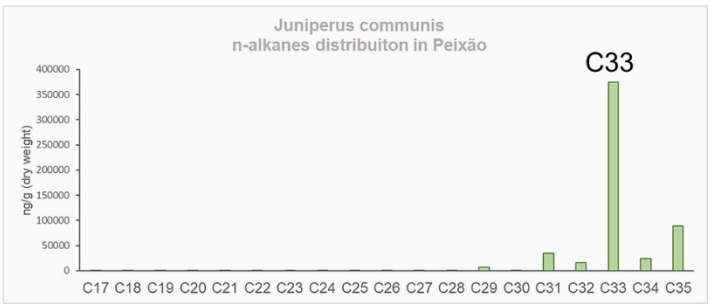

Figure A62 – n-alkane distribution of modern-day Juniperus communis.

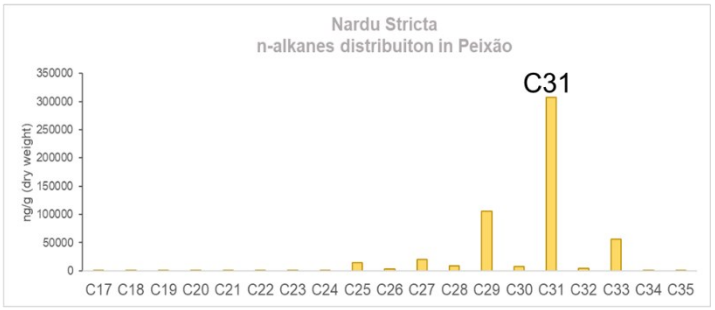

Figure A63 – n-alkane distribution of modern-day Nardus stricta.

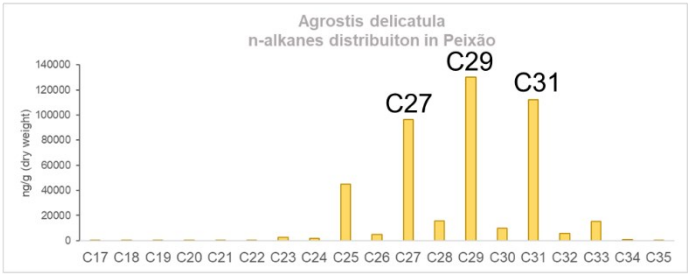

Figure A64 – n-alkane distribution of modern-day Agrostis delicatula.

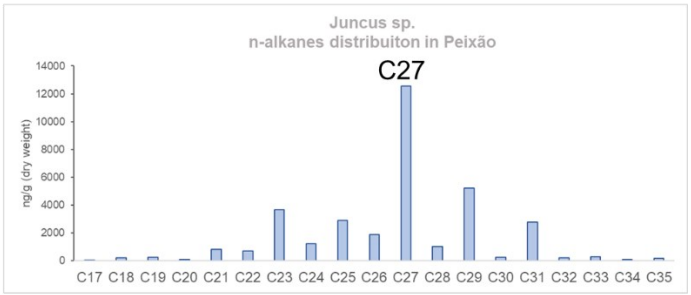

Figure A65 – n-alkane distribution of modern-day Juncus sp.

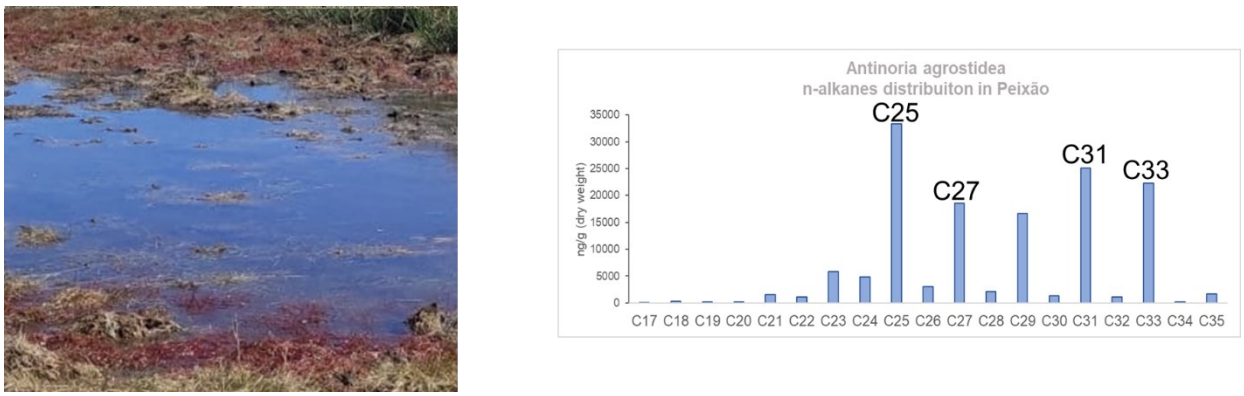

Figure A66 – n-alkane distribution of modern-day of water grasss Antinoria agrostidea (?).

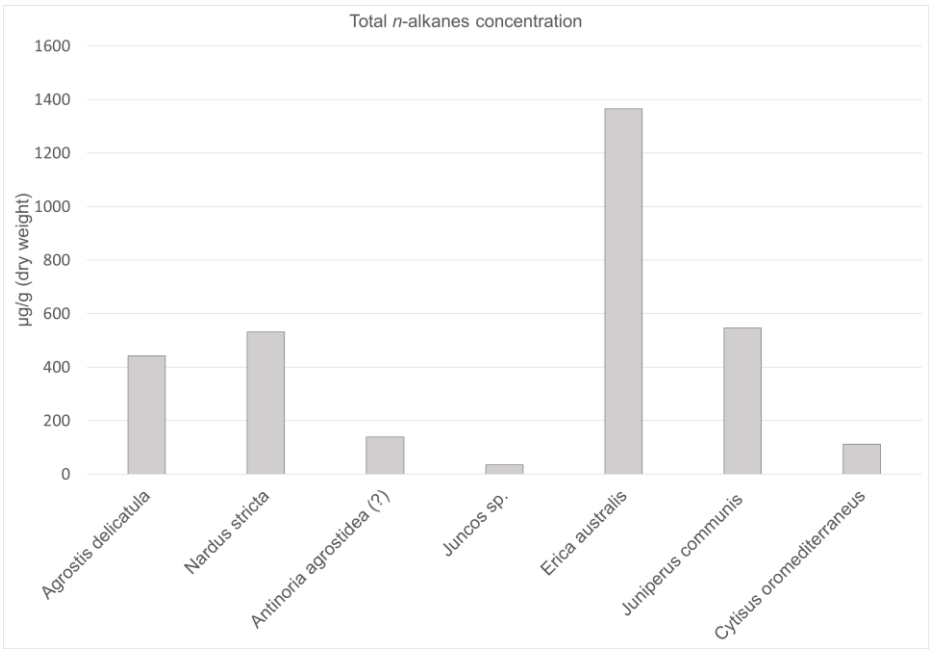

Figure A67 – Total n-alkanes extracted from modern-day dominant vegetation, concentration by dry weight.

9.5. PCA of sedimentary *n*-alkanes in Pex19-1

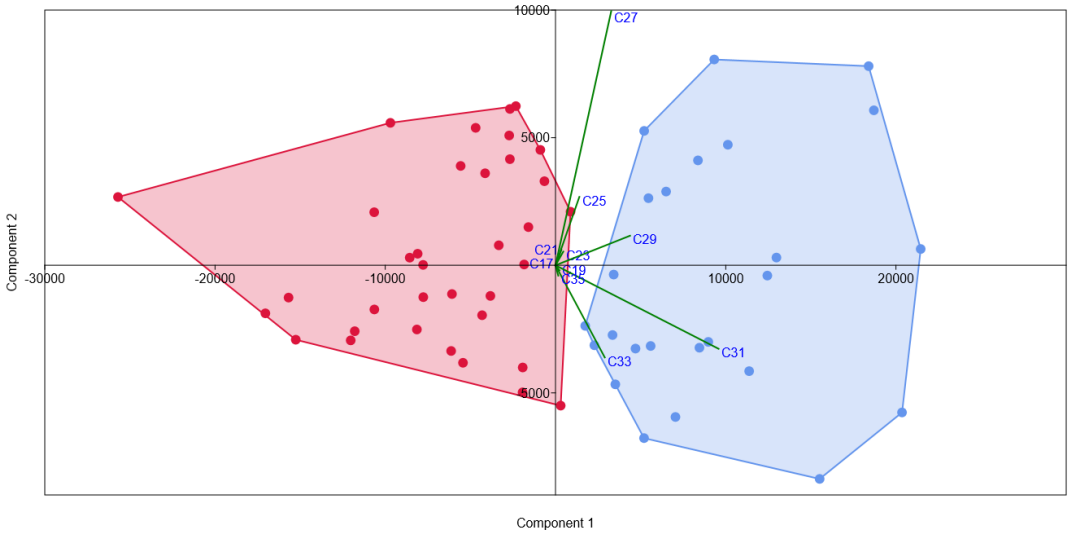

Figure A68 – Biplot diagram with PC1 and PC2 axis variations using the not normalized odd n-alkanes concentrations of Lake Peixão sediments for the last 2000 cal yrs BP. The colored convex hulls represent the two optimal data clusters within the data.

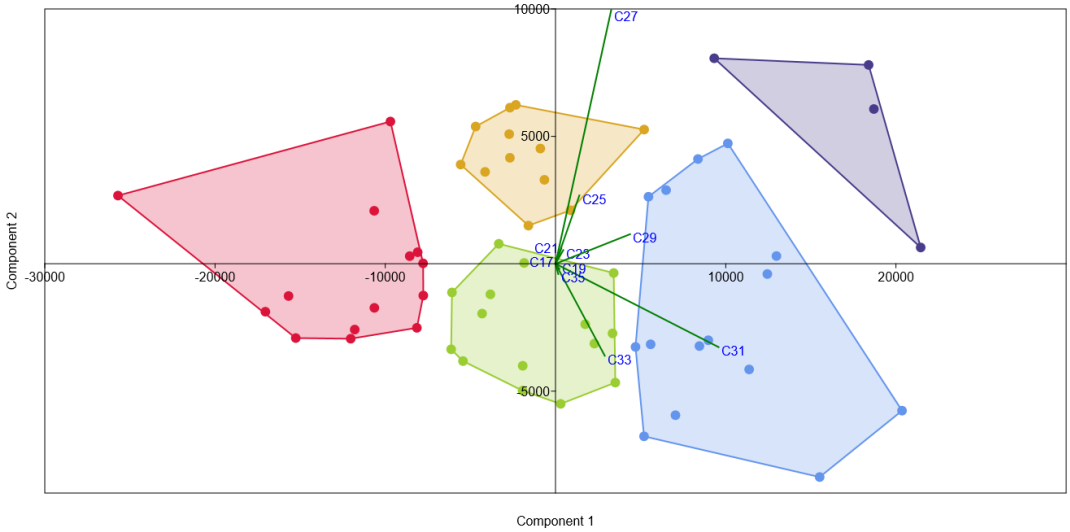

Figure A69 – Biplot diagram with PC1 and PC2 axis variations using the no normalized odd n-alkanes concentrations of Lake Peixão sediments for the last 2000 cal yrs BP. The colored convex hulls represent the 5 optimal data clusters within the data.

9.6. Examples of GC-chronograms for the PEX19-01

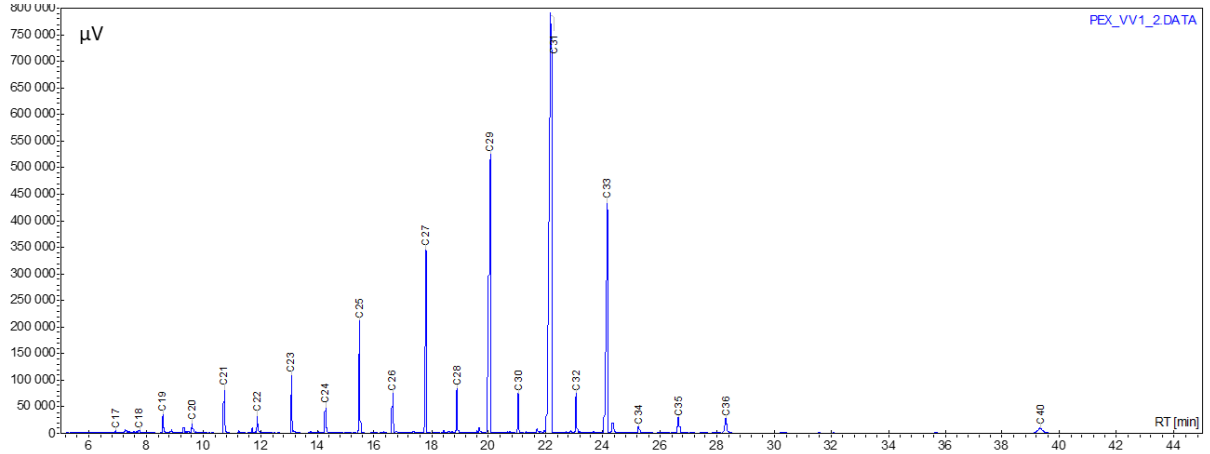

Figure A70 – GC- profile of the sample: PEX19-01_VV_1 (16-17 cm depth)

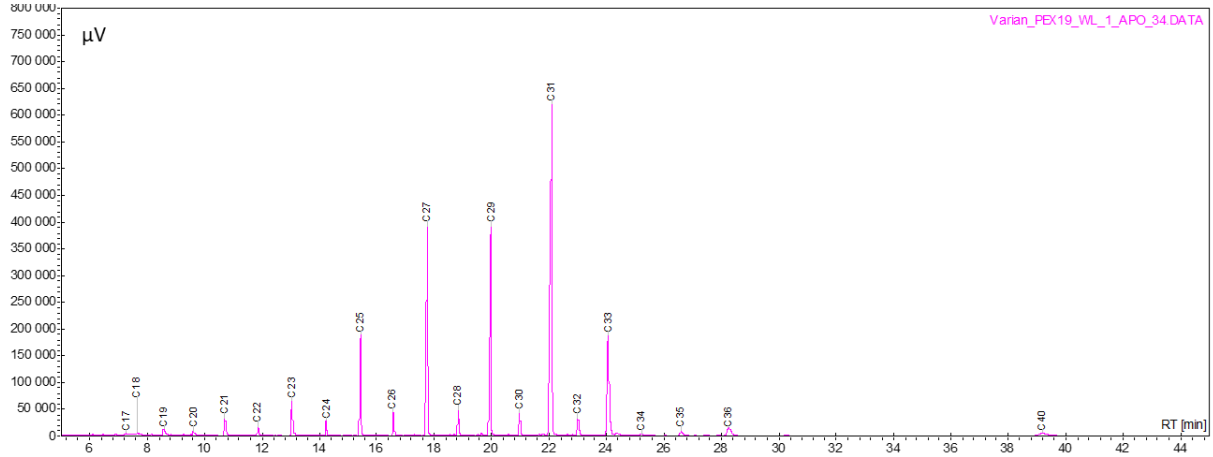

Figure A71 – GC- profile of the sample: PEX19-01_01_WL_1 (28-29 cm depth)

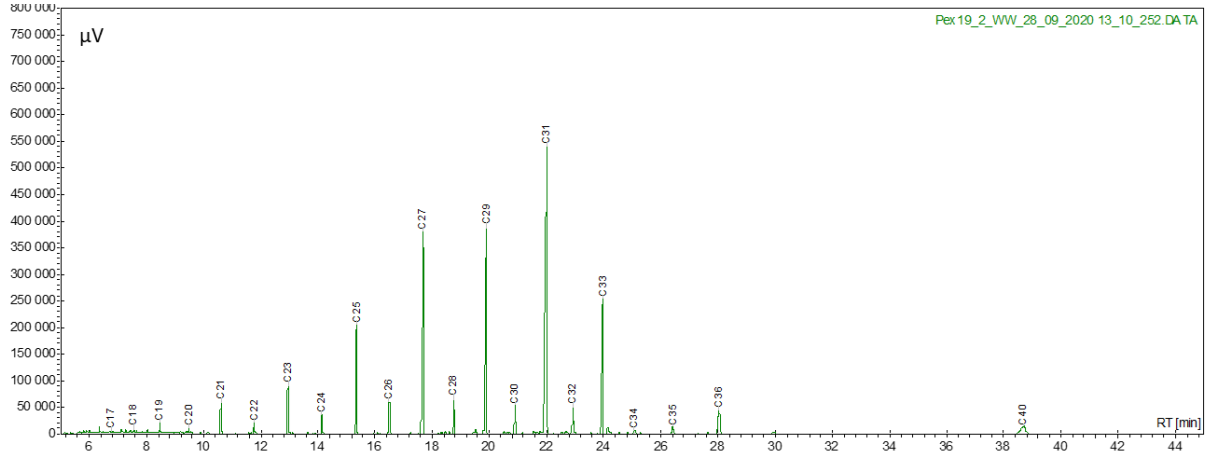

Figure A72 – GC- profile of the sample: PEX19-01_01_WW_2 (68-69 cm depth)

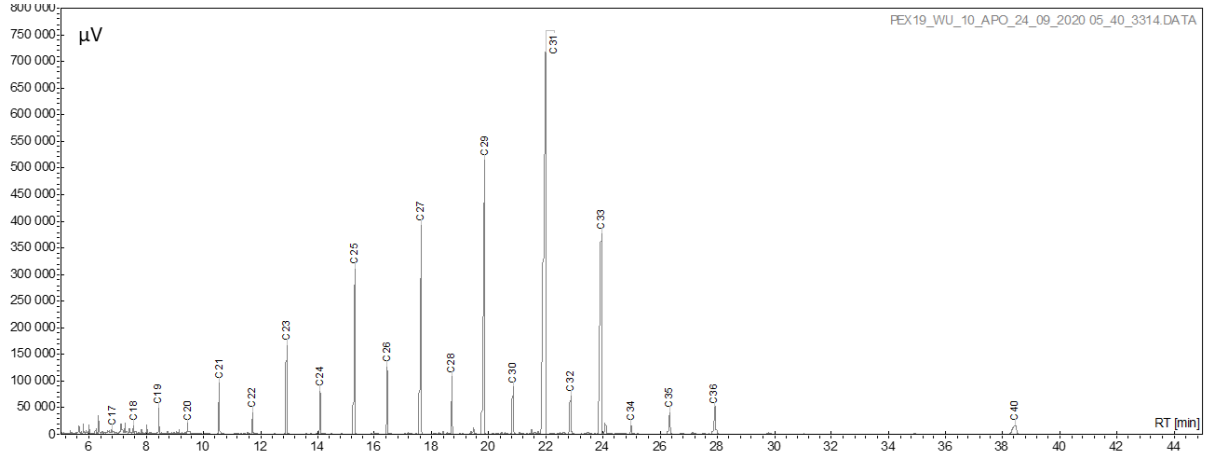

Figure A73 – GC- profile of the sample: PEX19-01_01_WU_10 (120-121 cm depth)

9.7. Abrupt Changes analysis

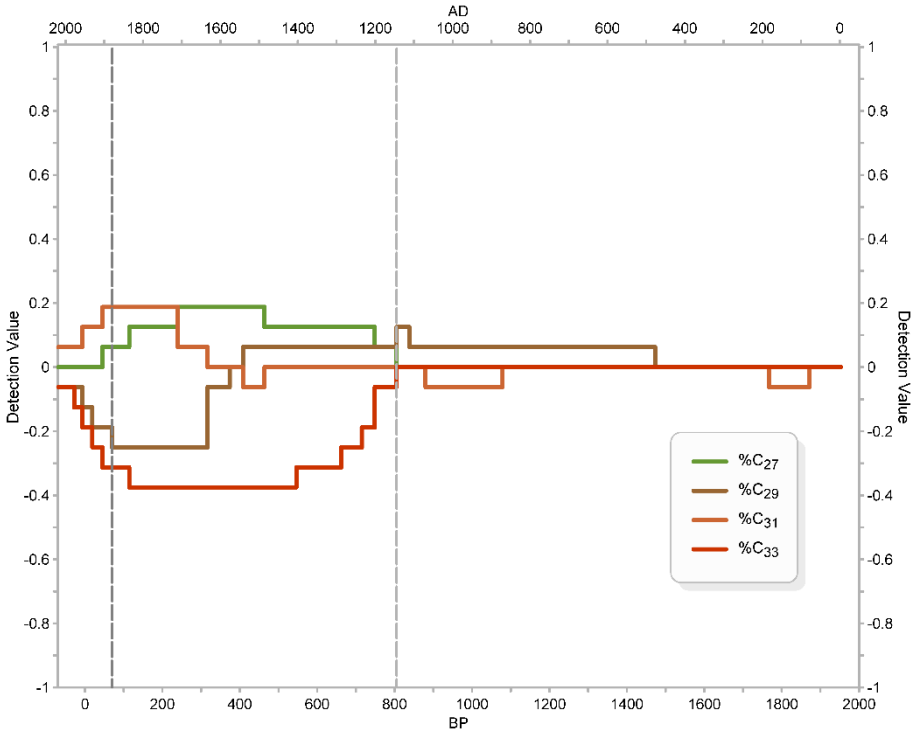

Figure A74 – Abrupt changes analysis performed on the relative percentage of the main n-alkanes of Pex19-01. The dashed lines represent general abrupt change events detected on the gradient of the indicators, with the darker line of 1880 indicating higher abruptness.

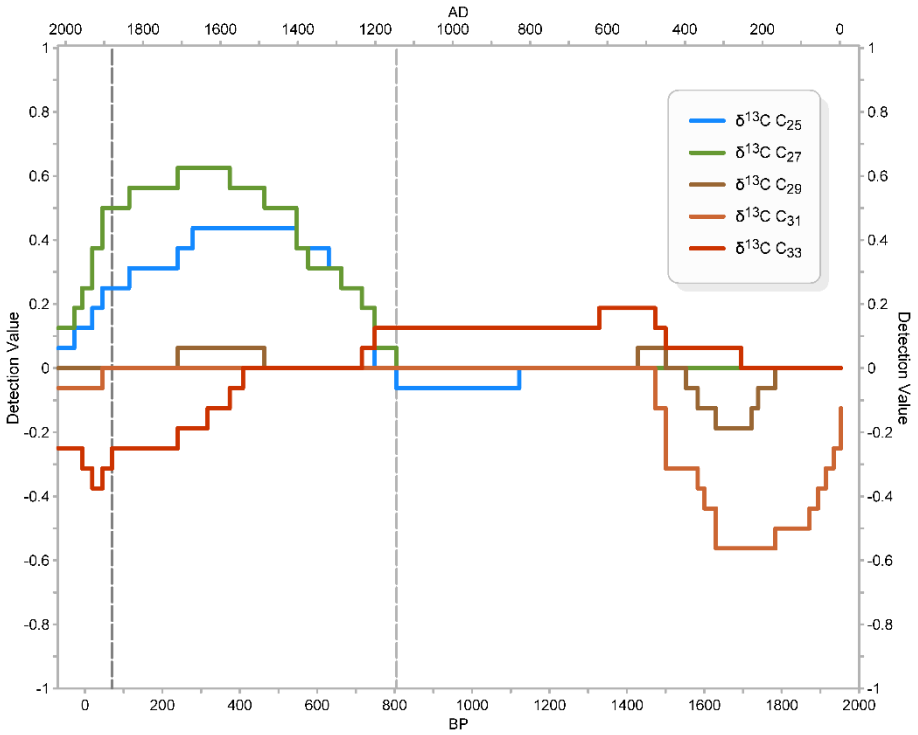

Figure A75 – Abrupt changes analysis performed on the $\delta^{13}C$ signal of C_{25} – C_{33} n-alkanes of Pex19-01. The dashed lines represent general abrupt change events detected on the gradient of the indicators, with the darker line of 1880 indicating higher abruptness.

9.8. Cross-correlation

Table A.7 – Cross-correlation between PC2 and TSI (LOESS 0.2) Steinhilber et al., 2012

Lag	*Correlation*	*p-value*
-30	0.10994	0.58515
-29	0.20476	0.29591
-28	0.29886	0.11529
-27	0.4268	0.018668
-26	0.57056	0.000804
-25	0.70179	7.62E-06
-24	0.83986	9.93E-10
-23	0.90963	9.46E-14
-22	0.90989	3.70E-14
-21	0.81757	1.16E-09
-20	0.6757	4.46E-06
-19	0.50899	0.001101
-18	0.38196	0.016418
-17	0.28358	0.076186
-16	0.23755	0.13478
-15	0.21441	0.17271
-14	0.2092	0.1782
-13	0.19602	0.20224
-12	0.17672	0.24552
-11	0.18573	0.21653
-10	0.22706	0.12483
-9	0.29759	0.039956
-8	0.34856	0.014111
-7	0.38846	0.005308
-6	0.38176	0.005705
-5	0.34342	0.012682
-4	0.26952	0.050982
-3	0.15002	0.2789
-2	0.019665	0.88668
-1	-0.11974	0.3794
0	-0.24446	0.066857
1	-0.35795	6.26E-03
2	-0.43978	6.20E-04
3	-0.50067	7.30E-05
4	-0.55457	9.21E-06
5	-0.62855	2.77E-07
6	-0.67489	2.19E-08
7	**-0.69203**	**9.52E-09**
8	-0.68739	1.82E-08
9	-0.62599	8.99E-07
10	-0.53273	6.82E-05
11	-0.43023	0.002032
12	-0.34848	0.015211
13	-0.28537	0.051853
14	-0.25906	0.08212
15	-0.3087	0.039091
16	-0.34447	0.022037
17	-0.34506	0.023441
18	-0.27184	0.081595

19	-0.20012	0.20966
20	-0.16206	0.31777
21	-0.13601	0.40903
22	-0.10716	0.52195
23	-0.04351	0.79821
24	0.047235	0.78442
25	0.16756	0.336
26	0.36866	0.03192
27	0.50326	0.002833
28	0.58032	0.000498
29	0.65983	5.39E-05
30	0.66836	5.42E-05